



THE UNIVERSITY
of ADELAIDE

**Production of Chemicals from Air Through
Electrocatalytic Nitrogen and Oxygen reduction**

By Laiquan Li

School of Chemical Engineering and Advanced Materials
Faculty of Engineering, Computer and Mathematical Science

A thesis submitted for the degree of Doctor of Philosophy.

The University of Adelaide

August 2021

Table of Contents

Abstract	1
Declaration	3
Acknowledgements	5
Chapter 1: Introduction	7
1.1 Significance of the Project	7
1.2 Research Objective	8
1.3 Thesis Outline	9
1.4 References	10
Chapter 2: Literature Review	11
2.1 Introduction and Significance	11
2.2 Main group elements boost electrochemical nitrogen reduction.	11
Chapter 3: Two-dimensional Mosaic Bismuth Nanosheets for Highly Selective Ambient Electrochemical Nitrogen Reduction	35
3.1 Introduction and Significance	35
3.2 Two-dimensional Mosaic Bismuth Nanosheets for Highly Selective Ambient Electrochemical Nitrogen Reduction	36
Chapter 4: Electrochemical Nitrogen Reduction: Identification and Elimination of Contamination from Electrolyte	69
4.1 Introduction and Significance	69
4.2 Electrochemical Nitrogen Reduction: Identification and Elimination of Contamination from Electrolyte	70
Chapter 5: Efficient Nitrogen Fixation to Ammonia through Integration of Plasma Oxidation with Electrochemical Reduction	89
5.1 Introduction and Significance	89
5.2 Efficient Nitrogen Fixation to Ammonia through Integration of Plasma Oxidation with Electrochemical Reduction.	90

Chapter 6: Tailoring Selectivity of Electrochemical Hydrogen Peroxide Generation by Tunable Pyrrolic-Nitrogen-Carbon	127
6.1 Introduction and Significance	127
6.2 Tailoring Selectivity of Electrochemical Hydrogen Peroxide Generation by Tunable Pyrrolic-Nitrogen-Carbon	128
Chapter 7: Conclusion and Perspective	161
7.1 Conclusions.....	161
7.2 Perspectives.....	162
Appendix: Publications during PhD Candidature	165

Abstract

The development of efficient energy conversion technologies, such as electrocatalysis process converting electricity derived from renewable energy to various forms of chemical energy, provides a highly desired pathway to produce transportable fuels and value-added chemicals from low-cost feedstocks like water and air, simultaneously to ease the fossil fuel reliance as well as the greenhouse gases emissions. Ammonia (NH_3) and hydrogen peroxide (H_2O_2) are globally important chemicals as basic building blocks in industry and promising carbon-free hydrogen carriers. Production of NH_3 from N_2 (NRR) or H_2O_2 from O_2 (2e^- ORR) through the sustainable and energy-saving electrocatalysis process are therefore highly meaningful. A crucial step in conducting these processes is to develop efficient electrocatalysts for effective activation of the reactants and selective formation of the desired products. Therefore, this Thesis aims to design and synthesize novel nanostructured materials as efficient electrocatalysts for nitrogen and oxygen reduction reactions. Besides the electrocatalyst engineering, energy devices combining various reactions/techniques are also elaborately designed as demonstration for future practical applications.

In this Thesis, a systematic review on the recent research progress for the application of main group elements on NRR is firstly provided by investigating their interaction with N_2 and the strategies for suppression of the undesired hydrogen evolution reaction (HER) (Chapter 2). This chapter provides a concise but comprehensive understanding on various reaction pathways for NRR and strategies towards N_2 activation and HER suppression.

The first part of this Thesis (Chapter 3 and 4) focus on a comprehensive optimization and accurate evaluation of NRR performance by investigating aspects such as electrocatalyst and electrolyte. Firstly, semiconducting bismuth nanosheet was for the first time reported to be promising candidate for ambient NRR. The high NRR electrocatalytic activity of the Bi NS

originates from the sufficient exposure of edge sites coupled with effective p-orbital electron delocalization. Secondly, trace amount of nitrate and nitrite were found to exist in some lithium salts such as Li_2SO_4 and LiClO_4 , which are usually used as electrolytes. Reduction of those nitrogen oxyanions (NO_x^-) causes false positive results for NRR. To avoid these false positive results and to make the best practice of NRR research, simple but versatile spectrophotometric methods were employed to quantitatively determine NO_x^- contaminations, followed by effective high-temperature annealing strategy to eliminate them.

The second part of this Thesis (Chapter 5) focus on exploration of novel strategy for efficient nitrogen fixation other than the present one-step NRR process. It is proposed that fixation of N_2 -to- NH_3 can be decoupled to a two-step process with one problem effectively solved in each step, in which facile activation of N_2 to NO_x^- is realized by a non-thermal plasma technique and highly selective conversion of NO_x^- to NH_3 by electrocatalytic reduction.

In the third part of this Thesis (Chapter 6), the electrochemical reduction of O_2 via a two-electron reaction pathway for sustainable and decentralized H_2O_2 production was investigated on a nitrogen-rich few-layered graphene (N-FLG). A positive correlation between the content of pyrrolic-N and the H_2O_2 selectivity is experimentally observed. The critical role of pyrrolic-N is elucidated by the variable intermediate adsorption profiles as well as the dependent negative shifts of the pyrrolic-N peak on X-ray absorption near edge structure spectra. A practical device coupling electrochemical H_2O_2 production with furfural oxidation was then assembled to achieve high-value products on both anode and cathode with optimized energy efficiency.

Declaration

I certify that that this work contains no material which has been accepted for the award of any other degree or diploma in my name, in any university or other tertiary institution and, to the best of my knowledge and belief, contains no material previously published or written by another person, except where due reference has been made in the text. In addition, I certify that no part of this work will, in the future, be used in a submission in my name, for any other degree or diploma in any university or other tertiary institution without the prior approval of the University of Adelaide and where applicable, any partner institution responsible for the joint-award of this degree.

I acknowledge that copyright of published works contained within this thesis resides with the copyright holder(s) of those works.

I also give permission for the digital version of my thesis to be made available on the web, via the University's digital research repository, the Library Search and also through web search engines, unless permission has been granted by the University to restrict access for a period of time.

Name of Candidature: Laiquan Li

Signature: _____

Date: 29/07/2021

Acknowledgements

First and foremost, I would like to convey my sincere appreciation to my principal supervisor, Prof. Shi-Zhang Qiao, and my co-supervisor, A/Prof. Yao Zheng for their unwavering support and encouragement throughout my PhD study. Prof. Qiao has enlightened me in the past four years with his profound knowledge, dedication to work, enthusiasm for research and rigorous academic attitude. I also thank A/Prof. Yao Zheng for his insightful suggestions and continuous guidance on how to do research in a right and smart way.

In the past several years, I have received warm companionship and strong support from my colleagues. My deepest gratitude goes to Dr. Cheng Tang, who has been an incredible source of encouragement, support, and guidance to me. I would also like to extend my thanks to other colleagues including: A/Prof. Yan Jiao, Dr. Dongliang Chao, Dr. Anthony Vasileff, Dr. Dongdong Zhu, Dr. Fangxi Xie, Dr. Xuesi Wang, Dr. Huanyu Jin, Dr. Chao Ye, Dr. Junnan Hao, Dr. Pengtang Wang, Dr. Jieqiong Shan, Dr. Xing Zhi, Dr. Xin Liu, Mr. Bingquan Xia, Mr. Huan Li, Mr. Xianlong Zhou, Ms. Xin Xu, Mr. Dazhi Yao, Mr. Yanzhao Zhang and Mr Chun-Chuan Kao for their generous help and enlightening discussions.

I owe my appreciation to several research and technical staff whose hard work greatly assisted the completion of this Thesis. Special thanks go to Dr. Qiuhong Hu for her generous support with the analytical equipment, Dr. Ashley Slattery and Mr. Ken Neubauer for TEM and SEM imaging. Prof. Tao Shao, Prof. Shuai Zhang, and Dr. Xiaoyang Cui from Chinese Academy of Science for their collaboration on Plasma experiment. Prof. Haolan Xu and Dr. Ting Gao at the University of South Australia for their help with XPS measurement. Dr. Kenneth Davey for his generous help with manuscript revision and his professional suggestions on my career development.

Friendship made my life in Adelaide more colourful. To Eddie, Fei, Eva, and Mia, thank you for your companion and I appreciate the happy hours spent together with you. To Mr. Stephen Bone, thank you for those “culture cultivation” sessions, which made me have a deeper understanding in Australian culture and learn to view and think in a different way towards the world.

Last but not least, I am forever grateful to my families for their continuous love and support. To Mum, Dad, and Liang, thank you for your unconditional love and belief in me. To my wife Hongyu, who gives me perpetual happiness and the belief in wonderful future, thank you for your continual love and healing encouragement.

Chapter 1: Introduction

1.1 Significance of the Project

Compared to traditional fossil-fuel driven industry, the emerging electrocatalytic refinery serves as a more reliable, sustainable and environmentally friendly approach to transform renewable energy and low-cost feedstocks into transportable fuels and value-added chemicals.¹ For example, the electrocatalytic N₂ reduction to NH₃ (NRR) provides a possibility for replacing the traditional Haber-Bosch process and the electrocatalytic reduction of O₂ via a two-electron pathway to H₂O₂ (2e⁻ ORR) could be a promising alternative for the current anthraquinone process.^{2,3} Both NRR and 2e⁻ ORR provide not only green and sustainable, but also decentralized and scalable approach for on-site/-demand production of value-added chemicals (NH₃, H₂O₂). These electrochemical refinery reactions could facilitate the development of electrochemical industry to produce high value chemicals and important commodities from low-cost feedstocks powered by renewable energy sources.

A key bone of this blueprint is to develop efficient electrocatalysts with high activity, selectivity, and stability for the desired transformation reactions. In recent years, various strategies have been developed to design materials with multiple dimensions and various surface properties. For example, two-dimensional (2D) materials with unique electronic structure and tunable exposed facet has recently attracted much attention as electrocatalysts.⁴ Since the electrochemical reactions happen on the solid-liquid interface between electrode and electrolyte, the surface properties of the electrocatalysts are vital for binding key reaction intermediates, thus greatly impact the selectivity and activity.⁵ To effectively tune the surface properties, tactics such as alloying, defect engineering, heteroatom doping, facet engineering constructing core-shell structure, etc have shown great effectiveness.⁶

Besides the rational design and synthesis of materials, advances in surface characterization techniques are vital to bridge the gap in mechanistic understanding of electrolysis process. For example, physical characterizations such as scanning/transmission electron microscopy, X-ray photoelectron spectroscopy and synchrotron-based X-ray absorption spectroscopy allow confirmation of structure and composition of the electrocatalyst. In-situ spectroscopic techniques such as surface enhanced Raman spectroscopy (SERS) and surface enhanced infrared spectroscopy (SEIRS) can provide meaningful information about the species produced on the heterogenous interface during the electrocatalysis process.⁷ Therefore, this Thesis aims at design and synthesis of advanced electrocatalysts for production of transportable fuels and value-added chemicals. Meanwhile, combining electrochemical measurement with a series of ex-situ and in-situ characterizations, reaction mechanisms are investigated in detail and expected to inspire future advances in electrocatalysis.

1.2 Research Objective

The major aim of this Thesis is to produce transportable fuels and value-added chemicals through electrocatalysis from renewable feedstocks like water and air. This requires development of efficient electrocatalysts and comprehensive understanding on reaction mechanisms. In this regard, a combination of materials synthesis, physical characterizations, electrochemical measurement and in situ spectroscopy is employed to study the structure-activity relationship. In particular, the objectives of this Thesis are:

To design two-dimensional nanostructured materials as electrocatalysts for NRR.

To identify and eliminate the contamination in commonly used electrolyte in NRR for more rigorous measurement and product quantification practice.

To explore a system integration between plasma oxidation with electrocatalytic reduction for N₂ fixation that simultaneously solves N₂ activation and ensures NH₃ selectivity.

To tailor the selectivity of electrochemical hydrogen peroxide generation by tunable pyrrolic-nitrogen-carbon.

To assemble a practical device for production of valuable chemicals on both anode and cathode.

1.3 Thesis Outline

This Thesis is presented in the form of journal publications. It contains several research findings on electrocatalytic NRR and $2e^-$ ORR. Novel nanomaterials were designed and synthesized to produce NH_3 and H_2O_2 from electrocatalytic reduction of nitrogen and oxygen, respectively. Recent progress and challenges for the application of the main-group elements on nitrogen reduction reaction were reviewed followed by exploring the application of several nanomaterials in electrocatalysis. Specifically, the chapters in the Thesis are presented in the following sequence:

Chapter 1 introduces the significance of this project and outlines the research objectives and key contributions to the field of electrocatalysis.

Chapter 2 reviews the recent progress and challenges for the application of main-group elements on nitrogen reduction reaction.

Chapter 3 presents two-dimensional mosaic bismuth nanosheets for highly selective ambient electrocatalytic nitrogen reduction.

Chapter 4 identifies and eliminates contamination in electrolyte for nitrogen reduction reaction.

Chapter 5 reports efficient nitrogen fixation to ammonia through integration of plasma oxidation with electrocatalytic reduction.

Chapter 6 tailors the selectivity of electrochemical hydrogen peroxide generation by tunable pyrrolic-nitrogen-carbon.

Chapter 7 presents the conclusion and perspectives for future work on design and application of novel nanomaterials for electrocatalysis.

1.4 References

1. Tang, C.; Zheng, Y.; Jaroniec, M.; Qiao, S.-Z., Electrocatalytic Refinery for Sustainable Production of Fuels and Chemicals. *Angew Chem Int Ed* **60**, DOI: 10.1002/anie.202101522.
2. Jia, H. P.; Quadrelli, E. A., Mechanistic Aspects of Dinitrogen Cleavage and Hydrogenation to Produce Ammonia in Catalysis and Organometallic Chemistry: Relevance of Metal Hydride Bonds and Dihydrogen. *Chem Soc Rev* **2014**, *43* (2), 547-564.
3. Perry, S. C.; Pangotra, D.; Vieira, L.; Csepei, L.-I.; Sieber, V.; Wang, L.; Ponce de León, C.; Walsh, F. C., Electrochemical Synthesis of Hydrogen Peroxide from Water and Oxygen. *Nat. Rev. Chem.* **2019**, *3* (7), 442-458.
4. Chia, X.; Pumera, M., Characteristics and Performance of Two-dimensional Materials for Electrocatalysis. *Nat Catal* **2018**, *1* (12), 909-921.
5. Stamenkovic, V. R.; Strmcnik, D.; Lopes, P. P.; Markovic, N. M., Energy and Fuels from Electrochemical Interfaces. *Nat Mater* **2017**, *16* (1), 57-69.
6. Jin, H.; Guo, C.; Liu, X.; Liu, J.; Vasileff, A.; Jiao, Y.; Zheng, Y.; Qiao, S.-Z., Emerging Two-Dimensional Nanomaterials for Electrocatalysis. *Chem Rev* **2018**, *118* (13), 6337-6408.
7. Malkani, A. S.; Anibal, J.; Chang, X.; Xu, B., Bridging the Gap in the Mechanistic Understanding of Electrocatalysis via In Situ Characterizations. *iScience* **2020**, *23* (12), 101776.

Chapter 2: Literature Review

2.1 Introduction and Significance

Electrocatalytic nitrogen reduction reaction (NRR) is widely recognized as a promising alternative to traditional Haber-Bosch process. Despite the rapid progress in recent years, the application of NRR is still suffering from low Faradaic efficiency and low ammonia yield due to the high energy barrier of N_2 activation, the low solubility of N_2 in aqueous solutions and the competing HER. To address these issues, selection of catalyst materials that can effectively activate the inert N_2 and meanwhile restrain the HER is indispensable. Main group elements with partially occupied valence p orbitals and intrinsic poor hydrogen adsorption ability could provide more ideal active centres for nitrogen activation and fixation.

In this Chapter, mechanisms for main group elements-based electrocatalysts boosting N_2 activation are comprehensively summarized, mainly including Lewis acid-base interaction, p-electron backdonation, Li-mediated pathway, vacancy engineering and heteroatoms doping. Meanwhile, mechanisms for HER suppression are also discussed. Namely, intrinsic poor proton binding, limiting the electron accessibility, constructing hydrophobic layer and electrolyte engineering and ions effect. This literature review provides a concise but comprehensive understanding on various reaction mechanisms for NRR and strategies towards N_2 activation and HER suppression, which is expected to inspire the future catalyst design for NRR. Highlights of this work include:

1. *First Review of MGEs for boosted NRR.* We critically assess and comparatively summarize MGEs-based materials design and regulating strategies for optimal NRR

- performance. We do this by identifying the functional mechanisms for boosted NRR and suppressed HER rather than enumerating catalysts by elements, or type.
2. *Comprehensive strategies in electrolyte and interface based on MGEs.* We critically assess and compare methods for engineering and optimization of electrolyte and electrode surface based on MGEs. We show how these can be gainfully used to boost NRR.
 3. *Universal principles and methodologies to explore new catalysts and strategies.* We show that MGEs-based functional mechanisms are generalizable, and how they might be judiciously applied as a basis for smart design of advanced catalyst materials for N₂ fixation.


2.2 Main group elements boost electrochemical nitrogen reduction.

This Chapter is included as it appears as a journal paper in preparation for publication by Laiquan Li, Cheng Tang, Huanyu Jin, and Shizhang Qiao. Main group elements boost electrochemical nitrogen reduction. Minor revision before acceptance.

Statement of Authorship

Title of Paper	Main Group Elements Boost Electrochemical Nitrogen Fixation
Publication Status	<input type="checkbox"/> Published <input type="checkbox"/> Accepted for Publication <input checked="" type="checkbox"/> Submitted for Publication <input type="checkbox"/> Unpublished and Unsubmitted work written in manuscript style
Publication Details	Laiquan Li, Cheng Tang, Huanyu Jin, Kenneth Davey, Shizhang Qiao. Main group elements boost electrochemical N ₂ fixation. Minor revision before acceptance.


Principal Author


Name of Principal Author (Candidate)	Laiquan Li		
Contribution to the Paper	Proposed the review topic, reviewed and organised the literatures, and wrote the manuscript.		
Overall percentage (%)	80		
Certification:	This paper reports on original research I conducted during the period of my Higher Degree by Research candidature and is not subject to any obligations or contractual agreements with a third party that would constrain its inclusion in this thesis. I am the primary author of this paper.		
Signature	 <table border="1" style="float: right; margin-left: 20px;"> <tr> <td>Date</td> <td>05/09/2021</td> </tr> </table>	Date	05/09/2021
Date	05/09/2021		

Co-Author Contributions

By signing the Statement of Authorship, each author certifies that:

- i. the candidate's stated contribution to the publication is accurate (as detailed above);
- ii. permission is granted for the candidate to include the publication in the thesis; and
- iii. the sum of all co-author contributions is equal to 100% less the candidate's stated contribution.

Name of Co-Author	Cheng Tang		
Contribution to the Paper	Helped to revise the manuscript and organise the figures.		
Signature	 <table border="1" style="float: right; margin-left: 20px;"> <tr> <td>Date</td> <td>05/09/2021</td> </tr> </table>	Date	05/09/2021
Date	05/09/2021		

Name of Co-Author	Huanyu Jin		
Contribution to the Paper	Helped to revised the manuscript.		
Signature	 <table border="1" style="float: right; margin-left: 20px;"> <tr> <td>Date</td> <td>05/09/2021</td> </tr> </table>	Date	05/09/2021
Date	05/09/2021		

Name of Co-Author	Kenneth Davey		
Contribution to the Paper	Helped to evaluate and edit the manuscript.		
Signature		Date	05/09/2021

Name of Co-Author	Shi-Zhang Qiao		
Contribution to the Paper	Supervised development of work, helped in manuscript evaluation and acted as corresponding author		
Signature		Date	05/09/2021

Review

Main Group Elements Boost Electrochemical Nitrogen Fixation

Laiquan Li,¹ Cheng Tang,^{1,*} Huanyu Jin,¹ Kenneth Davey,¹ and Shi-Zhang Qiao^{1,2,*}¹School of Chemical Engineering and Advanced Materials, The University of Adelaide, SA 5005, Australia

*Correspondence: s.qiao@adelaide.edu.au (S.Q.), cheng.tang@adelaide.edu.au (C.T.)

SUMMARY

Renewable energy-derived electrocatalytic nitrogen reduction reaction (NRR) is practically promising for production of green ammonia (NH₃), an important chemical for sustainability and carbon-neutrality in global agriculture and energy demand. However, application of NRR is limited by low Faradaic efficiency and NH₃ yield because of a high-energy barrier for N₂ activation and competing hydrogen evolution reaction (HER). In contrast to widely investigated transition metals, main group elements (MGEs) with manifold physicochemical properties and intrinsically poor hydrogen adsorption ability could provide superiority to address the above challenges. In this Review we: 1) Critically assess the use of MGEs in NRR by identifying the functional mechanism of boosting NRR and suppressing HER, rather than by catalyst elements or type; 2) Present a comprehensive summary of methodologies for N₂ activation and HER suppression, which are generalizable to advanced catalysts for N₂ fixation, and; 3) Show MGEs-based mechanisms that can be judiciously applied for smart design of highly active and selective materials, electrolytes, and interface for electrocatalytic N₂ reduction. We conclude that MGEs can significantly boost electrochemical N₂ fixation. Findings will be of interest to a wide range of researchers to guide practical development in electrochemical N₂ fixation.

KEYWORDS: main group elements, Lewis acid, p-electron backdonation, hydrogen evolution suppression, vacancy engineering, heteroatom doping, lithium mediation

INTRODUCTION

Ammonia (NH₃) is an important and globally produced chemical (>175 million tonne annually). As a building block for fertilizers it underpins agriculture to grow food for some half of the global population.¹ It is a practically promising carrier for renewable energies because of its high hydrogen content (17.7 wt.%), high gravimetric energy density (3 kWh kg⁻¹), carbon-free feature, and mature technologies for storage, transportation and operation.² The Haber-Bosch (HB) process dominates industrial synthesis of NH₃. However drawbacks include, that it uses fossil fuel-derived hydrogen, consumes large amounts of energy that accounts for 1–2% of global consumption and around 1% of greenhouse gas emissions.³ For a sustainable and carbon neutral future, next-generation NH₃ synthesis should be efficient, environmentally friendly, compatible with intermittent renewable energies, and operated at mild conditions. Amongst various artificial nitrogen fixation methods, electrocatalytic nitrogen (N₂) reduction reaction (NRR) driven by renewable electricity has emerged as a practically attractive approach with significant advantages, including mild reaction conditions, variable proton sources and simplified reaction infrastructure.⁴ However, NRR is currently limited by low Faradaic efficiency (FE) and low NH₃ yield as a result of the high energy barrier for N₂ activation, low solubility of N₂ in aqueous solutions, and competing hydrogen evolution reaction (HER).^{5,6}

Current strategies to address these issues have focused on catalyst design for effective N₂ activation and concomitant HER suppression.⁷ Transition metals (TMs)-based electrocatalysts e.g. Fe, Mo, V and Ti are widely investigated owing to their considerable activity for N₂

The bigger picture

As the precursor for nitrogen-rich fertilizers, ammonia (NH₃) is globally important. The widely used Haber-Bosch process for industrial production requires harsh operating conditions and relies on fossil fuels that increase global energy consumption and greenhouse gas emission. The renewable energy-derived electrocatalytic nitrogen reduction reaction (NRR) that produces green NH₃ under mild conditions is a promising alternative. However, high-energy barrier for N₂ activation and competing hydrogen evolution reaction (HER) limits practical application of NRR.

Solutions lie on the development of novel electrocatalysts for boosted N₂ activation and advanced strategies for suppressed HER. In contrast to widely investigated transition metals, main group elements (MGEs) with manifold physicochemical properties and intrinsically poor hydrogen adsorption ability could provide superiority in realising the above goals. In this Review MGEs-based NRR research is critically assessed for the first time. The overarching aim is to critically assess application and provide a comprehensive understanding of MGEs-based materials design and functional mechanisms for boosted N₂ activation and suppressed HER.

activation.⁸⁻¹⁰ N_2 molecules can be activated by either accepting σ electrons from N_2 via empty d-orbitals, or donating electrons from partially occupied d-orbitals to the π^* antibonding orbitals of N_2 .¹¹ However, d-electrons also contribute significantly to the formation of metal–H bonds,¹² resulting in undesired hydrogen (H_2) evolution and thus low FE for NH_3 formation. In contrast, main group elements (MGEs), such as B, C and Bi, with TMs-like partially occupied valence p-orbitals but intrinsically poor hydrogen adsorption ability, have attracted increasing research interest for selective N_2 activation and fixation.^{13,14} In contrast to the dominant ‘acceptance-donation’ mechanism for TMs-based NRR electrocatalysts, MGEs boost NRR and suppress HER via various mechanisms because of diverse physical and chemical properties.^{12,14} Research in MGEs-based NRR electrocatalysis however remains limited, and therefore poorly explored. It is necessary to develop a more comprehensive understanding of MGEs-derived high activity and selectivity for NRR, and to use this to guide rational design of MGEs-based electrocatalysts and/or regulation methods for selective N_2 fixation. A targeted and critical assessment of fundamentals and methods to boost MGEs-based electrocatalytic NRR is therefore highly relevant and timely.

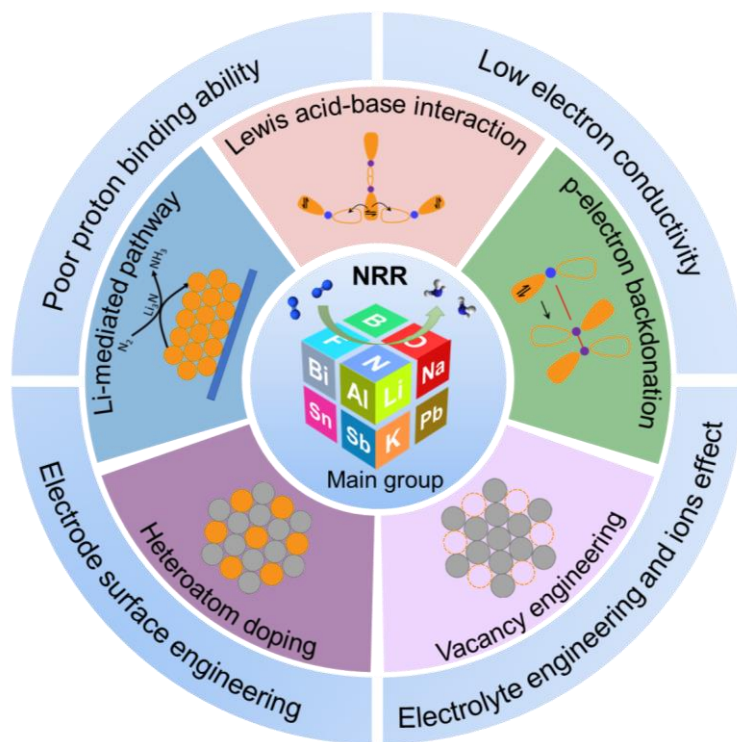


Figure 1. Unique Advantages and Application of MGEs in NRR to boost N_2 activation and suppress HER.

In this Review, we critically assess and summarize reaction mechanisms and intrinsic challenges of NRR, which calls for elaborate electrocatalyst design to concomitantly activate N_2 and suppress HER. We then discuss the advantages and recent advances in MGEs-based NRR. Significantly, in contrast with literature that is more general in enumerating catalysts by elements or types, we focus on the role and application of MGEs with different mechanisms to boost N_2 activation or suppress H_2 evolution (Figure 1). Because of various electronic structures and physicochemical properties, MGEs can boost N_2 activation via Lewis acid-base interaction, p-electron backdonation, Li-mediated pathway, vacancy engineering and heteroatom doping, and; suppress H_2 evolution via intrinsically poor proton binding, limited electron accessibility, hydrophobic electrode surface engineering and alkali metal cations effects. We assess prospects in development of electrocatalytic NRR, including establishing rigorous protocols, synergetic design of MGEs-based catalysts, implementation of *in situ/operando* characterizations, and integration of multiple advanced methods. We show that MGEs-based functional mechanisms are generalizable, and how they might be judiciously applied as a basis for smart design of advanced catalyst materials for N_2 fixation.¹⁵ We conclude that MGEs can significantly boost electrochemical N_2 fixation.

¹ School of Chemical Engineering and Advanced Materials, The University of Adelaide, SA 5005, Australia

² Lead Contact

*Correspondence: s.qiao@adelaide.edu.au (S.Q.), cheng.tang@adelaide.edu.au (C.T.)

FUNDAMENTALS OF ELECTROCHEMICAL N₂ REDUCTION

Reaction Pathways of NRR

Generally, reaction pathways of NRR are classified into two categories: dissociative and associative. In the dissociative pathway, the N≡N bond is firstly broken, followed by hydrogenation on each N atom to form two NH₃ molecules (Figure 2A). However, it is extremely difficult to directly break the N≡N bond due to its high bond energy of 944 kJ mol⁻¹.⁵ This is an explanation of why industrial HB process, which follows the dissociative pathway, requires harsh reaction conditions. However, NRR on surface of most electrocatalysts follows the associative pathway, which can be further divided into distal and alternating pathways in the hydrogenation sequence (Figure 2B).¹⁶ In the distal pathway, hydrogenation preferentially occurs on the terminal N atom to form the first NH₃ molecule, whilst in the alternating pathway, hydrogenation concomitantly occurs on both the two N atoms.¹⁷ The possible formation of N₂H₄ byproduct is a key distinction between these two pathways.¹⁸ It is noteworthy that the alternating pathway can also initiate with a side-on N₂ adsorption, known as the enzymatic pathway (Figure 2B).¹⁷

Two other reaction pathways have been revealed for some electrocatalysts with unique structure and properties, namely the Mars-van Krevelen (MvK) mechanism, and Li-mediated pathway. For certain nitrogen-containing materials, especially transition metal nitrides, hydrogenation can occur on the surface lattice N atoms to form the first NH₃ molecule, and the generated nitrogen vacancy (N_v) is then replenished by the adsorbed N₂ to release the second NH₃ molecule on the terminal N atom (Figure 2C).¹⁹ Although it is predicted to require relatively low overpotentials,²⁰ the MvK mechanism has recently been questioned (decomposition versus catalysis) due to the readiness of lattice N atoms stripping, and difficulty in refilling N₂ into N_v.²¹ In Li-mediated N₂ fixation pathway, Li metal reacts directly with N₂ to form lithium nitride (Li₃N), that then reacts with a proton source (e.g. ethanol, water) to release NH₃ (Figure 2D).²² A practical obstacle with this pathway is how to efficiently reduce the generated Li⁺ ions back to Li metal to make the process safe and continuous.^{23,24}

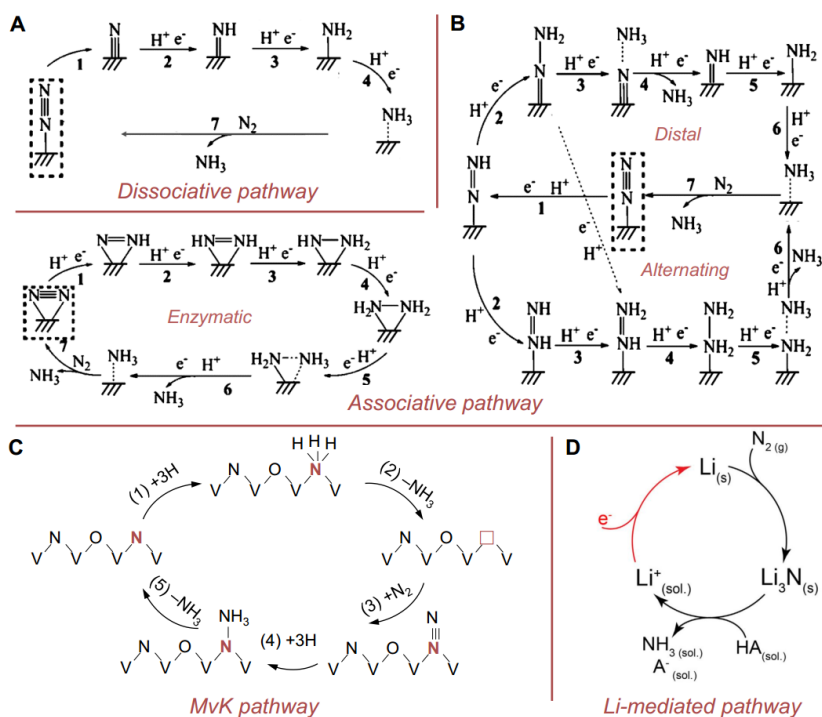


Figure 2. Reaction Pathways of NRR.

(A) Dissociative pathway and (B) associative pathway. Reproduced with permission from Cui *et al.*¹⁸ Copyright 2018 Wiley-VCH Verlag GmbH & Co. KGaA, Weinheim.

(C) MvK pathway. Reproduced with permission from Yang *et al.*¹⁹ Copyright 2018 American Chemical Society.

(D) Li-mediated pathway. Reproduced with permission from Lazouski *et al.*²⁴ Copyright 2019 Elsevier.

Intrinsic Obstacles to NRR Development

Factors that hinder development of NRR mainly stem from the, 1) inertness of N₂ in thermodynamics and kinetics, 2) competing HER, and 3) technical limitations with the reaction system.

The extremely strong triple bond (N≡N) results in the inert properties of N₂. From the thermodynamic perspective, activation and reduction of N₂ is plagued with the short bond length (109.76 pm) and high dissociation energy (944 kJ mol⁻¹) of N≡N bond,⁵ the large enthalpy change for direct N₂ protonation ($\Delta H^0 = 37.6$ kJ mol⁻¹),²⁵ and the low electron affinity (-1.9 eV) and high ionization potential (15.85 eV) for N₂ adsorption on catalyst surface.^{18,25} From the kinetic perspective, the large energy gap (10.82 eV) between the highest occupied molecular orbital and the lowest unoccupied molecular orbital of N₂, the lack of a dipole moment, and the low polarizability of N₂, impede electron transfer and reaction kinetics for N₂ reduction and NH₃ production.^{5,18}

Selectivity of NRR for NH₃ production is restrained by competing HER. Although a thermodynamically potential window exists between NRR and HER, NRR usually proceeds at a high overpotential because of the difficulty of N₂ activation and unfavorable scaling relation between intermediates.²⁶ It is well documented that the majority of investigated materials, especially the d-block TMs-based electrocatalysts, exhibit more negative onset potentials for NRR compared with those for HER.²⁷ Further, evaluation of designed electrocatalysts and improvements in NRR performance face technical limitations, including extremely low solubility of N₂ in aqueous solutions (0.66 mmol L⁻¹) that limits N₂ coverage on electrode surface,⁶ and ubiquitous NH₃ contaminations (from NO_x, NO_x⁻, NH₃ and NH₄⁺) that lead to uncertainty and possible false positives.^{28,29}

Advantages of Main Group Elements for Selective N₂ Activation

To obviate intrinsic limitations with NRR, it is necessary to develop proper electrocatalysts and effective strategies for simultaneous activation of N₂ and suppression of HER. In comparison with the TMs-based electrocatalysts, main group elements, including the s-block alkali metals, p-block metals, metalloids, and non-metals with multifarious physical and chemical properties, are predicted to give practical opportunities for selective N₂ activation and fixation (Figure 3).

Li 3	Be 4		B 5	C 6	N 7	O 8	F 9
Na 11	Mg 12	Lewis acid-base interaction	Al 13	Si 14	P 15	S 16	Cl 17
K 19	Ca 20	p-electron backdonation	Ga 31	Ge 32	As 33	Se 34	Br 35
Rb 37	Sr 38	Li-mediated pathway	In 49	Sn 50	Sb 51	Te 52	I 53
Cs 55	Ba 56	Vacancy engineering	Tl 81	Pb 82	Bi 83	Po 84	At 85
Fr 87	Ra 88	Heteroatom doping	Nh 113	Fl 114	Mc 115	Lv 116	Ts 117

Figure 3. MGEs boost N₂ activation via various mechanisms.

MGEs have strong interactions with N₂ in various forms. Resembling TMs with partially occupied valence d-orbitals,¹¹ some MGEs also possess donor/acceptor frontier p-orbitals that are energetically accessible.¹³ Empty p-orbitals can accept lone pair electrons from N₂ via a Lewis acid-base interaction, whilst partially occupied p-orbitals can activate N₂ by p-electron backdonation.^{11,14,30} Beyond these TMs-like properties, MGEs exhibit more superiorities for N₂ activation. For example, Li, a main group element in s-block, is the only metal that can spontaneously split N≡N bonds at ambient condition.^{24,31} Some main group non-metals (e.g. C, B, P, S and F) can construct abundant defect sites, either via vacancy engineering or heteroatom doping, to provide favorable chemical environments for N₂ adsorption and accommodation.³² Moreover, MGEs exhibit unique advantages in suppressing HER. The weak hydrogen binding ability of MGEs and abundant valence electrons are less favorable for competing H₂ evolution, rendering more ideal active sites for N₂ adsorption and reduction.^{33,34} Solvation and steric effects arisen from alkali cations (e.g. Li⁺)^{35,36} and electrode engineering with hydrophobic

layers^{37,38} can effectively regulate proton accessibility on the heterogeneous electrocatalyst surface, therefore steering selectivity to NRR.³⁹

MAIN GROUP ELEMENTS BOOST N₂ ACTIVATION

Lewis Acid-Base Interaction

Each nitrogen atom in N₂ has a pair of lone electrons, which can donate electrons to strong electron acceptors, acting as a weak Lewis base. To effectively activate N₂ and avoid formation of metal–H bonds, Lewis acid catalytic sites with strong electrophilicity are highly expected.¹² Optimized Lewis acid pair at both ends of N₂ molecules can haul and activate N≡N bonds through a ‘pull-pull’ effect (Figure 4A).¹²

Creation of Lewis acid sites depends on unoccupied orbitals for accommodating the lone pair electrons of N₂ molecules. Boron (B) with three valence electrons (2s²2p¹) and empty p-orbitals, has been widely investigated as a typical Lewis acid-based active site for NRR.^{40,41} Both sp² and sp³ hybridization of B can form empty orbitals to capture the lone pair electrons (Figure 4B).^{12,41} Following hybridization, the unoccupied orbital of B can effectively activate N₂ via capture of the lone pair electrons,^{40,41} whilst the partially filled orbitals can donate electrons to the antibonding orbitals of N₂.^{12,42} A number of B-containing electrocatalysts have been reported that exhibit high activity and selectivity for NRR, including two-dimensional (2D) boron nanosheets,⁴³ B-doped graphene,⁴⁴ B-decorated black phosphorus,¹² BN⁴⁵ and B₄C.⁴⁶ In addition to B, Gallium (Ga), a member of boron group elements, has similar electronic structure to B, including occupied and empty orbitals. It was theoretically demonstrated that Ga is also able to facilitate N₂ adsorption and activation by a similar Lewis acid-base interaction.⁴² Through introducing Se vacancies in the GaSe monolayer, a special chemical environment with exposure of three sp³-hybridized Ga atoms was created, that provided empty sp³-orbitals to accommodate σ-electrons of N₂.⁴² For other p-block elements without unoccupied orbitals such as Bi, it might be difficult to apply such Lewis acid-base interaction to activate N₂ due to lack of intrinsic Lewis acid sites. Nevertheless, unoccupied orbitals can be intentionally created by surface molecular modification. For example, an integrated introduction of oxygen vacancy and hydroxyl radical on surface of Bi₄O₅I₂ can result in unoccupied orbitals by breaking Bi–Bi bonds (Figure 4C).⁴⁷ The induced vacant p-orbitals will serve as Lewis acid sites to accommodate the lone pair electrons of N₂ molecules.

The NRR activity of Lewis acid electrocatalyst can be further boosted by increasing the density of Lewis acid sites or tuning the Lewis acidity.^{48,49} To augment the electron-deficient B sites, a B-rich covalent organic framework (COF) was designed and synthesized via self-condensation of 1,4-benzenediboronic acid on conductive N-doped carbon nanosheets.⁵⁰ Density functional theory (DFT) calculations revealed that the B sites with localized positive charge facilitate N₂ adsorption and dissociation, and bond with nitrogenous species under NRR conditions, as verified by molecular dynamics (MD) simulation, *in situ* X-ray powder diffraction (XRD) and *in situ* Raman measurement. A lattice distortion induced by bonding at B sites led to a virtuous cycle of more excited sites and stronger N₂ affinity until the whole system reached a high-point reaction status (Figure 4D), thus resulting in a high NH₃ yield of 12.53 μg mg_{cat}⁻¹ h⁻¹ and superior FE of 45.43% at –0.2 V versus reversible hydrogen electrode (RHE) in 0.10 M KOH.⁵⁰ To tune the Lewis acidity, one can either introduce heteroatoms with higher electronegativity or multiple elements to form dopant pairs.^{49,51} For example, because of much higher electronegativity of F (3.98) compared with that for C (2.55), F-doped carbon is reported to possess much more Lewis acid sites than the un-doped counterpart, as evidenced by NH₃ temperature-programmed desorption.⁵¹ Both experimental and theoretical studies confirmed that Lewis acid sites boosted the binding of N₂, facilitated dissociation of N₂ into *N₂H, and suppressed HER, leading to a high NH₃ yield of 197.7 μg mg_{cat}⁻¹ h⁻¹ at –0.3 V versus RHE and a high FE of 54.8% at –0.2 V versus RHE in 0.05 M H₂SO₄.⁵¹ In the case of B-doped graphene, the lower electronegativity of B (2.04) compared with C (2.55) leads to a local electron-deficient environment at the B sites, which not only promotes adsorption of N₂ due to the Lewis acid-base interaction, but also prohibits the binding of proton (Lewis acid) for H₂ evolution.⁴⁴ Moreover, the Lewis acidity of B-doped carbon can also be enhanced by introducing a second heteroatom dopant such as N⁴⁸ and S⁵².

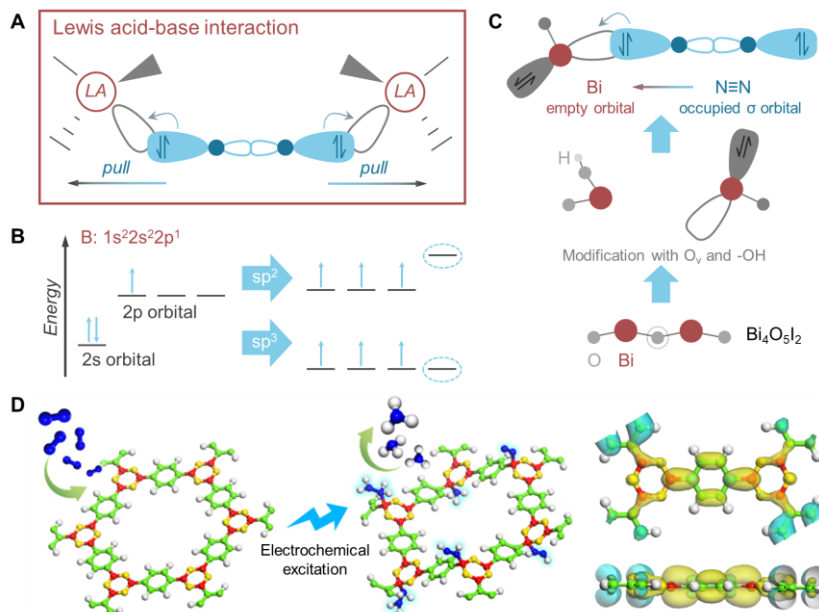


Figure 4. N₂ activation via Lewis acid-base interaction.

(A) Schematic of N₂ activation by Lewis acid sites through a “pull-pull” effect. LA means Lewis acid sites.

(B) Hybridization diagrams of Boron. (A) and (B) are reproduced with permission from Shi *et al.*¹² Copyright 2019 The Royal Society of Chemistry.

(C) Creation of empty orbital on Bi by introducing oxygen vacancy and hydroxyl on Bi₄O₅I₂. Reproduced with permission from Lv *et al.*⁴⁷ Copyright 2020 Elsevier.

(D) Schematic of electrochemical excitation of B-rich COF for more active sites and stronger N₂ affinity. Reproduced with permission from Liu *et al.*⁵⁰ Copyright 2019 Springer Nature.

Because N atoms are significantly electronegative, the lone pair electrons in N₂ molecules are not readily be donated. Therefore, smart design of MGEs-based electrocatalysts for boosted interaction between N₂ and Lewis acid sites is highly preferred. This might be achieved by: 1) Introducing relatively strong Lewis acid sites with high electrophilicity, 2) Increasing the number of Lewis acid sites on the surface of designed electrocatalysts, and; 3) Tuning the surrounding chemical environments of Lewis acid sites for optimized N₂ accommodation.

p-electron Backdonation

In addition to empty frontier orbitals (acceptor), certain MGEs possess partially occupied orbitals (donor),¹³ and enable efficient activation of N₂ via p-electron backdonation (Figure 5A). Specifically, the occupied p-orbitals of MGEs donate electrons back into the unoccupied antibonding orbitals of N₂, resulting in weakening or cleaving of the strong N≡N triple bond.²⁵

Recently, bismuth (Bi) was found to exhibit advantages in electrocatalytic N₂ reduction. DFT calculation has shown that the density of states (DOS) near the Fermi level mainly localize around Bi atoms in Bi-based catalysts, indicating that Bi atoms can activate N₂ by back-donating p-electrons.⁵³ In 2019, it was reported that metallic Bi is a promising candidate for electrochemical N₂ fixation (Figure 5B).³⁰ Derived from BiOI precursors, the *in situ* reduced 2D mosaic Bi nanosheets exhibited sufficient exposure of edge sites and a decreased interlayer Bi–Bi bond length, which could effectively promote the delocalization of Bi p-electrons.⁵⁴ The achieved NRR performance in 0.10 M Na₂SO₄ was almost 10-fold that for bulk Bi nanoparticles. The structural reconstruction and chemical transformation of bismuth species during electroreduction was investigated by *in situ* Raman spectroscopy, confirming the intrinsic activity origin from metallic Bi sites.⁵⁵ The intrinsic NRR activity of Bi was revealed to be higher than that for TMs because of the strong interaction between Bi 6p band and N 2p orbitals.⁵⁶ Specifically, N₂ molecule can be stretched and activated by accepting electrons from the partially occupied Bi band to its antibonding orbitals (π^*2p_y , π^*2p_z and σ^*2p_x) (Figure 5C).⁵² In addition, the semiconducting property of Bi, especially for thin films with quantum confinement effect,⁵⁷ can suppress competing HER by limiting the surface electron accessibility and promote selectivity of NRR.^{30,39}

In addition to Bi, other p-block metals also possess high affinity for N adatoms, such as aluminium (Al). It is reported that Al has the strongest N-binding ability amongst the post-transition metals, owing to the interaction between Al 3p band with N 2p orbitals.³⁴ For example, a porous Al-based metal–organic framework (MOF) material, MIL-100 (Al), was designed for electrochemical NRR in alkaline media, and exhibited a significant FE toward NH₃ of 22.6% at a low overpotential of 177 mV.⁵⁸ Investigations revealed that the unsaturated Al sites within the unique porous MOF structure should play a synergistic role in facilitating electrochemical N₂ fixation (Figure 5D). Based on the strong interaction between Al and N₂, Zhi and co-workers proposed and demonstrated a rechargeable Al–N₂ battery with an ionic-liquid electrolyte, a graphene-supported Pd catalyst cathode, and an Al anode (Figure 5E).⁵⁹ This innovative Al–N₂ battery exhibited not only efficient power supply, but also electrochemical N₂ fixation to NH₃ with a significant FE of 51.2% and high NH₃ yield of 27.1 μg mg_{cat}⁻¹ h⁻¹. The mechanism of the battery and N₂ fixation involved a reversible reaction between Al and AlN (2Al + N₂ ↔ 2AlN) and the release of NH₃ (AlN + NaOH + 2H₂O → NaAlO₂ + NH₃ + H₂O).

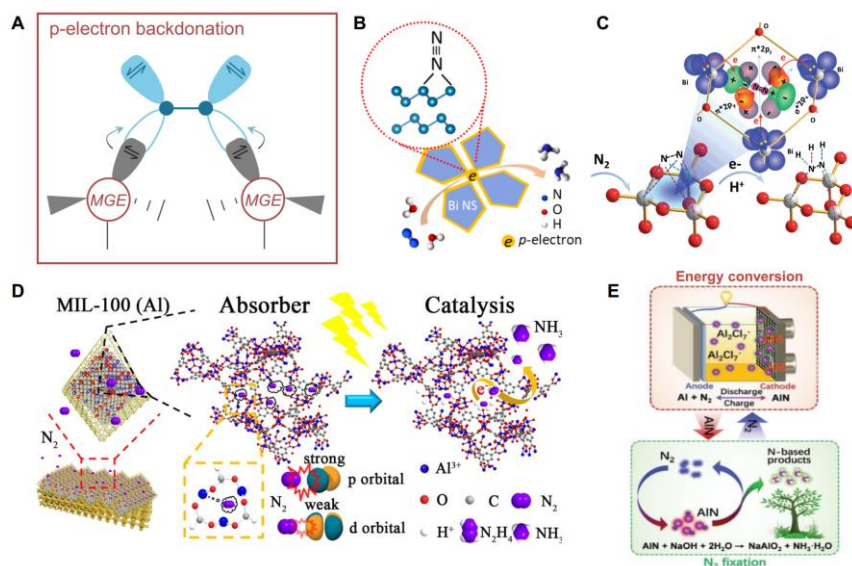


Figure 5. N₂ activation by p-electron backdonation.

(A) Schematic of N₂ activation by p-electron backdonation. MGE means main group element.
 (B) Schematic of NRR activity origin on 2D mosaic Bi nanosheet. Reproduced with permission from Li *et al.*³⁰ Copyright 2019 American Chemical Society.
 (C) Schematic electron donation from the p-electrons of Bi atoms to the unoccupied antibonding orbitals (π^*2p_x , π^*2p_y and σ^*2p_z) of the N₂ molecule. Reproduced with permission from Sun *et al.*⁵³ Copyright 2017 The Royal Society of Chemistry.
 (D) Schematic of strong interaction between Al 3p orbital and N₂. Reproduced with permission from Fu *et al.*⁵⁸ Copyright 2020 American Chemical Society.
 (E) Schematic of Al–N₂ battery achieving both energy conversion and N₂ fixation. Reproduced with permission from Guo *et al.*⁵⁹ Copyright 2020 The Royal Society of Chemistry.

To further boost the interaction between p-electrons of MGEs with π^* antibonding orbitals of N₂, more strategies are anticipated to tune the accessibility and delocalization status of p-electrons, such as morphology modification and facet control.^{30,54} Moreover, certain MGEs exhibit multiple characteristics with synergistic effect and are advantageous for selective N₂ reduction. For example, the B atoms with sp³ hybridization possess both empty orbitals for Lewis acid-base interaction and occupied orbitals for electron backdonation,⁴¹ whilst the metallic Bi simultaneously boost N₂ activation via back-donating p-electrons and suppress HER due to the semiconducting property.³⁰ Therefore, p-block MGEs have significant practical potential for N₂ fixation under ambient conditions. This is however an area that requires further investigation both experimentally and theoretically.

Vacancy Engineering

Vacancy engineering is considered an effective strategy to improve catalytic behavior of electrocatalysts.^{32,60} Vacancies can effectively improve the ability to capture electrons, adjust the energy band structure, and lower reaction barriers.³² For NRR, a series of MGEs-derived

vacancies have been reported to boost N_2 activation and fixation, including oxygen vacancy (O_v),⁶¹ nitrogen vacancy (N_v),⁶² sulfur vacancy (S_v),⁶³ selenium vacancy (Se_v)⁶⁴ and bismuth vacancy (Bi_v).⁶⁵

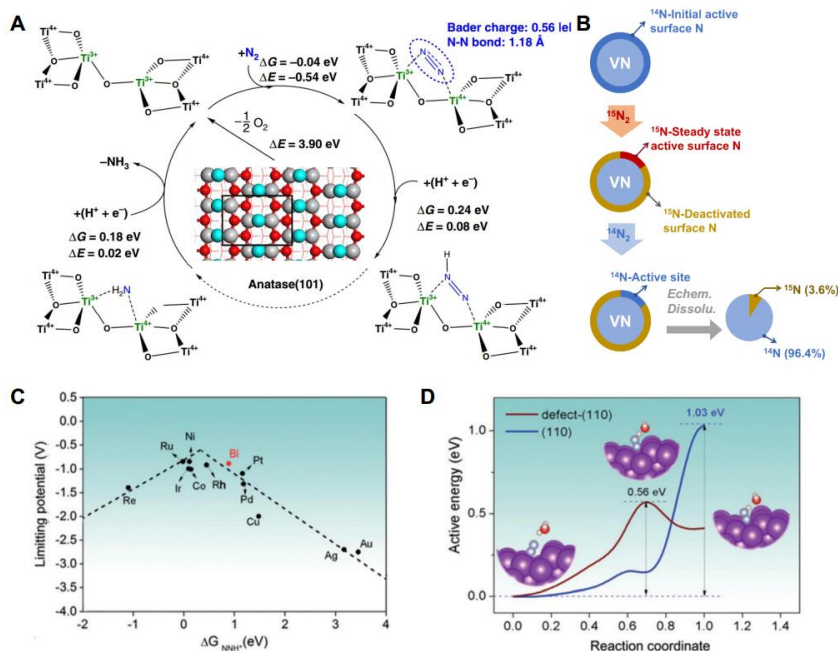


Figure 6. N_2 activation by vacancy engineering.

(A) NRR on adjacent bi- Ti^{3+} sites on anatase (101) surfaces with oxygen vacancy. Reproduced with permission from Cao *et al.*¹⁰ Copyright 2019 Springer Nature.

(B) Schematic of isotopic exchange experiment on $V^{14}NO$ to unravel the real active sites for NRR. Reproduced from Yang *et al.*⁶⁶ Copyright 2019 Wiley-VCH Verlag GmbH & Co. KGaA, Weinheim.

(C) Limiting potential for NRR on various metals as a function of binding energy of N_2H^* .

(D) Comparison of the activation energy for NRR on perfect Bi (110) sites and defective Bi (110) sites. (C) and (D) are reproduced with permission from Wang *et al.*⁶⁵ Copyright 2019 Wiley-VCH Verlag GmbH & Co. KGaA, Weinheim.

Amongst various vacancies, O_v is reported to have the lowest formation energy.⁶⁷ Importantly, it can be facilely synthesized by different methods, including thermal annealing, heterogeneous ion doping, wet chemical reduction and high-energy particle bombardment.⁶¹ The fundamental contribution of O_v to NRR activity has been well demonstrated with a number of metal oxide substrates, e.g. TiO_2 ,¹⁰ Fe_2O_3 ,⁶⁸ MoO_2 ,⁶⁹ $BiVO_4$ ⁷⁰ and $LaCoO_3$.⁷¹ As active sites for NRR, O_v facilitates adsorption and activation of N_2 by boosting the electron-donating ability of adjacent metal atoms to the π^* antibonding orbitals of N_2 molecule.^{10,69} For example, for a noble-metal-free $BiVO_4$ electrocatalyst, the introduction of O_v was shown to boost N_2 adsorption and activation at the V atoms with lower coordination and higher spin-polarization with a localized magnetic moment.⁷⁰ Via DFT calculations and experimental verification, Zheng and co-workers unravelled the functional mechanism of O_v in TiO_2 -based NRR electrocatalysts. The two adjacent Ti^{3+} sites on O_v -rich anatase TiO_2 (101) were confirmed as the most active electrocatalytic centers, which effectively induced N_2 chemisorption in a lying-down manner, significantly elongated the N-N bond from 1.12 to 1.18 Å, and favorably reduced the reaction free energies of the first hydrogenation step by 0.26 eV (Figure 6A).¹⁰ Considering the chemical properties akin to O, constructing S and Se vacancies was also investigated as effective strategies to boost NRR.^{63,64} For example, introduction of S_v into MoS_2 shifts the d-band center of edge Mo sites toward the Fermi level (-0.26 eV \rightarrow -0.14 eV), leading to a stronger interaction with N_2 molecule.⁶³ However, the vacancy-induced positive shift of d-band center simultaneously impacts NRR and HER with poor selectivity. To boost NRR and suppress HER, Liu and co-workers buried Se_v -rich $ReSe_2$ electrocatalysts between two super-hydrophobic carbonized bacterial cellulose layers. This resulted in a significantly improved FE toward NH_3 of 42.5% at -0.25 V versus RHE in 0.10 M Na_2SO_4 .⁶⁴

Nitrogen vacancy is also ideal for NRR because of its similar structure and size with N atoms in N_2 molecule. For example, electron paramagnetic resonance spectra and UV-Vis diffuse reflection spectra confirm that N_v significantly modulates the π -electron delocalization in the

conjugated system of a polymeric carbon nitride catalyst.⁷² It constructs a binuclear end-on bound configuration that is favorable for spatial electron transfer and effectively activates N₂ via electron backdonation, leading to > 10-fold enhancement in NH₃ yield compared with N_v-free counterpart.⁷² For N_v in metal nitrides, however, the reaction mechanism is more complicated. Although N_v can be stable in some specific nitrides (e.g. 2D W₂N₃)⁶² and provide an electron-deficient environment to facilitate N₂ adsorption and activation, it is widely reported to be dynamically involved in NRR via the MvK mechanism. With a combination of *operando* X-ray absorption spectroscopy, quantitative isotope exchange experiments and DFT calculations, Xu and co-workers confirmed that NRR followed the MvK mechanism on VN nanoparticles with VN_{0.7}O_{0.5} as the active phase (Figure 6B).^{19,66} Both the surface N atoms adjacent to a surface O and the N_v sites were revealed to be the catalytic active sites. The surface N_v sites however are unstable during NRR, and can be preferentially healed by filling with N atoms, or trigger decomposition of nitrides, leading to deactivation or false positive results.^{21,66,73} Therefore, it is important to quantitatively examine the density of initial and steady-state active sites on NRR catalysts, and to develop effective strategies (e.g. via introducing dopants) to increase density and stability of surface vacancies.⁶⁶

In addition to anionic vacancies, cationic vacancies have also been reported to effectively activate N₂. For example, Yan and co-workers prepared Bi_v-rich Bi (100) nanoplates by plasma-assisted reduction of Bi₂O₃.⁶⁵ DFT calculations revealed the key role of Bi_v defects in boosting the adsorption and activation of N₂ both thermodynamically and kinetically (Figure 6C and D). Meanwhile, Bi exhibited significantly weaker HER activity than TMs-based catalysts because of poor binding with H adatoms. Consequently, the vacancies transformed the nearly non-catalytic material (pristine Bi) into a practically promising NRR electrocatalyst, exhibiting a high FE of 11.68% and NH₃ yield of 5.453 μg mg_{Bi}⁻¹ h⁻¹ at -0.6 V versus RHE in 0.2 M Na₂SO₄.

These research findings are intended to guide rational design and effective utilization of vacancies for high-performance NRR at ambient condition. However, vacancy engineering for NRR electrocatalysts is still facing some critical challenges, which require further investigation in the following aspects: 1) Smart materials design for controllable concentration, configuration and location of vacancies; 2) Exploration of advanced vacancy engineering with dual- or multi-compositions (e.g. N/O);¹⁹ 3) Implementation of *in situ/operando* techniques to precisely monitor reaction intermediates and exactly understand vacancy-mediated reaction mechanism, and; 4) Knowledge-guided improvement of the durability of vacancies under NRR conditions.

Heteroatom Doping

Heteroatom doping is another effective strategy, especially for the nonmetal MGEs, to boost N₂ activation and hydrogenation. Incorporation of one or multiple heteroatoms into metal-free substrates or metal compounds has been widely employed to develop efficient electrocatalysts for energy conversion reactions.⁷⁴ These regulated catalytic performances are generally ascribed to tuned surface properties, such as electronic structure, spin polarization, metal valence and coordination environment.^{52,75-77}

To date, various heteroatoms have been doped into nanocarbon materials for boosting N₂ activation and fixation, including B,^{44,46,50} N,⁷⁸⁻⁸⁰ F,^{51,81} S,⁵² P⁸⁰ and Cl.⁸² In general, the difference in electronegativity alters the charge distribution of the sp²-conjugated carbon matrix, thereby optimizing intermediate chemisorption and facilitating electron transfer. Heteroatoms with electronegativity lower than C (2.55), such as B (2.04),⁴⁴ were reported to form a local electron-deficient environment and Lewis acid sites at the dopant sites; whilst those with greater electronegativity, such as F (3.98),⁵¹ N (3.04)⁷⁹ and O (3.44),⁸³ induce Lewis acid sites at the dopant-adjacent C sites. DFT calculations showed that the positively charged sites can strongly interact with N₂ and significantly elongate the N≡N bond.⁸³ Via a combination of theoretical calculations and experimental verification, a systematic investigation of chalcogen/oxygen group elements (O, S, Se and Te) doped nanocarbon materials highlighted the doping effect and functional mechanism for boosted NRR.⁷⁶ The doping-induced charge accumulation facilitated N₂ adsorption on adjacent C atoms (Figure 7A), whilst the spin polarization boosted the potential-determining step of the first protonation to form *NNH (Figure 7B). Te-doped carbon, with enriched charge accumulation and the largest amount of polarized spin moment, was demonstrated to exhibit significantly boosted electrocatalytic NRR activity (Figure 7C).⁷⁶

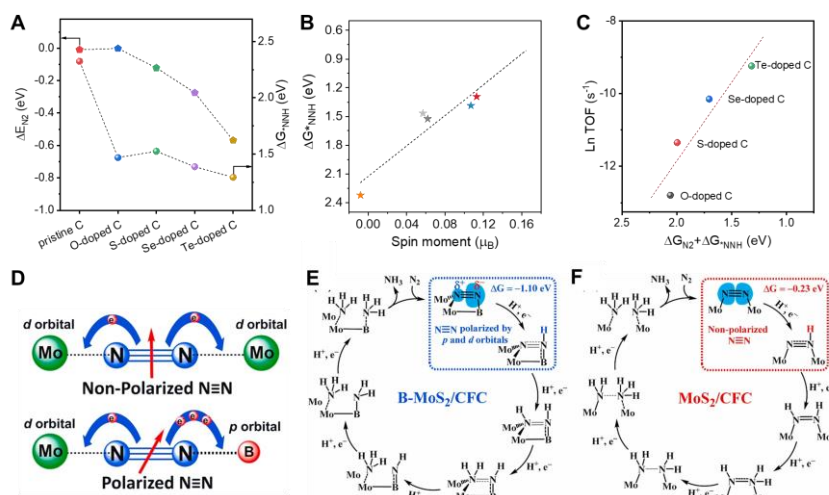


Figure 7. N₂ activation by heteroatom doping.

(A) Absorption free energy of N₂ (ΔE_{N_2}) and Gibbs free energy for formation of *NNH (ΔG_{*NNH}) on pristine and heteroatom-doped carbon catalysts.

(B) Correlation between ΔG_{*NNH} and spin moment of active carbon atoms.

(C) Maximum ln(TOF) as a function of $\Delta G_{N_2} + \Delta G_{*NNH}$ for O, S, Se and Te doped C catalysts. (A–C) are reproduced with permission from Yang *et al.*⁷⁶ Copyright 2020 Wiley-VCH Verlag GmbH & Co. KGaA, Weinheim.

(D) Schematic of proposed strong-weak electron polarization (SWEP) of N≡N bond by boron-doped MoS₂.

(E, F) Proposed NRR process with first protonation step highlighted on B-MoS₂/CFC and MoS₂/CFC, respectively. (D–F) are reproduced with permission from Guo *et al.*⁷⁷ Copyright 2020 Elsevier.

The efficacy of heteroatom doping on catalytic activity can be further enhanced by regulating the doping configuration and inducing a second heteroatom. For example, amongst various N dopants (e.g. pyridinic-, pyrrolic- and graphitic-N), pyridinic-N is revealed as the critical site to boost the adsorption and activation of N₂. A smart catalyst design for high-density pyridinic-N sites on carbon network is highly expected.^{78,79} It is however possible that N dopants are protonated and decomposed, leading to inferior stability and false positive NRR activity.²¹ Therefore, the stability of N dopants should also be evaluated for catalyst design, for example, by thermodynamic evaluation, to compare the theoretically predicted NRR limiting potential and the substrate decomposition potential.⁸⁴ Further, NRR activity of N-doped carbon can be promoted by additional doping with B, F, P or S atoms, amongst which N, B co-doping exhibits greatest enhancement effect.⁸⁰ In the case of B-doped carbon nanofiber, inducing the S co-dopant shifts the p-band center position of B dopant, thereby boosting the adsorption of N₂ on S-C-B sites and reducing energy barriers for the rate-determining step.⁵²

In addition to carbon substrate, heteroatom doping on TMs-based materials can effectively tune d-band structure, enrich the catalytic active sites and thus boost interaction with N₂.^{77,85} Sun and co-workers reported a boron-doped molybdenum disulfide (B-MoS₂) electrocatalyst with a highly significant NH₃ production and efficiency in acidic aqueous electrolyte.⁷⁷ Through taking advantage of the difference in N₂ activation properties of B and Mo (namely the electron accepting ability of the empty 2p orbitals of B and the electron backdonation capacity of the 5d orbitals of Mo), they established a strong-weak electron polarization (SWEP) pair to significantly polarize and activate the non-polar N≡N triple bond (Figure 7D). Compared with the MoS₂ model, B-MoS₂ exhibited a polarized charge distribution with more negative charge transfer toward B and positive charge toward Mo. It significantly elongated the N≡N bond to 1.33 Å (versus 1.24 Å for MoS₂) and facilitated the first protonation of adsorbed N₂ with a significant decrease in free energy (–1.1 eV versus –0.23 eV) (Figure 7E and F). Similar promotion effect of heteroatom doping was also observed on other metal oxides or hydroxides, such as B-doped MnO₂⁸⁵ and F-doped β-FeOOH.⁸⁶

Compared with other primary electrocatalytic reactions, investigation of heteroatom doping for NRR is in its early stages with limited choice of catalyst, poor mechanism understanding and limited performance enhancement. In future, attention should be given to: 1) Precise identification of doping configuration and a more refined understanding of correlation with performance; 2) Knowledge-guided design and controllable synthesis of doping configuration

and position; 3) Enrichment of optimal dopants on the catalyst surface; 4) Careful tailoring of substrate nanostructure to facilitate mass transfer, and; 5) Development of reliable methods for mass production of designed heteroatom-doped materials.

Li-Mediated Pathway

Lithium-mediated pathway offers an innovative route to achieve superior activity and selectivity for electrocatalytic N_2 fixation.^{23,24,87} This is because, from the activity perspective the highly reactive Li is an excellent N_2 -reducing agent that spontaneously splits $N\equiv N$ bonds at ambient condition,^{24,31} and from the selectivity perspective, rational design of Li-mediated reaction process can separate N_2 activation from subsequent protonation and therefore circumvent competing HER.^{88,89} This Li-mediated NRR pathway involves three steps, namely, 1) Li deposition, 2) Li nitridation, and 3) NH_3 formation. Reports differ primarily in the method for Li generation from Li^+ ,²² which is related to the type of proton source e.g. ethanol, H_2 or H_2O and will determine the operation mode as *Continuous* or *Stepwise*.

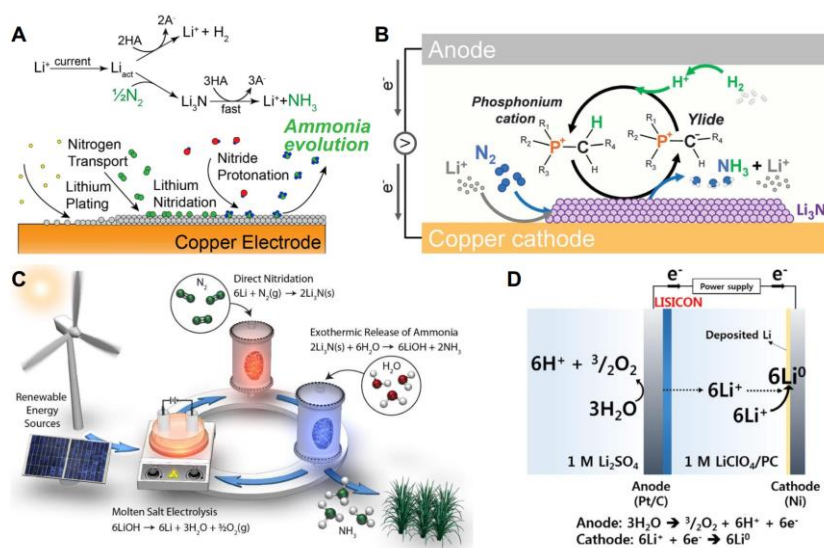


Figure 8. N_2 activation via Li-mediated pathway.

(A) Chemistry involved in continuous Li-mediated NRR. Reproduced with permission from Lazouski *et al.*²⁴ Copyright 2019 Elsevier.

(B) Schematic of Li-mediated NRR based on a phosphonium proton shuttle. Reproduced with permission from Suryanto *et al.*⁸⁷ Copyright 2021 AAAS.

(C) Schematic of stepwise Li-mediated NRR. Reproduced with permission from McEnaney *et al.*⁸⁸ Copyright 2017 The Royal Society of Chemistry.

(D) Electrochemical Li deposition at cathode (organic electrolyte) using electrons that originate from water oxidation at the anode (aqueous electrolyte). Reproduced with permission from Kim *et al.*⁸⁹ Copyright 2018 Wiley-VCH Verlag GmbH & Co. KGaA, Weinheim.

Continuous Mode

Given the intense interaction between metallic Li and water ($Li^0 + H_2O \rightarrow LiOH + 1/2 H_2$) and competing HER in aqueous electrolyte ($H_2O + e^- \rightarrow OH^- + 1/2 H_2$), it is more favorable to use non-aqueous electrolyte and proton carrier for Li-mediated NRR. In 1993, Sakata and co-workers first proposed and demonstrated this concept via electrolysis in a solution of $LiClO_4$ with ethanol in tetrahydrofuran (THF), achieving a highly significant current efficiency of 8% and 59% under 1 and 50 atm of N_2 , respectively.^{31,90} They proposed a Li-mediated mechanism as follows: 1) Electrons are transferred from the working electrode to reduce Li^+ and deposit Li metal on the electrode surface, 2) N_2 reacts with the deposited Li to form Li_3N , and; 3) Li_3N is protonated by ethanol additive to form NH_3 and lithium ethoxide (EtOLi). Investigation of various metal alloys revealed that the Li deposition on the electrode surface plays an important role in Li-mediated NRR.⁹¹ Additionally, a moderate protic additive (ethanol as optimum choice) is critical to regulate the proton supply, increase NH_3 yield, and suppress HER. However, the reaction mechanism and intrinsic kinetics of Li nitridation (toward Li_3N and NH_3) competing with Li protonation (toward H_2) was not clear. In 2019, Manthiram and co-workers refined the understanding of this process by using a coupled kinetic-transport model (Figure

8A).²⁴ They found that although these two reactions are first order in N_2 and ethanol, the nitridation reaction is more sensitive to the amount of plated Li. Through a series of improvements in the experimental setup, including using of a separator, drying of solvent, purification of reagents, and galvanostatic operation, a high FE of 18.5% was obtained with a NH_3 yield of $7.9 \text{ nmol cm}^{-2} \text{ s}^{-1}$.

Ethanol however is sacrificial as a proton donor in the electrolyte. It cannot be fully generated at the anode and impedes the stable operation in reasonable long-term.⁸⁷ For a more continuous and durable Li-mediated NRR, it is necessary to improve the recyclability and electrochemical stability of ethanol, or develop an improved recycling proton carrier. Manthiram and co-workers addressed the incomplete ethanol-ethoxide recycling by coupling H_2 oxidation reaction (HOR) at the anode, which produces protons to regenerate ethanol from the ethoxide and meanwhile avoids solvent oxidation.²² By using stainless-steel cloth (SSC)-based non-aqueous gas diffusion electrodes to improve transport of gaseous species in THF, they achieved a high FE of $35 \pm 6\%$ with a significant NH_3 partial current density of $8.8 \pm 1.4 \text{ mA cm}^{-2}$. Very recently, MacFarlane and colleagues proposed a phosphonium salt as the proton shuttle with high stability, recyclability and additional ionic conductivity for continuous Li-mediated NRR.⁸⁷ As is shown in Figure 8B, the phosphonium cation transforms into a ylide structure after reacting with Li_3N to release NH_3 . The ylide is then readily re protonated and transformed back to the original phosphonium form by HOR-derived H^+ at the anode. As the proton shuttle was not consumed in NRR, stability during the long-term operation was significantly enhanced, resulting in a highly significant NH_3 yield of $53 \text{ nmol cm}^{-2} \text{ s}^{-1}$ and a high FE of 69% in 20 h.

Stepwise Mode

Although the continuous mode for Li-mediated NRR exhibits high FE and high NH_3 yield, it requires high-cost non-aqueous electrolyte (e.g. THF) with strict-drying and expensive proton sources (ethanol and H_2).²⁴ It is more attractive to get NH_3 from atmospheric N_2 and H_2O in aqueous conditions, but practically difficult because of intense interaction between the Li deposits with H_2O . To circumvent this issue a direct and effective strategy is to physically separate Li deposition, Li nitridation and NH_3 formation.

In 2017, Nørskov and co-workers demonstrated a Li cycling electrification strategy using H_2O as the proton source by stepwise LiOH electrolysis, Li nitridation with N_2 and Li_3N hydrolysis to release NH_3 (Figure 8C).⁸⁸ Separation of the proton from electron transfer process, as well as the metallic Li from water, effectively circumvents HER, leading to a high initial overall current efficiency of 88.5% to NH_3 . However, LiOH electrolysis required a total cell potential of $> 3.0 \text{ V}$ and a high temperature at $450 \text{ }^\circ\text{C}$ that significantly limited energy efficiency. Moreover, separation of the deposited Li (liquid state at $450 \text{ }^\circ\text{C}$) from the molten salt electrolyte is practically difficult. To address this issue, Kim et al. immobilized the Li deposits on a Ni substrate in an organic electrolyte (propylene carbonate), using electrons that originated from water oxidation at the anode (aqueous electrolyte).⁸⁹ The consumed Li in the organic phase was complemented by aqueous anodic electrolyte through a Li-ion conducting glass ceramic material (LISICON) (Figure 8D). Following Li electro-deposition, Li nitridation in N_2 and Li_3N hydrolysis in diluted sulfuric acid were conducted to form NH_4^+ with a high FE of 52.3%. The biphasic system was optimized by polymethyl methacrylate (PMMA) to reinforce the immiscibility of aqueous/organic electrolytes, and omit using expensive LISICON membranes.⁹² PMMA in the organic phase ensured a water-proof nature of the organic solvent, and boosted Li plating efficiency, leading to an increased FE of 57.2 % compared to that with a physical membrane.⁸⁹

Another approach for Li-mediated N_2 fixation in ambient condition is to construct Li- N_2 batteries, in which discharging and charging process drives formation and decomposition of Li_3N ($6Li^+ + N_2 \leftrightarrow 2Li_3N$). NH_3 is obtained by Li_3N hydrolysis with water. In 2017, Zhang and co-workers first constructed a rechargeable Li- N_2 battery consisting of a Li anode, ether-based electrolyte, glass-fiber separator, and carbon-cloth cathode.⁹³ Following fine tuning of the operating current density and discharging periods, the battery exhibited a high FE of 59% for N_2 fixation. It is notable that the hygroscopicity and instability of Li_3N product during charging/discharging makes the Li- N_2 system rechargeable, but irreversible.⁹⁴ Therefore future research is needed to understand the interface chemistry and to improve electrode stability and cyclability.

Li-mediated approach is appealing and powerful for N_2 activation and fixation to NH_3 because of intrinsic advantages in high activity and selectivity. However, this approach faces significant technical obstacles, such as formation of solid electrolyte interphase (SEI) layer during Li deposition,²³ complex process in stepwise mode,⁸⁸ diffusion limitation with gaseous reactants

in electrolytes,²⁴ and; limited recyclability and durability.^{89,94} To address these issues progress is needed in: 1) Elaborate design of reaction apparatus for continuous operation with increased stability; 2) Development of new electrode materials to facilitate Li electro-deposition; 3) Understanding of kinetic-transport in the whole system including electrode, electrolyte and SEI interface, and; 4) Use of solvent additives and engineering of new electrolytes for faster Li⁺ transportation and favorable SEI layer.⁸⁷

MAIN GROUP ELEMENTS SUPPRESS H₂ EVOLUTION

In addition to boosting N₂ activation, the high-performance electrocatalytic synthesis of NH₃ also relies on suppression of competing HER. Present research mainly focuses on optimizing electronic structures of electrocatalysts to regulate intermediate adsorption and reaction pathway to NRR versus HER.⁹⁶ However, it is a prerequisite to more clearly understand the mechanistic origin of NRR/HER competition, such as differences in electron and proton transfer³⁹ and dependence on applied potential.⁹⁵ From a qualitative analysis, Nørskov and co-workers revealed that the reaction rate of NRR is not meaningfully impacted by electron and proton concentration (zeroth order), whilst that for HER is first order in both.³⁹ Additionally, a more recent theoretical investigation reported that the surface proton and N₂ coverage crossover leads to a significant decrease in NRR activity and selectivity, originating from the large charge transfer in adsorption of proton over N₂.⁹⁵ Therefore, it is reasonable to limit accessibility of protons, electrons or both for kinetically suppressed HER whilst maintaining NH₃ yield (Figure 9A and B). In this regard, MGEs have the unique advantage of being able to suppress HER.

Poor Proton Binding Ability

Controlling the surface coverage of proton with increased binding barriers has been well demonstrated as an effective strategy to retard HER and facilitate NRR (Figure 9A).^{39,95} Most TMs-based electrocatalysts are good binders of protons than nitrogen due to their d-orbital structures, while MGEs have intrinsically poor proton binding ability. As is shown in Figure 9C, MGEs, such as Bi, Sn, Pb and Ga, are all located on the left-leg of the volcano-type activity plot for HER, indicating their weak hydrogen binding strength.^{33,34} For example, Pb was introduced into HER-active electrocatalysts (Pd nanospheres and RuO₂) to regulate the reaction selectivity.⁹⁷ Experimental results and DFT calculations confirmed that the incorporation of Pb can effectively reduce *H adsorption to inhibit HER activity, and to decrease *NNH generation free energy to boost NRR activity. Nonmetallic MGEs, such as carbon-based materials, are also reported to have high free energy toward *H adsorption, leading to highly significantly reduced HER activity.⁹⁸ Consequently, carbon substrates are widely used in NRR electrocatalysts and are anticipated to show great potentials when combining with the above mentioned N₂ activation approaches.⁹⁶

Low Electron Conductivity

In addition to protons, limiting electron accessibility is also an effective strategy which significantly lowers production of H₂ whilst not impacting the formation rate of NH₃ (Figure 9B).⁹⁵ DFT calculation showed that the free energy of proton adsorption, ΔG (*H), rapidly becomes more negative with negative shifts of applied potentials, whilst the value for N₂ adsorption, ΔG (*N₂), does not change meaningfully (Figure 9D). This is consistent with previous reports that the rate of H₂ evolution is dependent on surface concentration of electrons, whilst the rate of NH₃ is not.³⁹ Therefore, when the electron transfer becomes rate-limiting, HER will be significantly suppressed. Most metallic MGEs are semiconducting with intrinsically sluggish electron conductivity, and therefore are favorable for suppressing HER. For example, Bi-based nanomaterials have been widely investigated as highly selective electrocatalysts for NRR.^{30,56} The *in situ* reduced Bi⁰ species was demonstrated to be the active phase,⁵⁵ and its semiconducting feature limits surface electron accessibility and suppresses HER.^{30,39} A similar finding is reported for Sn- and Sb-based electrocatalysts.^{99,100} Analogously, some conductive polymers have been reported as practically promising HER inhibitors, such as polypyrrole,¹⁰¹ polyaniline¹⁰² and polyimide.¹⁰³ The electron transfer rate and reaction selectivity can be regulated by tuning the thickness of the polymer film,¹⁰² or by optimizing the Mott–Schottky interface between metals and semiconductors.¹⁰³

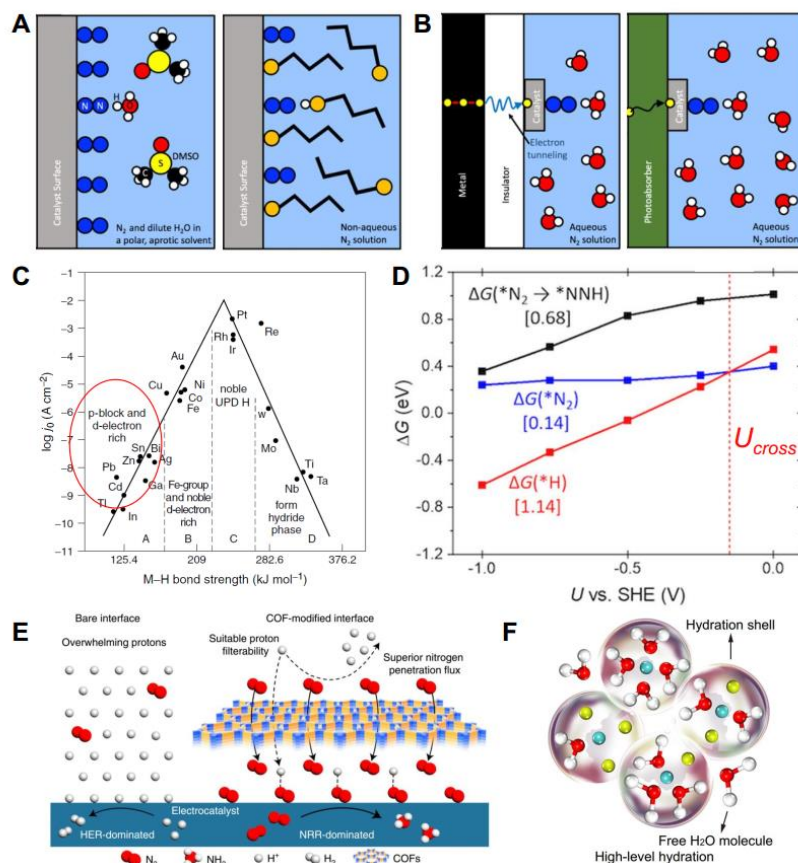


Figure 9. MGEs contribute to HER suppression.

(A) Strategies to suppress HER through limiting proton transfer either by reducing concentration of proton (left), or increasing barriers for proton transfer (right).

(B) Strategies to suppress HER through limiting electron transfer either by introducing a thin insulator (left), or using semi-conductors to limit the stream of electrons (right). (A) and (B) are reproduced with permission from Singh *et al.*³⁹ Copyright 2016 American Chemical Society.

(C) Volcano plot of exchange current ($\log j_0$) for HER as a function of M-H bond energy. Reproduced with permission from Conway *et al.*³³ Copyright 2000 Elsevier.

(D) Change of $\Delta G(*H)$, $\Delta G(*N_2)$, and $\Delta G(*N_2 \rightarrow *NNH)$ with potential. The red-color dash line indicates crossover potential of HER and NRR. Reproduced with permission from Choi *et al.*⁹⁵ Copyright 2021 Springer Nature.

(E) Schematic of HER suppression using proton-filtering COFs. Reproduced with permission from Liu *et al.*³⁷ Copyright 2021 Springer Nature.

(F) Illustration of water content in LiCl solution with high-level hydration system. Reproduced with permission from Wang *et al.*³⁶ Copyright 2021 Springer Nature.

Electrode Surface Engineering

In addition to the direct use as promising electrocatalysts, the unique physiochemical properties of MGEs-based materials offer an opportunity to rationally control proton accessibility and mass diffusion via electrode surface engineering. For example, the surface hydrophobic treatment of electrocatalysts by MGEs-based molecules, e.g. polytetrafluoroethylene (PTFE) and 1-octadecanethiol, can be used to tailor reaction selectivity in aqueous gas-involving electrochemical applications, such as CO_2 reduction reaction (CRR).¹⁰⁴ Similarly, hydrophobic layers (e.g. PTFE,³⁸ fluorosilane¹⁰⁵) can regulate concentration of reactants (H^+ and N_2) by impeding water adsorption and attracting N_2 at the electrode surface. This simultaneously suppresses undesired HER and boosts N_2 reduction to NH_3 . The FE toward NH_3 for PTFE-treated Au nanoparticles in photoelectrochemical NRR significantly increased by 4 times compared with that for the untreated counterpart.³⁸ Additionally, the local diffusion of H^+ and N_2 in the near-electrode region can be precisely regulated by engineering the surface layer. Very recently, Yan and co-workers proposed a proton-filtering exfoliated covalent-organic-framework (COF) layer with moderate proton filterability and significant nitrogen penetration

flux (Figure 9E), realizing a high NH_3 yield of $287.2 \mu\text{g mg}_{\text{cat}}^{-1} \text{h}^{-1}$ with FE of 54.5% on a routine B-doped carbon electrode.³⁷

Electrolyte Engineering and Ions Effect

Another method using MGEs to suppress HER during NRR is addition of alkali metal cations (Li^+ , Na^+ , K^+) in the electrolyte, especially at high concentration. The cation-derived solvation and steric effects will significantly impact the local pH, selectively stabilize specific intermediates, and limit proton migration within the electrical double-layer (EDL) region, resulting in steered-reaction selectivity.^{35,36} For example, Rondinone and co-workers reported that alkali metal cations form a dehydrated cation layer surrounding the nanoscale tip of a carbon material to exclude water whilst allowing access to N_2 molecules.³⁵ The suppression was critically dependent on size and N_2 binding energy of cations. However, the mechanism origin remains unknown, leading to uncertainty of the best choice (Li^+ versus K^+).^{35,36} Very recently, Yan and co-workers optimized this strategy using a highly concentrated LiCl electrolyte (10 M) to suppress HER and concomitantly boost nitrogen accessibility.³⁶ By combining MD simulations, finite element simulations, and various *in situ* characterizations, a ‘salting-out’ effect was confirmed as illustrated in Figure 9F. In contrast to dilute solutions, highly concentrated salt solutions can break or distort hydrogen bond networks, immobilize H_2O molecules around Li^+ ions, and significantly decrease free water within the Stern layer. The resulting appropriate proton supply and ideal nitrogen enrichment enables superior NRR performance with a high FE of 71% and a high NH_3 yield of $9.5 \times 10^{-10} \text{ mol cm}^{-2} \text{ s}^{-1}$ at -0.3 V versus RHE in 10 M LiCl on a metal-free electrocatalyst. Li^+ ions can also be used to occupy and poison HER active sites because of their high Lewis acidity. For example, the association of Li^+ ions with polyimides has been employed to passivate HER in aqueous rechargeable lithium-ion batteries.¹⁰⁶ In 2017, Wang and co-workers introduced Li^+ ions to suppress HER during NRR.¹⁰⁷ The association of Li^+ ions with the electron-rich C=O groups in poly(N-ethylbenzene-1,2,4,5-tetracarboxylic diimide) electrocatalyst, confirmed by electrochemical characterizations and DFT calculations, can induce a higher energy barrier for H_2 evolution, giving a larger potential window to a higher-selectivity NRR.

Besides cationic ions, MGEs-based anionic ions are also critically important to regulate the adsorption behavior of gaseous reactant and protons. For instance, it has been reported that halide anions with high affinity to the electrode can not only strongly restrain CO_2 on electrode surface, but also suppress the adsorption of proton, leading to a higher HER overpotential.¹⁰⁸ This halide anion effect provides new opportunity for boosted N_2 capture and suppressed protons adsorption, which however is current receiving few attentions in NRR.

CONCLUSION AND PERSPECTIVE

The performance of electrocatalytic NRR is critically limited by the high-energy barrier for N_2 activation and competing HER. Based on a critical assessment and comparative summary of MGEs-based materials design for optimal NRR performance, it is concluded that: 1) MGEs are significantly advantageous in boosting N_2 activation and suppressing HER in comparison with conventional TMs-based electrocatalysts; 2) Optimization of electrolyte and electrode surface can be gainfully used to boost NRR, and; 3) Importantly, MGEs-based functional mechanisms are generalizable, and could be judiciously applied as a basis for smart design of advanced catalyst materials for N_2 fixation. This review is expected to be a springboard for the smart design of advanced catalyst materials for NRR in the future. There are however four key areas that will need to be addressed in future investigation:

Establishment of Rigid Protocols for NRR Evaluation

Due to low nanomole NH_3 yields with NRR, and possibility for a level of contamination in experiment e.g. from the environment, consumables and chemicals,^{28,109} a rigorous measurement protocol for reliable determination of NRR-derived NH_3 is needed. This will permit direct comparison and evaluation of different reports. Several protocols have been proposed in previous reports,^{4,29,109} amongst which $^{15}\text{N}_2$ isotope experiment is the most powerful and indispensable to effectively obviate false positive results.¹¹⁰ Chorkendorff and co-workers reported the best practice for quantitative isotope measurement by cycling $^{15}\text{N}_2$ gas with consideration of reducing both contamination and cost.²⁹ For day-to-day experiments, integration of multiple quantitative methods, such as indophenol blue method, Nessler’s method, and ion chromatography, is recommended for accurate quantification of NH_3 concentration. To permit meaningful comparison of results collected under varying conditions and experimental set-ups among research groups, it is important to have a standardized test procedure and transparent reporting.⁴ An appropriate benchmark catalyst, akin to Pt/C widely used in O_2 reduction and HER, is highly desired to accelerate the research efforts for NRR.

Synergetic Design of MGEs-based Electrocatalysts and Strategies

Owing to unique electronic structure and physiochemical properties, MGEs-based materials are advantageous for N₂ activation and HER suppression following various mechanisms. Based on the understanding of each mechanism, it is highly promising to design advanced strategies with synergetic effects. For example, it is possible to simultaneously: 1) Introduce Lewis acid sites on g-C₃N₄ nanosheets with nitrogen vacancies for electrocatalyst; 2) Apply Li-mediated pathways with highly concentrated Li⁺ solution as electrolyte, and; 3) Decorate a hydrophobic layer with optimal proton and nitrogen supply as interface. Research efforts to optimize electrolyte, electrolyte additives and electrode/electrolyte interface based on the distinctive features of MGEs, is likely to return significant growth in understanding of NRR. In addition to NRR, the MGEs-based functional mechanisms and methodologies are generalizable in other multi-electron reactions with sluggish kinetics and H₂ evolution competition such as CO₂ reduction and nitrate/nitrite reduction.^{54, 111} Therefore, future theoretical and experimental study needs to comprehensively consider intrinsic properties, surface electrochemical environment and catalytic stability, to design advanced catalysts and strategies for NRR and other reaction systems.

In Situ/Operando Measurement for Insight into N₂ Reduction Mechanism

In situ and *operando* techniques are powerful tools to monitor electrocatalyst change and reaction intermediates within the EDL region under reaction conditions, thus bridging the gap between mechanistic understanding and electrocatalysis process.¹¹² Real-time and *in situ* observations by various techniques, such as *in situ/operando* surface-enhanced infrared absorption spectroscopy,¹¹³ Raman,^{36,37} XRD,⁵⁰ and X-ray absorption spectroscopy,¹⁹ can be used to confirm occurrence of NRR, detect specific *N_xH_y intermediates to refine reaction pathway, identify the actual catalytic active sites, and develop understanding of electrocatalysts deactivation. However, present *in situ* spectroscopic techniques have limitations, such as the ambiguous assignment of spectroscopic peaks, environment-sensitive variation of signals, high requirements on controlling testing configurations, and insufficient acquisition speed for short-lived intermediate species. Future research will need to include: 1) Optimization and benchmarking of existing methods, 2) Development of *in situ* techniques with better sensitivity and greater resolution, 3) Establishment of a database for NRR-related *in situ* characterizations, and; 4) Integration of multiple *in situ* methods with varying function for comprehensive and unambiguous mechanistic understanding.

Integration of Multiple Techniques for New N₂ Fixation Approaches

Instead of typically one-step N₂ fixation to NH₃, a multiple-step approach is promising by more effectively solving one problem in each step. For example, we recently realized efficient N₂ fixation to NH₃ through integration of plasma oxidation with electrocatalytic reduction.¹¹⁴ A non-thermal plasma technique is used to effectively activate N₂ to nitrogen oxyanions (NO_x⁻), whilst the following electrocatalysis ensures highly selective conversion of NO_x⁻ to NH₃. Therefore, integration of multiple techniques for complementarity could provide opportunity to realize high-efficiency conversion of N₂ to NH₃. Demonstration of the whole from N₂ (or even air) to NH₃, together with techno-economic analyses could underpin an acceleration in development of sustainable and efficient N₂ fixation.

In summary, the remarkable progress that MGEs-based catalysts and strategies have achieved in the field of NRR has confirmed their great potential in electrochemical reduction of N₂ to NH₃. Despite great challenges ahead, it is envisioned that a combination of synergetic catalyst design with in-depth fundamental understanding, together with reliable *in situ/operando* characterizations and efficient integration of multiple techniques will promisingly accelerate the development of more sustainable, efficient, and durable NH₃ synthesis technologies in the near future.

ACKNOWLEDGMENTS

The authors gratefully acknowledge financial support from the Australian Research Council through the Discovery Project (FL170100154, DP160104866).

AUTHOR CONTRIBUTIONS

All authors devised the concept and built the framework of the Review. L. L., C. T., and H. J. wrote the manuscript and organized the figures. C. T., K. D., and S.-Z. Q. edited and revised the manuscript.

REFERENCES

1. Erisman, J.W., Sutton, M.A., Galloway, J., Klimont, Z., and Winiwarter, W. (2008). How a century of ammonia synthesis changed the world. *Nat. Geosci.* *1*, 636.
2. Guo, J., and Chen, P. (2017). Catalyst: NH_3 as an energy carrier. *Chem* *3*, 709-712.
3. MacFarlane, D.R., Cherepanov, P.V., Choi, J., Suryanto, B.H.R., Hodgetts, R.Y., Bakker, J.M., Ferrero Vallana, F.M., and Simonov, A.N. (2020). A roadmap to the ammonia economy. *Joule* *4*, 1186-1205.
4. Tang, C., and Qiao, S.-Z. (2019). How to explore ambient electrocatalytic nitrogen reduction reliably and insightfully. *Chem. Soc. Rev.* *48*, 3166-3180.
5. Tyler, D.R., Balesdent, C.G., and Kendall, A.J. (2013). 8.14 - Nitrogen activation. In *Comprehensive inorganic chemistry II* (second edition), J. Reedijk, and K. Poeppelmeier, eds. (Elsevier), pp. 525-552.
6. Goodman, J.B., and Krase, N.W. (1931). Solubility of nitrogen in water at high pressures and temperatures. *Ind. Eng. Chem.* *23*, 401-404.
7. Ren, Y., Yu, C., Tan, X., Huang, H., Wei, Q., and Qiu, J. (2021). Strategies to suppress hydrogen evolution for highly selective electrocatalytic nitrogen reduction: Challenges and perspectives. *Energy Environ. Sci.* *14*, 1176-1193.
8. Zhao, X., Hu, G., Chen, G.-F., Zhang, H., Zhang, S., and Wang, H. (2021). Comprehensive understanding of the thriving ambient electrochemical nitrogen reduction reaction. *Adv. Mater.* *33*, 2007650.
9. Liu, J., Kelley, M.S., Wu, W., Banerjee, A., Douvalis, A.P., Wu, J., Zhang, Y., Schatz, G.C., and Kanatzidis, M.G. (2016). Nitrogenase-mimic iron-containing chalcogenides for photochemical reduction of dinitrogen to ammonia. *Proc. Natl. Acad. Sci.* *113*, 5530-5535.
10. Cao, N., Chen, Z., Zang, K., Xu, J., Zhong, J., Luo, J., Xu, X., and Zheng, G. (2019). Doping strain induced Bi-Ti^{3+} pairs for efficient N_2 activation and electrocatalytic fixation. *Nat. Commun.* *10*, 2877.
11. Broere, D.L.J., and Holland, P.L. (2018). Boron compounds tackle dinitrogen. *Science* *359*, 871-871.
12. Shi, L., Li, Q., Ling, C., Zhang, Y., Ouyang, Y., Bai, X., and Wang, J. (2019). Metal-free electrocatalyst for reducing nitrogen to ammonia using a Lewis acid pair. *J. Mater. Chem. A* *7*, 4865-4871.
13. Power, P.P. (2010). Main-group elements as transition metals. *Nature* *463*, 171-177.
14. Sun, Y., Wang, Y., Li, H., Zhang, W., Song, X.-M., Feng, D.-M., Sun, X., Jia, B., Mao, H., and Ma, T. (2021). Main group metal elements for ambient-condition electrochemical nitrogen reduction. *J. Energy Chem.* *62*, 51-70.
15. Tang, C., Zheng, Y., Jaroniec, M., and Qiao, S.-Z. (2021). Electrocatalytic refinery for sustainable production of fuels and chemicals. *Angew. Chem. Int. Ed.* *60*, 19572-19590.
16. Shipman, M.A., and Symes, M.D. (2017). Recent progress towards the electrosynthesis of ammonia from sustainable resources. *Catal. Today* *286*, 57-68.
17. Li, X.-F., Li, Q.-K., Cheng, J., Liu, L., Yan, Q., Wu, Y., Zhang, X.-H., Wang, Z.-Y., Qiu, Q., and Luo, Y. (2016). Conversion of dinitrogen to ammonia by FeN_3 -embedded graphene. *J. Am. Chem. Soc.* *138*, 8706-8709.
18. Cui, X., Tang, C., and Zhang, Q. (2018). A review of electrocatalytic reduction of dinitrogen to ammonia under ambient conditions. *Adv. Energy Mater.* *8*, 1800369.
19. Yang, X., Nash, J., Anibal, J., Dunwell, M., Kattel, S., Stavitski, E., Attenkofer, K., Chen, J.G., Yan, Y., and Xu, B. (2018). Mechanistic insights into electrochemical nitrogen reduction reaction on vanadium nitride nanoparticles. *J. Am. Chem. Soc.* *140*, 13387-13391.
20. Abghoui, Y., Garden, A.L., Hlynsson, V.F., Björgvinsdóttir, S., Ólafsdóttir, H., and Skúlason, E. (2015). Enabling electrochemical reduction of nitrogen to ammonia at ambient conditions through rational catalyst design. *Phys. Chem. Chem. Phys.* *17*, 4909-4918.
21. Du, H.-L., Gengenbach, T.R., Hodgetts, R., MacFarlane, D.R., and Simonov, A.N. (2019). Critical assessment of the electrocatalytic activity of vanadium and niobium nitrides toward dinitrogen reduction to ammonia. *ACS Sustainable Chem. Eng.* *7*, 6839-6850.
22. Lazouski, N., Chung, M., Williams, K., Gala, M.L., and Manthiram, K. (2020). Non-aqueous gas diffusion electrodes for rapid ammonia synthesis from nitrogen and water-splitting-derived hydrogen. *Nat. Catal.* *3*, 463-469.
23. Andersen, S.Z., Statt, M.J., Bukas, V.J., Shapel, S.G., Pedersen, J.B., Krempl, K., Saccoccio, M., Chakraborty, D., Kibsgaard, J., Vesborg, P.C.K., et al. (2020). Increasing stability, efficiency, and fundamental understanding of lithium-mediated electrochemical nitrogen reduction. *Energy Environ. Sci.* *13*, 4291-4300.
24. Lazouski, N., Schiffer, Z.J., Williams, K., and Manthiram, K. (2019). Understanding continuous lithium-mediated electrochemical nitrogen reduction. *Joule* *3*, 1127-1139.
25. Shi, L., Yin, Y., Wang, S., and Sun, H. (2020). Rational catalyst design for N_2 reduction under ambient conditions: Strategies toward enhanced conversion efficiency. *ACS Catal.* *10*, 6870-6899.
26. Skulason, E., Bligaard, T., Gudmundsdóttir, S., Studt, F., Rossmeisl, J., Abild-Pedersen, F., Vegge, T., Jonsson, H., and Norskov, J.K. (2012). A theoretical evaluation of possible transition metal electrocatalysts for N_2 reduction. *Phys. Chem. Chem. Phys.* *14*, 1235-1245.
27. Martín, A.J., Shinagawa, T., and Pérez-Ramírez, J. (2019). Electrocatalytic reduction of nitrogen: From Haber-Bosch to ammonia artificial leaf. *Chem* *5*, 263-283.
28. Li, L., Tang, C., Yao, D., Zheng, Y., and Qiao, S.-Z. (2019). Electrochemical nitrogen reduction: Identification and elimination of contamination in electrolyte. *ACS Energy Lett.* *4*, 2111-2116.
29. Andersen, S.Z., Čolić, V., Yang, S., Schwalbe, J.A., Nielander, A.C., McEnaney, J.M., Enemark-Rasmussen, K., Baker, J.G., Singh, A.R., Rohr, B.A., et al. (2019). A rigorous electrochemical ammonia synthesis protocol with quantitative isotope measurements. *Nature* *570*, 504-508.
30. Li, L., Tang, C., Xia, B., Jin, H., Zheng, Y., and Qiao, S.-Z. (2019). Two-dimensional mosaic bismuth nanosheets for highly selective ambient electrocatalytic nitrogen reduction. *ACS Catal.* *9*, 2902-2908.
31. Tsuneto, A., Kudo, A., and Sakata, T. (1994). Lithium-mediated electrochemical reduction of high pressure N_2 to NH_3 . *J. Electroanal. Chem.* *367*, 183-188.

32. Yan, D., Li, H., Chen, C., Zou, Y., and Wang, S. (2019). Defect engineering strategies for nitrogen reduction reactions under ambient conditions. *Small Methods* 3, 1800331.
33. Conway, B.E., and Jerkiewicz, G. (2000). Relation of energies and coverages of underpotential and overpotential deposited H at Pt and other metals to the 'volcano curve' for cathodic H₂ evolution kinetics. *Electrochim. Acta* 45, 4075-4083.
34. Dražević, E., and Skúlason, E. (2020). Are there any overlooked catalysts for electrochemical NH₃ synthesis—new insights from analysis of thermochemical data. *iScience* 23, 101803.
35. Song, Y., Johnson, D., Peng, R., Hensley, D.K., Bonnesen, P.V., Liang, L., Huang, J., Yang, F., Zhang, F., Qiao, R., et al. (2018). A physical catalyst for the electrolysis of nitrogen to ammonia. *Sci. Adv.* 4, e1700336
36. Wang, M., Liu, S., Ji, H., Yang, T., Qian, T., and Yan, C. (2021). Salting-out effect promoting highly efficient ambient ammonia synthesis. *Nat. Commun.* 12, 3198.
37. Liu, S., Qian, T., Wang, M., Ji, H., Shen, X., Wang, C., and Yan, C. (2021). Proton-filtering covalent organic frameworks with superior nitrogen penetration flux promote ambient ammonia synthesis. *Nat. Catal.* 4, 322-331.
38. Zheng, J., Lyu, Y., Qiao, M., Wang, R., Zhou, Y., Li, H., Chen, C., Li, Y., Zhou, H., Jiang, S.P., and Wang, S. (2019). Photoelectrochemical synthesis of ammonia on the aerophilic-hydrophilic heterostructure with 37.8% efficiency. *Chem* 5, 617-633.
39. Singh, A.R., Rohr, B.A., Schwalbe, J.A., Cargnello, M., Chan, K., Jaramillo, T.F., Chorkendorff, I., and Nørskov, J.K. (2016). Electrochemical ammonia synthesis—the selectivity challenge. *ACS Catal.* 7, 706-709.
40. Liu, C., Li, Q., Wu, C., Zhang, J., Jin, Y., MacFarlane, D.R., and Sun, C. (2019). Single-boron catalysts for nitrogen reduction reaction. *J. Am. Chem. Soc.* 141, 2884-2888.
41. Légaré, M.-A., Bélanger-Chabot, G., Dewhurst, R.D., Welz, E., Krummenacher, I., Engels, B., and Braunschweig, H. (2018). Nitrogen fixation and reduction at boron. *Science* 359, 896-900.
42. Li, M., Cui, Y., Sun, L., Zhang, X., Peng, L., and Huang, Y. (2020). Boosting electrocatalytic N₂ reduction to NH₃ over two-dimensional gallium selenide by defect-size engineering. *Inorg. Chem.* 59, 4858-4867.
43. Fan, Q., Choi, C., Yan, C., Liu, Y., Qiu, J., Hong, S., Jung, Y., and Sun, Z. (2019). High-yield production of few-layer boron nanosheets for efficient electrocatalytic N₂ reduction. *Chem. Commun.* 55, 4246-4249.
44. Yu, X., Han, P., Wei, Z., Huang, L., Gu, Z., Peng, S., Ma, J., and Zheng, G. (2018). Boron-doped graphene for electrocatalytic N₂ reduction. *Joule* 2, 1610-1622.
45. Mao, X., Zhou, S., Yan, C., Zhu, Z., and Du, A. (2019). A single boron atom doped boron nitride edge as a metal-free catalyst for N₂ fixation. *Phys. Chem. Chem. Phys.* 21, 1110-1116.
46. Qiu, W., Xie, X.-Y., Qiu, J., Fang, W.-H., Liang, R., Ren, X., Ji, X., Cui, G., Asiri, A.M., Cui, G., et al. (2018). High-performance artificial nitrogen fixation at ambient conditions using a metal-free electrocatalyst. *Nat. Commun.* 9, 3485.
47. Lv, C., Zhong, L., Yao, Y., Liu, D., Kong, Y., Jin, X., Fang, Z., Xu, W., Yan, C., Dinh, K.N., et al. (2020). Boosting electrocatalytic ammonia production through mimicking "π back-donation". *Chem* 6, 2690-2702.
48. Chen, C., Yan, D., Wang, Y., Zhou, Y., Zou, Y., Li, Y., and Wang, S. (2019). B-N pairs enriched defective carbon nanosheets for ammonia synthesis with high efficiency. *Small* 15, 1805029.
49. Chang, B., Li, L., Shi, D., Jiang, H., Ai, Z., Wang, S., Shao, Y., Shen, J., Wu, Y., Li, Y., and Hao, X. (2021). Metal-free boron carbonitride with tunable boron Lewis acid sites for enhanced nitrogen electroreduction to ammonia. *Appl. Catal. B* 283, 119622.
50. Liu, S., Wang, M., Qian, T., Ji, H., Liu, J., and Yan, C. (2019). Facilitating nitrogen accessibility to boron-rich covalent organic frameworks via electrochemical excitation for efficient nitrogen fixation. *Nat. Commun.* 10, 3898.
51. Liu, Y., Li, Q., Guo, X., Kong, X., Ke, J., Chi, M., Li, Q., Geng, Z., and Zeng, J. (2020). A highly efficient metal-free electrocatalyst of F-doped porous carbon toward N₂ electroreduction. *Adv. Mater.* 32, 1907690.
52. Wen, Y., Zhu, H., Hao, J., Lu, S., Zong, W., Lai, F., Ma, P., Dong, W., Liu, T., and Du, M. (2021). Metal-free boron and sulphur co-doped carbon nanofibers with optimized p-band centers for highly efficient nitrogen electroreduction to ammonia. *Appl. Catal. B* 292, 120144.
53. Sun, S., An, Q., Wang, W., Zhang, L., Liu, J., and Goddard III, W.A. (2017). Efficient photocatalytic reduction of dinitrogen to ammonia on bismuth monoxide quantum dots. *J. Mater. Chem. A* 5, 201-209.
54. He, S., Ni, F., Ji, Y., Wang, L., Wen, Y., Bai, H., Liu, G., Zhang, Y., Li, Y., Zhang, B., and Peng, H. (2018). The p-orbital delocalization of main-group metals to boost CO₂ electroreduction. *Angew. Chem. Int. Ed.* 130, 16346-16351.
55. Yao, D., Tang, C., Li, L., Xia, B., Vasileff, A., Jin, H., Zhang, Y., and Qiao, S.-Z. (2020). *In situ* fragmented bismuth nanoparticles for electrocatalytic nitrogen reduction. *Adv. Energy Mater.* 10, 2001289.
56. Hao, Y.-C., Guo, Y., Chen, L.-W., Shu, M., Wang, X.-Y., Bu, T.-A., Gao, W.-Y., Zhang, N., Su, X., Feng, X., et al. (2019). Promoting nitrogen electroreduction to ammonia with bismuth nanocrystals and potassium cations in water. *Nat. Catal.* 2, 448-456.
57. Yang, F.Y., Liu, K., Chien, C.L., and Searson, P.C. (1999). Large magnetoresistance and finite-size effects in electrodeposited single-crystal Bi thin films. *Phys. Rev. Lett.* 82, 3328-3331.
58. Fu, Y., Li, K., Batmunkh, M., Yu, H., Donne, S., Jia, B., and Ma, T. (2020). Unsaturated p-metal-based metal-organic frameworks for selective nitrogen reduction under ambient conditions. *ACS Appl. Mater. Interfaces* 12, 44830-44839.
59. Guo, Y., Yang, Q., Wang, D., Li, H., Huang, Z., Li, X., Zhao, Y., Dong, B., and Zhi, C. (2020). A rechargeable Al-N₂ battery for energy storage and highly efficient N₂ fixation. *Energy Environ. Sci.* 13, 2888-2895.
60. Tang, C., Wang, H.-F., Chen, X., Li, B.-Q., Hou, T.-Z., Zhang, B., Zhang, Q., Titirici, M.-M., and Wei, F. (2016). Topological defects in metal-free nanocarbon for oxygen electrocatalysis. *Adv. Mater.* 28, 6845-6851.

61. Liu, Y., Deng, P., Wu, R., Zhang, X., Sun, C., and Li, H. (2021). Oxygen vacancies for promoting the electrochemical nitrogen reduction reaction. *J. Mater. Chem. A* 9, 6694-6709.
62. Jin, H., Li, L., Liu, X., Tang, C., Xu, W., Chen, S., Song, L., Zheng, Y., and Qiao, S.-Z. (2019). Nitrogen vacancies on 2D layered W_2N_3 : A stable and efficient active site for nitrogen reduction reaction. *Adv. Mater.* 31, 1902709.
63. Li, X., Li, T., Ma, Y., Wei, Q., Qiu, W., Guo, H., Shi, X., Zhang, P., Asiri, A.M., Chen, L., et al. (2018). Boosted electrocatalytic N_2 reduction to NH_3 by defect-rich MoS_2 nanoflower. *Adv. Energy Mater.* 8, 1801357.
64. Lai, F., Zong, W., He, G., Xu, Y., Huang, H., Weng, B., Rao, D., Martens, J.A., Hofkens, J., Parkin, I.P., and Liu, T. (2020). N_2 electroreduction to NH_3 by selenium vacancy-rich $ReSe_2$ catalysis at an abrupt interface. *Angew. Chem. Int. Ed.* 59, 13320-13327.
65. Wang, Y., Shi, M.-M., Bao, D., Meng, F.-L., Zhang, Q., Zhou, Y.-T., Liu, K.-H., Zhang, Y., Wang, J.-Z., Chen, Z.-W., et al. (2019). Generating defect-rich bismuth for enhancing the rate of nitrogen electroreduction to ammonia. *Angew. Chem. Int. Ed.* 58, 9464-9469.
66. Yang, X., Kattel, S., Nash, J., Chang, X., Lee, J.H., Yan, Y., Chen, J.G., and Xu, B. (2019). Quantification of active sites and elucidation of the reaction mechanism of the electrochemical nitrogen reduction reaction on vanadium nitride. *Angew. Chem. Int. Ed.* 58, 13768-13772.
67. Sarkar, A., and Khan, G.G. (2019). The formation and detection techniques of oxygen vacancies in titanium oxide-based nanostructures. *Nanoscale* 11, 3414-3444.
68. Cui, X., Tang, C., Liu, X.-M., Wang, C., Ma, W., and Zhang, Q. (2018). Highly selective electrochemical reduction of dinitrogen to ammonia at ambient temperature and pressure over iron oxide catalysts. *Chem. Eur. J.* 24, 18494-18501.
69. Zhang, G., Ji, Q., Zhang, K., Chen, Y., Li, Z., Liu, H., Li, J., and Qu, J. (2019). Triggering surface oxygen vacancies on atomic layered molybdenum dioxide for a low energy consumption path toward nitrogen fixation. *Nano Energy* 59, 10-16.
70. Yao, J.-X., Bao, D., Zhang, Q., Shi, M.-M., Wang, Y., Gao, R., Yan, J.-M., and Jiang, Q. (2019). Tailoring oxygen vacancies of $BiVO_4$ toward highly efficient noble-metal-free electrocatalyst for artificial N_2 fixation under ambient conditions. *Small Methods* 3, 1800333.
71. Liu, Y., Kong, X., Guo, X., Li, Q., Ke, J., Wang, R., Li, Q., Geng, Z., and Zeng, J. (2020). Enhanced N_2 electroreduction over $LaCoO_3$ by introducing oxygen vacancies. *ACS Catal.* 10, 1077-1085.
72. Lv, C., Qian, Y., Yan, C., Ding, Y., Liu, Y., Chen, G., and Yu, G. (2018). Defect engineering metal-free polymeric carbon nitride electrocatalyst for effective nitrogen fixation under ambient conditions. *Angew. Chem. Int. Ed.* 57, 10246-10250.
73. Choi, J., Suryanto, B.H.R., Wang, D., Du, H.-L., Hodgetts, R.Y., Ferrero Vallana, F.M., MacFarlane, D.R., and Simonov, A.N. (2020). Identification and elimination of false positives in electrochemical nitrogen reduction studies. *Nat. Commun.* 11, 5546.
74. Jiao, Y., Zheng, Y., Davey, K., and Qiao, S.-Z. (2016). Activity origin and catalyst design principles for electrocatalytic hydrogen evolution on heteroatom-doped graphene. *Nat. Energy* 1, 16130.
75. Li, L., Tang, C., Zheng, Y., Xia, B., Zhou, X., Xu, H., and Qiao, S.-Z. (2020). Tailoring selectivity of electrochemical hydrogen peroxide generation by tunable pyrrolic-nitrogen-carbon. *Adv. Energy Mater.* 10, 2000789.
76. Yang, Y., Zhang, L., Hu, Z., Zheng, Y., Tang, C., Chen, P., Wang, R., Qiu, K., Mao, J., Ling, T., and Qiao, S.-Z. (2020). The crucial role of charge accumulation and spin polarization in activating carbon-based catalysts for electrocatalytic nitrogen reduction. *Angew. Chem. Int. Ed.* 59, 4525-4531.
77. Guo, Y., Yao, Z., Zhan, S., Timmer, B.J.J., Tai, C.-W., Li, X., Xie, Z., Meng, Q., Fan, L., Zhang, F., et al. (2020). Molybdenum and boron synergistically boosting efficient electrochemical nitrogen fixation. *Nano Energy* 78, 105391.
78. Liu, Y., Su, Y., Quan, X., Fan, X., Chen, S., Yu, H., Zhao, H., Zhang, Y., and Zhao, J. (2018). Facile ammonia synthesis from electrocatalytic N_2 reduction under ambient conditions on N-doped porous carbon. *ACS Catal.* 8, 1186-1191.
79. Mukherjee, S., Cullen, D.A., Karakalos, S., Liu, K., Zhang, H., Zhao, S., Xu, H., More, K.L., Wang, G., and Wu, G. (2018). Metal-organic framework-derived nitrogen-doped highly disordered carbon for electrochemical ammonia synthesis using N_2 and H_2O in alkaline electrolytes. *Nano Energy* 48, 217-226.
80. Ren, J.-T., Wan, C.-Y., Pei, T.-Y., Lv, X.-W., and Yuan, Z.-Y. (2020). Promotion of electrocatalytic nitrogen reduction reaction on N-doped porous carbon with secondary heteroatoms. *Appl. Catal. B* 266, 118633.
81. Yuan, D., Wei, Z., Han, P., Yang, C., Huang, L., Gu, Z., Ding, Y., Ma, J., and Zheng, G. (2019). Electron distribution tuning of fluorine-doped carbon for ammonia electrosynthesis. *J. Mater. Chem. A* 7, 16979-16983.
82. Zou, H., Rong, W., Long, B., Ji, Y., and Duan, L. (2019). Corrosion-induced Cl-doped ultrathin graphdiyne toward electrocatalytic nitrogen reduction at ambient conditions. *ACS Catal.* 9, 10649-10655.
83. Feng, Z., Tang, Y., Chen, W., Wei, D., Ma, Y., and Dai, X. (2020). O-doped graphdiyne as metal-free catalysts for nitrogen reduction reaction. *Mol. Catal.* 483, 110705.
84. Liu, X., Jiao, Y., Zheng, Y., Jaroniec, M., and Qiao, S.-Z. (2019). Building up a picture of the electrocatalytic nitrogen reduction activity of transition metal single-atom catalysts. *J. Am. Chem. Soc.* 141, 9664-9672.
85. Chu, K., Liu, Y.-P., Cheng, Y.-H., and Li, Q.-Q. (2020). Synergistic boron-dopants and boron-induced oxygen vacancies in MnO_2 nanosheets to promote electrocatalytic nitrogen reduction. *J. Mater. Chem. A* 8, 5200-5208.
86. Zhu, X., Liu, Z., Wang, H., Zhao, R., Chen, H., Wang, T., Wang, F., Luo, Y., Wu, Y., and Sun, X. (2019). Boosting electrocatalytic N_2 reduction to NH_3 on β - $FeOOH$ by fluorine doping. *Chem. Commun.* 55, 3987-3990.
87. Suryanto, B.H.R., Matuszek, K., Choi, J., Hodgetts, R.Y., Du, H.-L., Bakker, J.M., Kang, C.S.M., Cherepanov, P.V., Simonov, A.N., and MacFarlane, D.R. (2021). Nitrogen reduction to ammonia at high efficiency and rates

- based on a phosphonium proton shuttle. *Science* *372*, 1187-1191.
88. McEnaney, J.M., Singh, A.R., Schwalbe, J.A., Kibsgaard, J., Lin, J.C., Cargnello, M., Jaramillo, T.F., and Nørskov, J.K. (2017). Ammonia synthesis from N_2 and H_2O using a lithium cycling electrification strategy at atmospheric pressure. *Energy Environ. Sci.* *10*, 1621-1630.
89. Kim, K., Lee, S.J., Kim, D.-Y., Yoo, C.-Y., Choi, J.W., Kim, J.-N., Woo, Y., Yoon, H.C., and Han, J.-I. (2018). Electrochemical synthesis of ammonia from water and nitrogen: A lithium-mediated approach using lithium-ion conducting glass ceramics. *ChemSusChem* *11*, 120-124.
90. Akira, T., Akihiko, K., and Tadayoshi, S. (1993). Efficient electrochemical reduction of N_2 to NH_3 catalyzed by lithium. *Chem. Lett.* *22*, 851-854.
91. Dey, A.N. (1971). Electrochemical alloying of lithium in organic electrolytes. *J. Electrochem. Soc.* *118*, 1547.
92. Kim, K., Chen, Y., Han, J.-I., Yoon, H.C., and Li, W. (2019). Lithium-mediated ammonia synthesis from water and nitrogen: A membrane-free approach enabled by an immiscible aqueous/organic hybrid electrolyte system. *Green Chem.* *21*, 3839-3845.
93. Ma, J.-L., Bao, D., Shi, M.-M., Yan, J.-M., and Zhang, X.-B. (2017). Reversible nitrogen fixation based on a rechargeable lithium-nitrogen battery for energy storage. *Chem* *2*, 525-532.
94. Zhang, Z., Wu, S., Yang, C., Zheng, L., Xu, D., Zha, R., Tang, L., Cao, K., Wang, X.-g., and Zhou, Z. (2019). $Li-N_2$ batteries: A reversible energy storage system? *Angew. Chem. Int. Ed.* *58*, 17782-17787.
95. Choi, C., Gu, G.H., Noh, J., Park, H.S., and Jung, Y. (2021). Understanding potential-dependent competition between electrocatalytic dinitrogen and proton reduction reactions. *Nat. Commun.* *12*, 4353.
96. Zou, H., Rong, W., Wei, S., Ji, Y., and Duan, L. (2020). Regulating kinetics and thermodynamics of electrochemical nitrogen reduction with metal single-atom catalysts in a pressurized electrolyser. *Proc. Natl. Acad. Sci.* *117*, 29462-29468.
97. Zhao, H., Zhang, D., Wang, Z., Han, Y., Sun, X., Li, H., Wu, X., Pan, Y., Qin, Y., Lin, S., et al. (2020). High-performance nitrogen electroreduction at low overpotential by introducing Pb to Pd nanosponges. *Appl. Catal. B* *265*, 118481.
98. Zheng, Y., Jiao, Y., Zhu, Y., Li, L.H., Han, Y., Chen, Y., Du, A., Jaroniec, M., and Qiao, S.Z. (2014). Hydrogen evolution by a metal-free electrocatalyst. *Nat. Commun.* *5*, 3783.
99. Li, P., Fu, W., Zhuang, P., Cao, Y., Tang, C., Watson, A.B., Dong, P., Shen, J., and Ye, M. (2019). Amorphous Sn/crystalline SnS_2 nanosheets via *in situ* electrochemical reduction methodology for highly efficient ambient N_2 fixation. *Small* *15*, 1902535.
100. Zhao, Z., Choi, C., Hong, S., Shen, H., Yan, C., Masa, J., Jung, Y., Qiu, J., and Sun, Z. (2020). Surface-engineered oxidized two-dimensional Sb for efficient visible light-driven N_2 fixation. *Nano Energy* *78*, 105368.
101. Tian, Y., Liu, M., Zhou, X., Huang, L., Liu, Z., and An, B. (2013). Inhibition of hydrogen evolution reaction on polypyrrole-modified electrode in acid media. *J. Electrochem. Soc.* *161*, E23-E27.
102. Köleli, F., Röpke, D., Aydin, R., and Röpke, T. (2011). Investigation of N_2 -fixation on polyaniline electrodes in methanol by electrochemical impedance spectroscopy. *J. Appl. Electrochem.* *41*, 405-413.
103. Lin, Y.-X., Zhang, S.-N., Xue, Z.-H., Zhang, J.-J., Su, H., Zhao, T.-J., Zhai, G.-Y., Li, X.-H., Antonietti, M., and Chen, J.-S. (2019). Boosting selective nitrogen reduction to ammonia on electron-deficient copper nanoparticles. *Nat. Commun.* *10*, 4380.
104. Wakerley, D., Lamaison, S., Ozanam, F., Menguy, N., Mercier, D., Marcus, P., Fontecave, M., and Mougél, V. (2019). Bio-inspired hydrophobicity promotes CO_2 reduction on a Cu surface. *Nat. Mater.* *18*, 1222-1227.
105. Xiao, L., Zhu, S., Liang, Y., Li, Z., Wu, S., Luo, S., Chang, C., and Cui, Z. (2021). Effects of hydrophobic layer on selective electrochemical nitrogen fixation of self-supporting nanoporous Mo_4P_3 catalyst under ambient conditions. *Appl. Catal. B* *286*, 119895.
106. Wang, Y., Cui, X., Zhang, Y., Zhang, L., Gong, X., and Zheng, G. (2016). Achieving high aqueous energy storage via hydrogen-generation passivation. *Adv. Mater.* *28*, 7626-7632.
107. Chen, G.-F., Cao, X., Wu, S., Zeng, X., Ding, L.-X., Zhu, M., and Wang, H. (2017). Ammonia electrosynthesis with high selectivity under ambient conditions via a Li^+ incorporation strategy. *J. Am. Chem. Soc.* *139*, 9771-9774.
108. Ogura, K., and Salazar-Villalpando, M.D. (2011). CO_2 electrochemical reduction via adsorbed halide anions. *JOM* *63*, 35-38.
109. Chen, G.-F., Ren, S., Zhang, L., Cheng, H., Luo, Y., Zhu, K., Ding, L.-X., and Wang, H. (2019). Advances in electrocatalytic N_2 reduction—strategies to tackle the selectivity challenge. *Small Methods* *3*, 1800337.
110. Hodgetts, R.Y., Kiryutin, A.S., Nichols, P., Du, H.-L., Bakker, J.M., Macfarlane, D.R., and Simonov, A.N. (2020). Refining universal procedures for ammonium quantification via rapid 1H NMR analysis for dinitrogen reduction studies. *ACS Energy Lett.* *5*, 736-741.
111. Dortsiou, M., and Kyriacou, G. (2009). Electrochemical reduction of nitrate on bismuth cathodes. *J. Electroanal. Chem.* *630*, 69-74.
112. Zhu, Y., Wang, J., Chu, H., Chu, Y.-C., and Chen, H.M. (2020). *In situ/operando* studies for designing next-generation electrocatalysts. *ACS Energy Lett.* *5*, 1281-1291.
113. Yao, Y., Zhu, S., Wang, H., Li, H., and Shao, M. (2018). A spectroscopic study on the nitrogen electrochemical reduction reaction on gold and platinum surfaces. *J. Am. Chem. Soc.* *140*, 1496-1501.
114. Li, L., Tang, C., Cui, X., Zheng, Y., Wang, X., Xu, H., Zhang, S., Shao, T., Davey, K., and Qiao, S.-Z. (2021). Efficient nitrogen fixation to ammonia through integration of plasma oxidation with electrocatalytic reduction. *Angew. Chem. Int. Ed.* *60*, 14131-14137.

Chapter 3: Two-dimensional Mosaic Bismuth Nanosheets for Highly Selective Ambient Electrocatalytic Nitrogen Reduction

3.1 Introduction and Significance

Electrochemical fixation of N_2 to ammonia is a promising strategy to store renewable energy and mitigate greenhouse gas emissions. However, it usually suffers from extremely low ammonia yield and Faradaic efficiency due to the lack of efficient electrocatalysts and the competing HER. To address this issue, semiconducting main group metal, instead of those HER-active transition metals, can be applied to restrict the surface electron accessibility and allows for preferential adsorption of N_2 .

In this chapter, bismuth was chosen as a model material to investigate the nitrogen reduction reaction on semiconducting main group metals. Two-dimensional (2D) mosaic bismuth nanosheets (Bi NS) were fabricated by in situ electrochemical reduction of 2D BiOI nanosheets, which simultaneously served as precursor and template. By rational morphology and electronic structure engineering, sufficient exposure of edge sites coupled with delocalization of Bi p -electrons were achieved. Those Bi atoms with delocalized p -electron near the edge sites are supposed to be active sites for the reductive adsorption and activation of N_2 . As expected, the 2D Bi NS exhibited high average ammonia yield and Faradaic efficiency. The Highlights of this work include:

1. *Effective modification of electronic structure.* The decreased inter-layer Bi–Bi distance is believed to effectively promote the delocalization of Bi p -electrons, thus enhancing the reductive absorption and activation of N_2 .
2. *Intriguing material design.* The mosaic structure allows for sufficient exposure of the surface and edge sites, which could deliver more favourable electronic structures and catalytic activities than those in the bulk counterparts.

3. *High activity towards NRR.* The as-fabricated Bi NS delivered a favourable average ammonia yield as high as $2.54 \pm 0.16 \mu\text{g}_{\text{NH}_3} \text{cm}^{-2} \text{h}^{-1}$ at -0.8 V vs. reversible hydrogen electrode in $0.1 \text{ M Na}_2\text{SO}_4$. In addition, The Bi NS also demonstrated a high Faradaic efficiency ($10.46 \pm 1.45 \%$) towards NRR.

3.2 Two-dimensional Mosaic Bismuth Nanosheets for Highly Selective Ambient Electrocatalytic Nitrogen Reduction

This chapter is included as it appears as a journal paper published by **Laiquan Li**, Cheng Tang, Bingquan Xia, Huanyu Jin, Yao Zheng, Shi-Zhang Qiao.* Two-Dimensional Mosaic Bismuth Nanosheets for Highly Selective Ambient Electrocatalytic Nitrogen Reduction. *ACS Catalysis* 2019, 9, 2902-2908.

Statement of Authorship

Title of Paper	Two-Dimensional Mosaic Bismuth Nanosheets for Highly Selective Ambient Electrocatalytic Nitrogen Reduction
Publication Status	<input checked="" type="checkbox"/> Published <input type="checkbox"/> Accepted for Publication <input type="checkbox"/> Submitted for Publication <input type="checkbox"/> Unpublished and Unsubmitted work written in manuscript style
Publication Details	Laiquan Li, Cheng Tang, Bingquan Xia, Huanyu Jin, Yao Zheng, Shizhang Qiao. Two-Dimensional Mosaic Bismuth Nanosheets for Highly Selective Ambient Electrocatalytic Nitrogen Reduction. ACS Catal. 2019, 9, 2902–290

Principal Author

Name of Principal Author (Candidate)	Laiquan Li		
Contribution to the Paper	Research plan, materials synthesis, most of the physical characterization, electrochemical measurement, data analysis, and manuscript draft.		
Overall percentage (%)	80		
Certification:	This paper reports on original research I conducted during the period of my Higher Degree by Research candidature and is not subject to any obligations or contractual agreements with a third party that would constrain its inclusion in this thesis. I am the primary author of this paper.		
Signature		Date	29/07/2021

Co-Author Contributions

By signing the Statement of Authorship, each author certifies that:


- i. the candidate's stated contribution to the publication is accurate (as detailed above);
- ii. permission is granted for the candidate to include the publication in the thesis; and
- iii. the sum of all co-author contributions is equal to 100% less the candidate's stated contribution.

Name of Co-Author	Cheng Tang		
Contribution to the Paper	Discussion of research plan, Manuscript revision		
Signature		Date	29/07/2021

Name of Co-Author	Bingquan Xia		
Contribution to the Paper	Help with materials synthesis		
Signature		Date	29/07/2021

Name of Co-Author	Huanyu Jin		
Contribution to the Paper	Helped to analyse the characterization results.		
Signature		Date	29/07/2021

Name of Co-Author	Yao Zheng		
Contribution to the Paper	Helped to evaluate and edit the manuscript.		
Signature		Date	29/07/2021

Name of Co-Author	Shi-Zhang Qiao		
Contribution to the Paper	Supervised development of work, helped in manuscript evaluation and acted as corresponding author		
Signature		Date	29/07/2021

Two-Dimensional Mosaic Bismuth Nanosheets for Highly Selective Ambient Electrocatalytic Nitrogen Reduction

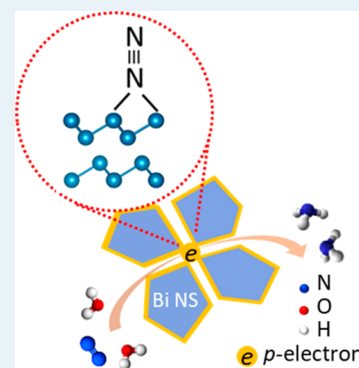
Laiquan Li,[#] Cheng Tang,[#] Bingquan Xia, Huanyu Jin,[†] Yao Zheng,[†] and Shi-Zhang Qiao^{*†}

School of Chemical Engineering, The University of Adelaide, Adelaide, SA 5005, Australia

Supporting Information

ABSTRACT: Electrochemical fixation of N₂ to ammonia is a promising strategy to store renewable energy and mitigate greenhouse gas emissions. However, it usually suffers from extremely low ammonia yield and Faradaic efficiency because of the lack of efficient electrocatalysts and the competing hydrogen evolution reaction. Herein, we report that the semiconducting bismuth can be a promising catalyst for ambient electrocatalytic N₂ reduction reaction (NRR). A two-dimensional mosaic bismuth nanosheet (Bi NS) was fabricated via an in situ electrochemical reduction process and exhibited favorable average ammonia yield and Faradaic efficiency as high as $2.54 \pm 0.16 \mu\text{g}_{\text{NH}_3} \text{cm}^{-2} \text{h}^{-1}$ ($\sim 13.23 \mu\text{g} \text{mg}_{\text{cat}}^{-1} \text{h}^{-1}$) and $10.46 \pm 1.45\%$ at -0.8 V versus reversible hydrogen electrode in $0.1 \text{ M Na}_2\text{SO}_4$. The high NRR electrocatalytic activity of the Bi NS could be attributed to the sufficient exposure of edge sites coupled with effective p-orbital electron delocalization in the mosaic bismuth nanosheets. In addition, the semiconducting feature, which limits surface electron accessibility, could effectively enhance the Faradaic efficiency. This work highlights the potential importance of less reactive main group elements with tunable p-electron density, semiconducting property, and ingenious nanostructure for further exploration of N₂ reduction reaction electrocatalysts.

KEYWORDS: electrocatalysis, nitrogen reduction reaction, bismuth, main group metals, electron delocalization



INTRODUCTION

The continuous growing of the worldwide population and the energy demand, climate change and fossil fuel shortage have been key challenges for the sustainable development of human society.^{1–3} This calls for the exploration and application of energy-dense carriers that can efficiently harvest, store, and transport the renewable energy (from solar, wind, etc.) to the site of demand without releasing greenhouse gas. Ammonia, with a high hydrogen content (17.7 wt %), high gravimetric energy density (3 kW h kg^{-1}), and technically ready operation, is one of the most green and promising energy carriers.^{4–6} Meanwhile, it is also one of the most largely produced and important chemicals in the world. More than 150 million tons of ammonia are produced every year by the known Haber-Bosch process, over 80% of which is used for fertilizers and has fed up to half of the world's population.^{7,8} However, this process requires high temperature and pressure and extremely relies on fossil fuels, accounting for 1–2% of the world's energy consumption and $\sim 1\%$ of global greenhouse gas emission annually.⁹ Thus, it is of paramount significance to explore environmentally friendly, sustainable, and highly efficient alternative methods for ammonia synthesis in the future.

So far, biological,¹⁰ photocatalytic,^{11,12} and electrochemical^{13–15} approaches have been explored for ammonia synthesis. Among those methods, the electrocatalytic nitrogen reduction reaction (NRR) driven by the electrical energy from renewable energy sources like solar and wind has emerged as an attractive technology. It is expected to realize facile and economic nitrogen fixation to ammonia even under ambient conditions

(room temperature and atmosphere pressure), without fossil fuel consumption and CO₂ emission. Various kinds of nanomaterials have been employed as NRR electrocatalysts, such as noble metals (Ru, Pd, Au, etc.),^{16,17} transition-metal compounds (Fe₂O₃,^{18–20} MoS₂,^{21,22} VN,²³ CoP,²⁴ Mo₂C,²⁵ etc.), and even metal-free catalysts (C₃N₄,²⁶ B-doped graphene,²⁷ N-doped carbon,²⁸ B₄C,²⁹ black phosphorus nanosheet,³⁰ etc.). Despite the encouraging advances during the past few years, the NRR activity and selectivity are still far from satisfactory. First, the extremely low solubility of N₂ in aqueous electrolyte limits the mass transfer and current density.³¹ Second, the competing hydrogen evolution reaction (HER) process strongly reduces the NRR selectivity.^{32,33} Theoretical studies revealed that the late transition-metal surface (Fe, Rh, Ru, etc.) is likely covered with H-adatoms instead of N-adatoms, while the early transition metals (Sc, Y, Ti, and Zr) require a large bias of -1 to -1.5 V versus standard hydrogen electrode, thus leading to limited candidates for favorable NRR electrocatalysts with high activity and selectivity.³⁴ To circumvent this problem, Nørskov et al. suggested surface engineering strategies to restrict the access of either protons or electrons, which allows enough sites for N₂ adsorption and is thus beneficial to NRR selectivity.³⁵ For example, one can induce a thin insulator or use semiconductors to supply a slow stream of electrons.

Received: January 24, 2019

Revised: February 18, 2019

Published: February 21, 2019

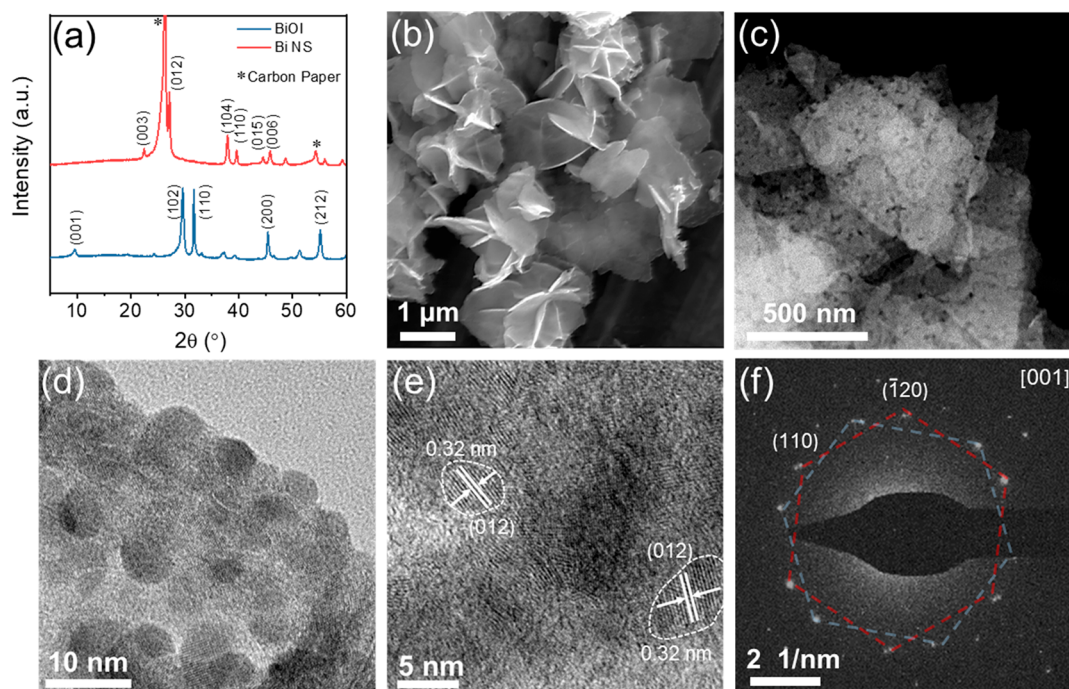


Figure 1. (a) XRD patterns of the BiOI precursor and Bi NS; (b) SEM and (c) dark-field TEM images showing the nanosheet feature of Bi NS; (d) TEM image of Bi NS showing the mosaic structure; (e) high-resolution TEM image of Bi NS; (f) SAED pattern of mosaic Bi NS.

Therefore, we turn our attention from those HER-active transition metals to some less reactive metals, especially the main group metals with semiconducting properties like Sn and Bi. These less reactive metals may be able to selectively promote the reductive adsorption of N_2 to form N_2H^* without affecting the binding energy of the later intermediates,³² and also limit the surface electron accessibility for a suppressed HER process. In fact, bismuth-based materials have been widely investigated in electrocatalytic CO_2 reduction reaction (CO_2RR) and artificial nitrogen fixation, demonstrating excellent activity and selectivity.^{36–39} Zhang and co-workers demonstrated that N_2 could be adsorbed on the oxygen vacancies (OVs) through coordinating with the OV connected and partially reduced Bi atoms with an end-on bound structure.^{40,41} Density functional theory (DFT) calculation has shown that for Bi-based photocatalysts, the density state near the Fermi level is mainly localized around Bi atoms, indicating that Bi atoms can serve as active centers to donate p-electrons and thus activate N_2 .⁴² We here hypothesize that by smart surface and electronic structure engineering, semiconducting main group metals could also be promising as efficient NRR catalysts.

Herein, we explored the NRR performance of metallic Bi catalyst under ambient conditions. Fine structure tuning was realized by in situ electrochemical reduction of 2D bismuth oxyiodide (BiOI) to achieve 2D mosaic bismuth nanosheets (Bi NS). Unexpectedly, the as-obtained Bi NS exhibited a superior average NH_3 formation rate and Faradaic efficiency as high as $2.54 \pm 0.16 \mu g_{NH_3} cm^{-2} h^{-1}$ ($\sim 13.23 \mu g mg_{cat}^{-1} h^{-1}$) and $10.46 \pm 1.45\%$ at -0.8 V versus reversible hydrogen electrode (RHE) in 0.1 M Na_2SO_4 . The activity origin was investigated by a series of control experiments and detailed characterizations. This work highlights the potential importance of less reactive main group elements with delocalized p-

electrons, the delicate nanostructure, and the semiconducting property for further exploration of NRR electrocatalysts.

RESULTS AND DISCUSSION

The 2D mosaic Bi NS was fabricated via in situ electrochemical reduction of BiOI precursors. The 2D BiOI nanosheets were synthesized by a routine hydrothermal method (see Experimental Section in the Supporting Information) to serve as both the precursor and template. Scanning electron microscopy (SEM) and transmission electron microscopy (TEM) images reveal that the obtained BiOI exhibits a microflower-like morphology assembled by intercalating ultrathin nanosheets (Figure S1), consistent with previous reports.⁴³ Although BiOI is generally stable under ambient conditions and photocatalytic NRR process, it cannot bear the large cathodic potential for electrocatalytic NRR. A pair of pronounced redox waves can be observed between -0.7 and 0.6 V versus RHE in the typical cyclic voltammetry (CV) curve of BiOI in 0.1 M Na_2SO_4 electrolyte (Figure S2). The reduction peak at around -0.15 V versus RHE is ascribed to the transformation from Bi^{3+} to Bi (insets of Figure S2), suggesting that electrochemical reduction is a facile method to fabricate Bi nanomaterials. To accomplish the thorough reduction process, the BiOI precursor was first loaded on a carbon paper electrode and then it underwent repeated CV scans between the cathodic potential from -0.7 to 0 V for 100 cycles (Figure S3). After 50 cycles, the CV curves are almost the same, indicating the complete reduction (Figure S3b). Figure 1a compares the X-ray diffraction (XRD) patterns of the as-obtained electrode with reduced Bi catalysts and the BiOI precursor. All the diffraction peaks of the BiOI precursor can be indexed to tetragonal BiOI (JCPDS No. 10-0445), while the diffraction peaks of the reduced sample are totally changed and can be assigned to rhombohedral Bi (JCPDS No. 44-1246). After the in situ transformation from BiOI precursors, the obtained Bi sample inherited the microflower-

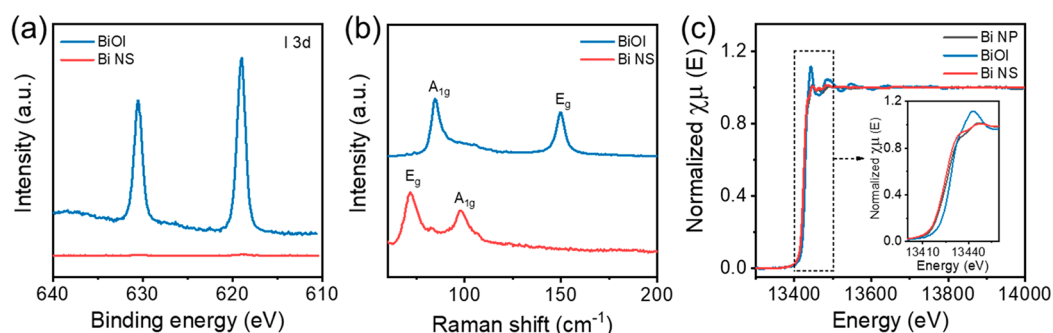


Figure 2. (a) High-resolution XPS I 3d spectra and (b) Raman spectra of the BiOI precursor and Bi NS; (c) Bi L_{III} -edge XAFS of BiOI precursor, Bi NS, and Bi NP.

like morphology assembled by nanosheets (Figure 1b). Despite retaining the 2D ultrathin nanosheet structure, the Bi NS appears to be less smooth and uniform (Figure 1c, Figure S1). The high-resolution TEM image shows that some ultrasmall nanoflakes with size less than 10 nm are scattered in the matrix of the 2D Bi NS, forming a mosaic morphology (Figure 1d). These scattered ultrasmall nanoflakes exhibit obvious and disoriented fringes with lattice spacing of 0.32 nm corresponding to the (012) facet of Bi (Figure 1e). Figure 1f shows the selected area electron diffraction (SAED) pattern of the obtained Bi NS whose zone axis is indexed along the [001] direction. Two sets of diffraction spots with typical hexagonal configuration can be obtained, further demonstrating the disoriented and heterogeneous feature of the mosaic nanosheets over a large area.

In contrast to the topotactic transformation with excellent 2D structure integrity and single crystallinity,³⁷ we obtained 2D mosaic Bi nanosheets through the in situ electrochemical reduction of BiOI nanosheets, which can be ascribed to the difference in the pH of electrolytes and the reduction techniques. Such phase transformation can be rationalized by an inhomogeneous mechanism.⁴⁴ The electrochemical reduction process is expected to occur simultaneously throughout the whole BiOI nanosheets, during which the Bi atoms are not only reduced but also migrate because of the escape of neighboring O and I atoms, thereby resulting in the formation of scattered Bi ultrasmall nanoflakes in the whole matrix.

To further examine the conversion from the BiOI precursor to metallic Bi, we collected X-ray photoelectron spectroscopy (XPS) and Raman spectra. Distinct I 3d peaks can be observed in the XPS spectrum of the BiOI precursor while the iodine signals disappeared in the XPS spectrum of Bi NS (Figure 2a and Figure S4). The Raman spectrum of BiOI precursor can be recognized by the two characteristic peaks at 85 and 150 cm^{-1} , which correspond to the A_{1g} and E_g stretching modes of Bi–I bonds, respectively (Figure 2b).^{43,45} After the electrochemical reduction process, the two Raman peaks at 71 and 98 cm^{-1} in the spectrum of Bi NS can be assigned to the first-order E_g and A_{1g} stretching modes of Bi–Bi bond.^{46,47} To shed light on the detailed structure of the formed Bi NS, X-ray absorption fine spectroscopy (XAFS) was then conducted on BiOI and Bi NS, as well as homemade Bi nanoparticles (Bi NP) as comparison (Figure 2c). The Bi NP was fabricated by the chemical reduction of Bi^{3+} aqueous solution using NaBH_4 . The XRD pattern confirms the crystal structure of rhombohedral Bi (Figure S5), while the SEM image shows a coral-like structure constructed by interconnected Bi nanoparticles with size around 80 nm (Figure S6). As shown in Figure 2c, the obvious

higher energy of the Bi L_{III} edge for the BiOI precursor indicates its high oxidation state. After reduction, the almost overlapped curves of Bi NS and Bi NP further imply the conversion from BiOI precursor to metallic Bi. Therefore, coupled with the above XRD measurement, these characterizations sufficiently demonstrate the complete conversion from the BiOI precursor to metallic Bi.

To preliminarily probe the NRR activity, we first evaluated the polarization curves of the in situ reduced Bi NS on glassy carbon electrode using a rotating disk electrode (RDE) with a rotating rate of 1600 rpm and scan rate of 5.0 mV s^{-1} . As shown in Figure 3a, the linear sweep voltammetry (LSV) curves in Ar or N_2 saturated 0.10 M Na_2SO_4 (pH 6.1) electrolytes are sequentially measured using the same working electrode and electrolyte. A cathodic current onset appears at around -0.6 V versus RHE because of HER for both Ar and N_2 saturated conditions, while an obvious higher current density can be clearly seen in N_2 saturated electrolyte, indicating the additional contribution from NRR. When more negative bias voltages are applied, the polarization curves in N_2 and Ar gradually coincide as the drastic HER dominates the electrode process. According to the polarization curves, the appropriate potential window for electrocatalytic NRR ranges from -0.7 to -1.1 V versus RHE.

The electrocatalytic NRR performance was then systematically investigated in a 0.10 M Na_2SO_4 aqueous solution using a gastight H-cell (Figure S7). A pretreated Nafion 117 membrane was used to separate the anode and cathode chambers with 30 mL of electrolyte in each. Before the NRR, a carbon paper coated with BiOI precursor (mass loading: 0.192 $\text{mg}_{\text{Bi}} \text{cm}^{-2}$) was first reduced by 100-cycle CV scans from -0.7 to 0 V versus RHE. Then the obtained carbon paper loaded with Bi NS was directly used as a working electrode for electrocatalytic NRR in refreshed electrolyte. Ultra-high-purity N_2 gas (99.999%) was first purged into the cathodic chamber for 30 min (50 mL min^{-1}) and then bubbled with a constant flow rate of 20 mL min^{-1} throughout the whole electrolysis process. Magnetic stirring was applied with a stirring rate of 600 rpm in the cathode chamber throughout the measurement. Consecutive acid traps were connected with the cathode chamber with 5 mL of 0.05 M H_2SO_4 in two 10 mL clean polypropylene tubes. After electrolysis at specified potentials from -0.7 to -1.1 V versus RHE for 2 h, the produced NH_3 was quantitatively determined by the indophenol blue method. The possible byproduct (N_2H_4) was determined by the method of Watt and Chrisp.⁴⁸ The calibration curves for quantitatively determining NH_3 and N_2H_4 are shown in Figures S8–S10.

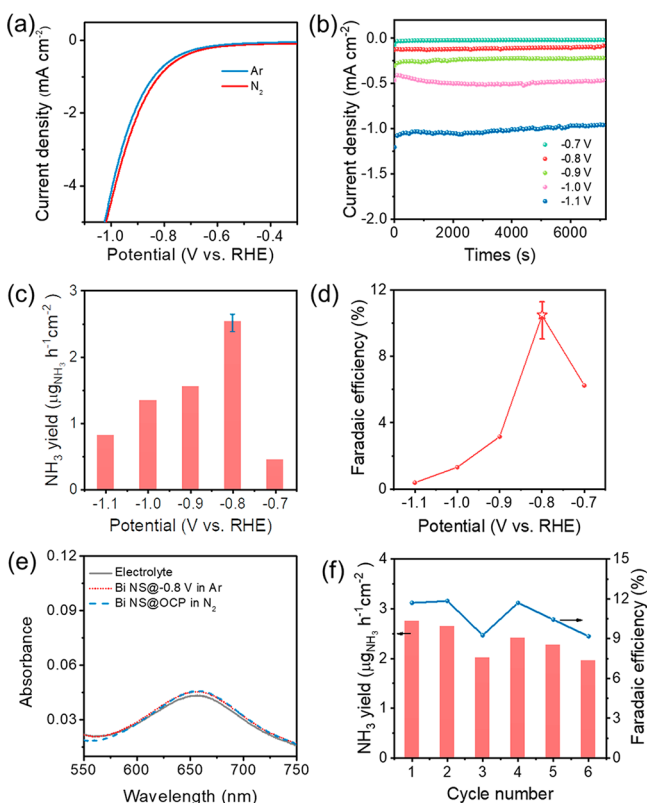


Figure 3. (a) LSV curves of Bi NS in Ar and N₂ saturated 0.10 M Na₂SO₄ measured by RDE electrode; (b) chrono-amperometry results at different applied potentials; (c) NH₃ formation rates of Bi NS at different potentials; (d) NRR Faradaic efficiency of Bi NS at different potentials; (e) UV-vis spectra of electrolytes stained with indophenol indicator for Bi NS at different conditions. (Black line for pure 0.1 M Na₂SO₄ electrolyte; red dotted line for electrolyte after electrolysis at -0.8 V for 2 h in Ar saturated 0.10 M Na₂SO₄; blue dashed line for electrolyte after electrolysis under OCP for 2 h in N₂ saturated 0.10 M Na₂SO₄.) (f) NH₃ formation rate and Faradaic efficiency of cycles at -0.8 V versus RHE.

Figure 3b shows the chronoamperometry curves at different applied potentials in which the steady current densities indicate the good chemical stability of Bi NS during the NRR tests. The UV-vis absorption spectra of the electrolytes stained with indophenol indicator after electrolysis for 2 h were collected to quantify the produced ammonia. The highest absorbance intensity, namely, the highest ammonia production rate, was obtained at -0.8 V versus RHE (Figure S11). As shown in Figure 3c, the highest NH₃ yield of $2.54 \pm 0.16 \mu\text{g h}^{-1} \text{cm}^{-2}$ is achieved at -0.8 V versus RHE, which is determined from three independent measurements using separately prepared electrodes under the same condition (Table S1). To obtain accurate and reliable results of the NH₃ production, we scrutinized the ammonia concentrations in the cathode chamber, anode chamber, and in-line acid traps. Considerable amounts of ammonia can be detected in both the anode chamber and acid traps, which respectively account for about 30% and 10% of the total ammonia production (Figure S11). Besides the high ammonia yield, the Bi NS demonstrated a high Faradaic efficiency of $10.46 \pm 1.45\%$ at -0.8 V versus RHE (Figure 3d). This Faradaic efficiency is among the best results achieved in aqueous conditions (Table S2). It is noteworthy to mention that the Faradaic efficiency could be easily affected by some catalyst-irrelevant issues, for example,

the gas flow rate. An optimized measurement configuration is investigated and proposed to accurately evaluate the Faradaic efficiency (Figures S7 and S12). When more negative potentials are applied, the NH₃ yield and Faradaic efficiency decreases dramatically (Figure 3c,d). It can be attributed to the blooming HER at lower potentials in which case more protons occupy the active sites and thus hinder the efficient adsorption of nitrogen. Besides the ammonia production, only a trace of the N₂H₄ byproduct was detected under all applied potentials (Figure S13), corresponding to N₂H₄ Faradaic efficiencies less than 0.05% (Table S3).

To identify the origin of the produced NH₃, we also conducted a series of control experiments, including the Bi NS electrode in N₂ saturated solution at open-circuit potential (OCP), the Bi NS electrode in Ar saturated solution at -0.8 V versus RHE (Figure S14), and the bare carbon paper electrode in N₂ saturated solution at -0.8 V versus RHE (Figure S15). The corresponding UV-vis spectra for all control samples show feeble signals comparable to that of the fresh electrolyte (Figure 3e, Table S1). The minor higher absorbance of those control experiments may come from the trace amount of ammonia in air.⁴⁹ Those control experiments convincingly indicate that the 2D mosaic Bi NS serves as active species for promising activity and selectivity toward electrocatalytic NRR. Stability is another important factor to fully evaluate an electrocatalyst, which was further investigated by cycling and chronoamperometric measurements at -0.8 V versus RHE. The durability toward NRR was performed by testing the ammonia production and replacing the electrolyte every 1 h without changing the electrode and Nafion membrane. Neither significant current density loss emerges during the long-term electrolysis process for 25 h at -0.8 V versus RHE (Figure S16), nor the NH₃ yield and corresponding Faradaic efficiency decrease obviously after six cycling tests (Figure 3f and Figure S17). Furthermore, the SEM image of the Bi NS after long-term NRR measurement shows the successful maintaining of nanosheet structure (Figure S18), indicating the high stability of Bi NS electrode for electrocatalytic nitrogen fixation.

To elucidate the remarkable activity of the 2D mosaic Bi NS, we further investigated the NRR performance of Bi NP. Although a similar current density ($\sim 0.1 \text{ mA cm}^{-2}$) can be obtained during the chronoamperometric measurement at -0.8 V versus RHE (Figure S19), the NH₃ yield and Faradaic efficiency of Bi NP are detected to be significantly inferior to those of Bi NS (Figure S20). As shown in Figure 4a, the NH₃ yield of Bi NP is determined to be $0.268 \mu\text{g h}^{-1} \text{cm}^{-2}$, and the Faradaic efficiency is 0.66%, which are both significantly less than those obtained from Bi NS sample (Table S1).

Compared to the Bi NP sample, the 2D mosaic Bi NS exhibits a smaller size and thickness for individual Bi nanoflakes, thereby leading to more exposed surface and edge sites. This hypothesis can be verified by Raman spectra. As shown in Figure 4b, the two Raman bands for Bi NS show distinct blue shift as compared to those of the Bi NP. Furthermore, the full width at half-maximum (fwhm) for the Raman bands of the Bi NS, especially for the A_{1g} modes, are much wider than that of the Bi NP. The blue shift and the broadened feature of the Raman bands are attributed to the significantly decreased grain size of the Bi NS in contrast to that of the Bi NP.⁴⁶ In addition, the double-layer capacitance measurement demonstrates that the Bi NS sample possesses a much larger capacitance and thereby exposes more electrochemically active surface area, nearly 4-fold, than Bi NP

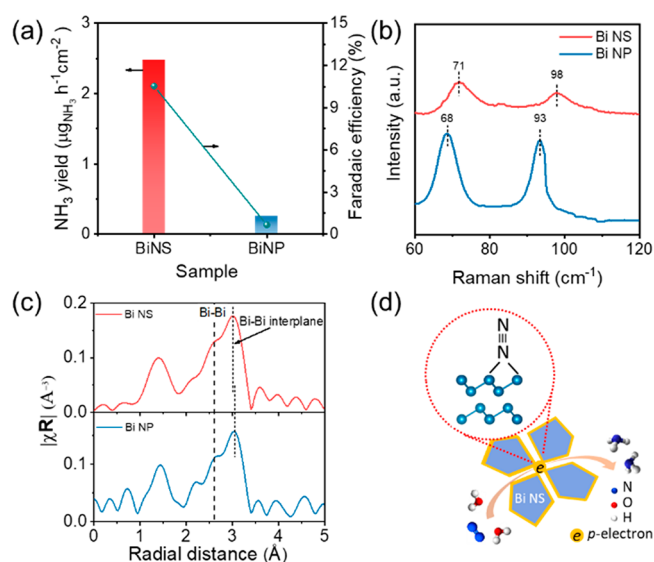


Figure 4. (a) Comparison of NH₃ yield and Faradaic efficiency of Bi NS and Bi NP; (b) Raman spectra of Bi NS and Bi NP; (c) Bi L_{III}-edge extended XAFS spectra of Bi NS and Bi NP; (d) schematic illustration of the NRR activity origin and N₂ absorption mode on mosaic Bi NS.

(Figure S21). To further investigate the local electronic structure difference between Bi NS and Bi NP, we further conducted Fourier transform extended X-ray absorption fine structure. As shown in Figure 4c, the Bi NS exhibits two typical main peaks at ~ 2.6 and 3.0 Å, which can be assigned to the intra- and interlayer Bi–Bi bonds.^{36,50} In contrast to the same peak position for intralayer Bi–Bi bond, the interlayer Bi–Bi bond peak for Bi NS apparently shifts toward lower radial distance, indicating a decreased interlayer Bi–Bi bond length. The decreased interlayer Bi–Bi distance is believed to effectively promote the delocalization of Bi p-electrons,⁵⁰ which could enhance the reductive absorption and activation of N₂. Therefore, the excellent NRR performance of Bi NS can be attributed to its special surface and electronic structure because of the 2D mosaic nanostructure and decreased interlayer Bi–Bi distance. Those Bi atoms with delocalized p-electron near the edge sites are expected to provide abundant catalytic active sites for the end-on adsorption and simultaneous activation of N₂ (Figure 4d), which is supported by the associative distal pathway due to the absence of N₂H₄ in the products. Moreover, electrochemical impedance spectrum (EIS) measurement was further conducted to study the electron transfer of Bi NS and Bi NP. As shown in Figure S22, both Bi NS and Bi NP exhibit resistance more than 200 Ω, demonstrating their inferior conductivity due to the semiconducting properties of bismuth. Compared to Bi NP, Bi NS shows larger charge-transfer resistance, which is consistent with its poorer HER performance than that of Bi NP (Figure S22b). Therefore, the high Faradaic efficiency of Bi NS could be attributed to the semiconducting feature of bismuth as well as the generally too positive free energy of H adsorption on Bi sites (e.g., 0.95 eV for Bi (001) facet).³⁷ Despite the addition of conductive carbon black to ensure the smooth electron transfer from catalyst to current collector, the catalyst itself is mainly semiconducting. It is believed to limit the electron availability at the catalyst surface, especially near the active sites, ensure preferential adsorption of N₂, and thus achieve a higher Faradaic efficiency toward NRR.³⁵

CONCLUSION

In summary, 2D mosaic Bi nanosheets were successfully developed for highly selective electrocatalytic nitrogen fixation, which demonstrates that Bi could be a superior NRR electrocatalyst after smart surface and electronic structure engineering. The as-obtained Bi catalyst attains average NH₃ yield and Faradaic efficiency as high as $2.54 \pm 0.16 \mu\text{g}_{\text{NH}_3} \text{cm}^{-2} \text{h}^{-1}$ ($\sim 13.23 \mu\text{g} \text{mg}_{\text{cat.}}^{-1} \text{h}^{-1}$) and $10.46 \pm 1.45\%$ at -0.8 V versus RHE, which are almost 10-fold of the performance obtained by Bi nanoparticle. The high performance of the obtained Bi NS toward NRR could be attributed to the sufficient exposure of edge sites coupled with effective p-orbital electron delocalization. The semiconducting feature, which limits surface electron accessibility, could effectively enhance the Faradaic efficiency. This work reveals that both the structure engineering and electronic structure modulation should be considered when investigating the performance of a specific family of materials for electrocatalytic NRR. Besides, we believe this work can pave new ways to develop and optimize more promising electrocatalysts, especially those from main group metals, for the electrocatalytic NRR at ambient conditions.

ASSOCIATED CONTENT

Supporting Information

The Supporting Information is available free of charge on the ACS Publications website at DOI: 10.1021/acscatal.9b00366.

Experimental details, physical characterization data, and spectroscopic data (PDF)

AUTHOR INFORMATION

Corresponding Author

*E-mail: s.qiao@adelaide.edu.au (S.-Z.Q.).

ORCID

Laiquan Li: 0000-0002-3301-9029

Huanyu Jin: 0000-0002-1950-2364

Yao Zheng: 0000-0002-2411-8041

Shi-Zhang Qiao: 0000-0002-4568-8422

Author Contributions

#L.L. and C.T. contributed equally to this work.

Notes

The authors declare no competing financial interest.

ACKNOWLEDGMENTS

The work is financially supported by the Australian Research Council (ARC) through the Discovery Project program (DP160104866, FL170100154). We acknowledge the Australian Synchrotron (ANSTO) for the X-ray absorption spectroscopy characterizations. L. L. thanks Dr. Hsin-Yi Wang from Stockholm University and Mr. Sung-Fu Hung from National Taiwan University for help with the discussion of XAS results.

REFERENCES

- (1) Smil, V. Detonator of the Population Explosion. *Nature* **1999**, *400*, 415–415.
- (2) Chu, S.; Majumdar, A. Opportunities and Challenges for a Sustainable Energy Future. *Nature* **2012**, *488*, 294–303.
- (3) Chen, J. G.; Crooks, R. M.; Seefeldt, L. C.; Bren, K. L.; Bullock, R. M.; Darensbourg, M. Y.; Holland, P. L.; Hoffman, B.; Janik, M. J.; Jones, A. K.; Kanatzidis, M. G.; King, P.; Lancaster, K. M.; Lymar, S.

- V.; Fromm, P.; Schneider, W. F.; Schrock, R. R. Beyond Fossil Fuel-driven Nitrogen Transformations. *Science* **2018**, *360*, eaar6611.
- (4) Guo, J.; Chen, P. Catalyst: NH_3 as an Energy Carrier. *Chem* **2017**, *3*, 709–712.
- (5) Fryzuk, M. D. Ammonia Transformed. *Nature* **2004**, *427*, 498–499.
- (6) Schlögl, R. Catalytic Synthesis of Ammonia—A “Never-Ending Story”? *Angew. Chem., Int. Ed.* **2003**, *42*, 2004–2008.
- (7) van der Ham, C. J.; Koper, M. T.; Hettler, D. G. Challenges in Reduction of Dinitrogen by Proton and Electron Transfer. *Chem. Soc. Rev.* **2014**, *43*, 5183–5191.
- (8) Kitano, M.; Inoue, Y.; Yamazaki, Y.; Hayashi, F.; Kanbara, S.; Matsuishi, S.; Yokoyama, T.; Kim, S.-W.; Hara, M.; Hosono, H. Ammonia Synthesis Using a Stable Electride as an Electron Donor and Reversible Hydrogen Store. *Nat. Chem.* **2012**, *4*, 934–940.
- (9) Guo, C.; Ran, J.; Vasileff, A.; Qiao, S.-Z. Rational Design of Electrocatalysts and Photo(electro) Catalysts for Nitrogen Reduction to Ammonia (NH_3) under Ambient Conditions. *Energy Environ. Sci.* **2018**, *11*, 45–56.
- (10) Fourmond, V.; Leger, C. Dinitrogen Reduction: Interfacing the Enzyme Nitrogenase with Electrodes. *Angew. Chem., Int. Ed.* **2017**, *56*, 4388–4390.
- (11) Hirakawa, H.; Hashimoto, M.; Shiraishi, Y.; Hirai, T. Photocatalytic Conversion of Nitrogen to Ammonia with Water on Surface Oxygen Vacancies of Titanium Dioxide. *J. Am. Chem. Soc.* **2017**, *139*, 10929–10936.
- (12) Zhang, N.; Jalil, A.; Wu, D.; Chen, S.; Liu, Y.; Gao, C.; Ye, W.; Qi, Z.; Ju, H.; Wang, C.; Wu, X.; Song, L.; Zhu, J.; Xiong, Y. Refining Defect States in $\text{W}_{18}\text{O}_{49}$ by Mo Doping: A Strategy for Tuning N_2 Activation towards Solar-Driven Nitrogen Fixation. *J. Am. Chem. Soc.* **2018**, *140*, 9434–9443.
- (13) Pickett, C. J.; Talarmin, J. Electrosynthesis of Ammonia. *Nature* **1985**, *317*, 652–653.
- (14) Cui, X.; Tang, C.; Zhang, Q. A Review of Electrocatalytic Reduction of Dinitrogen to Ammonia under Ambient Conditions. *Adv. Energy Mater.* **2018**, *8*, 1800369.
- (15) Chen, G.-F.; Ren, S.; Zhang, L.; Cheng, H.; Luo, Y.; Zhu, K.; Ding, L.-X.; Wang, H. Advances in Electrocatalytic N_2 Reduction Strategies to Tackle the Selectivity Challenge. *Small Methods* **2018**, *2*, 1800337.
- (16) Nash, J.; Yang, X.; Anibal, J.; Wang, J.; Yan, Y.; Xu, B. Electrochemical Nitrogen Reduction Reaction on Noble Metal Catalysts in Proton and Hydroxide Exchange Membrane Electrolyzers. *J. Electrochem. Soc.* **2017**, *164*, F1712–F1716.
- (17) Bao, D.; Zhang, Q.; Meng, F. L.; Zhong, H. X.; Shi, M. M.; Zhang, Y.; Yan, J. M.; Jiang, Q.; Zhang, X. B. Electrochemical Reduction of N_2 under Ambient Conditions for Artificial N_2 Fixation and Renewable Energy Storage Using N_2/NH_3 Cycle. *Adv. Mater.* **2017**, *29*, 1604799.
- (18) Chen, S.; Perathoner, S.; Ampelli, C.; Mebrahtu, C.; Su, D.; Centi, G. Electrocatalytic Synthesis of Ammonia at Room Temperature and Atmospheric Pressure from Water and Nitrogen on a Carbon-Nanotube-Based Electrocatalyst. *Angew. Chem., Int. Ed.* **2017**, *56*, 2699–2703.
- (19) Cui, X.; Tang, C.; Liu, X.; Wang, C.; Ma, W.; Zhang, Q. Highly-Selective Electrochemical Reduction of Dinitrogen to Ammonia at Ambient Temperature and Pressure over Iron Oxide Catalysts. *Chem. - Eur. J.* **2018**, *24*, 18494–18501.
- (20) Chen, S.; Perathoner, S.; Ampelli, C.; Mebrahtu, C.; Su, D.; Centi, G. Room-Temperature Electrocatalytic Synthesis of NH_3 from H_2O and N_2 in a Gas-Liquid-Solid Three-Phase Reactor. *ACS Sustainable Chem. Eng.* **2017**, *5*, 7393–7400.
- (21) Zhang, L.; Ji, X.; Ren, X.; Ma, Y.; Shi, X.; Tian, Z.; Asiri, A. M.; Chen, L.; Tang, B.; Sun, X. Electrochemical Ammonia Synthesis via Nitrogen Reduction Reaction on a MoS_2 Catalyst: Theoretical and Experimental Studies. *Adv. Mater.* **2018**, *30*, 1800191.
- (22) Li, X.; Li, T.; Ma, Y.; Wei, Q.; Qiu, W.; Guo, H.; Shi, X.; Zhang, P.; Asiri, A. M.; Chen, L.; Tang, B.; Sun, X. Boosted Electrocatalytic N_2 Reduction to NH_3 by Defect-Rich MoS_2 Nanoflower. *Adv. Energy Mater.* **2018**, *8*, 1801357.
- (23) Yang, X.; Nash, J.; Anibal, J.; Dunwell, M.; Kattel, S.; Stavitski, E.; Attenkofer, K.; Chen, J. G.; Yan, Y.; Xu, B. Mechanistic Insights into Electrochemical Nitrogen Reduction Reaction on Vanadium Nitride Nanoparticles. *J. Am. Chem. Soc.* **2018**, *140*, 13387–13391.
- (24) Guo, W.; Liang, Z.; Zhao, J.; Zhu, B.; Cai, K.; Zou, R.; Xu, Q. Hierarchical Cobalt Phosphide Hollow Nanocages toward Electrocatalytic Ammonia Synthesis under Ambient Pressure and Room Temperature. *Small Methods* **2018**, *2*, 1800204.
- (25) Cheng, H.; Ding, L. X.; Chen, G. F.; Zhang, L.; Xue, J.; Wang, H. Molybdenum Carbide Nanodots Enable Efficient Electrocatalytic Nitrogen Fixation under Ambient Conditions. *Adv. Mater.* **2018**, *30*, 1803694.
- (26) Lv, C.; Qian, Y.; Yan, C.; Ding, Y.; Liu, Y.; Chen, G.; Yu, G. Defect Engineering Metal-Free Polymeric Carbon Nitride Electrocatalyst for Effective Nitrogen Fixation under Ambient Conditions. *Angew. Chem., Int. Ed.* **2018**, *57*, 10246–10250.
- (27) Yu, X.; Han, P.; Wei, Z.; Huang, L.; Gu, Z.; Peng, S.; Ma, J.; Zheng, G. Boron-Doped Graphene for Electrocatalytic N_2 Reduction. *Joule* **2018**, *2*, 1610–1622.
- (28) Mukherjee, S.; Cullen, D. A.; Karakalos, S.; Liu, K.; Zhang, H.; Zhao, S.; Xu, H.; More, K. L.; Wang, G.; Wu, G. Metal-organic Framework-derived Nitrogen-doped Highly Disordered Carbon for Electrochemical Ammonia Synthesis Using N_2 and H_2O in Alkaline Electrolytes. *Nano Energy* **2018**, *48*, 217–226.
- (29) Qiu, W.; Xie, X.-Y.; Qiu, J.; Fang, W.-H.; Liang, R.; Ren, X.; Ji, X.; Cui, G.; Asiri, A. M.; Cui, G.; Tang, B.; Sun, X. High-performance Artificial Nitrogen Fixation at Ambient Conditions Using a Metal-Free Electrocatalyst. *Nat. Commun.* **2018**, *9*, 3485.
- (30) Zhang, L.; Ding, L.-X.; Chen, G.-F.; Yang, X.; Wang, H. Ammonia Synthesis Under Ambient Conditions: Selective Electroreduction of Dinitrogen to Ammonia on Black Phosphorus Nanosheets. *Angew. Chem., Int. Ed.* **2019**, *58*, 2612–2616.
- (31) Bratsch, S. G. Standard Electrode Potentials and Temperature Coefficients in Water at 298.15 K. *J. Phys. Chem. Ref. Data* **1989**, *18*, 1–21.
- (32) Montoya, J. H.; Tsai, C.; Vojvodic, A.; Nørskov, J. K. The Challenge of Electrochemical Ammonia Synthesis: A New Perspective on the Role of Nitrogen Scaling Relations. *ChemSusChem* **2015**, *8*, 2180–2186.
- (33) Howalt, J. G.; Bligaard, T.; Rossmeisl, J.; Vegge, T. DFT Based Study of Transition Metal Nano-clusters for Electrochemical NH_3 Production. *Phys. Chem. Chem. Phys.* **2013**, *15*, 7785–7795.
- (34) Skulason, E.; Bligaard, T.; Gudmundsdottir, S.; Studt, F.; Rossmeisl, J.; Abild-Pedersen, F.; Vegge, T.; Jonsson, H.; Nørskov, J. K. A Theoretical Evaluation of Possible Transition Metal Electrocatalysts for N_2 Reduction. *Phys. Chem. Chem. Phys.* **2012**, *14*, 1235–1245.
- (35) Singh, A. R.; Rohr, B. A.; Schwalbe, J. A.; Cargnello, M.; Chan, K.; Jaramillo, T. F.; Chorkendorff, I.; Nørskov, J. K. Electrochemical Ammonia Synthesis—The Selectivity Challenge. *ACS Catal.* **2017**, *7*, 706–709.
- (36) Kim, S.; Dong, W. J.; Gim, S.; Sohn, W.; Park, J. Y.; Yoo, C. J.; Jang, H. W.; Lee, J.-L. Shape-Controlled Bismuth Nanoflakes as Highly Selective Catalysts for Electrochemical Carbon Dioxide Reduction to Formate. *Nano Energy* **2017**, *39*, 44–52.
- (37) Han, N.; Wang, Y.; Yang, H.; Deng, J.; Wu, J.; Li, Y.; Li, Y. Ultrathin Bismuth Nanosheets from in Situ Topotactic Transformation for Selective Electrocatalytic CO_2 Reduction to Formate. *Nat. Commun.* **2018**, *9*, 1320.
- (38) Garcia de Arquer, F. P.; Bushuyev, O. S.; De Luna, P.; Dinh, C. T.; Seifitokaldani, A.; Saidaminov, M. I.; Tan, C. S.; Quan, L. N.; Proppe, A.; Kibria, M. G.; Kelley, S. O.; Sinton, D.; Sargent, E. H. 2D Metal Oxyhalide-Derived Catalysts for Efficient CO_2 Electroreduction. *Adv. Mater.* **2018**, *30*, 1802858.
- (39) Yao, J.-X.; Bao, D.; Zhang, Q.; Shi, M.-M.; Wang, Y.; Gao, R.; Yan, J.-M.; Jiang, Q. Tailoring Oxygen Vacancies of BiVO_4 toward

Highly Efficient Noble-Metal-Free Electrocatalyst for Artificial N₂ Fixation under Ambient Conditions. *Small Methods* **2018**, *2*, 1800333.

(40) Li, H.; Shang, J.; Ai, Z.; Zhang, L. Efficient Visible Light Nitrogen Fixation with BiOBr Nanosheets of Oxygen Vacancies on the Exposed {001} Facets. *J. Am. Chem. Soc.* **2015**, *137*, 6393–6399.

(41) Li, H.; Shang, J.; Shi, J.; Zhao, K.; Zhang, L. Facet-Dependent Solar Ammonia Synthesis of BiOCl Nanosheets via a Proton-Assisted Electron Transfer Pathway. *Nanoscale* **2016**, *8*, 1986–1993.

(42) Sun, S.; An, Q.; Wang, W.; Zhang, L.; Liu, J.; Goddard, W. A., III Efficient Photocatalytic Reduction of Dinitrogen to Ammonia on Bismuth Monoxide Quantum Dots. *J. Mater. Chem. A* **2017**, *5*, 201–209.

(43) Long, B.; Huang, Y. C.; Li, H. B.; Zhao, F. Y.; Rui, Z. B.; Liu, Z. L.; Tong, Y. X.; Ji, H. B. Carbon Dots Sensitized BiOI with Dominant {001} Facets for Superior Photocatalytic Performance. *Ind. Eng. Chem. Res.* **2015**, *54*, 12788–12794.

(44) Green, J. Calcination of Precipitated Mg(OH)₂ to Active MgO in the Production of Refractory and Chemical Grade MgO. *J. Mater. Sci.* **1983**, *18*, 637–651.

(45) Li, H. B.; Yang, Z. J.; Zhang, J. N.; Huang, Y. C.; Ji, H. B.; Tong, Y. X. Indium Doped BiOI Nanosheets: Preparation, Characterization and Photocatalytic Degradation Activity. *Appl. Surf. Sci.* **2017**, *423*, 1188–1197.

(46) Kumari, L.; Lin, J. H.; Ma, Y. R. Laser Oxidation and Wide-band Photoluminescence of Thermal Evaporated Bismuth Thin Films. *J. Phys. D: Appl. Phys.* **2008**, *41*, 025405.

(47) Reyes-Contreras, A.; Camacho-Lopez, M.; Camacho-Lopez, S.; Olea-Mejia, O.; Esparza-Garcia, A.; Banuelos-Muneton, J. G.; Camacho-Lopez, M. A. Laser-Induced Periodic Surface Structures on Bismuth Thin Films with ns Laser Pulses Below Ablation Threshold. *Opt. Mater. Express* **2017**, *7*, 1777–1786.

(48) Watt, G. W.; Chrisp, J. D. A Spectrophotometric Method for the Determination of Hydrazine. *Anal. Chem.* **1952**, *24*, 2006–2008.

(49) Greenlee, L. F.; Renner, J. N.; Foster, S. L. The Use of Controls for Consistent and Accurate Measurements of Electrocatalytic Ammonia Synthesis from Dinitrogen. *ACS Catal.* **2018**, *8*, 7820–7827.

(50) He, S.; Ni, F.; Ji, Y.; Wang, L.; Wen, Y.; Bai, H.; Liu, G.; Zhang, Y.; Li, Y.; Zhang, B.; Peng, H. The *p*-Orbital Delocalization of Main-Group Metals to Boost CO₂ Electroreduction. *Angew. Chem., Int. Ed.* **2018**, *130*, 16114–16119.

Supporting information for

**Two-Dimensional Mosaic Bismuth Nanosheets for Highly
Selective Ambient Electrocatalytic Nitrogen Reduction**

Laiquan Li,[#] Cheng Tang,[#] Bingquan Xia, Huanyu Jin, Yao Zheng, Shi-Zhang Qiao*

School of Chemical Engineering, The University of Adelaide, Adelaide, SA 5005, Australia

* E-mail: s.qiao@adelaide.edu.au (S.-Z.Q.).

Experimental Section

Material:

Sodium salicylate (S3007, $\geq 99.5\%$), potassium sodium tartrate ($\text{NaKC}_4\text{H}_4\text{O}_6 \cdot 4\text{H}_2\text{O}$), sodium nitroferricyanide ($\text{C}_5\text{FeN}_6\text{Na}_2\text{O}$, $\geq 99\%$), sodium hypochlorite (available chlorine 10-15 %), para-(dimethylamino) benzaldehyde (99%), NH_4Cl (99.998%), BiCl_3 ($\geq 98\%$), Potassium iodide ($\geq 99.5\%$) and acetic acid are purchased from Sigma-Aldrich Chemical Reagent Co., Ltd. Nafion 117 membrane (Dupont) is purchased from Fuelcell store. Ultrapure water used throughout all experiments was purified through a Millipore system. Ultra high purity N_2 (99.999%) and Ar (99.999%) were purchase from BOC gas, Australia.

Imaging and spectroscopic characterization:

Field-emission SEM imaging and EDS mapping were conducted on a FEI QUANTA 450 electron microscope. TEM and HRTEM images are collected on a Phiips CM 200 transmission electron microscope operated at 120 kV. XRD patterns were obtained using a D4 endeavour (Bruker) X-ray diffraction system with $\text{Co K}\alpha$ radiation. XPS data were collected under ultrahigh vacuum ($< 10^{-8}$ Torr) using a monochromatic Al $\text{K}\alpha$ X-ray source. Raman data were collected on a HORIBA LabRAM HR Evolution spectroscopy using the excitation wavelength of 532 nm. The absorbance data of spectrophotometer were collected on SHIMADZU UV-2600 ultraviolet-visible (UV-Vis) spectrophotometer; the Bi L_{III} -edge XAFS data were collected on the X-ray absorption spectroscopy beamline of Australian Synchrotron.

Synthesis of bismuth oxyiodide nanosheet:

In a typical procedure, 0.2 mmol of BiCl_3 was firstly dissolved in 20 mL of 1.2 M acetic acid and stirred for 30 min, followed by addition of 5 mL of 0.04 M KI solution. The pH of the above mixture solution was then adjusted to 6 using 3 M NaOH. After stirring for another 30 min, the solution was then transferred to a 50 mL Teflon-lined autoclave and heated at 160 °C for 2 hours. The BiOI nanosheets were finally obtained after collecting by centrifugation, washing by deionized water and freezing drying.

In-situ formation of Bi NS from BiOI precursor:

The in-situ formation of Bi NS was achieved by 100-cycle reductive CV scans at negative potentials. As shown in Figure S2, the CV scans were conducted with a scan rate of 100 mV s^{-1} from -0.7 V to 0 V vs. RHE. This range involves the reduction potential and is more negative than the oxidation potentials of BiOI. During the first 50 cycles, the BiOI converted to Bi; and during the second 50 cycles the Bi electrode gradually became stable.

Synthesis of Bismuth nanoparticle (Bi NP):

0.2 mmol of BiCl₃ was firstly dissolved in 20 mL of deionized water. After stirring for 20 min, 10 mL of 1 M NaBH₄ was then added by droplet. After vigorous stirring for another 2 hours, the black product was thoroughly washed by deionized water and dried in vacuum oven at 60°C.

Electrochemical measurements:

Carbon paper (Toray Paper 090) was first treated in O₂ plasma environment at a pressure of 500 mTorr for 20 min. After soaking in 3 M H₂SO₄ for 12 h, the carbon paper was then thoroughly washed with ethanol and deionized water and dried at 60°C. The Nafion 117 membrane was preconditioned by boiling in 5% H₂O₂ solution and ultrapure deionized water at 80 °C for 1 h respectively, followed by treatment in 0.05 M H₂SO₄ for 3 h and deionized water for another 1h.

Electrochemical data were collected with a CHI 1000 electrochemical workstation (CHI Instruments, Inc.). Three electrode system was used in the electrochemical measurement in which a saturated calomel electrode (SCE) was used as a reference electrode, and a graphite rod as a counter electrode. The NRR measurement apparatus is shown in Fig. S5. The volume of the electrolyte in the anode and cathode chamber is 30 mL for each. A consecutive acid trap is connected with the cathode chamber with 5 mL of 0.05 M H₂SO₄ in two 10 mL clean PP tube. A magnetic stirring with a stirring rate of 600 rpm is applied throughout the measurement. For the working electrode preparation, 4 mg of BiOI powder and 1 mg of carbon black were dispersed in 960 μL of the mixture of isopropanol and water (v/v=1:1) and 40 μL of 5wt% Nafion solution. The mixture was sonicated for 3 h to form a uniform catalyst ink. 80 μL of the resulting catalyst ink was drop-casted onto a 1 × 1 cm² carbon paper. The final mass loading was calculated based on the stoichiometric ratio of Bi in BiOI, namely 0.192 mg_{Bi} cm⁻². For the LSV test on RDE, 20 μL of the above mixture was drop-casted on to a glassy carbon electrode with diameter of 0.5 cm. The LSV curve was obtained at a scan rate of 5 mV s⁻¹ with a rotating speed of 1600 rpm. All potentials were referenced against the reversible hydrogen electrode (RHE) based on the Nernst equation ($E_{\text{RHE}} = E_{\text{SCE}} + 0.059 \times \text{pH} + 0.241$). All experiments were carried out at room temperature (25 °C). 0.10 M Na₂SO₄ was used as electrolyte, which was purged with ultra-high purity N₂ (99.999%) for 30 min before N₂ reduction measurement (~50 mL min⁻¹), and then bubbled with a constant flow rate of 20 mL min⁻¹ throughout the whole electrolysis process. The stability test was performed by replacing the electrolyte every 1 hour without changing the electrode and Nafion membrane.

Determination of ammonia:

a) Stock reagent:

- 1) Chromogenic reagent (A): 5 g of sodium salicylate and 5 g of potassium sodium tartrate were dissolved in 100 mL of 1 M NaOH.
- 2) Oxidizing solution (B): 3.5 mL of sodium hypochlorite (available chlorine 10-15 %) was added into 100 mL of deionized water.
- 3) Catalysing reagent (C): 0.2 g of sodium nitroferricyanide was dissolved in 20 mL of deionized water.

b) Standard solutions preparation

- 1) 1000 $\mu\text{g}_{\text{NH}_3}/\text{mL}$ stock: 0.3146 g of pre-dried NH_4Cl (105°C for 4 h) was added in 100 mL of 0.10 M Na_2SO_4 solution.
- 2) 10 $\mu\text{g}_{\text{NH}_3}/\text{mL}$ stock: 1 mL of 1000 $\mu\text{g}_{\text{NH}_3}/\text{mL}$ stock solution was added in a 100 mL volumetric flask, and add 0.10 M Na_2SO_4 solution to the scale mark.
- 3) 0.2, 0.4, 0.8, 1.2, 1.6 and 2 mL of 10 $\mu\text{g}_{\text{NH}_3}/\text{mL}$ stock solution were separately added into a 20 mL volumetric flask and added 0.10 M Na_2SO_4 solution to the scale mark to obtain 0.1, 0.2, 0.4, 0.6, 0.8 and 1 $\mu\text{g}_{\text{NH}_3}/\text{mL}$ standard solutions.

c) UV-vis measurement

2 mL of standard solutions or sample solution was added to test tubes, to which 2 mL of chromogenic reagent (A), 1 mL of oxidizing solution (B) and 0.2 mL of catalysing reagent (C) were then successively added. After shaking up and standing for 1 h, the concentration of the produced indophenol blue was measured using UV-vis spectrophotometer. The standard curve was plotted with the absorbance values at wavelength of 655 nm as y axis and the concentration of NH_3 as x axis.

Determination of hydrazine:

The possible hydrazine product in the electrolytes was estimated by the method of Watt and Chrisp. To prepare a sensitive chromogenic reagent, 2.0 g para-(dimethylamino)benzaldehyde was dissolved in a mixture of 10 mL concentrated HCl and 100 mL ethanol. The absorbance of hydrazine after mixing with the chromogenic reagent in the resulting electrolyte was estimated at 460 nm.

Calculation of NH_3 yield and Faradaic efficiency:

The ammonia formation rate was determined using the following equation:

$$r(\text{NH}_3) = (c \times V)/(t \times A)$$

where c is the measured NH_3 concentration, V is the volume of the electrolyte or acid trap, t is the reduction reaction time, and A is the effective area of the electrode, which is the geometric area of the electrode covering with Bi NS.

The Faradaic efficiency was calculated as follows:

$$\text{FE} = 3F \times c \times V / (17 \times Q)$$

where F is the Faraday constant, c is the measured NH_3 concentration, V is the volume of the electrolyte or acid trap, t is the reduction reaction time, M is the relative molecular mass of NH_3 and Q is the total charge used for the electrodes.

The total ammonia production is calculated as the summary of the ammonia products in cathode chamber, anode chamber, and also in-line acid traps.

Measurement of electrochemically active surface area:

The electrochemically active surface area was measured by double layer capacitance method. CV measurement was conducted at the potential window 0.3 V – 0.4 V vs. RHE with different scan rates of 10, 20, 40, 60, 80, 100 mV. By plotting the $(J_a - J_c)/2$ at 0.35 V vs. RHE against the scan rate, the slope value was calculated to be the double layer capacitance (C_{dl}).

Supplementary Results

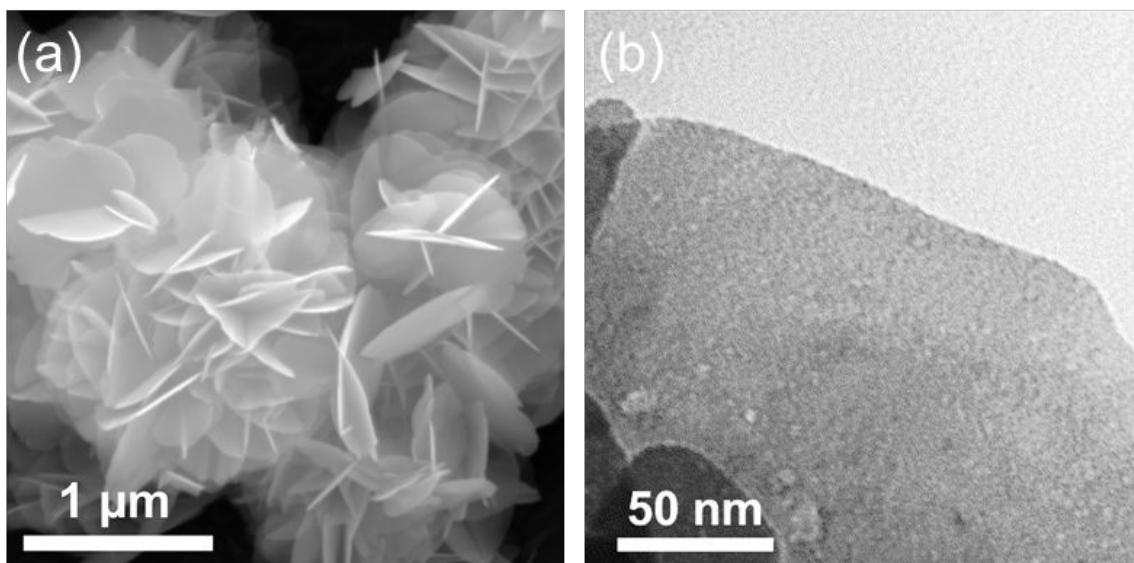


Figure S1. (a) SEM and (b) TEM images of BiOI precursor.

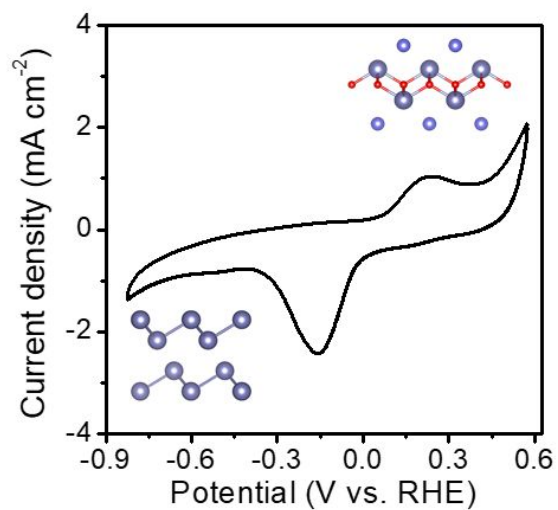


Figure S2. CV curve of BiOI shows the reduction to metallic Bi at cathodic potentials; insets shows the schematic crystal structure of BiOI and Bi.

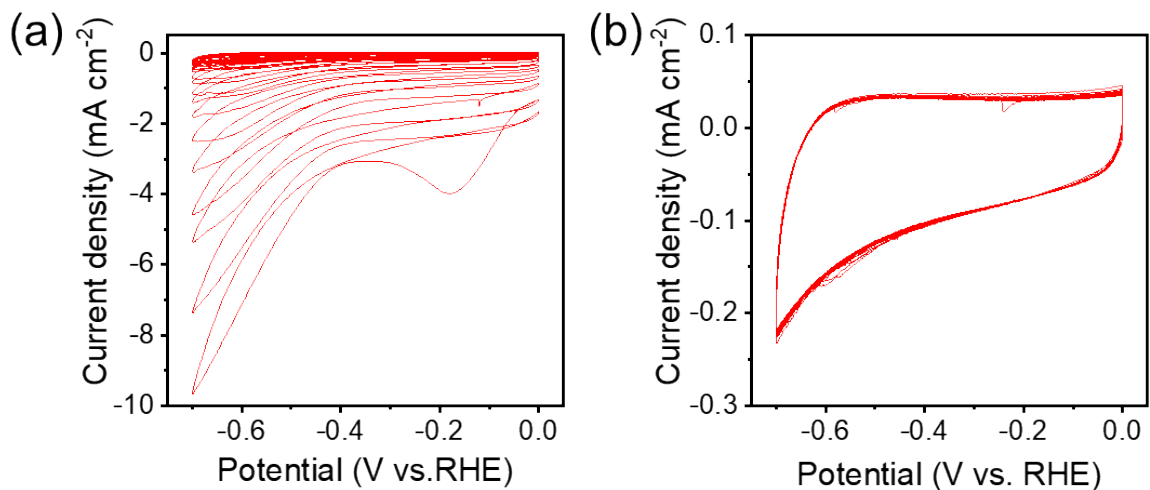


Figure S3. (a) CV scans of BiOI for the first 50 cycles and (b) next 50 cycles.

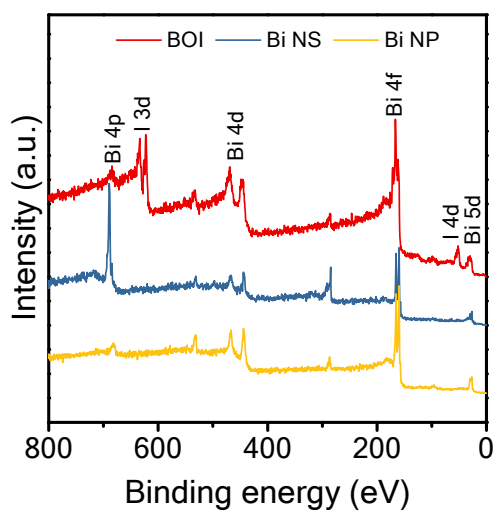


Figure S4. (a) XPS survey spectra of BiOI precursor, Bi NS and Bi NP.

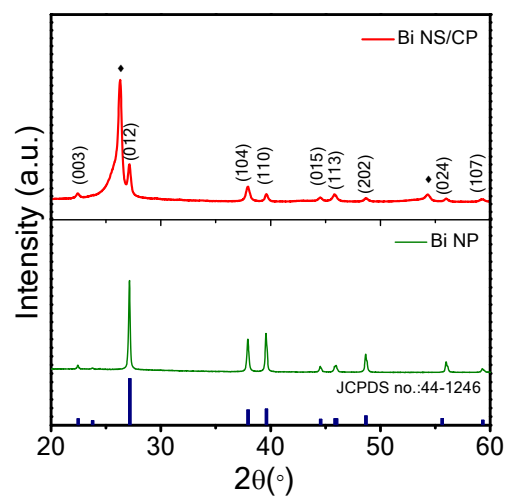


Figure S5. XRD patterns of Bi NS on carbon paper and Bi NP powder.

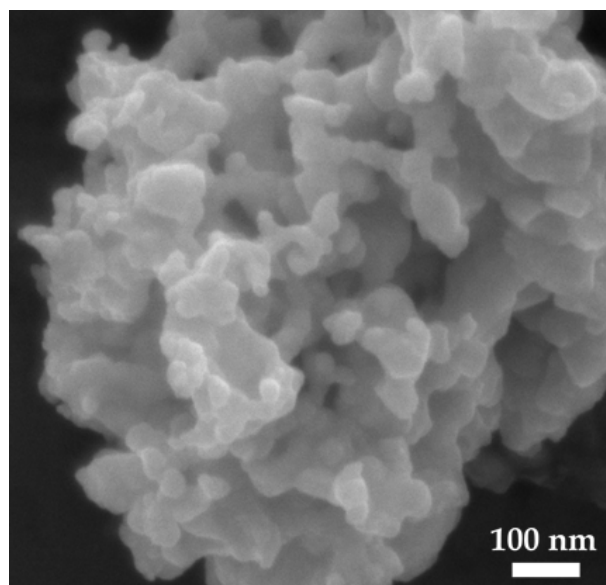


Figure S6. SEM image of Bi NP.

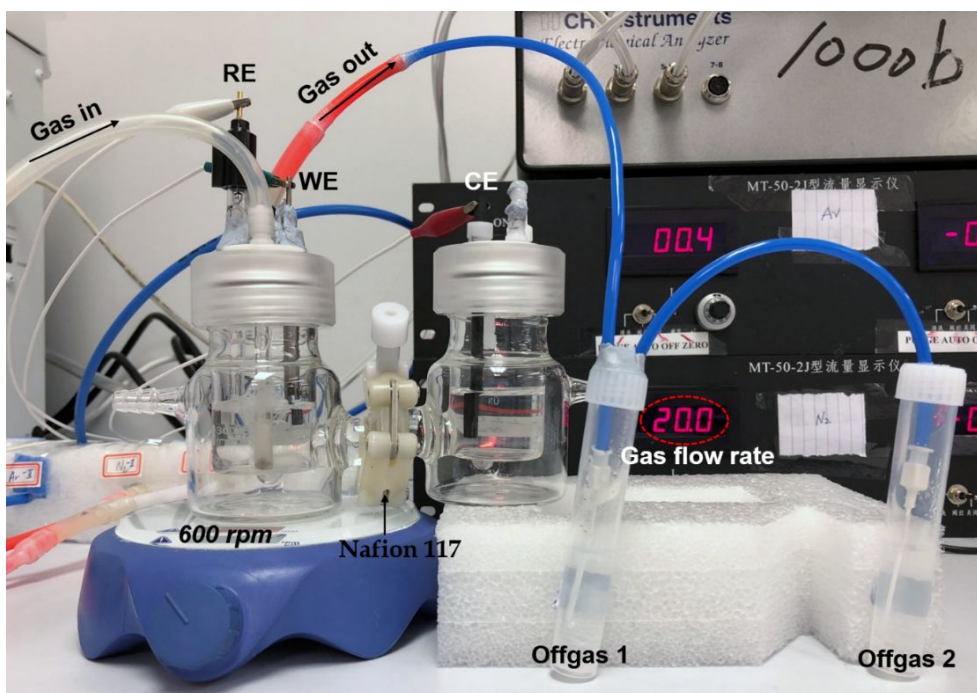


Figure S7. Image of the apparatus for NRR measurement.

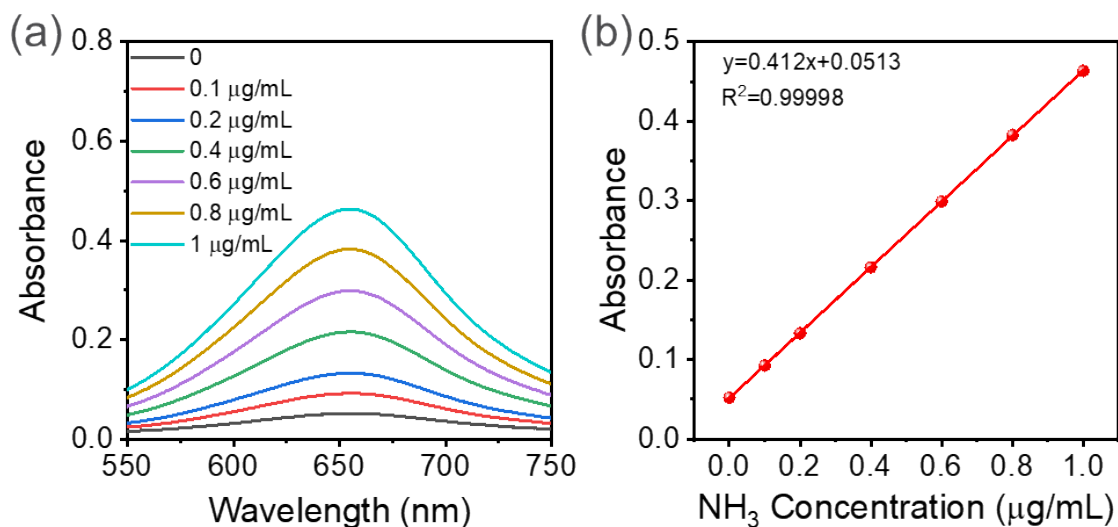


Figure S8. Calibration curve in 0.10 M Na_2SO_4 using ammonium chloride solutions of known concentration as standards. (a) UV-vis curves of indophenol assays after incubated for 1 hours and (b) calibration curve used for estimation of NH_3 concentration. The absorbance at 655 nm was measured by UV-Vis spectrophotometer, and the fitting curve shows good linear relation of absorbance with NH_3 concentration ($y = 0.412x + 0.0513$, $R^2=0.99998$).

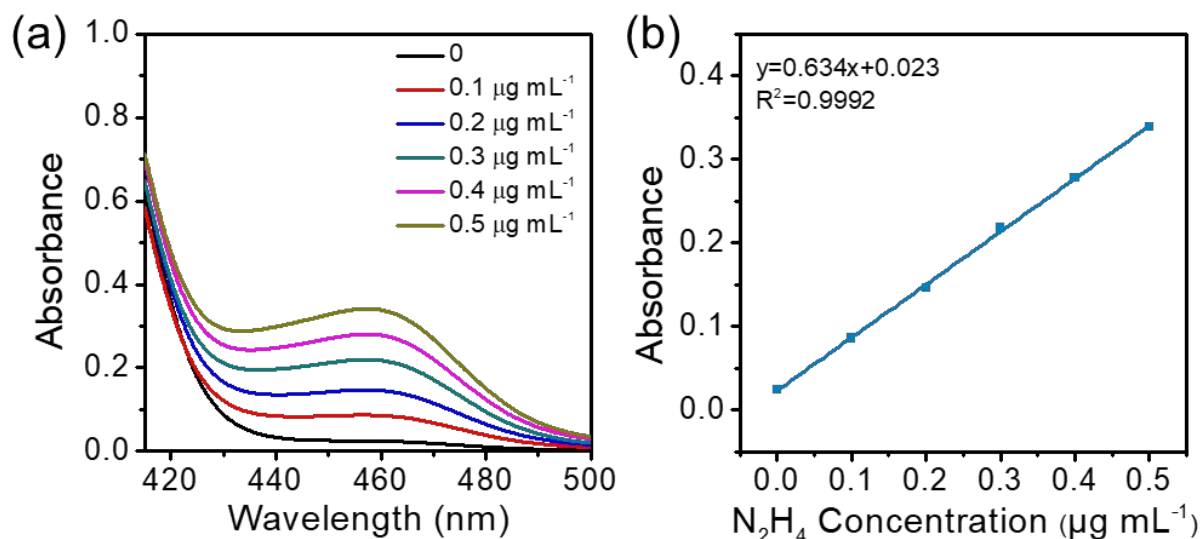


Figure S9. Calibration for N_2H_4 detection. (a) UV-Vis curves of various concentrations of N_2H_4 stained with $p-C_9H_{11}NO$ indicator and incubated for 20 min at room temperature. (b) A calibration curve used to calculate the concentrations of N_2H_4 .

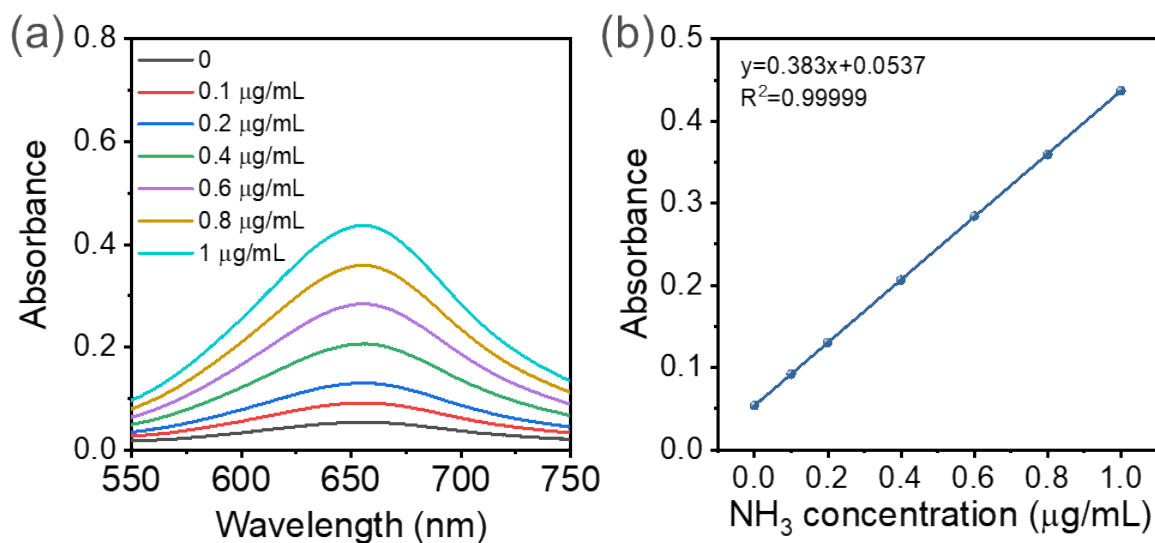


Figure S10. Calibration curve in 0.10 M H_2SO_4 using ammonium chloride solutions of known concentration as standards. (a) UV-vis curves of indophenol assays after incubated for 1 hours and (b) calibration curve used for estimation of NH_3 concentration. The absorbance at 655 nm was measured by UV-Vis spectrophotometer, and the fitting curve shows good linear relation of absorbance with NH_3 concentration ($y = 0.383x + 0.0513$, $R^2=0.99999$).

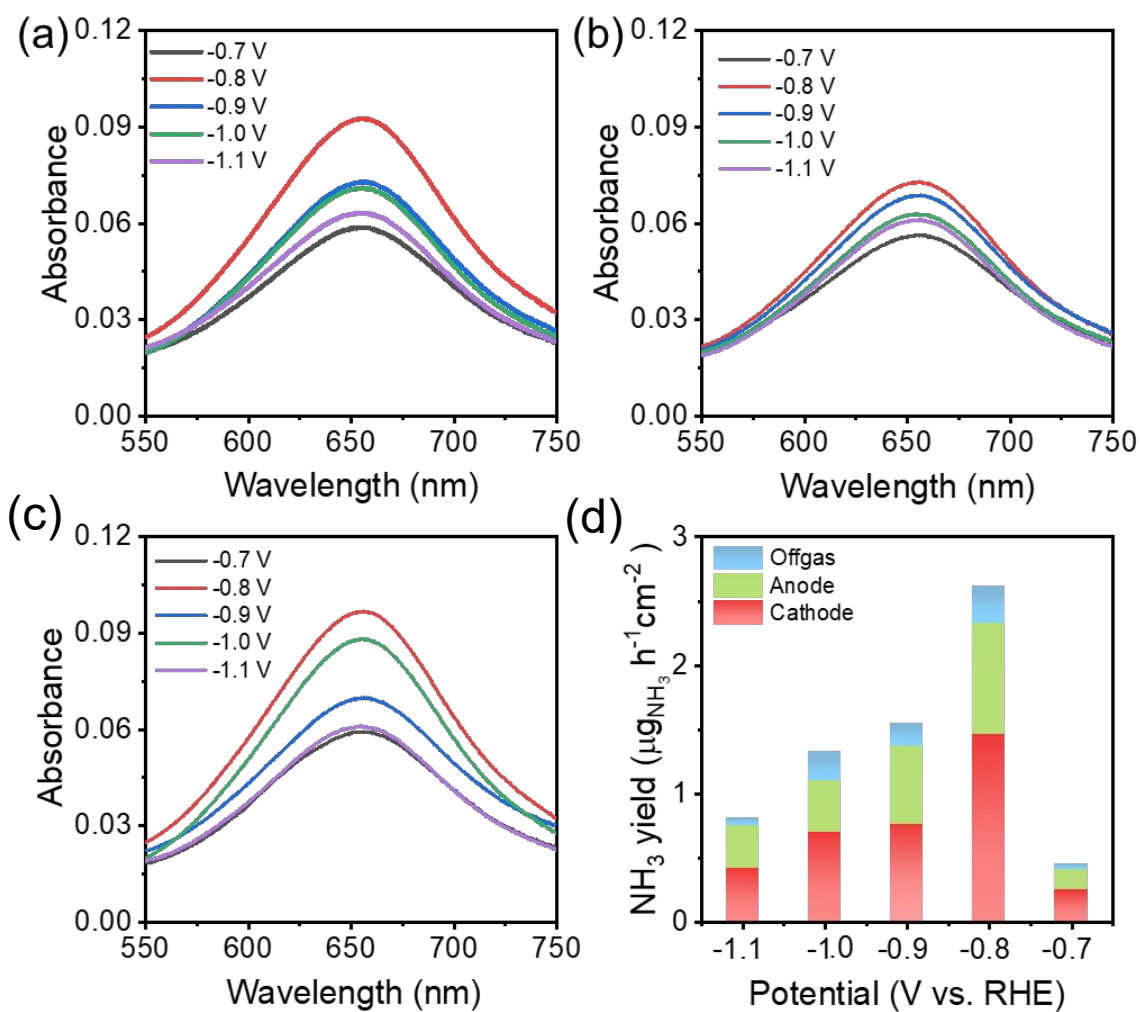


Figure S11. (a-c) Typical UV-vis spectra of electrolytes in the cathode chamber, anode chamber and acid trap (10 mL) solutions stained with indophenol indicator after electrolysis for 2 h at different potentials. (d) NH₃ formation rates of Bi NS at different potentials showing the contributions from the above solutions.

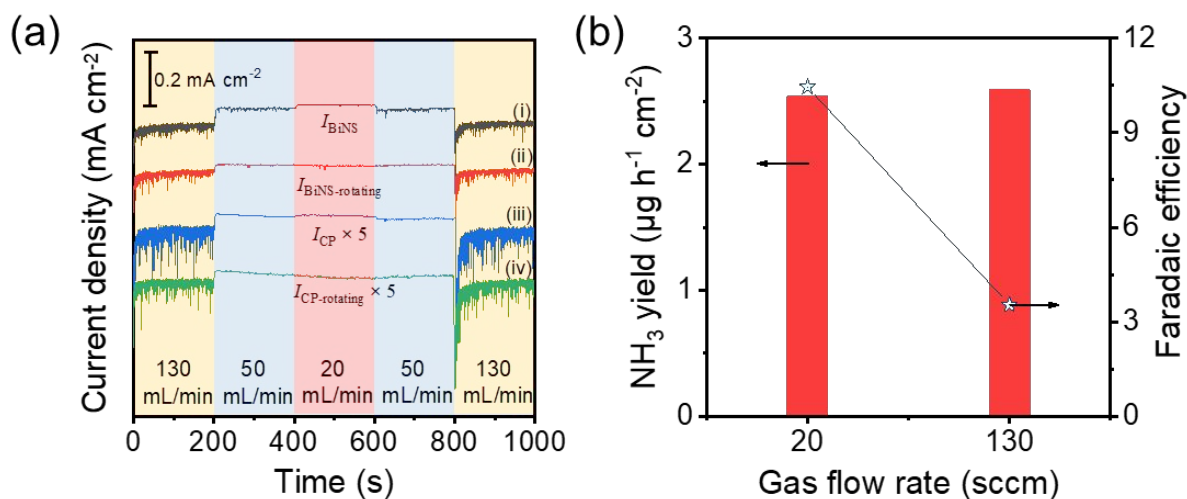


Figure S12. (a) Influence of N₂ gas flow on the total current density of electrodes at -0.7 V vs. RHE; from the top to bottom: (i) Bi NS, (ii) Bi NS under magnetic stirring, (iii) carbon paper, (iv) carbon paper under magnetic stirring; (b) NH₃ formation rate and corresponding Faradaic efficiency of Bi NS at N₂ flow rates of 20 and 130 sccm.

Note: Given the extremely low solubility (0.66 mmol L^{-1} under ambient conditions)¹ and low diffusion coefficient of N₂ in water, a significant variation of pH and N₂ gradient near the catalyst surface is likely to be generated during electrocatalysis, which can lead to unfavorable mass transfer effects on the resultant performance. As revealed in Figure S12, when the chronoamperometric measurements are conducted using a Bi NS-coated working electrode at -0.7 V vs. RHE, distinct current density drops can be observed when the gas flow changed from 130 to 50 and from 50 to 20 mL min⁻¹. Similar phenomenon is also found for the bare carbon paper substrate, indicating that such current density variation should be ascribed to catalyst-irrelevant issues, but can considerably influence the accurate measurement of Faradaic efficiency. As shown in Figure S12b, similar NH₃ formation rates are obtained at N₂ flow rate of 20 and 130 sccm, while the Faradaic efficiency obtained at N₂ flow rate of 130 sccm (3.53%) is much lower than that obtained at 20 sccm (10.46%). Therefore, to minimize the influence of gas flow rate on the current and to accurately measure the Faradaic efficiency, a small N₂ gas flow rate of 20 sccm is applied in this work. Furthermore, magnetic stirring is applied to alleviate pH gradient and promote N₂ diffusion.

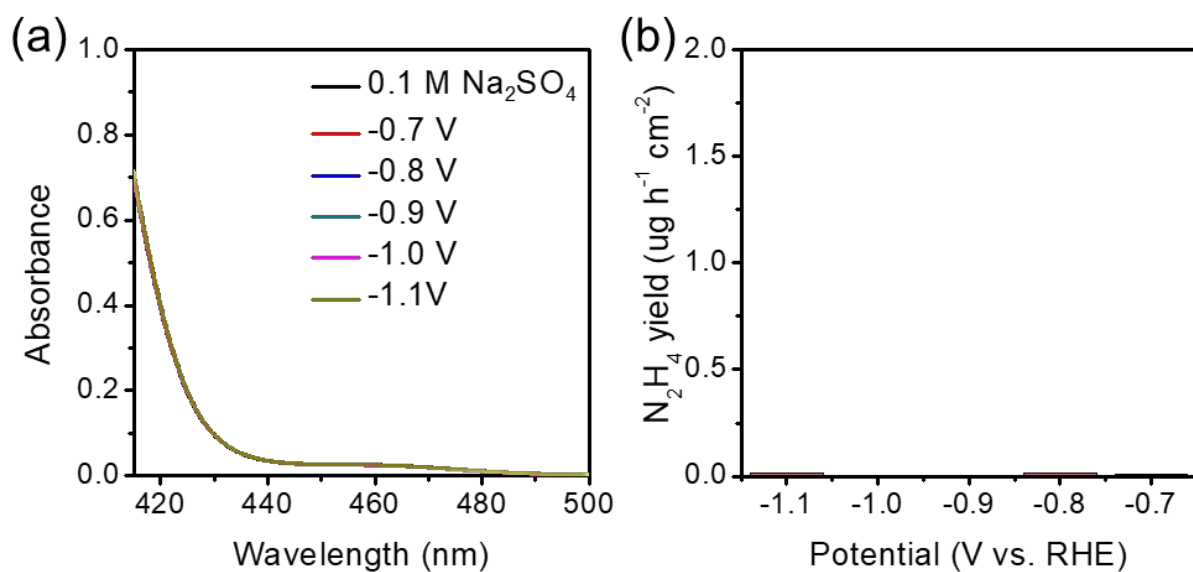


Figure S13. (a) UV-Vis absorption spectra of the electrolytes stained with p-C₉H₁₁NO indicator after NRR electrolysis at a series of potentials. (b) N₂H₄ yields obtained at different potentials.

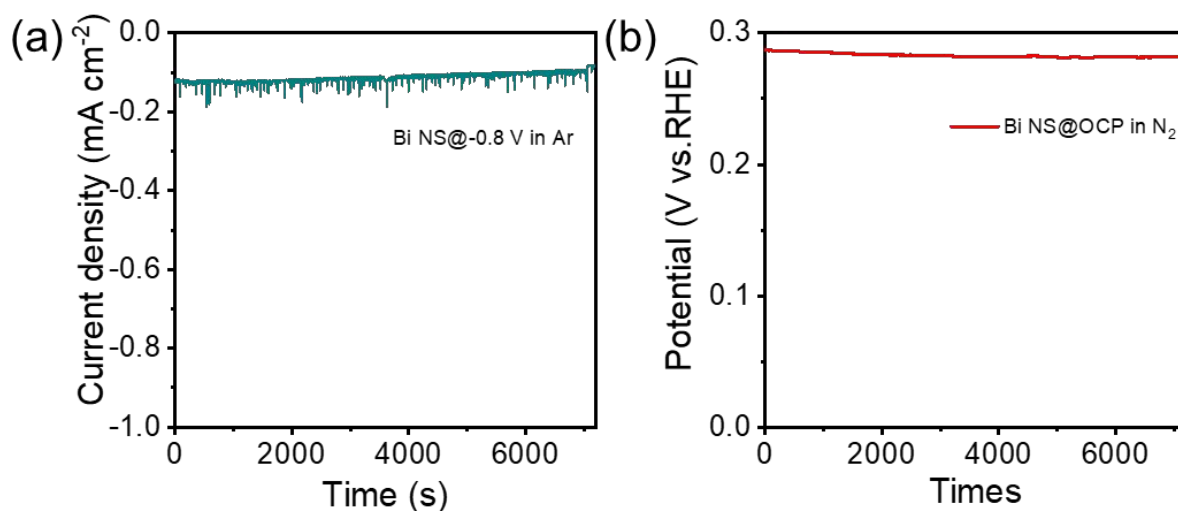


Figure S14. Chronoamperometry curves for different control experiments; (a) Bi NS at -0.8 V under Ar atmosphere. (b) Open circuit potential (OCP) test for Bi NS in 0.10 M Na₂SO₄ under N₂ atmosphere.

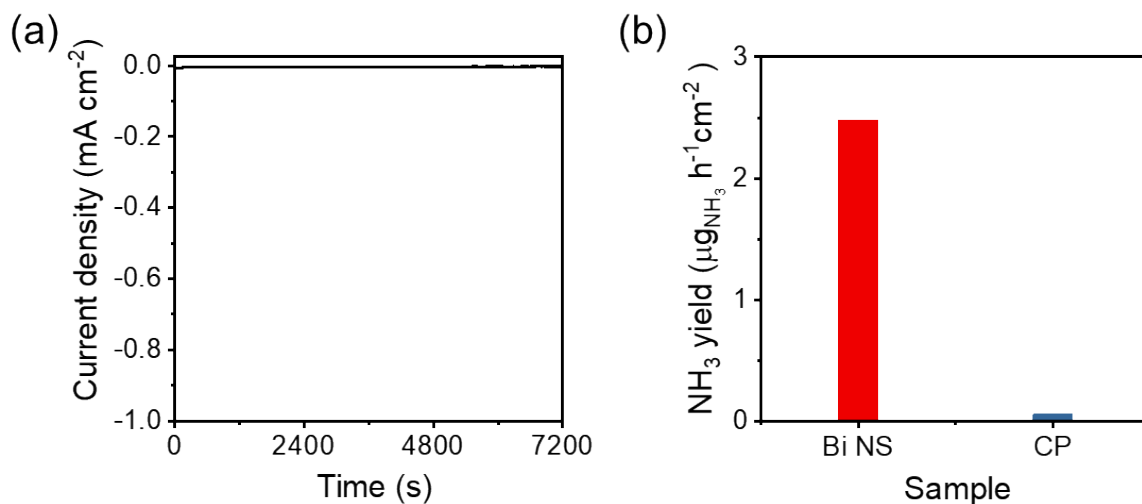


Figure S15. (a) Chronoamperometry curve of bare carbon paper; (b) NH₃ yield of Bi NS and bare carbon paper at -0.8 V at N₂ atmosphere.

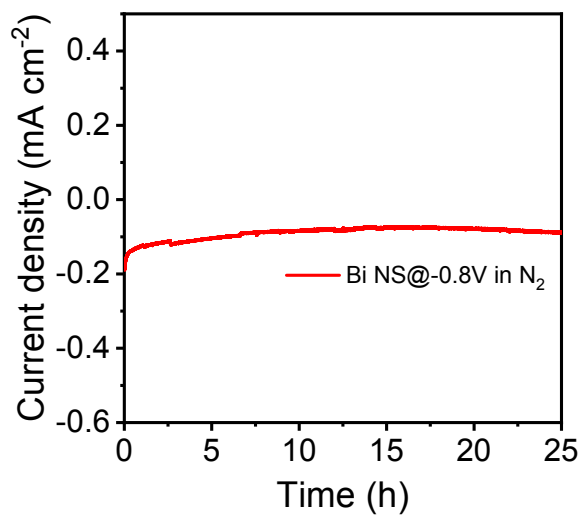


Figure S16. Long-term chronoamperometry curve of Bi NS electrode showing good stability.

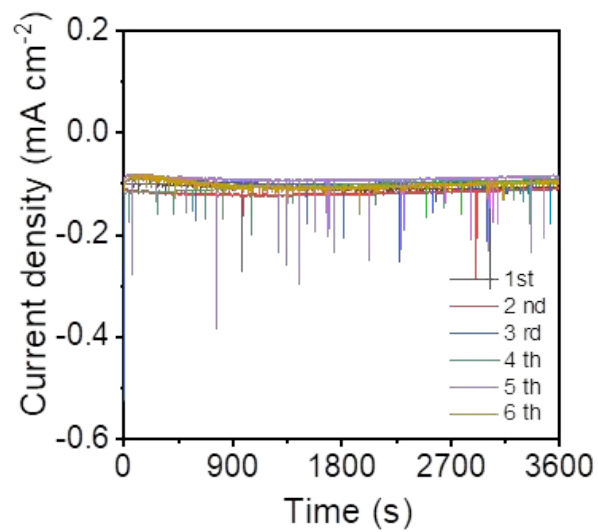


Figure S17. Chronoamperometry curves of Bi NS at -0.8 V vs. RHE for 6 cycles.

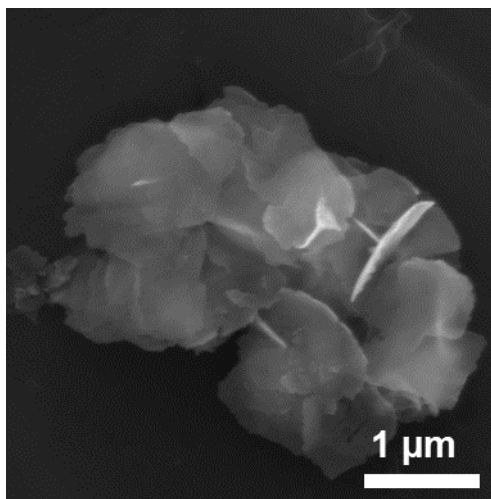


Figure S18. SEM image of Bi NS after NRR

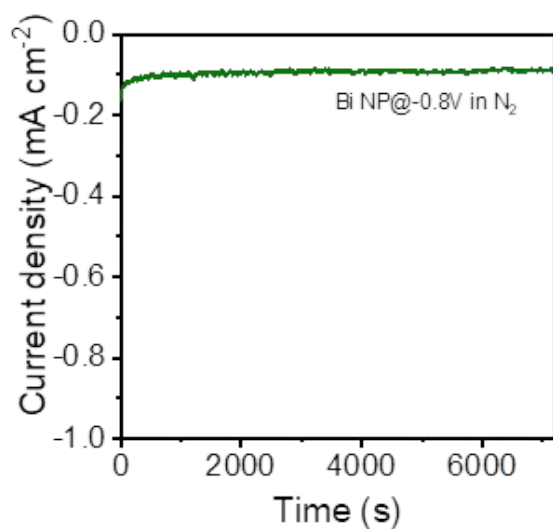


Figure S19. Chronoamperometry curves of Bi NP in N₂ saturated 0.10 M Na₂SO₄ at -0.8 V vs. RHE.

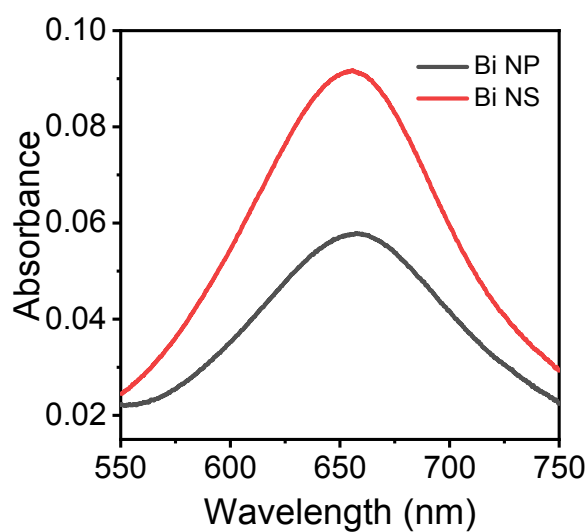


Figure S20. UV-Vis absorption spectra of the cathode electrolytes stained with Indophenol indicator after NRR electrolysis for Bi NS and Bi NP.

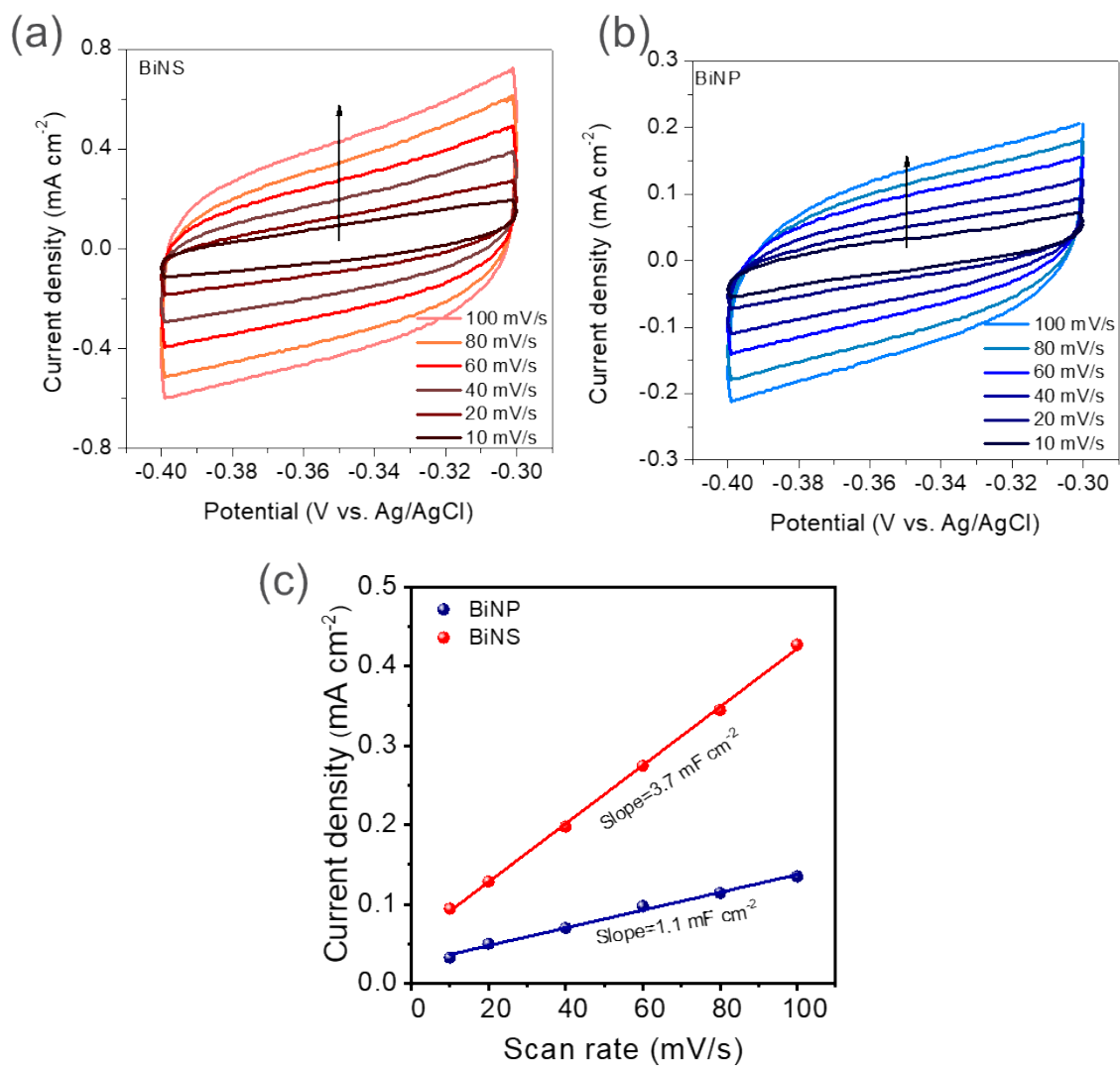


Figure S21. Electrochemically active surface area measurement. CV of (a) Bi NS and (b) Bi NP at various scan rates (10 to 100 mV s⁻¹) in the region of -0.4 to 0.3 V vs. Ag/AgCl; (c) The capacitive current densities at -0.35 V vs. Ag/AgCl as a function of scan rates for Bi NS and Bi NP.

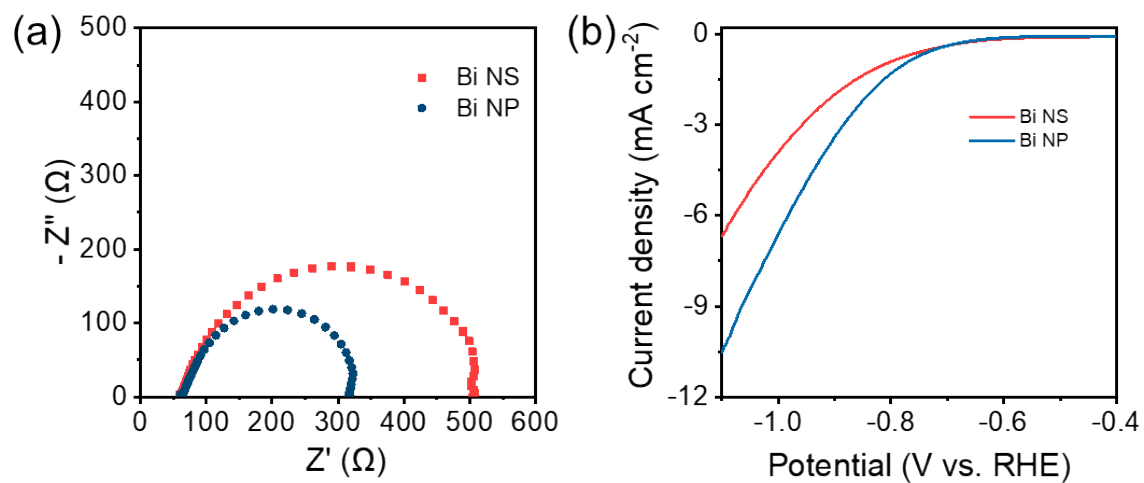


Figure S22. (a) Electrochemical impedance spectra of Bi NS and Bi NP at -0.8 V vs. RHE; (b) LSV curves of Bi NS and Bi NP.

Table S1. Ammonia yield and corresponding Faradaic efficiency of Bi NS and controls.

Sample	Potential	Peak _{WE}	Peak _{CE}	Peak _{offgas}	Yield ($\mu\text{g}_{\text{NH}_3} \text{cm}^{-2} \text{h}^{-1}$)	Q (C)	FE (%)
	-0.7 V	0.0587	0.0564	0.0593	2.27	0.247	6.25
	-0.8 V-1 st	0.0921	0.0760	0.0776	2.62	0.8	11.15
	-0.8 V-2 nd	0.0917	0.0762	0.0794	2.64	0.8	11.24
	-0.8 V-3 rd	0.0839	0.0754	0.0790	2.38	0.9	9.01
	-0.8 V-ave	0.0877	0.0741	0.0771	2.54	0.83	10.46
	-0.9 V	0.0729	0.0681	0.0691	1.56	1.68	3.16
	-1.0 V	0.071	0.0632	0.0730	1.34	3.49	1.31
Bi NS	-1.1 V	0.0633	0.0612	0.0611	0.82	7.3	0.38
	-0.8 V (Ar)	0.0542	0.0524	0.0555	0.095	0.74	0.43
	OCP (N ₂)	0.0542	0.0526	0.0555	0.102	--	--
Bi NP	-0.8 V (N ₂)	0.0579	0.0534	0.0555	0.268	1.38	0.66
CP	-0.8 V	0.0541	0.052	0.0555	0.08	--	--

Note: A typical calculation for ammonia yield and Faradaic efficiency:

The absorbance peak value for indophenol indicator stained blank 0.1 M Na₂SO₄ and 0.05 M H₂SO₄ (acid trap solution) are 0.052 and 0.0555, respectively. The volumes of electrolyte and acid trap are 30 and 10 mL, respectively. The electrode area is 1 cm² and reaction duration is 2 hours.

So taking “-0.8V-1st” as example, the amount of the ammonia produced can be calculated as below:

$$(0.0921 + 0.0760 - 2 \times 0.052) \times 30/0.412 + (0.0776 - 0.0555) \times 10/0.383 = 5.238 \mu\text{g NH}_3$$

The yield can be calculated as below:

$$5.238 \mu\text{g} / 1 \text{ cm}^2 / 2 \text{ h} = 2.619 \mu\text{g}_{\text{NH}_3} \text{ cm}^{-2} \text{ h}^{-1}$$

The corresponding faradaic efficiency can be calculated as below:

$$[(5.238 \times 10^{-6} \text{ g} \times 3 \times 96485 \text{ C/mol}) / (17 \text{ g/mol} \times 0.8 \text{ C})] \times 100 \% = 11.15\%$$

Table S2. Summary of the representative reports on electrocatalytic N₂ fixation at ambient conditions.

Catalysts	Electrolyte	NH ₃ yield	Faradaic efficiency	Detection method	Ref.
Ru/C	2 M KOH	0.21 μg ⁻¹ h ⁻¹ cm ⁻²	0.28%	Ion Chromatography	2
Pd/C	0.1 M PBS	1.35 μg ⁻¹ h ⁻¹ cm ⁻²	8.2%	Indophenol Blue	3
Au Nanorod	0.1 M KOH	6.042 μg ⁻¹ h ⁻¹ mg ⁻¹ _{cat.}	3.879%	Nessler's Reagent	4
Amorphous Au/CeO _x	0.1 M HCl	8.31 μg ⁻¹ h ⁻¹ mg ⁻¹ _{cat.}	7.79%	Indophenol Blue	5
AuHNCs	0.5 M LiClO ₄	3.90 μg ⁻¹ h ⁻¹ cm ⁻²	30.2%	Nessler's Reagent	6
TA reduced Au/TiO ₂	0.1 M HCl	21.4 μg ⁻¹ h ⁻¹ mg ⁻¹ _{cat.}	8.11%	Indophenol Blue	7
Ti ₃ C ₂ T _x	0.5 M Li ₂ SO ₄	4.72 μg ⁻¹ h ⁻¹ cm ⁻²	4.62%	Nessler's Reagent	8
Mo ₂ C	0.5 M Li ₂ SO ₄	11.2 μg ⁻¹ h ⁻¹ cm ⁻²	7.8%	Nessler's Reagent	9
Cr ₂ O ₃ microsphere	0.1 M Na ₂ SO ₄	3.04 μg ⁻¹ h ⁻¹ cm ⁻²	6.78%	Indophenol Blue	10
Defect-rich MoS ₂	0.1 M Na ₂ SO ₄	2.93 μg ⁻¹ h ⁻¹ cm ⁻²	8.34%	Indophenol Blue	11
Nb ₂ O ₅ nanofiber	0.1 M HCl	4.36 μg ⁻¹ h ⁻¹ cm ⁻²	0.52%	Indophenol Blue	12
Fe ₂ O ₃ -CNT	KHCO ₃	0.22 μg ⁻¹ h ⁻¹ cm ⁻²	0.15%	Ammonia selective electrode	13
BiVO ₄	0.2 M Na ₂ SO ₄	8.6 μg ⁻¹ h ⁻¹ mg ⁻¹ _{cat.}	10.04%	Indophenol Blue	14
Bi ₄ V ₂ O ₁₁ /C eO ₂	0.1 M HCl	23.21 μg ⁻¹ h ⁻¹ mg ⁻¹ _{cat.}	10.16%	Indophenol Blue	15
Fe-SS	Ionic Liquids	1.4 μg ⁻¹ h ⁻¹ cm ⁻²	60%	Indophenol Blue	16
B ₄ C	0.1 M HCl	2.657 μg ⁻¹ h ⁻¹ cm ⁻²	15.95%	Indopnehol Blue	17
PEBCD	0.5 M Li ₂ SO ₄	1.58 μg ⁻¹ h ⁻¹ cm ⁻²	2.58%	Nessler's Reagent	18
Bi NS	0.1 M Na₂SO₄	2.54 μg⁻¹ h⁻¹ cm⁻² 13.23 μg⁻¹ h⁻¹ mg⁻¹_{cat.}	10.49%	Indophenol Blue	This work

Table S3. N₂H₄ yield and Faradaic efficiency obtained at different potentials for Bi NS.

Potential (gas)	Yield ($\mu\text{g cm}^{-2} \text{h}^{-1}$)	FE (%)
-0.7V (N ₂)	0.011	0.108
-0.8V (N ₂)	0.016	0.049
-0.9V (N ₂)	0.001	0.002
-1.0V (N ₂)	0.001	0.001
-1.1V (N ₂)	0.014	0.005

Reference:

1. Battino, R.; Rettich, T. R.; Tominaga, T., The Solubility of Nitrogen and Air in Liquids. *J. of Phys. Chem. Ref. Data* **1984**, *13* (2), 563-600.
2. Kordali, V.; Kyriacou, G.; Lambrou, C., Electrochemical Synthesis of Ammonia at Atmospheric Pressure and Low Temperature in a Solid Polymer Electrolyte Cell. *Chem. Commun.* **2000**, *0* (17), 1673-1674.
3. Wang, J.; Yu, L.; Hu, L.; Chen, G.; Xin, H.; Feng, X., Ambient Ammonia Synthesis via Palladium-Catalyzed Electrohydrogenation of Dinitrogen at Low Overpotential. *Nat. Commun.* **2018**, *9* (1), 1795.
4. Bao, D.; Zhang, Q.; Meng, F. L.; Zhong, H. X.; Shi, M. M.; Zhang, Y.; Yan, J. M.; Jiang, Q.; Zhang, X. B. Electrochemical Reduction of N₂ under Ambient Conditions for Artificial N₂ Fixation and Renewable Energy Storage Using N₂/NH₃ Cycle. *Adv. Mater.* **2017**, *29*, 1604799.
5. Li, S. J.; Bao, D.; Shi, M. M.; Wulan, B. R.; Yan, J. M.; Jiang, Q., Amorphizing of Au Nanoparticles by CeO_x-RGO Hybrid Support towards Highly Efficient Electrocatalyst for N₂ Reduction under Ambient Conditions. *Adv. Mater.* **2017**, *29* (33), 1700001.
6. Nazemi, M.; Panikkanvalappil, S. R.; El-Sayed, M. A., Enhancing the Rate of Electrochemical Nitrogen Reduction Reaction for Ammonia Synthesis under Ambient Conditions Using Hollow Gold Nanocages. *Nano Energy* **2018**, *49*, 316-323.
7. Shi, M. M.; Bao, D.; Wulan, B. R.; Li, Y. H.; Zhang, Y. F.; Yan, J. M.; Jiang, Q., Au Sub-Nanoclusters on TiO₂ toward Highly Efficient and Selective Electrocatalyst for N₂ Conversion to NH₃ at Ambient Conditions. *Adv. Mater.* **2017**, *29* (17), 1606550 .
8. Luo, Y.; Chen, G.-F.; Ding, L.; Chen, X.; Ding, L.-X.; Wang, H., Efficient Electrocatalytic N₂ Fixation with MXene under Ambient Conditions. *Joule* **2018**, *3* (1), 279-289.
9. Cheng, H.; Ding, L. X.; Chen, G. F.; Zhang, L.; Xue, J.; Wang, H., Molybdenum Carbide Nanodots Enable Efficient Electrocatalytic Nitrogen Fixation under Ambient Conditions. *Adv. Mater.* **2018**, *30*, 1803694.
10. Zhang, Y.; Qiu, W.; Ma, Y.; Luo, Y.; Tian, Z.; Cui, G.; Xie, F.; Chen, L.; Li, T.; Sun, X., High-Performance Electrohydrogenation of N₂ to NH₃ Catalyzed by Multishelled Hollow Cr₂O₃ Microspheres under Ambient Conditions. *ACS Catal.* **2018**, *8* (9), 8540-8544.

11. Li, X.; Li, T.; Ma, Y.; Wei, Q.; Qiu, W.; Guo, H.; Shi, X.; Zhang, P.; Asiri, A. M.; Chen, L.; Tang, B.; Sun, X. Boosted Electrocatalytic N₂ Reduction to NH₃ by Defect-Rich MoS₂ Nanoflower. *Adv. Energy Mater.* **2018**, *8*, 1801357.
12. Han, J.; Liu, Z.; Ma, Y.; Cui, G.; Xie, F.; Wang, F.; Wu, Y.; Gao, S.; Xu, Y.; Sun, X., Ambient N₂ Fixation to NH₃ at Ambient Conditions: Using Nb₂O₅ Nanofiber as a High-performance Electrocatalyst. *Nano Energy* **2018**, *52*, 264-270.
13. Chen, S.; Perathoner, S.; Ampelli, C.; Mebrahtu, C.; Su, D.; Centi, G., Electrocatalytic Synthesis of Ammonia at Room Temperature and Atmospheric Pressure from Water and Nitrogen on a Carbon-Nanotube-Based Electrocatalyst. *Angew. Chem. Int. Ed.* **2017**, *56* (10), 2699-2703.
14. Yao, J.-X.; Bao, D.; Zhang, Q.; Shi, M.-M.; Wang, Y.; Gao, R.; Yan, J.-M.; Jiang, Q., Tailoring Oxygen Vacancies of BiVO₄ toward Highly Efficient Noble-Metal-Free Electrocatalyst for Artificial N₂ Fixation under Ambient Conditions. *Small Methods* **2018**, 1800333.
15. Lv, C.; Yan, C.; Chen, G.; Ding, Y.; Sun, J.; Zhou, Y.; Yu, G., An Amorphous Noble-Metal-Free Electrocatalyst Enables N₂ Fixation under Ambient Conditions. *Angew. Chem. Int. Ed.* **2018**, *57* (21), 6073-6076.
16. McEnaney, J. M.; Singh, A. R.; Schwalbe, J. A.; Kibsgaard, J.; Lin, J. C.; Cargnello, M.; Jaramillo, T. F.; Nørskov, J. K., Ammonia Synthesis From N₂ and H₂O Using a Lithium Cycling Electrification Strategy at Atmospheric Pressure. *Energy Environ. Sci.* **2017**, *10* (7), 1621-1630.
17. Qiu, W.; Xie, X.-Y.; Qiu, J.; Fang, W.-H.; Liang, R.; Ren, X.; Ji, X.; Cui, G.; Asiri, A. M.; Cui, G.; Tang, B.; Sun, X., High-performance artificial nitrogen fixation at ambient conditions using a metal-free electrocatalyst. *Nat. Commun.* **2018**, *9* (1), 3485.
18. Chen, G. F.; Cao, X.; Wu, S.; Zeng, X.; Ding, L. X.; Zhu, M.; Wang, H., Ammonia Electrosynthesis with High Selectivity under Ambient Conditions via a Li⁽⁺⁾ Incorporation Strategy. *J. Am. Chem. Soc.* **2017**, *139* (29), 9771-9774.

Chapter 4: Electrochemical Nitrogen Reduction: Identification and Elimination of Contamination from Electrolyte

4.1 Introduction and Significance

Electrochemical nitrogen fixation so far is plagued with extremely low ammonia yield and selectivity. Even trace amount of contamination may cause substantial influence on the detected ammonia yield, so that it is always challenging to discern the contribution of contaminants to electrocatalytic ammonia yields. As a result, the NRR field is now at a stage where it is unclear which catalyst design can be identified to be efficient and active for NRR without careful and rigorous measurement and excluding all the contaminations. It is therefore of critical significance to identify and eliminate all of contamination that influence the NRR measurement.

In this chapter, the presence of trace amount of nitrate and nitrite in some commonly used commercial lithium salts was quantitatively identified, which delivered deceiving NRR data with excellent reproducibility and accumulative effect. The possible nitrate and nitrite contamination in the electrolyte can be efficaciously prejudged by simple spectrophotometric methods and can be effectively removed by high-temperature treatment. This study gives rise to substantial cautiousness on contamination from electrolytes and contribute to more accurate measurement of NRR and establishment of reliable NRR catalyst. The Highlights of this work include:

1. *Identification of contamination from electrolyte.* For the first time the presence of nitrate and nitrite in some commonly used lithium salts such as Li_2SO_4 and LiClO_4 was identified.
2. *Elimination of NO_x^- contamination from lithium salts.* Taking advantage of the different boiling points of nitrates, nitrites and other salts, high temperature treatment was applied to effectively remove NO_x^- contamination from lithium salts.

3. *Contribution to establish reliable electrolytes and catalysts for NRR.* Simple spectrophotometric methods could serve as versatile and efficacious methods to prejudge the NO_x^- contamination in electrolyte.

4.2 Electrochemical Nitrogen Reduction: Identification and Elimination of Contamination from Electrolyte

This chapter is included as it appears as a journal paper published by **Laiquan Li**, Cheng Tang, Dazhi Yao, Yao Zheng, Shi-Zhang Qiao.* Electrochemical Nitrogen Reduction: Identification and Elimination of Contamination in Electrolyte. *ACS Energy Letters* 2019, 4, 2111-2116.

Statement of Authorship

Title of Paper	Electrochemical Nitrogen Reduction: Identification and Elimination of Contamination in Electrolyte
Publication Status	<input checked="" type="checkbox"/> Published <input type="checkbox"/> Accepted for Publication <input type="checkbox"/> Submitted for Publication <input type="checkbox"/> Unpublished and Unsubmitted work written in manuscript style
Publication Details	Laiquan Li, Cheng Tang, Dazhi Yao, Yao Zheng, Shizhang Qiao. Electrochemical Nitrogen Reduction: Identification and Elimination of Contamination in Electrolyte. ACS Energy Lett. 2019, 4, 9, 2111–2116.

Principal Author

Name of Principal Author (Candidate)	Laiquan Li		
Contribution to the Paper	Research plan, electrochemical measurement, data analysis, and manuscript draft.		
Overall percentage (%)	90		
Certification:	This paper reports on original research I conducted during the period of my Higher Degree by Research candidature and is not subject to any obligations or contractual agreements with a third party that would constrain its inclusion in this thesis. I am the primary author of this paper.		
Signature		Date	29/07/2021

Co-Author Contributions

By signing the Statement of Authorship, each author certifies that:

- the candidate's stated contribution to the publication is accurate (as detailed above);
- permission is granted for the candidate to include the publication in the thesis; and
- the sum of all co-author contributions is equal to 100% less the candidate's stated contribution.

Name of Co-Author	Cheng Tang		
Contribution to the Paper	Discussion of research plan, Manuscript revision		
Signature		Date	29/07/2021

Name of Co-Author	Dazhi Yao		
Contribution to the Paper	Discussion of research plan		
Signature		Date	29/07/2021

Name of Co-Author	Yao Zheng		
Contribution to the Paper	Discussion of research plan and helped to evaluate the manuscript		
Signature		Date	29/07/2021

Name of Co-Author	Shi-Zhang Qiao		
Contribution to the Paper	Supervised development of work, helped in manuscript evaluation and acted as corresponding author		
Signature		Date	29/07/2021

Electrochemical Nitrogen Reduction: Identification and Elimination of Contamination in Electrolyte

Large-scale ammonia production is always one of the most critical issues in regard to human survival and sustainable development.^{1–5} Nowadays, ammonia is industrially manufactured by the century-old Haber–Bosch process, which produces more than 170 million tons of ammonia every year.⁶ Despite its wide application, it is a massively energy-consuming process that uses fossil fuels as the hydrogen source and accounts for ~1% of annual global greenhouse gas emission.⁷ The electrochemical ammonia synthesis via nitrogen reduction reaction (NRR) driven by renewable energy under mild conditions is a highly attractive alternative and has received intensive attention and exploration over the past few years.^{1,8–11} However, electrochemical N₂ fixation is still plagued with poor ammonia yield and faradaic efficiency due to the extremely low solubility of N₂ in aqueous electrolytes, the competing hydrogen evolution, as well as the sluggish kinetics.^{12,13} The amount of produced ammonia is usually as low as the nanomole level; therefore, it is challenging to accurately measure and unequivocally attribute it to electrochemical N₂ fixation, especially with the interference of various contamination.

Recently, discussion has arisen among researchers in this field regarding the need to improve how ammonia detection and control tests are conducted.^{14–22} To ensure that the detected ammonia is produced from dinitrogen rather than other extraneous contamination, the key task is to identify and exclude all of the contamination sources as specifically and thoroughly as possible. Several groups have recently investigated various contamination sources present in laboratory environments.^{11,15,16} We also proposed a set of rigorous experimental protocols to study electrochemical NRR with a thorough discussion of various experimental parameters.¹⁷ The contamination sources can be classified into two groups: *out-system* and *intrasystem*. The out-system contamination mainly includes ammonia or NO_x present in the air, human breath, and rubber gloves. As a closed system is mandatory for NRR tests,^{16,17} such out-system contamination can be rationally excluded with careful and rigorous operation and may not cause substantial influence. However, the intrasystem contamination, such as nitrogen-containing compounds in the feed gas, electrocatalysts, and membrane, is more indeterminate and even cannot be probed independently, thus usually resulting in a significant impact on the ammonia yield and even unreliable results. Without sufficient and rigorous control experiments, it would be unreliable to evaluate the NRR activity of electrocatalysts. Although many papers have been reported to identify and exclude various contamination, no work claims that the electrolyte solution may also be a considerable source of contamination.

Herein, we found that trace amounts of nitrate and nitrite exist in some lithium salts, for example, Li₂SO₄ and LiClO₄, which are usually used in the preparation of electrolyte. Significant ammonia production with excellent reproducibility and a cumulative effect was observed using a bare substrate (Ti foil, carbon paper, or copper foam) without loading any catalyst in both N₂- and Ar-saturated Li₂SO₄ solution. The detected ammonia was demonstrated to be electrochemically reduced from the trace amount of nitrate and nitrite in Li₂SO₄ rather than N₂, as schematically shown in Figure 1. Simple and

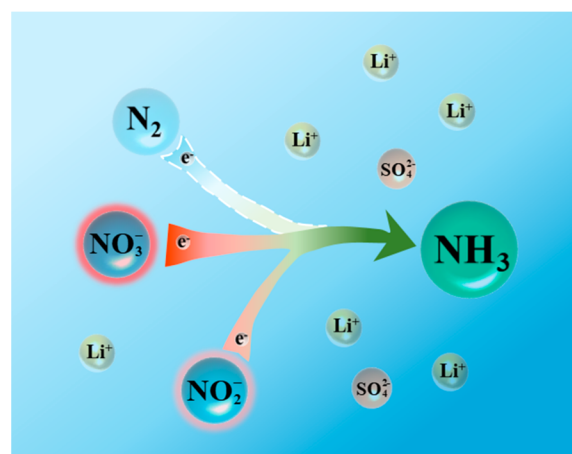


Figure 1. Schematic illustration showing the electrochemical conversion of various nitrogen-containing species in the Li₂SO₄ electrolyte. The nitrate and nitrite contamination in the electrolyte can be electrochemically reduced to ammonia, resulting in false positive N₂ reduction performance.

versatile spectrophotometric methods were employed to quantitatively determine such contamination, and an effective approach by high-temperature annealing was then proposed to eliminate nitrate and nitrite. This Viewpoint highlights several critical issues in regard to the identification and elimination of contamination in the electrolyte and will contribute to more accurate and reliable NRR research.

“Perfect” Data for NRR without Electrocatalysts. Due to the extremely low ammonia yield and influence of extraneous contamination in the laboratory, NRR study always suffers from fluctuation and variability when ammonia production is measured. As a result, it is usually very challenging to achieve ammonia yields with desirable reproducibility or a cumulative

Received: July 23, 2019

Accepted: August 2, 2019

Published: August 14, 2019

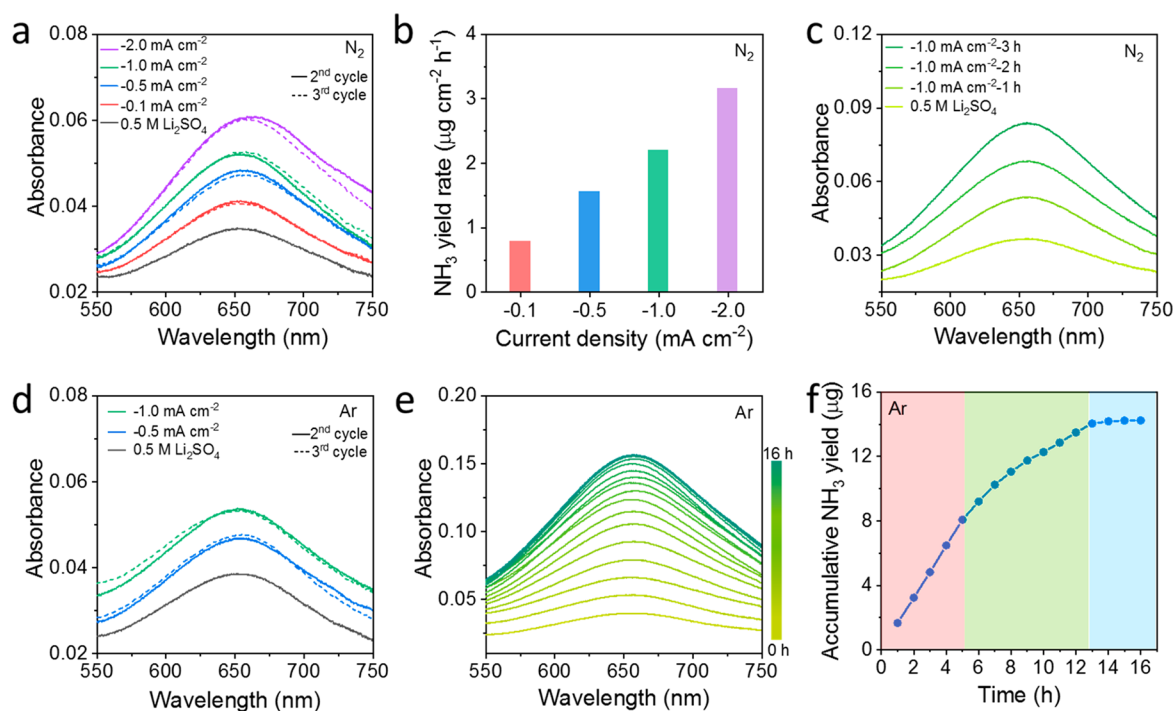


Figure 2. False positive NRR performance observed in both N_2 and Ar atmosphere using a bare Ti foil without loading any catalyst in a 0.5 M Li_2SO_4 solution. (a) UV-vis spectra for the indophenol blue indicator stained electrolytes after electrolysis at -0.1 , -0.5 , -1.0 , and -2.0 $mA\ cm^{-2}$ in N_2 for 1 h and (b) corresponding ammonia yield rates at each current density. (c) UV-vis spectra for the indophenol blue indicator stained electrolytes after electrolysis at -1.0 $mA\ cm^{-2}$ in N_2 for 1, 2, and 3 h. (d) UV-vis spectra for the indophenol blue indicator stained electrolytes after electrolysis at -0.5 and -1.0 $mA\ cm^{-2}$ in Ar for 1 h. (e) UV-vis spectra for the indophenol blue indicator stained electrolytes after electrolysis at -1.0 $mA\ cm^{-2}$ in Ar for 1–16 h and (f) corresponding accumulative ammonia yield. In (a) and (d), the solid lines exhibit the results for the second cycle, and the dashed lines show the results for the third cycle. In (a), (c), (d), and (e), the lowest line shows the result for the fresh electrolyte before electrolysis.

effect, especially in aqueous solutions. However, we observed excellent reproducibility and a cumulative effect only using a bare Ti foil in 0.5 M Li_2SO_4 electrolyte (Sigma-Aldrich, L6375, $\geq 98.5\%$). Initially, we conducted the NRR experiment by applying a fixed negative current density on a Ti foil ($1\ cm \times 1\ cm$) in N_2 atmosphere. For each current density, we repeated the NRR test three times with fresh Li_2SO_4 electrolyte and omitted the first cycle to exclude any possible preabsorbed ammonia contamination on the Ti foil. The produced ammonia was quantitatively determined by the indophenol blue method, in which the absorbance value at a wavelength of 655 nm for the indophenol blue indicator stained electrolyte is proportional to the ammonia concentration.²³ As shown in Figure 2a, the ammonia yields achieved for the second and the third cycles are almost the same on each applied current density, demonstrating excellent reproducibility. A considerable ammonia yield rate as high as $3.16\ \mu g\ cm^{-2}\ h^{-1}$ is obtained at a current density of $-2.0\ mA\ cm^{-2}$ (the ammonia calibration curve refers to Figure S1), which is comparable to and even higher than that of many reported electrocatalysts.^{16,17} It is noteworthy to mention that the ammonia yield rate increases with the applied current density (Figure 2b), indicating that the detected ammonia is electrochemically produced. Besides the excellent reproducibility, a good cumulative effect is also observed when different electrolysis periods are applied even though no catalyst is used. The concentration of the ammonia in the electrolyte increases linearly in the 3 h continuous electrolysis process (Figures 2c and S2). Such good reproducibility and a cumulative effect are very favorable indications of electrochemical NRR activity.

However, we finally realized that the ammonia was produced from contamination as a similar ammonia yield could also be observed in Ar atmosphere (Figure 2d), with as good reproducibility as that observed in the N_2 atmosphere. During long-term electrolysis in the Ar atmosphere, the good cumulative effect can also be observed within the initial 5 h, after which the ammonia increment decreases gradually and comes to a standstill after 13 h (Figure 2e,f). In addition, ammonia production can also be achieved using a bare carbon paper and copper foam in the same Li_2SO_4 electrolyte in an Ar atmosphere without using any catalyst (Figure S3). However, no ammonia yield can be observed using Ti foil in either 0.5 M Na_2SO_4 or K_2SO_4 electrolyte and in either N_2 or Ar atmosphere (Figure S4). Thus, the above results lead us to conclude that the detected ammonia is electrochemically synthesized but not derived from the electrocatalyst, electrode substrate, or inlet gas, which is most likely ascribed to the influence of electrolyte-dependent contamination.

Identification of Nitrate and Nitrite in the Electrolyte. Most of the extraneous ammonia contamination usually causes accidental positive results that are easy to be independently identified and rationally excluded by rigorous controls.^{14,15,17,18} However, NO_x in the feed gas or electrolyte can be electrochemically reduced to NH_3 and result in continuous production of ammonia.^{11,16} With the knowledge that the feed gases (N_2 and Ar) are of ultrahigh purity (99.999%), we focused our attention on the Li_2SO_4 electrolyte. It is thus assumed that the detected ammonia originates from the trace amount of the nitrogen-containing impurity in Li_2SO_4 , such as nitrate or nitrite. Therefore, we examined the presence of

NO_3^- and NO_2^- in Li_2SO_4 solution using spectrophotometric methods. Nitrate shows typical absorption to ultraviolet light at a wavelength of 220 nm,^{24,25} in which the absorbance value is in proportion to its concentration (Figure S5). As shown in Figure 3a,b, the presence of NO_3^- in Li_2SO_4 electrolyte is

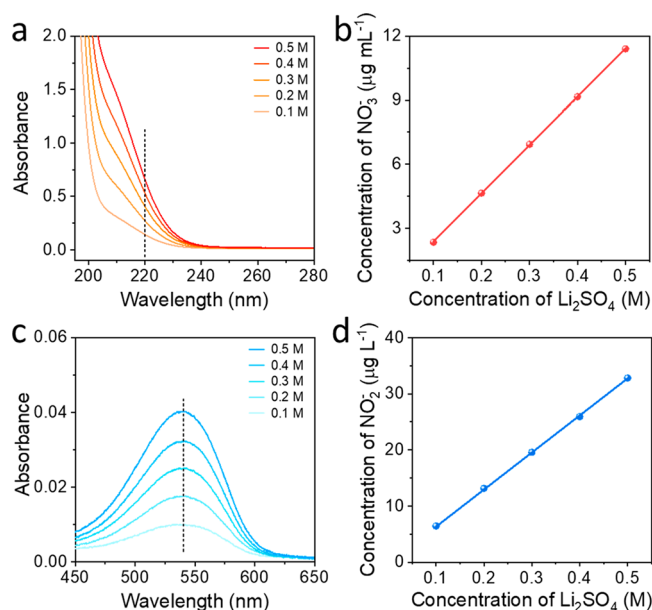


Figure 3. Quantitative detection of nitrate and nitrite in Li_2SO_4 solution. (a,c) UV-vis spectra for nitrate and nitrite determination. (b,d) Concentrations of detected nitrate and nitrite in different concentrations of Li_2SO_4 solutions.

identified as the absorbance value at 220 nm increases linearly with the concentration of Li_2SO_4 . The concentration of NO_3^- in 0.5 M Li_2SO_4 is measured to be as high as $11.19 \mu\text{g mL}^{-1}$ (Figure 3b). If all those nitrates were reduced to ammonia, the nitrate-derived NH_3 concentration would be up to $3.07 \mu\text{g mL}^{-1}$, which is much higher than those assigned to NRR reported so far ($< 1 \mu\text{g mL}^{-1}$).^{15,16} Moreover, when electrocatalysts with high activity toward nitrate reduction to ammonia were used in such nitrous electrolyte, false positive results and overestimation of the NRR activity would likely be delivered (Figure S3). The detection of NO_2^- is based on the Griess-Ilsovy reaction, in which nitrite reacts with two aromatic amines in sequence, producing pink azo dye that can be spectrophotometrically assayed by visible light at 540 nm (Figure S6).^{24,25} The presence of NO_2^- in Li_2SO_4 electrolyte is thus confirmed by the linear increase of the absorbance value at 540 nm with increasing Li_2SO_4 concentration (Figure 3c,d). The concentration of NO_2^- in 0.5 M Li_2SO_4 is determined to be $32.8 \mu\text{g L}^{-1}$, which is $\sim 0.3\%$ of the concentration of NO_3^- . Spectrophotometric tests also show that almost no NO_3^- exists in either 0.5 M Na_2SO_4 or K_2SO_4 solution (Figure S7), and only a very tiny amount of NO_2^- can be detected in K_2SO_4 . Given the high ammonia yield in 0.5 M Li_2SO_4 with undetectable ones in 0.5 M Na_2SO_4 and K_2SO_4 , we thus suppose that the produced ammonia stems from the electrochemical reduction of NO_x^- , especially NO_3^- in the Li_2SO_4 electrolyte, rather than N_2 .

Elimination of NO_x^- from Li_2SO_4 . It is known that metal sulfates usually possess much higher thermal stability than metal nitrates and nitrites. For example, Li_2SO_4 has a boiling point of 1377°C , much higher than that of LiNO_3 (600°C)

and LiNO_2 (350°C).²⁶ To eliminate the nitrate or nitrite from Li_2SO_4 and to further verify the origin of the detected ammonia, we annealed Li_2SO_4 in Ar atmosphere at 800°C for 4 h. The XRD pattern of the as-annealed Li_2SO_4 can be well assigned to monoclinic Li_2SO_4 (JCPDS No.: 20-0640) (Figure S8). We further tested the concentration of nitrate and nitrite in the annealed Li_2SO_4 using spectrophotometric methods. As shown in Figure 4a,b, both of the absorbance values at 220 nm

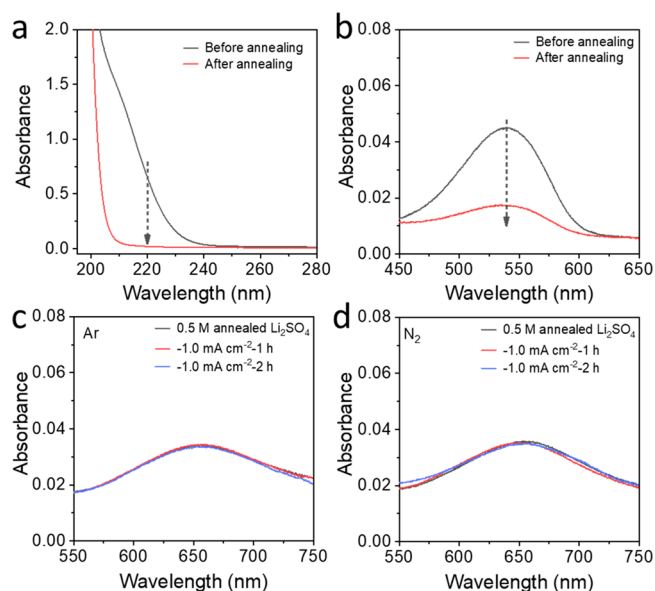


Figure 4. Elimination of nitrate and nitrite by high-temperature treatment. (a,b) UV-vis spectra for the determination of nitrate and nitrite in 0.5 M Li_2SO_4 before (gray lines) and after (red lines) annealing treatment. (c,d) UV-vis spectra for the 0.5 M annealed Li_2SO_4 electrolytes before (gray lines) and after (other lines) electrolysis with bare Ti foil at -1.0 mA cm^{-2} for 1 and 2 h in Ar and N_2 .

for NO_3^- and 540 nm for NO_2^- significantly decrease after annealing at high temperature. Furthermore, the concentrations of NO_3^- and NO_2^- do not change with the concentration of Li_2SO_4 after high-temperature annealing (Figures S9 and S10), indicating the successful elimination of nitrate and nitrite in Li_2SO_4 . The above results indicate that high-temperature treatment is highly effective for eliminating the nitrate and nitrite while keeping Li_2SO_4 unchanged. We further conducted electrolysis at a constant current density of -1.0 mA cm^{-2} in 0.5 M as-annealed Li_2SO_4 using Ti foil under otherwise identical conditions. No ammonia could be detected in either the Ar or N_2 atmosphere (Figure 4c,d). Notably, the Nafion membrane is not the ammonia source as it has not been replaced during all tests, including electrolysis in the pristine Li_2SO_4 , as-annealed Li_2SO_4 , Na_2SO_4 , and K_2SO_4 electrolytes. The above results on the one hand demonstrate that the Ti foil is inactive for NRR and on the other hand reveal that the feed gas is NO_x free. Therefore, we conclude that the detected ammonia is produced from the reduction of nitrate and nitrite in the pristine Li_2SO_4 .

Identification of NO_x^- Contamination in Various Lithium Salts. As Li_2SO_4 is a commonly used electrolyte in NRR, especially for investigation of the electrolyte effect on NRR performance, the trace amount of NO_x^- contamination may cause substantial interference for determining the activity of electrocatalysts and lead to unreliable conclusions. To probe

Table 1. Labeled NO_3^- Content in Various Lithium Salts and Detected NO_3^- Concentration in Their 0.5 M Solution

chemical	brand	product code	assay (%)	labeled NO_3^- content ^a	$[\text{NO}_3^-]$ in 0.5 M solution ($\mu\text{g mL}^{-1}$) ^b
$\text{Li}_2\text{SO}_4 \cdot \text{H}_2\text{O}$	Sigma-Aldrich	398152	≥ 99.0	$\leq 0.001\%$	–
$\text{Li}_2\text{SO}_4 \cdot \text{H}_2\text{O}$	Sigma-Aldrich	62612	≥ 99.0	$\leq 10 \text{ mg kg}^{-1}$	–
$\text{Li}_2\text{SO}_4 \cdot \text{H}_2\text{O}$	Sigma-Aldrich	62609	≥ 99.0	$\leq 10 \text{ mg kg}^{-1}$	–
Li_2SO_4	Sigma-Aldrich	203653	≥ 99.99	n.a. ^c	not detected
Li_2SO_4	Sigma-Aldrich	L6375	≥ 98.5	n.a.	11.19
Li_2SO_4	Sigma-Aldrich	62613	≥ 98.0	n.a.	1.02
Li_2SO_4	Alfa Aesar	13404	≥ 99.7	n.a.	2.82
Li_2SO_4	Aladdin	L130839	≥ 98.5	n.a.	not detected
LiClO_4	Sigma-Aldrich	431567	≥ 99.99	n.a.	1.39
LiClO_4	Sigma-Aldrich	205281	≥ 95.0	n.a.	2.38
Li_2CO_3	Sigma-Aldrich	431559	≥ 99.99	$\leq 5 \text{ mg kg}^{-1}$	–
Li_2CO_3	Sigma-Aldrich	62470	≥ 99.0	$\leq 5 \text{ mg kg}^{-1}$	–

^aThe content was read from the labels on the bottles of the chemicals. ^bThe concentration of NO_3^- in a 0.5 M solution of lithium salts was determined by the spectrophotometric method ^cn.a. means that no information about nitrate was available on the product specification label.

the universality of this issue, we measured the NO_x^- concentration in several Li_2SO_4 products with various brands and product codes (Table 1). The concentration of nitrate and nitrite is revealed to vary significantly among different Li_2SO_4 products (Figure 5a,b, Table 1, Figure S11). Most importantly,

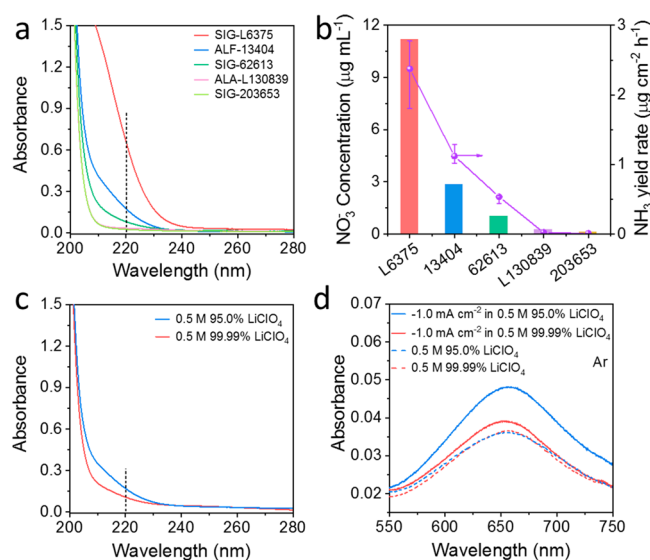


Figure 5. Identification of nitrate contamination in various lithium salts. (a) UV-vis spectra for determining nitrate and (b) relationship between the concentration of nitrate and the ammonia yield rate after electrolysis with bare Ti foil at -1.0 mA cm^{-2} in Ar for 1 h in 0.5 M Li_2SO_4 solutions with different brands and product codes (SIG: Sigma-Aldrich; ALF: Alfa Aesar; ALA: Aladdin). (c) UV-vis spectra for determining nitrate in different LiClO_4 solutions. (d) UV-vis spectra for indophenol blue indicator stained electrolytes before (dashed lines) and after (solid lines) electrolysis with bare Ti foil at -1.0 mA cm^{-2} in Ar for 1 h in different LiClO_4 solutions.

the ammonia yields achieved after electrolysis with bare Ti foil at -1.0 mA cm^{-2} in Ar for 1 h in different Li_2SO_4 electrolytes are positively correlated with the concentration of nitrate instead of nitrite (Figures 5b, S11), confirming that the false positive results are dominantly derived from the NO_3^- contamination. We realize that not all Li_2SO_4 chemicals contain nitrate or nitrite contamination because no obvious NO_3^- is detected in the fresh electrolyte and no ammonia yield

is achieved after electrolysis using some untreated Li_2SO_4 products (Sigma-Aldrich, 203653; Aladdin, L130839) (Figure 5b). The nitrate and nitrite in Li_2SO_4 most probably originate from lithium carbonate, which is the upstream product for most commercial lithium salts.²⁷ In fact, the lithium carbonate chemical (Sigma-Aldrich, 431559), even though with a high purity of 99.99%, is labeled with a NO_3^- content of 5 mg kg^{-1} . Generally, the lithium carbonate is industrially produced from either spodumene or continental brines.^{27,28} The spodumene route starts with a heating process at $1100 \text{ }^\circ\text{C}$ to transform α -spodumene to β -spodumene,²⁸ which could eliminate nitrate or nitrite for the downstream products. However, the production of lithium carbonate from brines, which contain trace amounts of nitrate and nitrite,²⁹ is generally realized by a series of evaporation, adsorption, solvent extraction, and membrane processes.^{28,30} As nitrate and nitrite are highly dissoluble in aqueous solutions, it is usually difficult to totally remove them in the industrial processes. As a result, all of the lithium sulfate monohydrates are labeled with a certain amount of nitrate (Table 1). Besides, other lithium salts that are produced from lithium carbonate may also contain a trace amount of NO_x^- contamination, such as LiClO_4 , another commonly used electrolyte in NRR. As shown in Figure 5c,d, nitrate is detected in 0.5 M LiClO_4 solutions with an assay of both 95.0% (Sigma-Aldrich, 205281) and 99.99% (Sigma-Aldrich, 431567). The nitrate-derived false positive ammonia yield is thus achieved for both cases and is more significant in the 95.0% LiClO_4 electrolyte due to its much higher content of NO_3^- contamination (Figure 5c,d).

In summary, we systematically identified, quantified, and eliminated the trace amount of nitrate and nitrite contamination in some commercial lithium salts toward more reliable electrocatalytic NRR study. Even though those impurities exist in ppm or lower levels, they could cause significant false positive results with deceptive reproducibility and a cumulative effect, which may misguide researchers. We experimentally demonstrated that the possible nitrate and nitrite contamination in the electrolyte can be efficaciously prejudged by simple spectrophotometric methods and can be effectively removed by high-temperature treatment. Although demonstrating false positive results for NRR, our study highlights several critical issues to which attention needs to be paid in order to develop both reliable electrocatalysts and electrolytes. First, we highlight that extra attention must be paid to the electrolyte in electrocatalytic NRR study, and the prejudgment

of NO_x^- in electrolyte is strongly recommended prior to NRR tests. Second, the electrolyte has been highly expected to play important roles in enhancing the NRR selectivity and activity by optimizing the solvent, concentration, pH value, cation, etc.^{31–35} However, the present results raise the demand for further investigation and even re-evaluation of the electrolyte effects on NRR performance, especially the reported improvement ascribed to Li^+ ions. Last but not least, we claim that understanding all of the negative results is just as important as identifying positive results, especially at the current stage of NRR research. We appeal to and encourage researchers to directly confront those “negative” results and thoroughly uncover the nature of potential interferences in this promising research area, which is believed to promote healthy development and reliable breakthrough in the electrochemical NRR field.

Laiquan Li^{1b}

Cheng Tang

Dazhi Yao

Yao Zheng^{1b}

Shi-Zhang Qiao^{*1b}

Center for Materials in Energy and Catalysis, School of Chemical Engineering and Advanced Materials, The University of Adelaide, Adelaide, South Australia 5005, Australia

■ ASSOCIATED CONTENT

📄 Supporting Information

The Supporting Information is available free of charge on the ACS Publications website at DOI: 10.1021/acseenergylett.9b01573.

Experimental details, material characterization, determination of ammonia, nitrate, and nitrite, and supplementary figures showing calibration curves, ammonia concentration with time, UV–vis spectra, XRD patterns and UV spectra (PDF)

■ AUTHOR INFORMATION

Corresponding Author

*E-mail: s.qiao@adelaide.edu.au.

ORCID^{1b}

Laiquan Li: 0000-0002-3301-9029

Yao Zheng: 0000-0002-2411-8041

Shi-Zhang Qiao: 0000-0002-4568-8422

Author Contributions

L.L. and C.T. contributed equally to this work.

Notes

Views expressed in this Viewpoint are those of the authors and not necessarily the views of the ACS.

The authors declare no competing financial interest.

■ ACKNOWLEDGMENTS

The work is financially supported by the Australian Research Council (ARC) through the Discovery and Linkage Project programs (FL170100154, DP160104866, LP160100927).

■ REFERENCES

(1) Chen, J. G.; Crooks, R. M.; Seefeldt, L. C.; Bren, K. L.; Bullock, R. M.; Darensbourg, M. Y.; Holland, P. L.; Hoffman, B.; Janik, M. J.; Jones, A. K.; Kanatzidis, M. G.; King, P.; Lancaster, K. M.; Lyman, S. V.; Pfomrom, P.; Schneider, W. F.; Schrock, R. R. Beyond Fossil Fuel-

driven Nitrogen Transformations. *Science* **2018**, *360* (6391), No. eaar6611.

(2) Nørskov, J.; Chen, J.; Miranda, R.; Fitzsimmons, T.; Stack, R. *Sustainable Ammonia Synthesis—Exploring the Scientific Challenges Associated with Discovering Alternative, Sustainable Processes for Ammonia Production*; US DOE Office of Science, 2016; <https://www.osti.gov/biblio/1283146/>.

(3) Smil, V. Detonator of the Population Explosion. *Nature* **1999**, *400* (6743), 415–415.

(4) Guo, J. P.; Chen, P. Catalyst: NH_3 as an Energy Carrier. *Chem* **2017**, *3* (5), 709–712.

(5) Fryzuk, M. D. Ammonia Transformed. *Nature* **2004**, *427*, 498–499.

(6) Soloveichik, G. Electrochemical Synthesis of Ammonia as a Potential Alternative to the Haber-Bosch Process. *Nat. Catal.* **2019**, *2* (5), 377–380.

(7) Ye, L.; Nayak-Luke, R.; Banares-Alcantara, R.; Tsang, E. Reaction: “Green” Ammonia Production. *Chem* **2017**, *3* (5), 712–714.

(8) Shipman, M. A.; Symes, M. D. Recent Progress towards the Electrosynthesis of Ammonia from Sustainable Resources. *Catal. Today* **2017**, *286*, 57–68.

(9) Guo, C.; Ran, J.; Vasileff, A.; Qiao, S.-Z. Rational Design of Electrocatalysts and Photo(electro) Catalysts for Nitrogen Reduction to Ammonia (NH_3) under Ambient Conditions. *Energy Environ. Sci.* **2018**, *11*, 45–56.

(10) Foster, S. L.; Bakovic, S. I. P.; Duda, R. D.; Maheshwari, S.; Milton, R. D.; Minter, S. D.; Janik, M. J.; Renner, J. N.; Greenlee, L. F. Catalysts for Nitrogen Reduction to Ammonia. *Nat. Catal.* **2018**, *1* (7), 490–500.

(11) Chen, G.-F.; Ren, S.; Zhang, L.; Cheng, H.; Luo, Y.; Zhu, K.; Ding, L.-X.; Wang, H. Advances in Electrocatalytic N_2 Reduction-Strategies to Tackle the Selectivity Challenge. *Small Methods* **2019**, *3* (6), 1800337.

(12) Montoya, J. H.; Tsai, C.; Vojvodic, A.; Nørskov, J. K. The Challenge of Electrochemical Ammonia Synthesis: A New Perspective on the Role of Nitrogen Scaling Relations. *ChemSusChem* **2015**, *8* (13), 2180–2186.

(13) Bratsch, S. G. Standard Electrode Potentials and Temperature Coefficients in Water at 298.15 K. *J. Phys. Chem. Ref. Data* **1989**, *18* (1), 1–21.

(14) MacLaughlin, C. Role for Standardization in Electrocatalytic Ammonia Synthesis: A Conversation with Leo Liu, Lauren Greenlee, and Douglas MacFarlane. *ACS Energy Lett.* **2019**, *4* (6), 1432–1436.

(15) Suryanto, B. H. R.; Du, H.-L.; Wang, D.; Chen, J.; Simonov, A. N.; MacFarlane, D. R. Challenges and Prospects in the Catalysis of Electroreduction of Nitrogen to Ammonia. *Nat. Catal.* **2019**, *2* (4), 290–296.

(16) Andersen, S. Z.; Čolić, V.; Yang, S.; Schwalbe, J. A.; Nielander, A. C.; McEnaney, J. M.; Enemark-Rasmussen, K.; Baker, J. G.; Singh, A. R.; Rohr, B. A.; Statt, M. J.; Blair, S. J.; Mezzavilla, S.; Kibsgaard, J.; Vesborg, P. C. K.; Cargnello, M.; Bent, S. F.; Jaramillo, T. F.; Stephens, I. E. L.; Nørskov, J. K.; Chorkendorff, I. A Rigorous Electrochemical Ammonia Synthesis Protocol with Quantitative Isotope Measurements. *Nature* **2019**, *570* (7762), 504–508.

(17) Tang, C.; Qiao, S.-Z. How to Explore Ambient Electrocatalytic Nitrogen Reduction Reliably and Insightfully. *Chem. Soc. Rev.* **2019**, *48* (12), 3166–3180.

(18) Greenlee, L. F.; Renner, J. N.; Foster, S. L. The Use of Controls for Consistent and Accurate Measurements of Electrocatalytic Ammonia Synthesis from Dinitrogen. *ACS Catal.* **2018**, *8* (9), 7820–7827.

(19) Minter, S. D.; Christopher, P.; Linic, S. Recent Developments in Nitrogen Reduction Catalysts: A Virtual Issue. *ACS Energy Lett.* **2019**, *4* (1), 163–166.

(20) Hu, B.; Hu, M.; Seefeldt, L.; Liu, T. L. Electrochemical Dinitrogen Reduction to Ammonia by Mo_2N : Catalysis or Decomposition? *ACS Energy Lett.* **2019**, *4* (5), 1053–1054.

- (21) Zhao, Y. X.; Shi, R.; Bian, X. A. N.; Zhou, C.; Zhao, Y. F.; Zhang, S.; Wu, F.; Waterhouse, G. I. N.; Wu, L. Z.; Tung, C. H.; Zhang, T. R. Ammonia Detection Methods in Photocatalytic and Electrocatalytic Experiments: How to Improve the Reliability of NH_3 Production Rates? *Adv. Sci.* **2019**, *6* (8), 1802109.
- (22) Tang, C.; Qiao, S.-Z. True or False in Electrochemical Nitrogen Reduction. *Joule* **2019**, *3* (7), 1573–1575.
- (23) Li, L.; Tang, C.; Xia, B.; Jin, H.; Zheng, Y.; Qiao, S.-Z. Two-Dimensional Mosaic Bismuth Nanosheets for Highly Selective Ambient Electrocatalytic Nitrogen Reduction. *ACS Catal.* **2019**, *9* (4), 2902–2908.
- (24) Carvalho, A. P.; Meireles, L. A.; Malcata, F. X. Rapid Spectrophotometric Determination of Nitrates and Nitrites in Marine Aqueous Culture Media. *Analisis* **1998**, *26* (9), 347–351.
- (25) Polatides, C.; Kyriacou, G. Electrochemical Reduction of Nitrate Ion on Various Cathodes-Reaction Kinetics on Bronze Cathode. *J. Appl. Electrochem.* **2005**, *35* (5), 421–427.
- (26) Stern, K. H. High Temperature Properties and Decomposition of Inorganic Salts Part 3, Nitrates and Nitrites. *J. Phys. Chem. Ref. Data* **1972**, *1* (3), 747–772.
- (27) Wietelmann, U.; Steinbild, M. Lithium and Lithium Compounds. *Ullmann's Encyclopedia of Industrial Chemistry* **2014**, 1–38.
- (28) Talens Peiro, L.; Villalba Mendez, G.; Ayres, R. U. Lithium: Sources, Production, Uses, and Recovery Outlook. *JOM* **2013**, *65* (8), 986–996.
- (29) *Analysis of Anions in Geological Brines Using Ion Chromatography*; Sandia National Laboratories: Albuquerque, NM, 1985.
- (30) Kumar, A.; Fukuda, H.; Hatton, T. A.; Lienhard, J. H. Lithium Recovery from Oil and Gas Produced Water: A Need for a Growing Energy Industry. *ACS Energy Lett.* **2019**, *4* (6), 1471–1474.
- (31) Wang, J.; Yu, L.; Hu, L.; Chen, G.; Xin, H.; Feng, X. Ambient Ammonia Synthesis via Palladium-catalyzed Electrohydrogenation of Dinitrogen at Low Overpotential. *Nat. Commun.* **2018**, *9* (1), 1795.
- (32) Mukherjee, S.; Cullen, D. A.; Karakalos, S.; Liu, K.; Zhang, H.; Zhao, S.; Xu, H.; More, K. L.; Wang, G.; Wu, G. Metal-organic Framework-derived Nitrogen-doped Highly Disordered Carbon for Electrochemical Ammonia Synthesis using N_2 and H_2O in Alkaline Electrolytes. *Nano Energy* **2018**, *48*, 217–226.
- (33) Song, Y.; Johnson, D.; Peng, R.; Hensley, D. K.; Bonnesen, P. V.; Liang, L.; Huang, J.; Yang, F.; Zhang, F.; Qiao, R.; Baddorf, A. P.; Tschaplinski, T. J.; Engle, N. L.; Hatzell, M. C.; Wu, Z.; Cullen, D. A.; Meyer, H. M.; Sumpter, B. G.; Rondinone, A. J. A Physical Catalyst for the Electrolysis of Nitrogen to Ammonia. *Sci. Adv.* **2018**, *4* (4), No. e1700336.
- (34) Chen, G. F.; Cao, X.; Wu, S.; Zeng, X.; Ding, L. X.; Zhu, M.; Wang, H. Ammonia Electrosynthesis with High Selectivity under Ambient Conditions via a Li^+ Incorporation Strategy. *J. Am. Chem. Soc.* **2017**, *139* (29), 9771–9774.
- (35) Zhou, F.; Azofra, L. M.; Ali, M.; Kar, M.; Simonov, A. N.; McDonnell-Worth, C.; Sun, C.; Zhang, X.; MacFarlane, D. R. Electro-synthesis of Ammonia from Nitrogen at Ambient Temperature and Pressure in Ionic Liquids. *Energy Environ. Sci.* **2017**, *10*, 2516–2520.

Supporting information for

Electrochemical Nitrogen Reduction: Identification and Elimination of Contamination in Electrolyte

*Laiquan Li, Cheng Tang, Dazhi Yao, Yao Zheng, Shi-Zhang Qiao**

Center for Materials in Energy and Catalysis, School of Chemical Engineering and Advanced
Materials, The University of Adelaide, Adelaide, South Australia 5005, Australia

Corresponding Author

*Email: s.qiao@adelaide.edu.au (S.-Z.Q.)

Experiment Details

Materials

Li₂SO₄ (Alfa Aesar, 13404, ≥99.7%), Li₂SO₄ (Sigma Aldrich, L6375, ≥98.5%), Li₂SO₄ (Sigma Aldrich, 203653, ≥99.99%), Li₂SO₄ (Sigma Aldrich, 62613, purum, ≥98.0%), Li₂SO₄ (Aladdin, L130839, ≥98.5%), LiClO₄ (Sigma Aldrich, 431567, ≥99.99%), LiClO₄ (Sigma Aldrich, 205281, ≥95.0%), salicylic acid (Sigma Aldrich, 84210, ≥99.0%), NH₄Cl (Sigma Aldrich, 254134, 99.998%), potassium sodium tartrate (NaKC₄H₄O₆·4H₂O, Sigma Aldrich, V800336, ≥99%), sodium nitroferrocyanide (C₅FeN₆Na₂O, Sigma Aldrich, 71778, ≥99%), sodium hypochlorite (Sigma Aldrich, 425004, available chlorine 10-15%), para-(dimethylamino) benzaldehyde (Sigma Aldrich, 156477, ≥99%), N-(1-Naphthyl)ethylenediamine dihydrochloride (Sigma Aldrich, 222488, >98%), sulfanilamide (Sigma Aldrich, S9251, ≥99%), sodium nitrite (Sigma Aldrich, 237213, ≥97%), potassium sulfate (Sigma Aldrich, P9458, ≥99.0%), sodium sulfate (Chem-supply, SA007, ≥99%) were used in this study. Nafion 211 membrane (Dupont) was purchased from Fuelcell store. Ultrapure water used throughout all experiments was purified through an Adelab Millipore system. Ultra high purity N₂ (99.999%) and Ar (99.999%) were purchase from BOC Gas, Australia.

Material characterization

XRD data were collected on a D4 endeavour (Bruker) X-ray diffraction system with Co K_α radiation. The absorbance data of spectrophotometer were collected on SHIMADZU UV-2600 ultraviolet-visible (UV-Vis) spectrophotometer.

Annealing treatment of Li₂SO₄

A certain amount of Li₂SO₄ was placed in a tube furnace, which was then heated up to 800°C under Ar atmosphere. After maintaining for 4 h, the tube furnace was naturally cooled down to room temperature.

Electrochemical measurements

Electrochemical data were collected with a CHI 760e electrochemical workstation (CHI Instruments, Inc.). Three-electrode system was used in the electrochemical measurement in which a Ag/AgCl electrode was used as the reference electrode, and a graphite rod as the counter electrode. Ti foil was polished using abrasive paper and then soaked in 0.1 M HCl. After rinsing with ethanol and deionized water, the Ti foil was directly used as a working electrode. Pre-treatment of Cu Foam was the same as the Ti foil without polish process. The Nafion 211 membrane was preconditioned by boiling in 5% H₂O₂ solution and deionized water

at 80°C for 1 h, respectively, followed by treatment in 0.05 M H₂SO₄ at 80°C for 3 h and deionized water at 80°C for another 1 h. The NRR test was conducted in a H-Cell with 30 mL of electrolyte in the anode and cathode chamber, respectively. The gas flow rate was fixed at 20 sccm throughout the whole electrolysis process. A PTFE coated stirrer bar with a rotation rate of 550 rpm was placed in the cathode chamber to enhance the mass diffusion.

Determination of ammonia

The produced ammonia was quantitatively determined by indophenol blue method. Briefly, 5.0 g of sodium salicylate and 5.0 g of potassium sodium tartrate were dissolved in 100.0 mL of 1.0 M NaOH to prepare the chromogenic reagent (reagent A). 3.50 mL of sodium hypochlorite (available chlorine 10-15 %) was added into deionized water and diluted to 100.0 mL to prepare the oxidizing reagent (reagent B). 0.20 g of sodium nitroferricyanide was dissolved in 20.0 mL of deionized water to obtain the catalysing reagent (reagent C). To quantitatively determine the amount of ammonia, 2.0 mL of sample solution was added to a test tube, to which 2.0 mL of reagent A, 1.0 mL of reagent B and 0.20 mL of reagent C were successively added. After mixing up and standing for 1 h, the absorption spectra were collected on UV-vis spectrophotometer using a standard 1 cm quartz cuvette. The concentration-dependent absorption spectra were calibrated using standard ammonia chloride solutions with different known concentrations.

Colorimetric detection of NO₃⁻

NO₃⁻ standard solution preparation (μg mL⁻¹ corresponds to the concentration of NO₃⁻)

- 1) 100.0 μg mL⁻¹ stock: 0.1112 g of pre-dried LiNO₃ was added into 1.0 L of deionized water.
- 2) 5.0 μg mL⁻¹ stock: 5.0 mL of the above 100 μg mL⁻¹ stock was added in a 100.0 mL volumetric flask, and add deionized water to the scale mark.
- 3) 0.1, 0.2, 0.5, 1.0, 1.5, 2.0, 2.5, 3.0, 4.0 and 5.0 mL of 5.0 μg mL⁻¹ stock solution were separately added into the test tube, to which the deionized water was then added to make up to 5.0 mL, 0.1, 0.2, 0.5, 1.0, 1.5, 2.0, 2.5, 3.0, 4.0 and 5.0 μg mL⁻¹ standard solutions were finally obtained.

UV-vis spectrophotometer measurement

Nitrates show typical absorption to ultraviolet light at the wavelength of 220 nm, in which the absorbance value is in proportion to the concentration of nitrates. Therefore, the content of the NO₃⁻ in Li₂SO₄ solution can be quantitatively determined. In a typical procedure, 5.0 mL of standard or sample solutions were added to the test tubes followed by addition of 0.10 mL of

1.0 M HCl. After shaking up and standing for 5 min, the concentration of NO_3^- was measured using UV-vis spectrophotometer at wavelength range from 200 nm to 300 nm. The standard curve NO_3^- determination was then plotted with the absorbance value difference at 220 nm and 275 nm as y axis and the concentration of NO_3^- as x axis.

Colorimetric detection of NO_2^-

NO_2^- standard solution preparation ($\mu\text{g mL}^{-1}$ corresponds to the concentration of NO_2^-)

- 1) $100.0 \mu\text{g mL}^{-1}$ stock: 0.15 g of pre-dried NaNO_2 was dissolved in 1.0 L Deionized water.
- 2) $1.0 \mu\text{g mL}^{-1}$ stock: 1.0 mL of $100.0 \mu\text{g mL}^{-1}$ stock was added into in a 100.0 mL volumetric flask and add deionized water to the scale mark.
- 3) $0.1 \mu\text{g mL}^{-1}$ stock: 2.0 mL of $1.0 \mu\text{g mL}^{-1}$ stock was added into a 20.0 mL volumetric flask, followed by adding deionized water to the scale mark.
- 4) 0.1, 0.2, 0.5, 1.0, 2.0, 3.0, 4.0 and 5.0 mL of $\mu\text{g mL}^{-1}$ stock were added into the test tube, then deionized water was added into the test tube to make up to 5.0 mL to obtain 2, 4, 10, 20, 40, 60, 80 and $100 \mu\text{g L}^{-1}$ standard solutions.

Chromogenic reagent preparation

0.50 g of sulfanilamide was dissolved in 50.0 mL of 2.0 M HCl solution to prepare sulfanilamide solution (reagent A). 20.0 mg of N-(1-Naphthyl) ethylenediamine dihydrochloride was dissolved in 20.0 mL of deionized water to prepare N-(1-Naphthyl) ethylenediamine dihydrochloride solution (reagent B).

UV-vis spectrophotometer measurement:

Nitrites can be diazotized by sulfanilamide under acid environment, and the diazotized compound can be coupled with N-(1-Naphthyl) ethylenediamine dihydrochloride, producing pink azo dyes which show typical absorption at wavelength of 540 nm. Therefore, the content of the nitrite in Li_2SO_4 solution can be quantitatively determined using this method. In a typical procedure, 5.0 mL of standard or sample solutions were added to the test tubes, followed by addition of 0.10 mL of reagent A. After mixing up and standing for 10 min, 0.10 mL of reagent B was added to the above solution. The solution was then shaken up and allowed to stand for 30 min, and the concentration of NO_2^- was measured using UV-vis spectrophotometer at wavelength range from 450 nm to 650 nm. The standard curve for NO_2^- determination was then plotted with the absorbance value difference at 540 nm and 650 nm as y axis and the concentration of NO_2^- as x axis.

Supplementary Figures

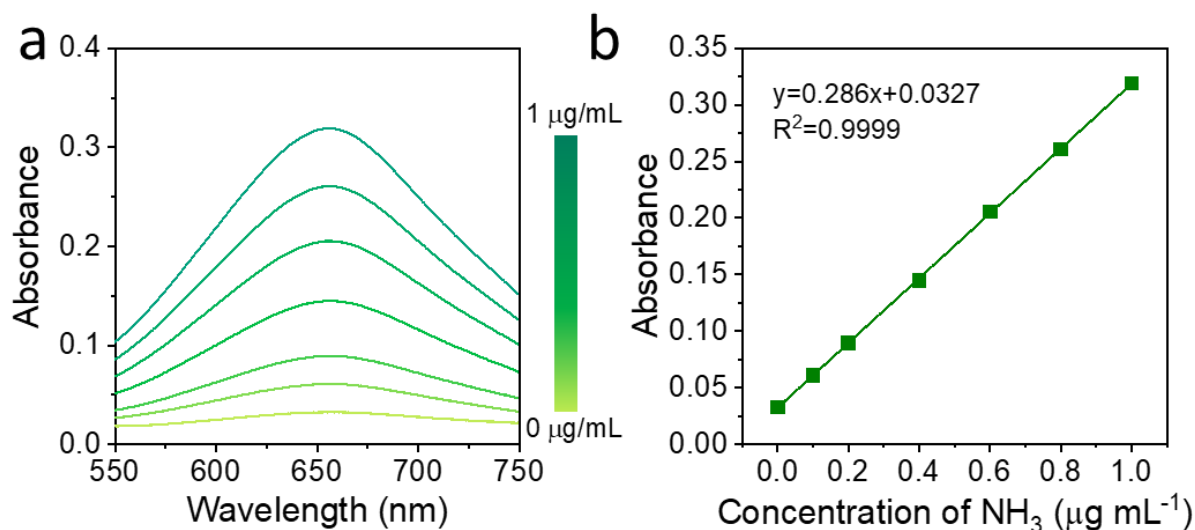


Figure S1. Calibration curve of NH₃ in 0.5 M Li₂SO₄ using ammonia chloride solutions with known concentration as standards. (a) UV-vis spectra of indophenol indicator stained 0.5 M Li₂SO₄ with various known NH₃ concentration after incubated for 1 h and (b) calibration curve used for the determination of NH₃ concentration. The absorbance values at 655 nm were measured by UV-vis spectrophotometer, and the fitting curve shows good linear relation of absorbance with NH₃ concentration ($y = 0.286x + 0.0327$).

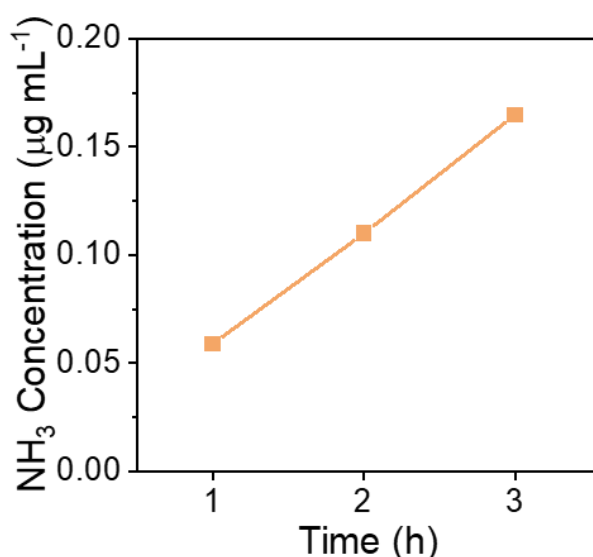


Figure S2. Ammonia concentration in 0.5 M Li₂SO₄ solution after electrolysis process using bare Ti foil at -1.0 mA cm^{-2} in N₂ atmosphere for 1, 2 and 3 h showing the linear increase of ammonia concentration with increasing electrolysis duration.

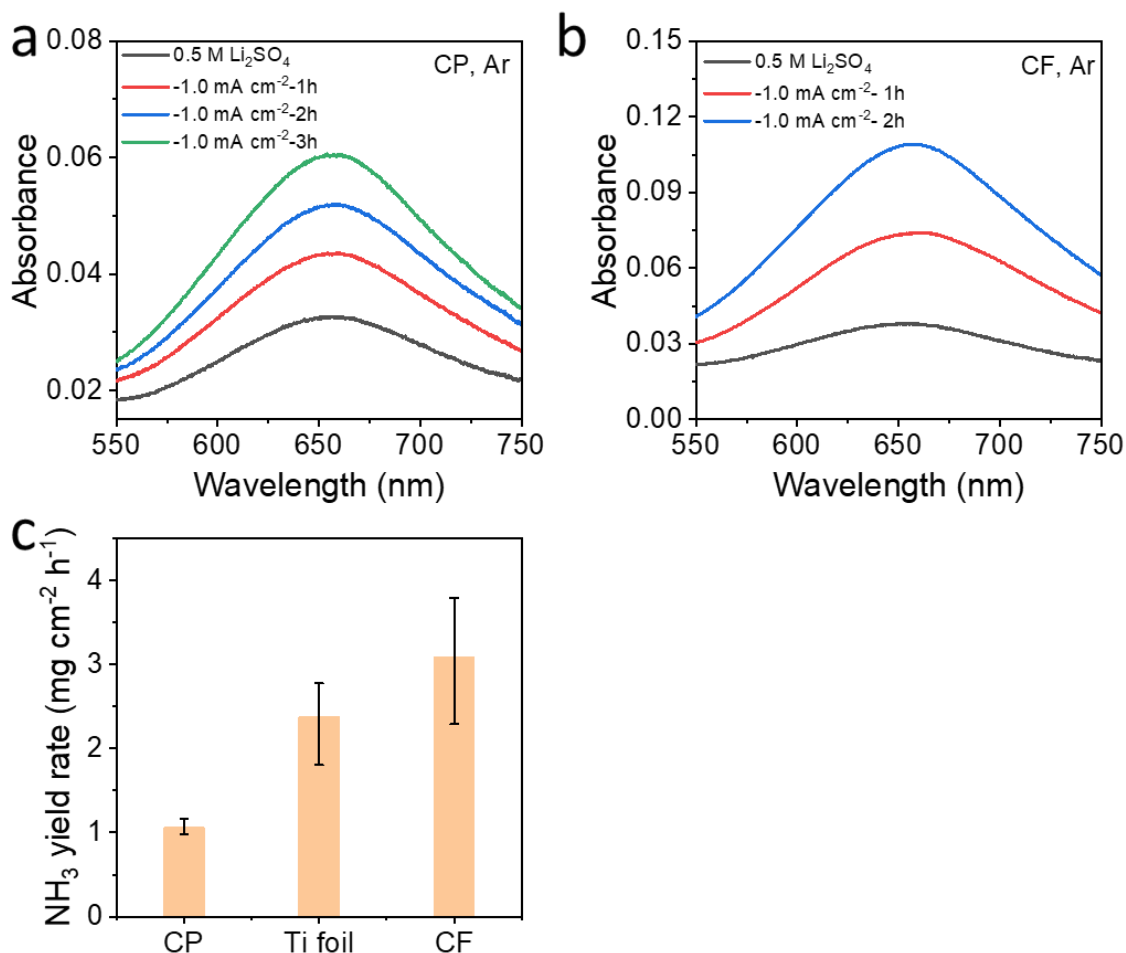


Figure S3. UV-vis spectra for the electrolytes stained with indophenol blue indicator after electrolysis on (a) carbon paper (CP) and (b) Cu foam (CF) in Ar at -1.0 mA cm^{-2} for various durations. (c) Average ammonia yield rates for CP, Ti foil and CF in Ar at -1.0 mA cm^{-2} .

Note: The ammonia production varies among different substrates due to their various abilities towards NO_3^- reduction. Remarkably, a high average ammonia yield rate up to $3.09 \mu\text{g cm}^{-2} \text{ h}^{-1}$ can be obtained in Ar atmosphere at -1.0 mA cm^{-2} when using Cu foam, a substrate with high activity towards NO_3^- reduction to ammonia.^{S1} Therefore, if electrocatalysts with high activity towards NO_3^- reduction to ammonia were used in nitrous electrolyte, false positive results or overestimation of the activity of the studied catalyst would be obtained. When comparing the NRR activities between the designed electrocatalysts and control samples, their different activities towards NO_3^- reduction to ammonia may cause deceptive illusion that the designed electrocatalysts is more favorable to NRR than the control samples, resulting in unreliable conclusion and thus misleading the catalyst design.

[S1] Polatides, C.; Kyriacou, G. Electrochemical Reduction of Nitrate Ion on Various Cathodes-Reaction Kinetics on Bronze Cathode. *J. Appl. Electrochem.* **2005**, *35* (5), 421-427.

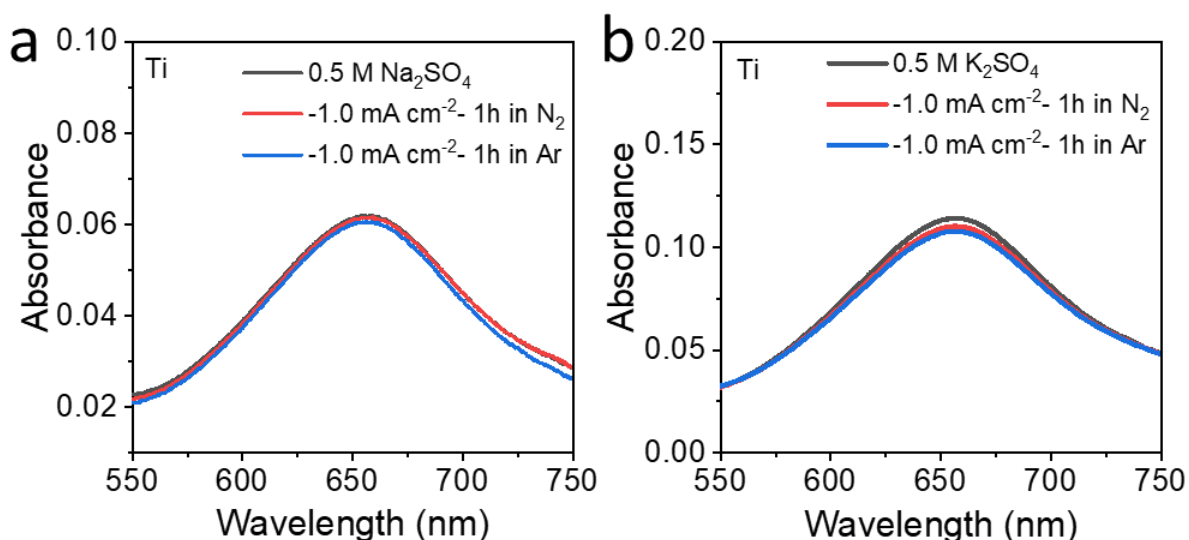


Figure S4. UV-vis spectra of the electrolyte stained with indophenol blue indicator before (grey lines) and after (other lines) electrolysis with bare Ti foil at -1.0 mA cm^{-2} in (a) $0.5 \text{ M Na}_2\text{SO}_4$ and (b) $0.5 \text{ M K}_2\text{SO}_4$ in Ar and N_2 atmosphere for 1 h.

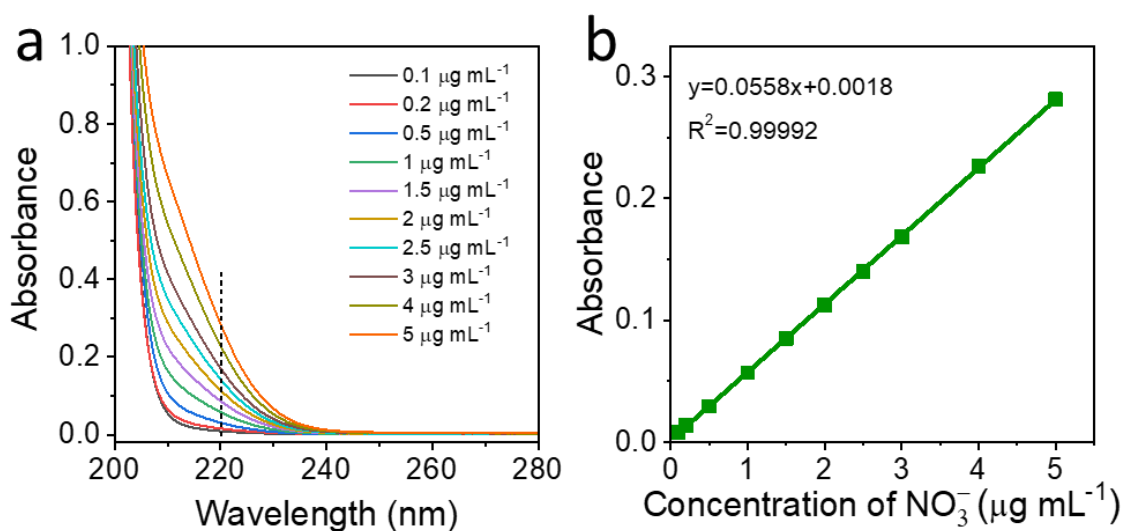


Figure S5. Calibration for nitrate determination. (a) UV-vis spectra for various concentrations of LiNO_3 . (b) Calibration curve used for calculating the concentration of nitrate.

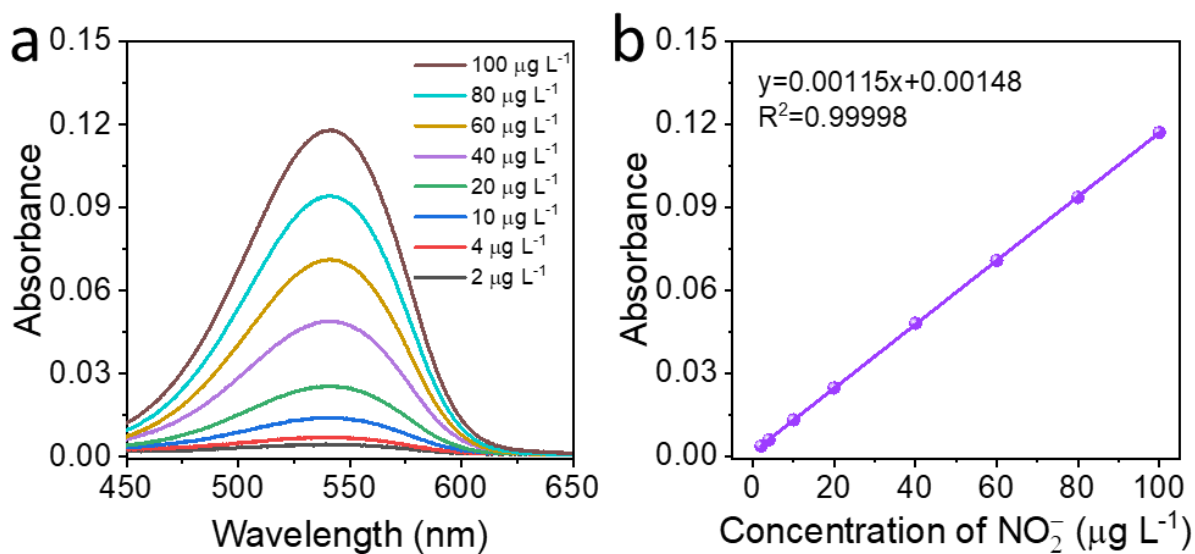


Figure S6. Calibration for nitrite determination. (a) UV-vis spectra for various concentrations of NaNO_2 . (b) Calibration curve used for calculating the concentration of nitrite.

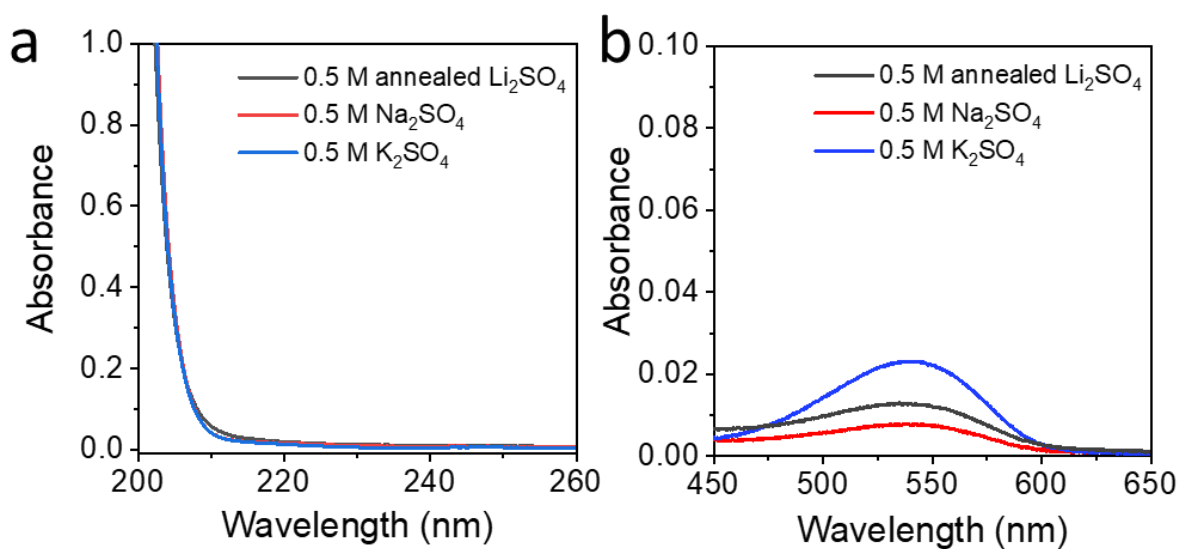


Figure S7. UV-vis spectra for determining the (a) NO_3^- and (b) NO_2^- concentration in 0.5 M Na_2SO_4 and K_2SO_4 , comparing with those in 0.5 M annealed Li_2SO_4 .

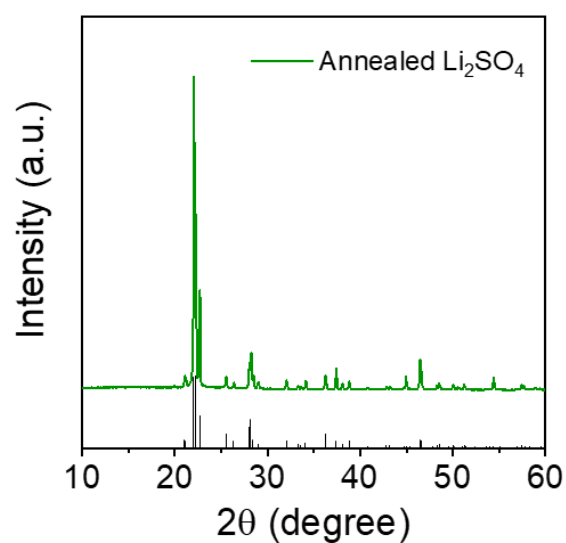


Figure S8. XRD pattern of Li_2SO_4 after annealing at 800°C for 4 h.

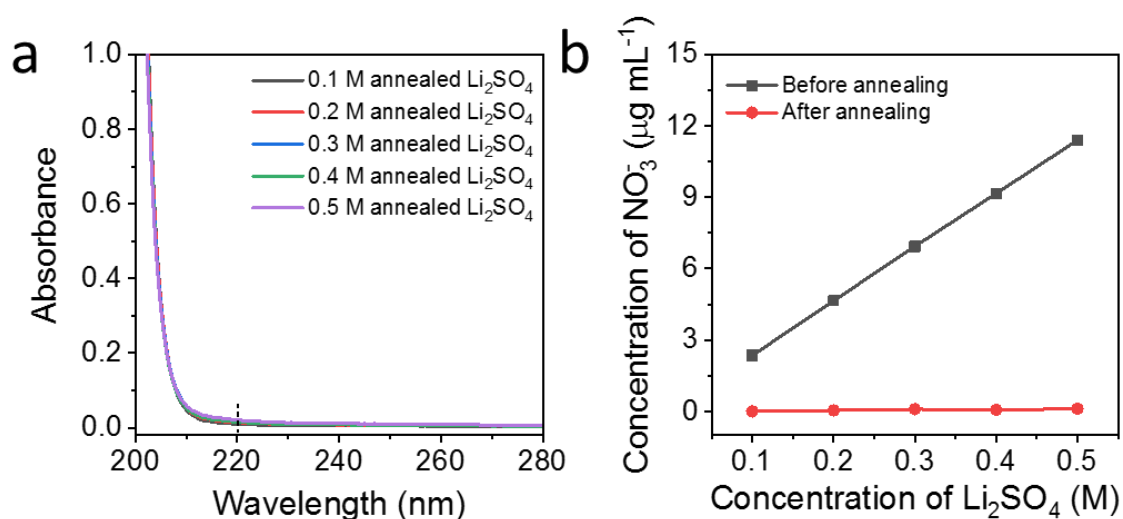


Figure S9. (a) UV spectra for determining the concentration of NO_3^- in annealed Li_2SO_4 . (b) The concentration of NO_3^- in various concentrations of Li_2SO_4 before and after annealing treatment.

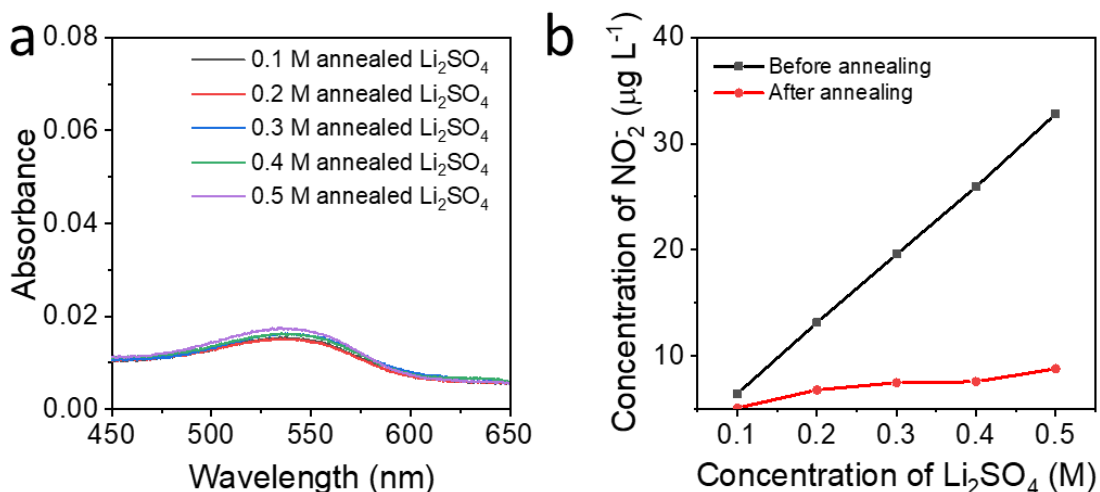


Figure S10. (a) UV-vis spectra for determining the concentration of NO_2^- in annealed Li_2SO_4 . (b) The concentration of NO_2^- in various concentrations of Li_2SO_4 before and after annealing treatment.

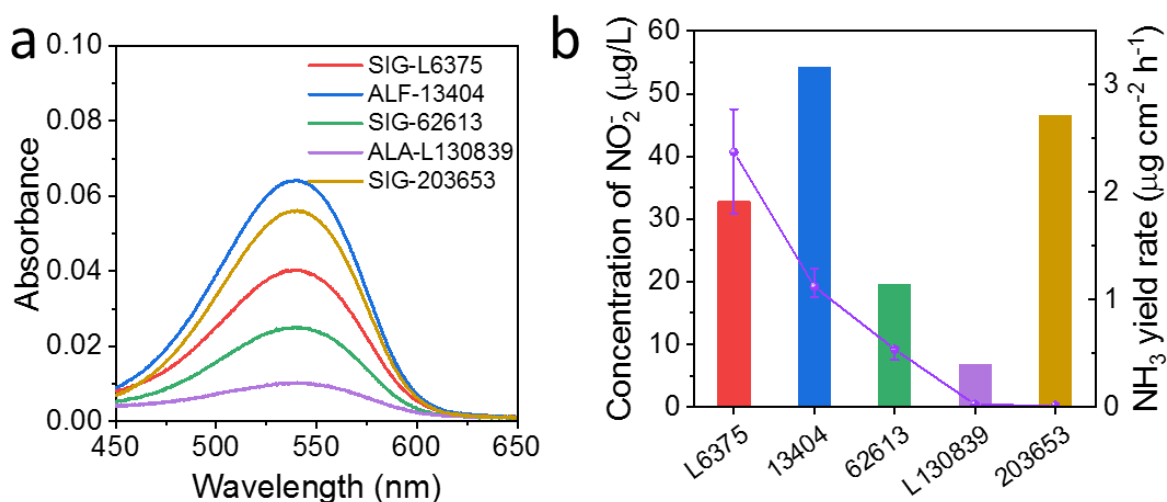


Figure S11. (a) UV-vis spectra for determining NO_2^- and (b) the corresponding nitrite concentrations as well as the ammonia yield rate after electrolysis with bare Ti foil at -1.0 mA cm^{-2} in Ar for 1 h in $0.5 \text{ M Li}_2\text{SO}_4$ solutions with different brands and product codes.

Chapter 5: Efficient Nitrogen Fixation to Ammonia through Integration of Plasma Oxidation with Electrocatalytic Reduction

5.1 Introduction and Significance

Global demand for nitrates and ammonia for use as fertilizers and industrial feedstocks continues to steadily increase. Transformation of atmospheric nitrogen to ammonia is a long-sought goal for human beings. However, one-step conversion through either a conventional Haber-Bosch process, or recently developed NRR process, suffers from drawbacks of a high energy consumption for activation of inert N_2 and low selectivity toward NH_3 product.

In this Chapter, the N_2 -to- NH_3 conversion was decoupled to a two-step process with one problem solved independently and effectively in each step, including: 1) facile activation of N_2 to NO_x^- by non-thermal plasma, and; 2) highly selective conversion of NO_x^- to NH_3 via electrocatalytic reduction. To achieve high selectivity of NO_x^- reduction to NH_3 (e NO_x RR), a surface boron-rich core-shell nickel boride nanoparticle ($Ni_3B@NiB_{2.74}$) was developed as an electrocatalyst. The surface B-rich feature was evidenced to boost activity, selectivity, and stability for e NO_x RR on Ni-based catalysts. The highlights of this work include:

1. *New two-step strategy for efficient N_2 activation and selective fixation to NH_3 .* Integration of plasma driven N_2 oxidation with electrocatalytic nitrate/nitrite reduction produced ammonia directly from air with an ammonia yield $\sim 2,500$ times higher than that for NRR process;
2. *High activity and selectivity for nitrate reduction to NH_3 .* Superior nitrate reduction performance was achieved on $Ni_3B@NiB_{2.74}$ with a significant ammonia yield of $198.3 \mu\text{mol h}^{-1} \text{cm}^{-2}$ with Faradaic efficiency of nearly 100% at -0.3 V vs RHE ;
3. *Critical role of surface-enriched B sites.* The electron-deficient B sites could not only serve as Lewis acid sites to enhance NO_x^- adsorption, but also suppress surface oxidation of Ni^0 sites and prevent overactive hydrogen evolution.

5.2 Efficient Nitrogen Fixation to Ammonia through Integration of Plasma Oxidation with Electrocatalytic Reduction.

This chapter is included as it appears as a journal paper published by **Laiquan Li**, Cheng Tang, Xiaoyang Cui, Yao Zheng, Xuesi Wang, Haolan Xu, Shuai Zhang, Tao Shao, Kenneth Davey, Shizhang Qiao.* Efficient Nitrogen Fixation to Ammonia through Integration of Plasma Oxidation with Electrocatalytic Reduction. *Angewandte Chemie* 2021, *60*, 14131-14137.

Statement of Authorship

Title of Paper	Efficient Nitrogen Fixation to Ammonia through Integration of Plasma Oxidation with Electrocatalytic Reduction
Publication Status	<input checked="" type="checkbox"/> Published <input type="checkbox"/> Accepted for Publication <input type="checkbox"/> Submitted for Publication <input type="checkbox"/> Unpublished and Unsubmitted work written in manuscript style
Publication Details	Laiquan Li, Cheng Tang, Xiaoyang Cui, Yao Zheng, Xuesi Wang, Haolan Xu, Shuai Zhang, Tao Shao, Kenneth Davey, Shizhang Qiao. Efficient Nitrogen Fixation to Ammonia through Integration of Plasma Oxidation with Electrocatalytic Reduction. Angewandte Chemie, 2021,60,14131-14137.

Principal Author

Name of Principal Author (Candidate)	Laiquan Li			
Contribution to the Paper	Research plan, materials synthesis, most of the physical characterization, electrochemical measurement, data analysis, and manuscript draft.			
Overall percentage (%)	70			
Certification:	This paper reports on original research I conducted during the period of my Higher Degree by Research candidature and is not subject to any obligations or contractual agreements with a third party that would constrain its inclusion in this thesis. I am the primary author of this paper.			
Signature	<table border="1" style="width: 100%;"> <tr> <td style="width: 60%;"></td> <td style="width: 20%;">Date</td> <td style="width: 20%;">29/07/2021</td> </tr> </table>		Date	29/07/2021
	Date	29/07/2021		

Co-Author Contributions

By signing the Statement of Authorship, each author certifies that:

- i. the candidate's stated contribution to the publication is accurate (as detailed above);
- ii. permission is granted for the candidate to include the publication in the thesis; and
- iii. the sum of all co-author contributions is equal to 100% less the candidate's stated contribution.

Name of Co-Author	Cheng Tang			
Contribution to the Paper	Discussion of research plan, Manuscript revision			
Signature	<table border="1" style="width: 100%;"> <tr> <td style="width: 60%;"></td> <td style="width: 20%;">Date</td> <td style="width: 20%;">29/07/2021</td> </tr> </table>		Date	29/07/2021
	Date	29/07/2021		

Name of Co-Author	Xiaoyang Cui			
Contribution to the Paper	Plasma experiment			
Signature	<table border="1" style="width: 100%;"> <tr> <td style="width: 60%;"></td> <td style="width: 20%;">Date</td> <td style="width: 20%;">29/07/2021</td> </tr> </table>		Date	29/07/2021
	Date	29/07/2021		

Name of Co-Author	Yao Zheng		
Contribution to the Paper	Supervised the development of the work, helped to evaluate and edit the manuscript		
Signature		Date	29/07/2021

Name of Co-Author	Xuesi Wang		
Contribution to the Paper	Helped with In-situ Raman measurement.		
Signature		Date	29/07/2021

Name of Co-Author	Haolan Xu		
Contribution to the Paper	Helped with XPS measurement.		
Signature		Date	29/07/2021

Name of Co-Author	Shuai Zhang		
Contribution to the Paper	Provided the Plasma equipment and helped with the plasma experiment		
Signature		Date	29/07/2021

Name of Co-Author	Tao Shao		
Contribution to the Paper	Provided the Plasma equipment and helped with the plasma experiment		
Signature		Date	29/07/2021

Name of Co-Author	Kenneth Davey		
Contribution to the Paper	Manuscript revision		
Signature		Date	29/07/2021

Name of Co-Author	Shi-Zhang Qiao		
Contribution to the Paper	Supervised development of work, helped in manuscript evaluation and acted as corresponding author		
Signature		Date	29/07/2021

Efficient Nitrogen Fixation to Ammonia through Integration of Plasma Oxidation with Electrocatalytic Reduction

Laiquan Li⁺, Cheng Tang⁺, Xiaoyang Cui⁺, Yao Zheng, Xuesi Wang, Haolan Xu, Shuai Zhang, Tao Shao, Kenneth Davey, and Shi-Zhang Qiao*

Abstract: Present one-step N₂ fixation is impeded by tough activation of the N≡N bond and low selectivity to NH₃. Here we report fixation of N₂-to-NH₃ can be decoupled to a two-step process with one problem effectively solved in each step, including: 1) facile activation of N₂ to NO_x⁻ by a non-thermal plasma technique, and 2) highly selective conversion of NO_x⁻ to NH₃ by electrocatalytic reduction. Importantly, this process uses air and water as low-cost raw materials for scalable ammonia production under ambient conditions. For NO_x⁻ reduction to NH₃, we present a surface boron-rich core-shell nickel boride electrocatalyst. The surface boron-rich feature is the key to boosting activity, selectivity, and stability via enhanced NO_x⁻ adsorption, and suppression of hydrogen evolution and surface Ni oxidation. A significant ammonia production of 198.3 μmol cm⁻² h⁻¹ was achieved, together with nearly 100 % Faradaic efficiency.

Introduction

Ammonia (NH₃) is a globally important chemical, which is currently widely produced in large-scale by one-step Haber–Bosch (H-B) process.^[1] However, the harsh operating conditions and overreliance on fossil fuels make H-B process highly costly, energy- and emission-intensive and centralized (Figure 1 a-i).^[2] Electrocatalytic nitrogen reduction reaction (eNRR) has therefore attracted increasing attention because of more mild operating conditions and high compatibility with renewable energy (Figure 1 a-ii).^[3] However eNRR suffers from extremely low NH₃ yield and low Faradaic efficiency (FE) because of: 1) low solubility of N₂, 2) difficulty in N₂ activation, and 3) competing hydrogen evolution reaction (HER).^[4] This also results in troublesome ammonia detection

and practically indistinguishable yield from adventitious nitrogen-containing species.^[5] There is therefore a significant demand for an alternative process that is efficient, sustainable and scale-adjustable for ammonia production.

Taken together, one-step conversions of N₂ to NH₃ either by H-B process or eNRR have practical drawbacks due to the difficulties and high energy consumption in N₂ activation and poor NH₃ selectivity. Alternatively, this conundrum can be decoupled to a two-step process with one problem effectively solved in each step. To achieve this goal, a feasible approach is to transform the sluggish N₂ into more reactive species, such as nitrogen oxyanions (NO_x⁻),^[6] followed by an effective reduction process (Figure 1 a-iii). N≡N bond breaking is practically difficult because of high bond energy of 941 kJ mol⁻¹. Inspired by N₂ fixation by lightning in nature, the use of plasma, especially non-thermal plasma with low energy input, is reckoned to provide effective N₂ activation.^[7] It is reported that the theoretical limit of the energy consumption for plasma-based N₂ fixation is over 2.5 times lower than that for H-B process.^[8] Importantly, air can be used directly as a gas source for converting N₂ to nitrogen oxides (NO_x), that can then be absorbed by water to form reactive NO_x⁻. To achieve selective conversion of NO_x⁻ to NH₃, electrocatalytic reduction is advantageous owing to the high activity and selectivity that can be flexibly tuned in catalysts, electrolyte, interface and potential.^[9]

Numerous efforts have been undertaken to optimize plasma reactors for N₂ oxidation with relatively low energy consumption.^[7,8,10] For example, a reverse vortex flow gliding arc plasma was reported with a high NO_x yield of 1.5 % with a low cost of 3.6 MJ mol⁻¹ NO_x.^[11] The production of ammonia via electrochemical NO_x⁻ reduction reaction (eNO_xRR) however is less developed, suffering from issues including low selectivity to NH₃, high overpotentials and poor stability.^[12] Cu-based nanomaterials are conventionally used as electrocatalysts for eNO_xRR^[13] but require high overpotentials (ca. 1.2 V) to obtain practically acceptable yields and FEs. This can be ascribed to the low binding affinity and nucleophilicity of NO_x⁻ on Cu surface, and sluggish water dissociation failing to provide sufficient protons.^[14] In contrast, Ni is reported to have strong adsorption of intermediates such as *NO₃⁻, *NO₂⁻ and *NH₂.^[15] However, HER activity on Ni surface is too strong, leading to low selectivity and efficiency for ammonia production.^[16] Therefore, rational design and fine modulation of Ni-based nanomaterials for efficient eNO_xRR and concomitantly suppressed HER is important in realizing selective production of ammonia, and ultimately fulfilling the two-step nitrogen fixation.

[*] L. Li,^[†] Dr. C. Tang,^[†] Dr. Y. Zheng, Dr. X. Wang, Prof. K. Davey, Prof. S.-Z. Qiao

School of Chemical Engineering and Advanced Materials
The University of Adelaide, Adelaide SA 5005 (Australia)
E-mail: s.qiao@adelaide.edu.au

Dr. X. Cui,^[†] Dr. S. Zhang, Prof. T. Shao
Beijing International S&T Cooperation Base for Plasma Science and Energy Conversion, Institute of Electrical Engineering
Chinese Academy of Sciences, Beijing 100190 (P. R. China)

Prof. H. Xu
Future Industries Institute, University of South Australia
Mawson Lakes SA 5095 (Australia)

[†] These authors contributed equally to this work.

Supporting information and the ORCID identification number(s) for the author(s) of this article can be found under:
https://doi.org/10.1002/anie.202104394.

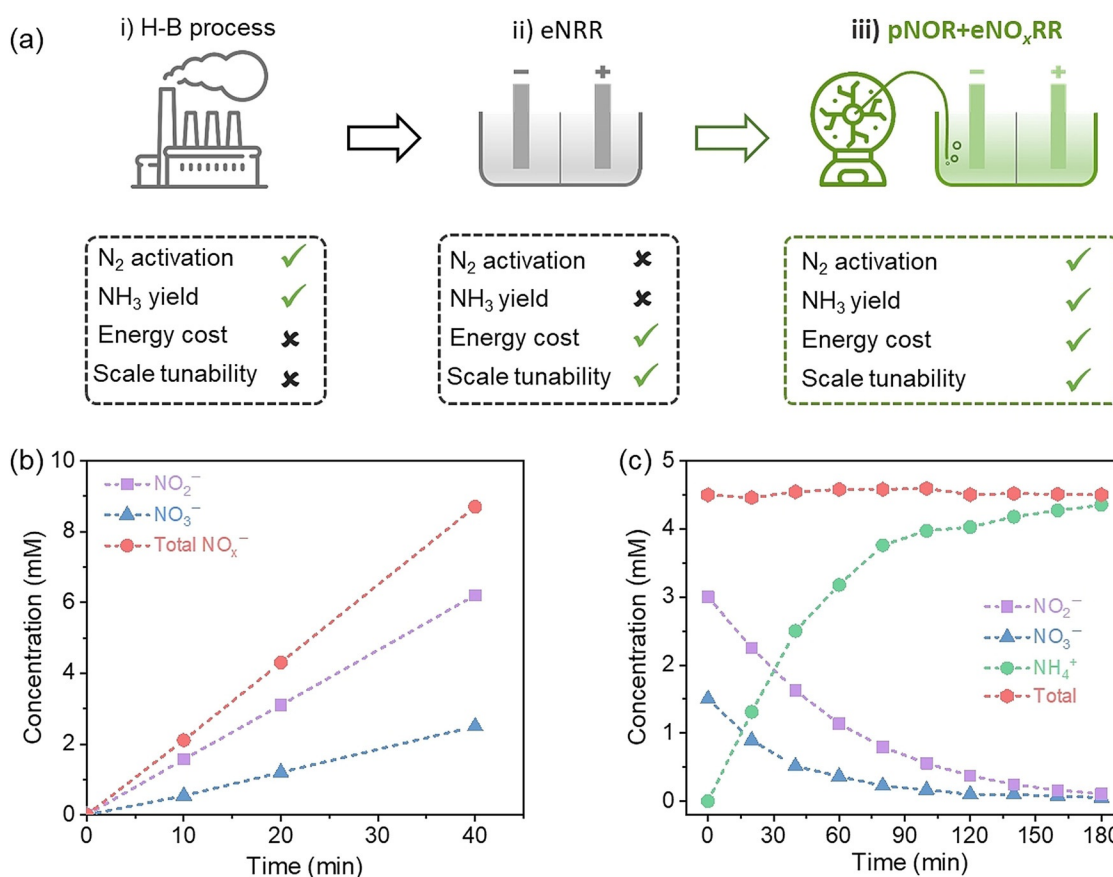


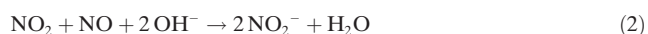
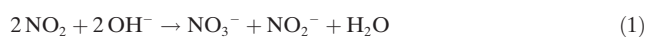
Figure 1. Proof-of-concept of two-step N₂-to-NH₃ conversion. a) Three nitrogen fixation routes. b) pNOR: Yield of NO_x⁻ as a function of plasma treatment time (100 mL 0.10 M KOH as absorbent). c) eNO_xRR: Batch experiment at -0.3 V vs. RHE (50 mL electrolyte taken after 20 min plasma treatment) with successive consumption of NO_x⁻ and ammonia production.

In this work, we exploited advantages of the two-step N₂-to-NH₃ fixation by serially integrating a plasma-driven N₂ oxidation (pNOR) to activate inert N₂ with an eNO_xRR process to achieve highly selective ammonia production (Figure 1a-iii). To boost activity, selectivity, and stability of eNO_xRR to ammonia, we developed a novel surface boron-rich core-shell nickel boride nanoparticle (denoted as Ni₃B@NiB_{2.74}) as electrocatalyst. Following facile N₂ activation by pNOR process and electrolyte absorption, the Ni₃B@NiB_{2.74} catalyst exhibited ca. 100% conversion of as-obtained NO_x⁻ to NH₃, resulting in a significant ammonia yield of ca. 2500 times higher than that for eNRR. The activity origins and structure-property relations of the new Ni₃B@NiB_{2.74} catalyst were studied by a series of physical characterizations, poisoning experiments, and in situ Raman and infrared spectroscopy.

Results and Discussion

We carried out a proof-of-concept using a model air (N₂/O₂ mixture, v/v = 4:1) as the gas feed for pNOR, 0.10 M KOH as the absorbent and the as-obtained solution as electrolyte for eNO_xRR. Inert N₂ was activated by pNOR (Supporting Information, Figure S1), where the plasma-excited nitrogen

(^{*}N) reacts with the activated oxygen species (^{*}O, O₃) to convert N₂ to NO_x, such as NO₂ and NO.^[17] Alkaline absorption generates an aqueous mix of NO₂⁻ and NO₃⁻ via:



Yield of NO_x⁻ was found to increase linearly with plasma operation time (Figure 1b). A high total NO_x⁻ yield of ca. 1.35 mmol h⁻¹ was achieved, in which the concentration of NO₂⁻ is over two times higher than that of NO₃⁻ (Figure 1b). The as-obtained NO_x⁻ solution was used directly as electrolyte for eNO_xRR with Ni₃B@NiB_{2.74} as electrocatalyst at a fixed potential of -0.3 V vs. reversible hydrogen electrode (RHE). The concentration of NO₃⁻, NO₂⁻ and NH₃ was quantified by UV-vis measurements (Supporting Information, Figures S2–S4). As shown in Figure 1c, NO₂⁻ and NO₃⁻ ions were rapidly consumed, whilst NH₃ was simultaneously produced. The total concentration of N-containing species remained constant during the batch experiment. A significant average ammonia yield of 160.4 μmol h⁻¹ was achieved in the initial 1 h, which then declined due to NO_x⁻ consumption. The conversion of NO_x⁻ to NH₃ approached 96.7% within an extended reaction time of 3 h, which is superior to most

reported batch experiments on varying catalysts (Supporting Information, Table S1). Significantly, the ammonia yield from $e\text{NO}_x\text{RR}$ is ca. 2500 times higher than that from $e\text{NRR}$ using the same electrocatalyst within the same reaction period (Supporting Information, Figure S5). It is therefore concluded that the two-step integration of plasma N_2 oxidation (pNOR) with electrocatalytic reduction ($e\text{NO}_x\text{RR}$) is practically feasible for highly efficient and selective nitrogen fixation to ammonia at ambient conditions.

Since nitrogen oxyanions are weak Lewis bases, it is reasonable to induce abundant Lewis acid sites on the surface of electrocatalysts to boost NO_x^- adsorption. Boron atoms with unoccupied 2p orbital in valence shell can accept electrons from donors, readily serving as Lewis acid sites.^[18] We therefore developed a surface B-rich core-shell nickel boride structure ($\text{Ni}_3\text{B@NiB}_{2.74}$), which was synthesized by calcination of an amorphous nickel boride precursor ($\text{Ni}_3\text{B@NiB}_{0.72}$). Transmission electron microscopy (TEM) image shows that as-synthesized $\text{Ni}_3\text{B@NiB}_{2.74}$ is composed of interconnected nanoparticles (Figure 2a), and it resembles the morphology of the precursor (Supporting Information, Figure S6). High-resolution TEM image (HRTEM) shows that $\text{Ni}_3\text{B@NiB}_{2.74}$ has a core-shell structure for each nanoparticle (Figure 2b). The core is crystalline exhibiting lattice fringes with a spacing of 0.204 nm and 0.219 nm, assigned, respectively to the (220) and (002) facets of Ni_3B . The formation of Ni_3B core is also confirmed by X-ray diffraction (XRD; Supporting Information, Figure S7) and selected area electron diffraction pattern (SAED; inset of Figure 2a). In contrast, the thin shell layer is amorphous with an average

thickness of 3 nm. Such core-shell structure is advantageous in providing an active surface and a stable bulk, leading to both high activity and stability.

The composition distribution was investigated by energy-dispersive X-ray (EDX) analysis and X-ray photoelectron spectroscopy (XPS) measurements. As shown in Figure 2c and d, the EDX mapping and line analyses clearly verify distinct B and Ni distribution in the core and shell regions, featuring a B-rich shell. Point EDX spectroscopy analysis reveals that atomic content of Ni and B in the shell region were 18.8% and 56.0%, whilst in the core were 59.5% and 15.5% (Figure 2e), respectively. This surface B-rich feature is distinctive from the precursor prior to annealing, for which Ni and B distribute uniformly throughout the entire structure with a higher content of Ni than B also on the surface (Supporting Information, Figure S6). XPS survey reveals a B/Ni atomic ratio of 2.74 for the shell of annealed sample, and a lower value of 0.72 for the precursor (Supporting Information, Figure S8), consistent with the EDX results. Samples before and after annealing are therefore denoted as $\text{Ni}_3\text{B@NiB}_{0.72}$ and $\text{Ni}_3\text{B@NiB}_{2.74}$, respectively. It is apparent that annealing is vital for the surface B/Ni distribution. During annealing, the core became crystalline (Supporting Information, Figure S7) and the obtained nanoparticles slightly agglomerated into larger particles (Supporting Information, Figure S9). Meanwhile, the light B atoms diffused to the surface and formed a B-rich shell owing to different diffusion behavior of heavy metal and light non-metal elements at high temperature.^[19]

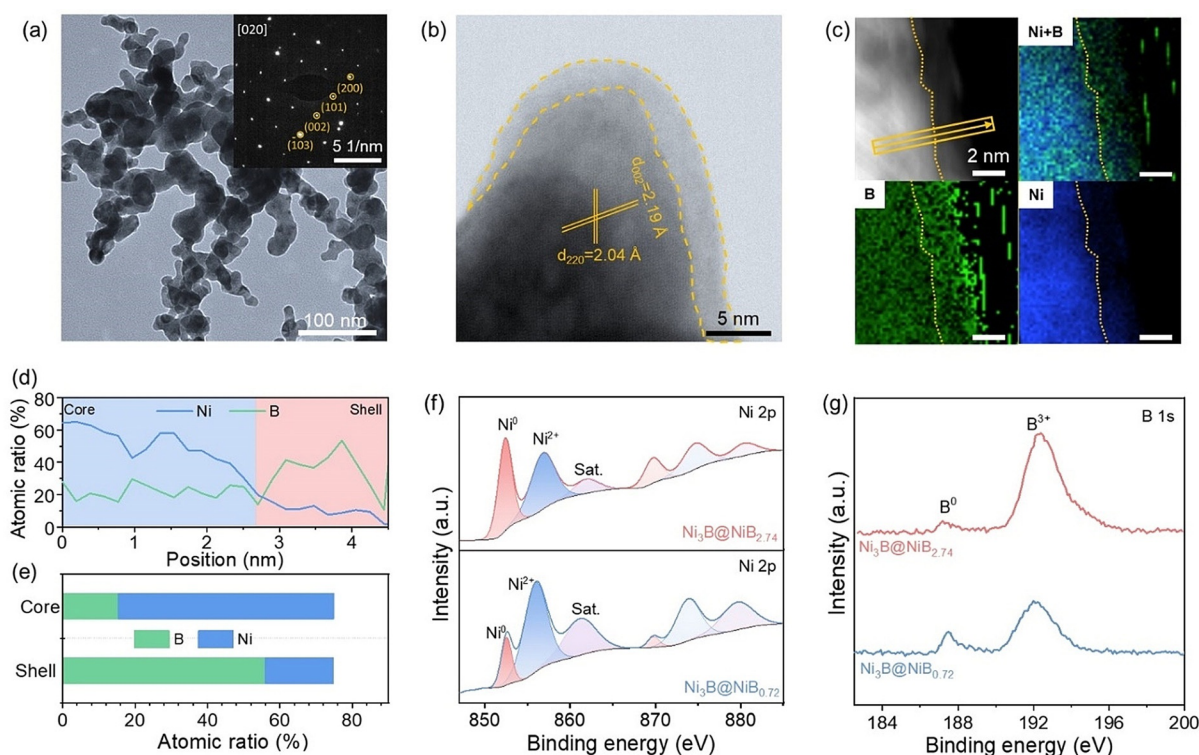


Figure 2. Characterization of $\text{Ni}_3\text{B@NiB}_{2.74}$. a) TEM and b) HRTEM images for $\text{Ni}_3\text{B@NiB}_{2.74}$. Inset of (a) shows SAED pattern. c) EDX mapping. d) EDX linear scan of selected area in (c). e) Point EDX results adopted from shell and core regions of $\text{Ni}_3\text{B@NiB}_{2.74}$. f) Ni 2p XPS spectra and g) B 1s XPS spectra for $\text{Ni}_3\text{B@NiB}_{0.72}$ and $\text{Ni}_3\text{B@NiB}_{2.74}$.

The electronic structure of obtained samples was then investigated by surface sensitive XPS and electron energy loss spectra (EELS). As displayed in Figure 2 f, Ni 2p XPS spectra show the coexistence of Ni⁰ and Ni²⁺ signals on the surface for both samples.^[20] Significantly, Ni₃B@NiB_{2.74} exhibits a higher Ni⁰/Ni²⁺ ratio of 1.63 than that for Ni₃B@NiB_{0.72} of 0.54. The Ni L edge EELS spectra, in which L₃/L₂ area ratio increases as the oxidation state of Ni decreases,^[21] was then conducted. The higher L₃/L₂ area ratio (3.89) recorded in the shell regions of Ni₃B@NiB_{2.74} than that of Ni₃B@NiB_{0.72} (3.37) further confirms the lower Ni valence state for Ni₃B@NiB_{2.74} (Supporting Information, Figure S10). These findings confirm the enrichment of Ni⁰ sites on the B-rich surface after annealing.^[22] Figure 2g shows the B 1s XPS spectra for the two samples. The peak at around 187.5 eV is assigned to B⁰ in nickel boride and the other at around 192.2 eV to B–O bonding in borate or boron oxide.^[20] The B⁰/B³⁺ ratio for Ni₃B@NiB_{2.74} is determined to be lower than that for Ni₃B@NiB_{0.72} (0.19 versus 0.28), revealing a higher B valence state on the surface of Ni₃B@NiB_{2.74}. This can be explained by the electron transfer from B atoms to the 3d bands of Ni atoms occurring on the B-rich surface. The resulting electron-deficient B sites are expected to serve as Lewis acid sites for boosted NO_x⁻ adsorption.^[18b]

The eNO_xRR performance was systematically evaluated in Ar-saturated 0.10 M KOH with certain amount of NO_x⁻ (NO₂⁻ or NO₃⁻). Linear sweep voltammetry (LSV) curves were recorded for Ni₃B@NiB_{2.74} in the electrolyte containing varying NO₃⁻ concentration from 0 to 100 mM (Figure 3a). The onset potentials are found to positively shift with increasing NO₃⁻ concentration, implying more favorable kinetics for eNO₃RR than those for HER. The low value of reaction order with respect to NO₃⁻ concentration (< 0.5) for Ni₃B@NiB_{2.74} suggests strong adsorption of NO₃⁻ (Supporting Information, Figure S11).^[14a,23] Figure 3b shows the maximum NH₃ yields and FEs for Ni₃B@NiB_{2.74} at varying NO₃⁻ concentration. A significant FE of 90.7% was achieved at a low NO₃⁻ concentration of 1 mM. The FE increases to 100% at a high NO₃⁻ concentration of 100 mM, with a significant ammonia yield of 198.3 μmol cm⁻² h⁻¹. Additionally, reduction of NO₂⁻ (eNO₂RR) on Ni₃B@NiB_{2.74} was also evaluated in 0.10 M KOH containing 10 mM NO₂⁻. As shown in the Supporting Information, Figure S12, over a wide potential from 0.1 to -0.4 V vs. RHE the FEs for eNO₂RR to NH₃ are nearly ca. 100%, indicating superior thermodynamics and kinetics. Note that eNO₂RR can be regarded as a part of eNO₃RR on Ni₃B@NiB_{2.74},^[24] nonetheless, it is not the rate-determining step (RDS). This is evidenced by the Tafel slope of 105.3 mV dec⁻¹ for eNO₃RR on Ni₃B@NiB_{2.74} (Supporting Information, Figure S13), which value is approximate to 120 mV dec⁻¹ and implies the conversion of *NO₃ to *NO₂ as the RDS.^[25] For this reason in this work we mainly focus on eNO₃RR.

The potential-dependent eNO₃RR performance of Ni₃B@NiB_{2.74} was evaluated in 0.10 M KOH with 10 mM NO₃⁻ (Supporting Information, Figure S14). As shown in Figure 3c, high NO₃⁻-to-NH₃ selectivity is achieved on Ni₃B@NiB_{2.74} over a significant potential range from 0.1 to -0.5 V vs. RHE. A maximum FE of 98.7% was achieved at

-0.3 V vs. RHE with a NH₃ yield of 107.1 μmol cm⁻² h⁻¹. Little nitrite ions and H₂ were detected at potentials higher than -0.3 V vs. RHE, after which HER rises with increased FE toward H₂ (Figure 3c; Supporting Information, Figure S15). Electrocatalytic stability was then evaluated through replacing electrolyte every 0.5 h for 10 cycles. As shown in Figure 3d, no meaningful change to ammonia production and FE is seen during long-term electrolysis. The LSV curves for Ni₃B@NiB_{2.74} are almost identical before and after stability testing (Supporting Information, Figure S16) and the B-rich shell layer was found to be well maintained (Supporting Information, Figure S17). The LSV curve for Ni₃B@NiB_{0.72} following stability testing however exhibited severe degradation in both the onset potential and current density (Supporting Information, Figure S16). It is therefore concluded that Ni₃B@NiB_{2.74} exhibits outstanding activity, selectivity, and durability for eNO_xRR to NH₃, which is superior to reported catalysts with respect to overpotential, FE and ammonia yield (Supporting Information, Table S2).

A nickel nanoparticle (Ni NP) sample with similar morphology (Supporting Information, Figure S18) and electrochemically active surface area (Supporting Information, Figure S19) to Ni₃B@NiB_{2.74} but without B incorporation was synthesized to investigate the role of surface-enriched B sites. The surface B content therefore increases gradually from Ni-NP to Ni₃B@NiB_{0.72}, and to Ni₃B@NiB_{2.74}. As shown in Figure 3e and f, both FE and NH₃ yield show a positive relationship with surface B content, demonstrating that incorporation of B can effectively boost eNO_xRR activity for Ni-based catalysts. Note that surface oxygen contributes negligibly to eNO_xRR activity, which is verified by a series of control experiments (Supporting Information, Figures S20 and S21). It is therefore concluded that the surface-enriched B sites are critical to boosting both eNO_xRR activity and stability, which are further elucidated below.

The eNO_xRR activity and selectivity origins were investigated by a series of LSV tests in different electrolytes on Ni₃B@NiB_{2.74}, Ni₃B@NiB_{0.72} and Ni NP. Figure 4a presents the LSV curves obtained in 0.10 M KOH with and without 10 mM NO₃⁻. More negative HER onset potential and larger eNO₃RR current density are observed with increasing surface B content. The suppressed HER activity is attributed to the gradually diluted surface nickel sites,^[26] whilst the boosted eNO₃RR activity can be ascribed to the enhanced NO₃⁻ adsorption on Lewis acid B sites. To verify this hypothesis of Lewis acid-base interaction between B sites and NO₃⁻, poisoning experiments using a stronger Lewis base, potassium thiocyanide (KSCN), were carried out. As shown in Figure 4b, following addition of SCN⁻ ions into the NO₃⁻-containing solution, the current density for eNO₃RR is seriously plummeted down while that for HER remains almost unchanged. In contrast, eNO₃RR performance on Ni NP is nearly unaffected by addition of SCN⁻ ions (Supporting Information, Figure S22). These findings indicate that SCN⁻ ions compete with NO₃⁻ to adsorb on B sites, due to higher Lewis basicity, rather than Ni sites. Additionally, the formation of B–N bonds on Ni₃B@NiB_{2.74} during eNO₃RR, as evidenced by the adsorption peak at 805 cm⁻¹,^[18b,27] was confirmed by in situ attenuated total reflectance surface

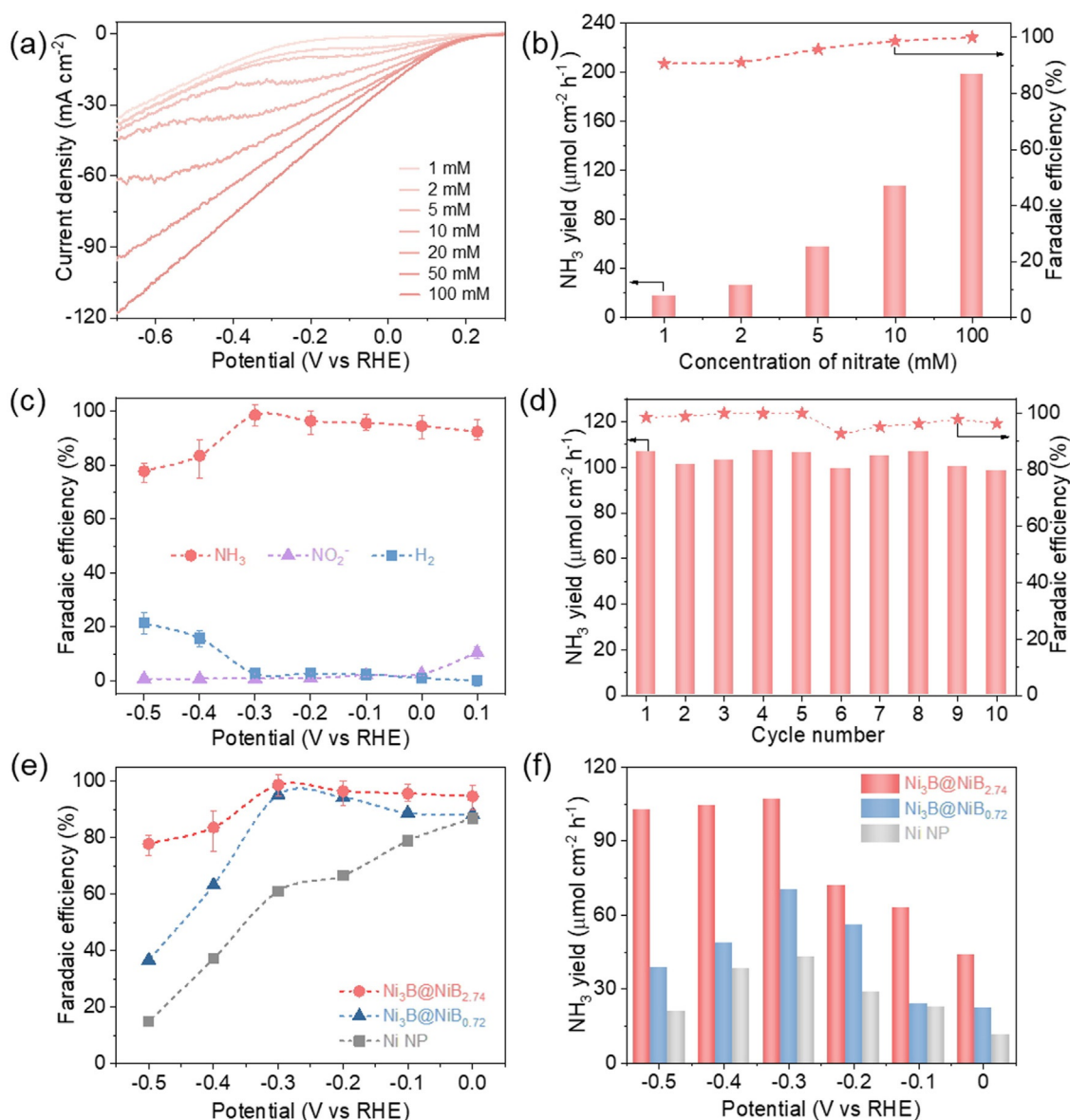


Figure 3. Electrochemical NO_3RR performance. a) LSV curves for $\text{Ni}_3\text{B@NiB}_{2.74}$ and b) achieved maximum FE and NH_3 yield in 0.10 M KOH with varying nitrate concentration. c) FE for NH_3 , NO_2^- and H_2 production for $\text{Ni}_3\text{B@NiB}_{2.74}$ at varying potential in 0.10 M KOH with 10 mM NO_3^- . d) Stability tests for $\text{Ni}_3\text{B@NiB}_{2.74}$ at -0.3 V vs. RHE in 0.10 M KOH with 10 mM NO_3^- . e) FE for NH_3 and f) ammonia yield for Ni NP, $\text{Ni}_3\text{B@NiB}_{0.72}$ and $\text{Ni}_3\text{B@NiB}_{2.74}$ in 0.10 M KOH with 10 mM NO_3^- .

enhanced infrared absorption spectroscopy (ATR-SEIRAS) (Figure 4c). It is therefore concluded that the surface-enriched electron-deficient B sites are responsible for enhanced NO_3^- adsorption and thereby contribute to the boosted catalytic activity.

Mechanism for the improved stability of $\text{Ni}_3\text{B@NiB}_{2.74}$ was studied via ex situ XPS, EELS spectra, and in situ Raman and ATR-SEIRAS measurements. For $\text{Ni}_3\text{B@NiB}_{0.72}$, severe surface oxidation is evidenced by the markable decrease in the L_3/L_2 area ratio in EELS spectrum (Figure 4d; Supporting Information, Figure S23) and the disappearance of the Ni^0 signal in Ni 2p XPS spectrum after stability testing (Supporting Information, Figure S24). The $\text{Ni}_3\text{B@NiB}_{2.74}$ sample however exhibited only a slight decrease in L_3/L_2 area ratio of 0.07 (Figure 4d; Supporting Information, Figure S23) and main-

tained a significant portion of Ni^0 sites (Supporting Information, Figure S24). In situ Raman spectra monitor the surface variation during e NO_3RR with additional clarity. As shown in Figure 4e, two bands appeared at 458 cm^{-1} and 496 cm^{-1} upon applying potentials on $\text{Ni}_3\text{B@NiB}_{0.72}$, which are assigned to the vibration of Ni-OH bond stretching and Ni-O stretching in $\text{Ni}(\text{OH})_2$ (Supporting Information, Figure S25), respectively.^[28] However, no such peaks appeared in the in situ Raman spectra for $\text{Ni}_3\text{B@NiB}_{2.74}$ (Figure 4f). In situ ATR-SEIRAS measurements also verified the formation of $\text{Ni}(\text{OH})_2$ on surface of $\text{Ni}_3\text{B@NiB}_{0.72}$, but not on $\text{Ni}_3\text{B@NiB}_{2.74}$, during e NO_3RR (Supporting Information, Figure S26). We therefore reveal that the surface oxidation, a common problem causing activity degradation on Ni-based e NO_3RR electrocatalysts in alkaline solution,^[29] is due to formation of a thin layer of

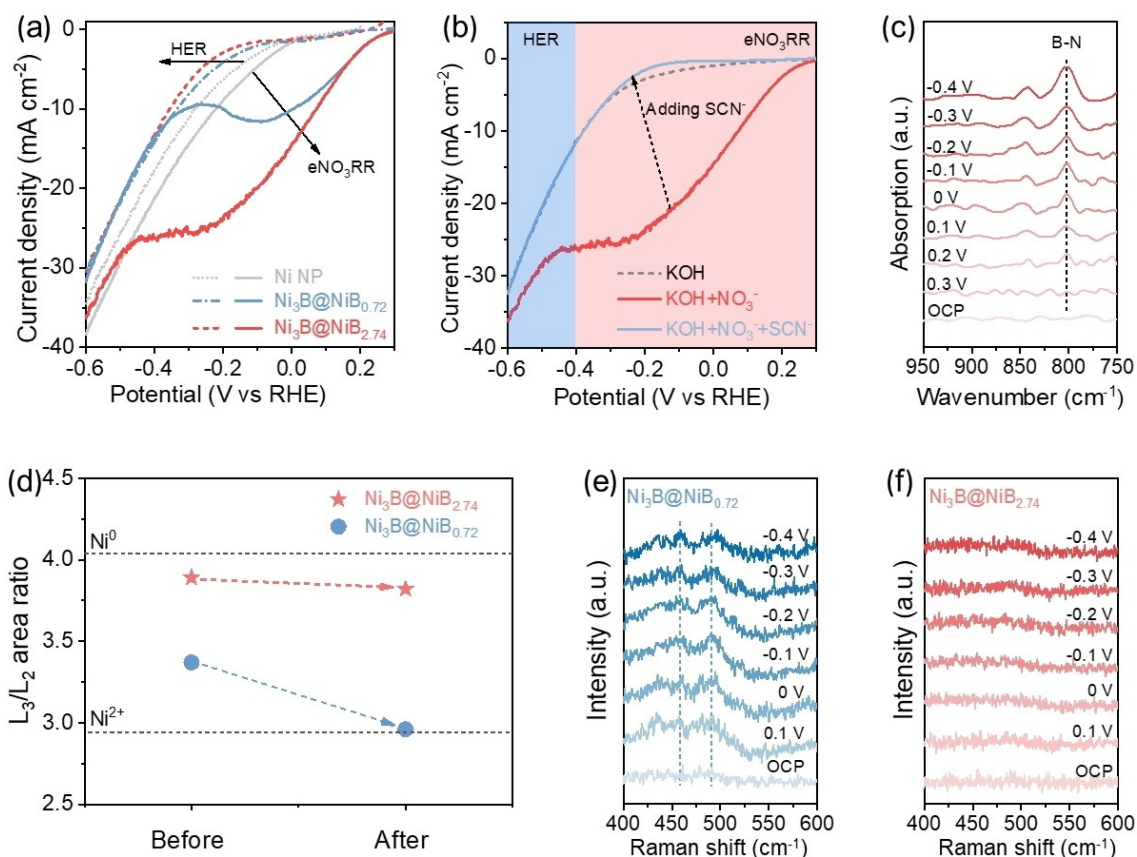


Figure 4. Reaction mechanism investigation for Ni-based materials during eNO₃RR. a) LSV curves for Ni NP, Ni₃B@NiB_{0.72}, and Ni₃B@NiB_{2.74} in 0.10 M KOH with and without 10 mM NO₃⁻. b) LSV curves for poisoning experiment on Ni₃B@NiB_{2.74}. c) In situ ATR-SEIRAS measurement for Ni₃B@NiB_{2.74} in 0.10 M KOH with 10 mM NO₃⁻, OCP: open-circuit potential. d) L₃/L₂ area ratio for Ni₃B@NiB_{2.74} and Ni₃B@NiB_{0.72} before and after stability testing. e) In situ Raman spectra for Ni₃B@NiB_{0.72} and f) Ni₃B@NiB_{2.74} in 0.10 M KOH with 10 mM NO₃⁻.

Ni(OH)₂ that exhibits a very low activity for eNO₃RR (Supporting Information, Figure S27). This issue can be effectively obviated through enriching B atoms on catalyst surface to induce electrons transfer to Ni sites and thus impede the surface oxidation of Ni.

Conclusion

A two-step N₂-to-NH₃ fixation through serial integration of plasma-driven N₂ oxidation with electrocatalytic nitrogen oxyanions reduction to ammonia is demonstrated, enabling facile N₂ activation and efficient NH₃ production in each step (Figure 5). A novel surface B-rich core-shell nickel boride nanoparticle Ni₃B@NiB_{2.74} electrocatalyst was developed and delivered a significant ammonia yield of 198.3 μmol cm⁻² h⁻¹ with a near 100% Faradaic efficiency. By combining a series of ex situ characterizations and in situ spectrometric measurements, we revealed a dual-site reaction mechanism for eNO₃RR on boron-rich nickel-

based electrocatalysts (Figure 5). The Ni sites are responsible for water dissociation to provide protons for NO_x⁻ hydrogenation. The enriched electron-deficient B sites on the surface could not only enhance adsorption of NO_x⁻, but also alleviate surface oxidation of Ni⁰ sites and prevent overactive hydrogen evolution. The synergistic contribution from Ni and B sites lead to excellent activity, selectivity, and durability for eNO_xRR to NH₃. This work provides new insights and

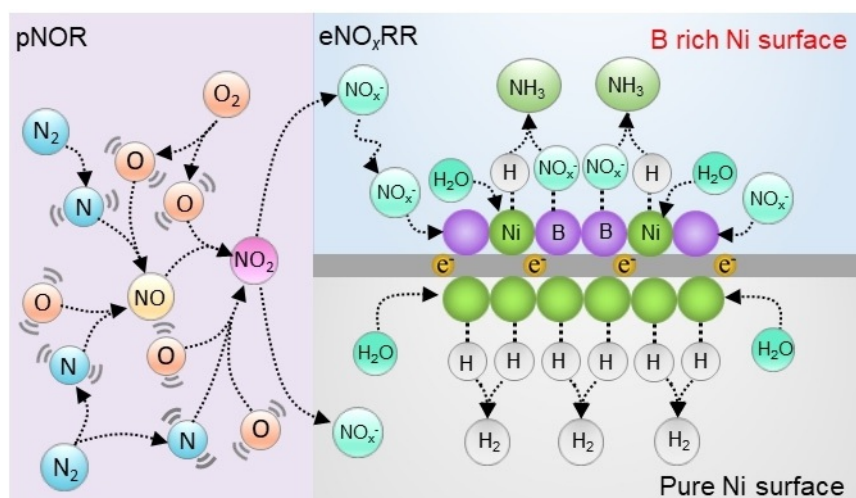


Figure 5. The pNOR + eNO_xRR process and dual-site mechanism for boosted eNO_xRR activity.

opportunities for renewable chemicals production by decoupling the challenges of molecule activation and product selectivity, and by integrating various advanced technologies such as plasma catalysis and electrocatalysis.

Acknowledgements

This work was financially supported by the Australian Research Council (FL170100154). SEM and TEM measurements were undertaken at Adelaide Microscopy, the Centre for Advanced Microscopy and Microanalysis. L.L. thanks Dr. Ashley Slattery from Adelaide Microscopy for assistance with TEM imaging and EELS analyzes, and Dr. Ting Gao from University of South Australia, for XPS measurements.

Conflict of interest

The authors declare no conflict of interest.

Keywords: ammonia production · boron-rich surface · electrocatalytic nitrate reduction · nitrogen fixation · plasma

- [1] a) J. G. Chen, R. M. Crooks, L. C. Seefeldt, K. L. Bren, R. M. Bullock, M. Y. Darensbourg, P. L. Holland, B. Hoffman, M. J. Janik, A. K. Jones, M. G. Kanatzidis, P. King, K. M. Lancaster, S. V. Lymar, P. Pfomrom, W. F. Schneider, R. R. Schrock, *Science* **2018**, *360*, eaar6611; b) J. W. Erisman, M. A. Sutton, J. Galloway, Z. Klimont, W. Winarwarter, *Nat. Geosci.* **2008**, *1*, 636–639.
- [2] a) M. D. Fryzuk, *Nature* **2004**, *427*, 498–499; b) R. Schlögl, *Angew. Chem. Int. Ed.* **2003**, *42*, 2004–2008; *Angew. Chem.* **2003**, *115*, 2050–2055.
- [3] a) C. Tang, S.-Z. Qiao, *Chem. Soc. Rev.* **2019**, *48*, 3166–3180; b) L. Li, C. Tang, B. Xia, H. Jin, Y. Zheng, S.-Z. Qiao, *ACS Catal.* **2019**, *9*, 2902–2908.
- [4] a) J. B. Goodman, N. W. Krase, *Ind. Eng. Chem.* **1931**, *23*, 401–404; b) N. I. Kolev, *Turbulence, Gas Adsorption and Release, Diesel Fuel Properties*, Springer, Heidelberg, **2011**; c) Q. Hao, C. Liu, G. Jia, Y. Wang, H. Arandiyani, W. Wei, B.-J. Ni, *Mater. Horiz.* **2020**, *7*, 1014–1029; d) J. H. Montoya, C. Tsai, A. Vojvodic, J. K. Nørskov, *ChemSusChem* **2015**, *8*, 2180–2186; e) J. G. Howalt, T. Bligaard, J. Rossmeisl, T. Vegge, *Phys. Chem. Chem. Phys.* **2013**, *15*, 7785–7795.
- [5] a) S. Z. Andersen, V. Čolić, S. Yang, J. A. Schwalbe, A. C. Nielander, J. M. McEnaney, K. Enemark-Rasmussen, J. G. Baker, A. R. Singh, B. A. Rohr, M. J. Statt, S. J. Blair, S. Mezzavilla, J. Kibsgaard, P. C. K. Vesborg, M. Cargnello, S. F. Bent, T. F. Jaramillo, I. E. L. Stephens, J. K. Nørskov, I. Chorkendorff, *Nature* **2019**, *570*, 504–508; b) L. Li, C. Tang, D. Yao, Y. Zheng, S.-Z. Qiao, *ACS Energy Lett.* **2019**, *4*, 2111–2116.
- [6] Y. Wang, Y. Yu, R. Jia, C. Zhang, B. Zhang, *Nat. Sci. Rev.* **2019**, *6*, 730–738.
- [7] a) L. R. Winter, J. G. Chen, *Joule* **2021**, *5*, 300–315; b) N. Cherkasov, A. O. Ibadon, P. Fitzpatrick, *Chem. Eng. Process.* **2015**, *90*, 24–33.
- [8] A. Bogaerts, E. C. Neyts, *ACS Energy Lett.* **2018**, *3*, 1013–1027.
- [9] C. Tang, Y. Zheng, M. Jaroniec, S.-Z. Qiao, *Angew. Chem. Int. Ed.* **2021**, <https://doi.org/10.1002/anie.202101522>; *Angew. Chem.* **2021**, <https://doi.org/10.1002/ange.202101522>.
- [10] L. Hollevoet, F. Jardali, Y. Gorbanev, J. Creel, A. Bogaerts, J. A. Martens, *Angew. Chem. Int. Ed.* **2020**, *59*, 23825–23829; *Angew. Chem.* **2020**, *132*, 24033–24037.
- [11] E. Vervloessem, M. Aghaei, F. Jardali, N. Hafezkhiani, A. Bogaerts, *ACS Sustainable Chem. Eng.* **2020**, *8*, 9711–9720.
- [12] P. H. van Langevelde, I. Katsounaros, M. T. M. Koper, *Joule* **2021**, *5*, 290–294.
- [13] a) Y. Wang, W. Zhou, R. Jia, Y. Yu, B. Zhang, *Angew. Chem. Int. Ed.* **2020**, *59*, 5350–5354; *Angew. Chem.* **2020**, *132*, 5388–5392; b) T. Wu, X. Kong, S. Tong, Y. Chen, J. Liu, Y. Tang, X. Yang, Y. Chen, P. Wan, *Appl. Surf. Sci.* **2019**, *489*, 321–329.
- [14] a) Y. Li, Y. K. Go, H. Ooka, D. He, F. Jin, S. H. Kim, R. Nakamura, *Angew. Chem. Int. Ed.* **2020**, *59*, 9744–9750; *Angew. Chem.* **2020**, *132*, 9831–9837; b) B. K. Simpson, D. C. Johnson, *Electroanalysis* **2004**, *16*, 532–538; c) S. Jain, A. Bansiwala, R. B. Biniwale, S. Milmlle, S. Das, S. Tiwari, P. Siluvai Antony, *J. Environ. Chem. Eng.* **2015**, *3*, 2342–2349.
- [15] Y. Wang, A. Xu, Z. Wang, L. Huang, J. Li, F. Li, J. Wicks, M. Luo, D.-H. Nam, C.-S. Tan, Y. Ding, J. Wu, Y. Lum, C.-T. Dinh, D. Sinton, G. Zheng, E. H. Sargent, *J. Am. Chem. Soc.* **2020**, *142*, 5702–5708.
- [16] L. Mattarozzi, S. Cattarin, N. Comisso, P. Guerriero, M. Musiani, L. Vázquez-Gómez, E. Verlato, *Electrochim. Acta* **2013**, *89*, 488–496.
- [17] J. Sun, D. Alam, R. Daiyan, H. Masood, T. Zhang, R. Zhou, P. J. Cullen, E. C. Lovell, A. Jalili, R. Amal, *Energy Environ. Sci.* **2021**, *14*, 865–872.
- [18] a) L. Shi, Q. Li, C. Ling, Y. Zhang, Y. Ouyang, X. Bai, J. Wang, *J. Mater. Chem. A* **2019**, *7*, 4865–4871; b) S. Liu, M. Wang, T. Qian, H. Ji, J. Liu, C. Yan, *Nat. Commun.* **2019**, *10*, 3898.
- [19] a) Y. Yin, R. M. Rioux, C. K. Erdonmez, S. Hughes, G. A. Somorjai, A. P. Alivisatos, *Science* **2004**, *304*, 711–714; b) W.-J. Jiang, S. Niu, T. Tang, Q.-H. Zhang, X.-Z. Liu, Y. Zhang, Y.-Y. Chen, J.-H. Li, L. Gu, L.-J. Wan, J.-S. Hu, *Angew. Chem. Int. Ed.* **2017**, *56*, 6572–6577; *Angew. Chem.* **2017**, *129*, 6672–6677.
- [20] W. Cai, H. Yang, J. Zhang, H.-C. Chen, H. B. Tao, J. Gao, S. Liu, W. Liu, X. Li, B. Liu, *ACS Mater. Lett.* **2020**, *2*, 624–632.
- [21] R. D. Leapman, L. A. Grunes, P. L. Fejes, *Phys. Rev. B* **1982**, *26*, 614–635.
- [22] a) T. Riedl, T. Gemming, K. Wetzig, *Ultramicroscopy* **2006**, *106*, 284–291; b) Y. Koyama, T. Mizoguchi, H. Ikeno, I. Tanaka, *J. Phys. Chem. B* **2005**, *109*, 10749–10755.
- [23] A. C. A. de Vooyo, R. A. van Santen, J. A. R. van Veen, *J. Mol. Catal. A* **2000**, *154*, 203–215.
- [24] V. Rosca, M. Duca, M. T. de Groot, M. T. M. Koper, *Chem. Rev.* **2009**, *109*, 2209–2244.
- [25] G. E. Dima, A. C. A. de Vooyo, M. T. M. Koper, *J. Electroanal. Chem.* **2003**, *554–555*, 15–23.
- [26] H. Jin, X. Wang, C. Tang, A. Vasileff, L. Li, A. Slattery, S.-Z. Qiao, *Adv. Mater.* **2021**, *33*, 2007508.
- [27] B. Yu, W. Xing, W. Guo, S. Qiu, X. Wang, S. Lo, Y. Hu, *J. Mater. Chem. A* **2016**, *4*, 7330–7340.
- [28] a) S. Deabate, F. Fourgeot, F. Henn, *J. Power Sources* **2000**, *87*, 125–136; b) H. Wang, Y. Zhang, Q. Wang, C. Jia, P. Cai, G. Chen, C. Dong, H. Guan, *RSC Adv.* **2019**, *9*, 9126–9135.
- [29] I. Mikami, Y. Yoshinaga, T. Okuhara, *Appl. Catal. B* **2004**, *49*, 173–179.

Manuscript received: March 29, 2021
Accepted manuscript online: April 14, 2021
Version of record online: May 11, 2021

Supporting Information

Efficient Nitrogen Fixation to Ammonia through Integration of Plasma Oxidation with Electrocatalytic Reduction

*Laiquan Li⁺, Cheng Tang⁺, Xiaoyang Cui⁺, Yao Zheng, Xuesi Wang, Haolan Xu, Shuai Zhang, Tao Shao, Kenneth Davey, and Shi-Zhang Qiao**

anie_202104394_sm_miscellaneous_information.pdf

Experimental Procedures

1. Materials Preparation and Characterization

Chemicals and Materials

All chemicals were purchased from Sigma-Aldrich and used without further purification. Milli-Q water with a resistivity of 18.2 M Ω ·cm was obtained from a Bio-strategy Option-Q water purification system. Carbon paper (Toray Paper 60) and anion exchange membrane (Fumasep FAA-3-50) used in this work were purchased from Fuel Cell Store (Texas, USA). Ultra-high purity Ar (99.999%) and N₂ (99.999%) were purchased from BOC Gas, Australia.

Synthesis Methods

Synthesis of Ni₃B@NiB_{0.72} and Ni₃B@NiB_{2.74}: Ni₃B@NiB_{0.72} was synthesized by a facile wet chemistry method. Typically, 1.0 g of Ni(CH₃CO₂)₂·4H₂O was added to 50 mL of 0.01 M NaOH solution under magnetic stirring, followed by rapid addition of 5 mL of 1.2 M NaBH₄ solution. Intense gas evolution and instantaneous formation of a dark precipitate were observed. Following agitation for 10 min the dark precipitate was collected by centrifugation, and washed by ethanol and deoxygenated deionized water several times (> 3), then dried overnight by freeze-drying to obtain Ni₃B@NiB_{0.72} catalyst. To prepare Ni₃B@NiB_{2.74}, Ni₃B@NiB_{0.72} was carefully annealed in 5% H₂/Ar atmosphere in a tube-furnace at 300 °C for 2 h with a slow ramp rate of 2 °C min⁻¹. All the above products were stored under vacuum at room temperature (RT, 20 °C) to prevent oxidation.

Synthesis of Ni NP: 1.0 g of Ni(CH₃CO₂)₂·4H₂O was added to 7.5 mL of ethanol. A white slurry prepared by mixing 2.5 g of NaOH with 5 mL of 50% N₂H₄·H₂O solution was added to the above solution under magnetic stirring. The produced dark precipitate was washed with aqua-ammonia to remove Ni(OH)₂ by-product, followed by rinsing with ethanol and water several times (> 3) and freeze-drying. The product was then obtained by annealing at 300 °C in 5% H₂/Ar atmosphere for 2 h.

Synthesis of NiO: NiO was prepared via annealing Ni₃B@NiB_{2.74} at 500 °C in air for 2 h.

Synthesis of Ni(OH)₂: Synthesis of Ni(OH)₂ was conducted by Yu *et al.*^[1] Typically, 0.291 g of Ni(NO₃)₂·6H₂O was added to 20 mL of ethanol under magnetic stirring for 10 min. Subsequently, 2 mL of oleylamine in 10 mL of ethanol was added rapidly. Following stirring for 30 min, the solution was transferred to a sealed, Teflon-lined autoclave and heated to 180 °C for 15 h. The obtained green precipitates were collected by centrifugation and washed by ethanol several times and dried to powder by freeze-drying.

Synthesis of Ni₃(BO₃)₂: Synthesis of Ni₃(BO₃)₂ was by the method of Liu *et al.*^[2] 0.713 g of NiCl₂·6H₂O, 0.201 g of Na₂B₄O₇ and 0.088 g of NaCl were mixed in an agate-mortar and ground for 30

min. The obtained light-green powder was transferred into a porcelain-boat in a quartz tube-furnace and annealed at 800 °C in air for 2 h. Following cooling to RT the green-product was collected and washed with deionized water several times (> 3) and dried at 60 °C.

Imaging and Spectroscopic Characterization

Field-emission SEM images were collected on a FEI QUANTA 450 electron microscope. The TEM images, HAADF-STEM images, EDX analyses and EELS spectra were collected on a FEI Titan Themis 80-200 operating at 200 kV. XRD patterns were obtained using a Rigaku MiniFlex 600 X-Ray Diffractometer with Co K α radiation. XPS data were collected under ultrahigh vacuum ($< 10^{-8}$ Torr) using a monochromatic Al K α X-ray source. The absorbance data of spectrophotometer were collected on SHIMADZU UV-2600 ultraviolet-visible (UV-Vis) spectrophotometer.

2. Plasma-driven Nitrogen Oxidation Experiment

A nanosecond pulsed spark discharge system was employed to activate and dissociate N₂ and O₂ molecules to produce NO_x. The experimental setup is shown in Figure S1, which mainly consists of three parts: a plasma reactor, a power supply, and an electrical measurement system. The plasma reactor is composed of a quartz tube and two stainless-steel rods (diameter 12 mm, thickness 5 mm) that serve as the high voltage and ground electrodes, respectively. The discharge gap was fixed at 3 mm. The discharge was driven by a nanosecond pulsed power supply (HV-2015, Xi'an Smart Maple Electronic Technology Co., Ltd) with a voltage of 10 kV, rising time of 100 ns, pulse width of 100 ns, falling time of 100 ns, and repetition frequency of 1 kHz. The applied voltage and the discharge current were measured by a high voltage probe (Tektronix P6015, 75 MHz, 1000/1) and Rogowski coil (Pearson 6585, 1 V/A), then recorded by an oscilloscope (Tektronix DPO 2024).

Simulated air with a N₂ and O₂ volume ratio of 4:1 generated by an air generator was fed into the discharge chamber at a constant gas flow of 40 sccm. The outlet gas was driven into a Fourier transform infrared spectroscopy (Thermo-Fisher Nicolet iS50) equipped with a Herriott cell (volume: 100 mL) for the detection and measurement of gaseous products. After a gas flow of 20 min, the outlet gas was fed into a sealed cell containing 100 mL of 0.1 M KOH aqueous solution as the absorbent.

3. Electrochemical Measurements

Electrochemical data were collected with a CHI-650D electrochemical workstation (CHI Instrument, Inc.). An H-type cell with three-electrode system was used in the electrochemical measurement in which a graphite-rod was used as counter electrode and an Ag/AgCl (filled with saturated KCl) as reference electrode. The cathodic chamber was separated from the anodic chamber by an anion exchange membrane (Fumasep FAA-3-50). For the working electrode, 5 mg of the obtained catalyst was dispersed in 1 mL of ethanol containing 40 μ L of 5 wt% Nafion solution. The mixture was ultra-sonicated for 3 h to form a

uniform catalyst ink. 40 μL of the resulting catalyst ink was drop-cast onto a $1 \times 0.5 \text{ cm}^2$ carbon paper. All experiments were carried out at RT and all potentials were referenced against reversible hydrogen electrode (RHE) based on the Nernst equation ($E_{\text{RHE}} = E_{\text{Ag/AgCl}} + 0.0592 \times \text{pH} + 0.2$). 0.10 M KOH with various concentrations of nitrate/nitrite were used as electrolyte, which was purged with the ultra-high purity Ar throughout electrolysis process.

Measurement of electrochemically active surface area (ECSA): The ECSA was measured by a double-layer capacitance method. Cyclic Voltammetry (CV) scans were conducted at a potential range from 0.55 V to 0.65 V vs RHE with increasing scan rates of 10, 20, 30, 40 and 50 mV s^{-1} . The capacitance current densities (half the difference between the anodic current density and cathodic current density) at 0.60 V vs RHE were plotted against scan rates, and the double-layer capacitance (C_{dl} , mF cm^{-2}) was derived from the slope.

4. Product Quantification

Quantification of ammonia: The product ammonia was quantitatively determined by the indophenol blue method. Briefly, 5.0 g of sodium salicylate and 5.0 g of potassium sodium tartrate were dissolved in 100.0 mL of 1.0 M NaOH to prepare the chromogenic reagent (Reagent A). 3.50 mL of sodium hypochlorite (available chlorine 10% to 15%) was added to deionized water and diluted to 100.0 mL to prepare the oxidizing reagent (Reagent B). 0.20 g of sodium nitroferricyanide was dissolved in 20.0 mL of deionized water to obtain the catalysing reagent (Reagent C).

To quantitatively determine the amount of ammonia, 2.0 mL of diluted sample solution was added to a test tube, to which 2.0 mL of Reagent A, 1.0 mL of Reagent B and 0.20 mL of Reagent C were successively added. Following mixing and left-standing for 1 h the absorption spectra were collected on UV-vis spectrophotometer using a standard 1 cm quartz cuvette. The concentration-dependent absorption spectra were calibrated using standard ammonia chloride solutions with varying concentration (Figure S4).

Quantification of nitrate: Nitrates exhibit typical absorption to ultraviolet light at a wavelength of 220 nm, where the absorbance value is proportional to concentration of nitrate. In a typical procedure, 5.0 mL of standard solution, or (diluted) sample solution was added to a test-tube followed by addition of 0.10 mL of 6.0 M HCl solution. Following shaking and left-standing for 5 min the concentration of NO_3^- was measured using UV-vis spectrophotometer at wavelength range from 200 to 300 nm. The standard curve for NO_3^- determination was plotted with absorbance value difference at 220 nm and 275 nm as y-axis (ordinate) and concentration of NO_3^- as x-axis (abscissa). The concentration-dependent absorption spectra were calibrated using standard potassium nitrate (KNO_3) solution of varying concentration (Figure S2).

Quantification of nitrite: Nitrites (NO_2^-) can be diazotized by sulfanilamide under acid environment, and the diazotized compound can be coupled with N-(1-Naphthyl) ethylenediamine dihydrochloride, producing pink azo dyes that show typical absorption at a wavelength of 540 nm.

To prepare the chromogenic reagent, 0.50 g of sulfanilamide was dissolved in 50.0 mL of 2.0 M HCl solution to prepare sulfanilamide solution (Reagent A). 20.0 mg of N-(1-Naphthyl) ethylenediamine dihydrochloride was dissolved in 20.0 mL of deionized water to prepare N-(1-Naphthyl) ethylenediamine dihydrochloride solution (Reagent B). In a typical procedure, 5.0 mL of standard solutions or samples were added to the test tubes, followed by addition of 0.10 mL of Reagent A. Following mixing and left standing for 10 min, 0.10 mL of Reagent B was added to the solution. The solution was then shaken and allowed to stand for 30 min, and the concentration of NO_2^- was measured using UV-vis spectrophotometer at wavelength range from 450 nm to 650 nm. The standard curve for NO_2^- determination was plotted with the absorbance value difference at 540 nm and 650 nm as y-axis and the concentration of NO_2^- as x-axis. The concentration-dependent absorption spectra were calibrated using standard potassium nitrite (KNO_2) solutions with different known concentrations (Figure S3).

Quantification of gas product: H_2 was detected via a gas chromatograph (GC, 8890B, Agilent) equipped with a thermal conductivity detector (TCD) and flame ionization detector (FID).

5. Computation of Faradaic Efficiency and Yield

Faradaic efficiency (FE) was computed by dividing the charge used for a product synthesis by the total charge consumption (Q), namely:

For nitrate to ammonia this is given by;

$$\text{FE} = (8 \times F \times C(\text{NH}_3) \times V) / Q \quad (1)$$

For nitrite to ammonia, by;

$$\text{FE} = (6 \times F \times C(\text{NH}_3) \times V) / Q \quad (2)$$

For nitrate to nitrite, by;

$$\text{FE} = (2 \times F \times C(\text{NO}_2^-) \times V) / Q \quad (3)$$

where F is Faraday constant (96485 C mol^{-1}), C measured concentration ($\mu\text{mol L}^{-1}$) and V volume of electrolyte (L).

The yield rate of ammonia, $v(\text{NH}_3)$, was computed from:

$$v(\text{NH}_3) = (C(\text{NH}_3) \times V) / (t \times A) \quad (4)$$

where t is reaction time (h) and A effective area of electrode (cm^2).

6. In situ Measurements

In situ Raman: *In situ* Raman measurement was conducted on a confocal Raman microscope (HORIBA LabRAM HR Evolution) equipped with a 532 nm laser. An 1800 gr cm^{-1} grating was used for

all measurements. The electrochemical tests were conducted in a three-electrode electrochemical cell with a quartz window. A graphite rod and an Ag/AgCl (filled with saturated KCl) were used, respectively, as the counter and reference electrode. A glassy-carbon plate loaded with catalyst was used as the working electrode, and 0.10 M KOH with 10 mM NO_3^- as electrolyte. The Raman spectra were collected at the applied potential every five accumulations (10 s per accumulation).

***In situ* ATR-SEIRAS measurement:** *In situ* ATR-SEIRAS was performed on a Nicolet iS20 spectrometer equipped with an HgCdTe (MCT) detector cooled with liquid nitrogen and a VeeMax III (PIKE technologies) accessory. The electrochemical test was conducted in a custom-made three-electrode electrochemical single-cell. A Pt-wire and a saturated Ag/AgCl were used as counter and reference electrode. A fixed-angle Ge prism (60°) was used to load catalysts and served as the working electrode. The Au thin-layer was coated according to reported method with slight modification.^[3] The reflecting plane of the Ge prism was polished with diamond compound (0.05 μm , Kemet. Int. Ltd.), and sonicated in ethanol and water. The surface was contacted with 40% NH_4F for 90 s. Deposition of Au was performed at a temperature of 60 $^\circ\text{C}$ by immersing the reflecting plane of the prism in a mixture of a plating solution (0.015 M $\text{NaAuCl}_4 \cdot 2\text{H}_2\text{O}$ + 0.15 M Na_2SO_3 + 0.05 M $\text{Na}_2\text{S}_2\text{O}_3 \cdot 5\text{H}_2\text{O}$ + 0.05 M NH_4Cl) and 2% hydrofluoric acid (1:2 by vol) for 5 min, after which the prism was rinsed with Milli-Q water. For ATR-SEIRAS measurement, 32 scans were collected with a spectral resolution of 4 cm^{-1} for each spectrum.

Results and Discussion

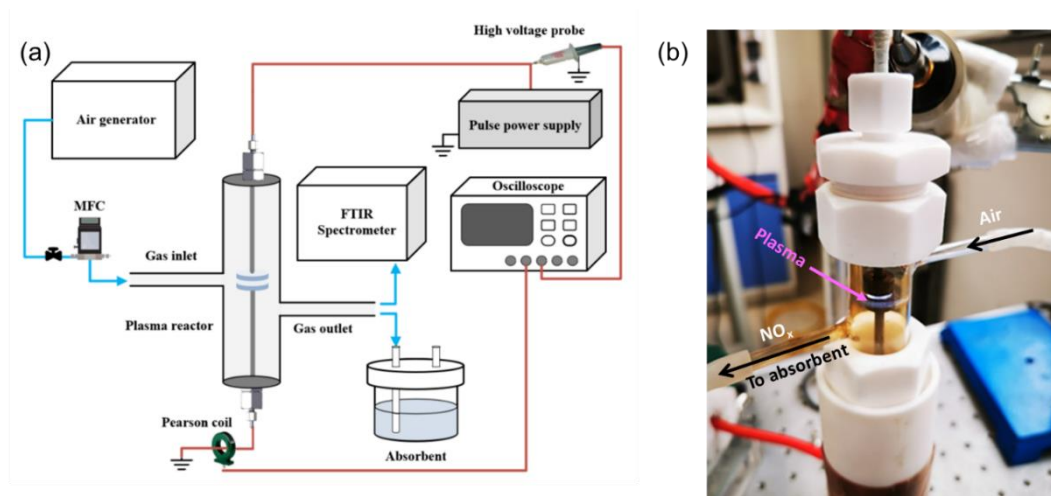


Figure S1. (a) Scheme for apparatus for plasma-driven N₂ oxidation. Gas product (NO_x) was quantified by Fourier transform infrared spectroscopy (FTIR). (b) Photograph of the plasma reaction chamber.

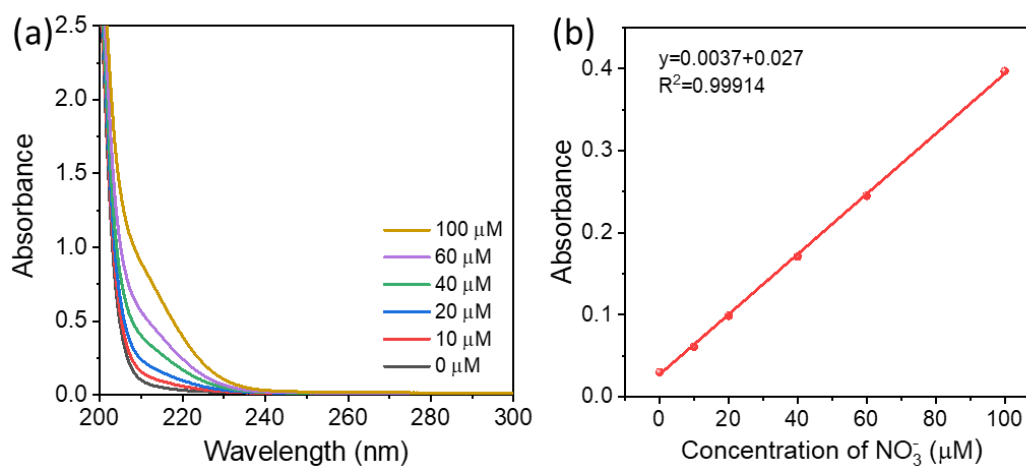


Figure S2. Calibration curves for nitrate concentration.

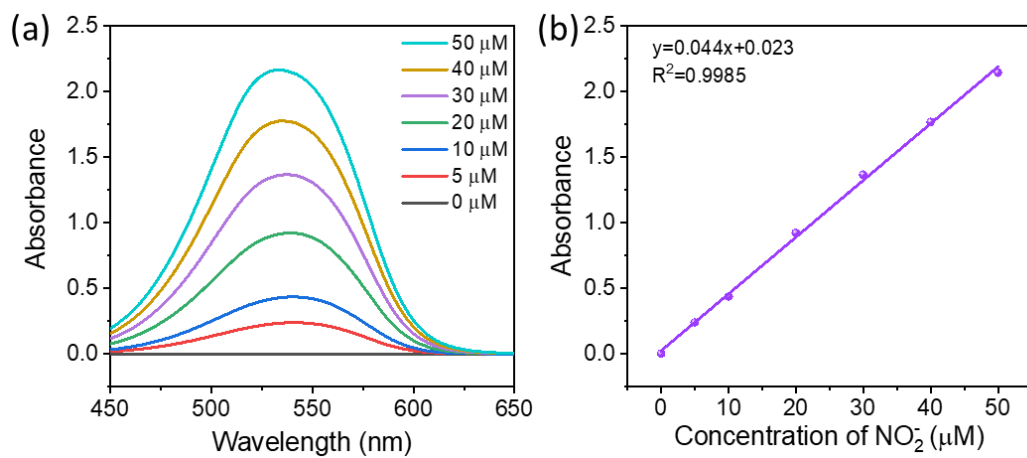


Figure S3. Calibration curves for nitrite concentration.

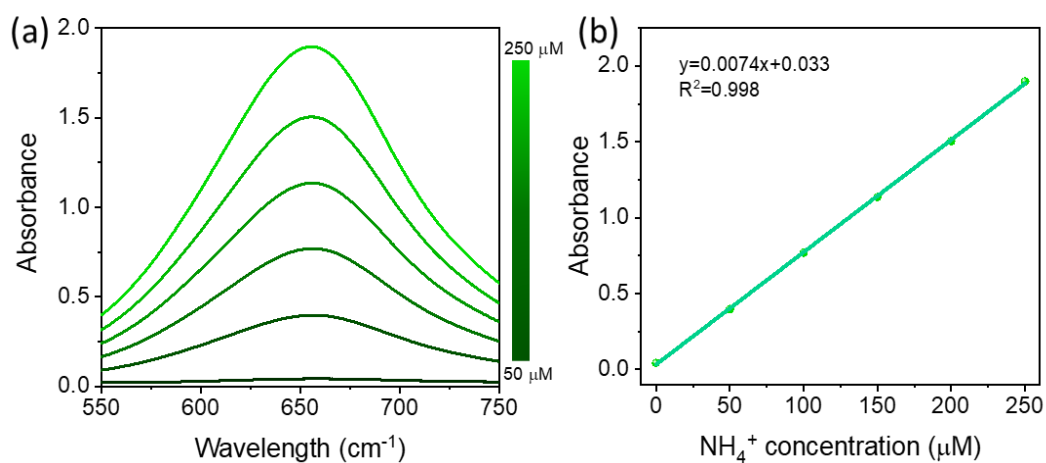


Figure S4. Calibration curves for NH₄⁺ concentrations.

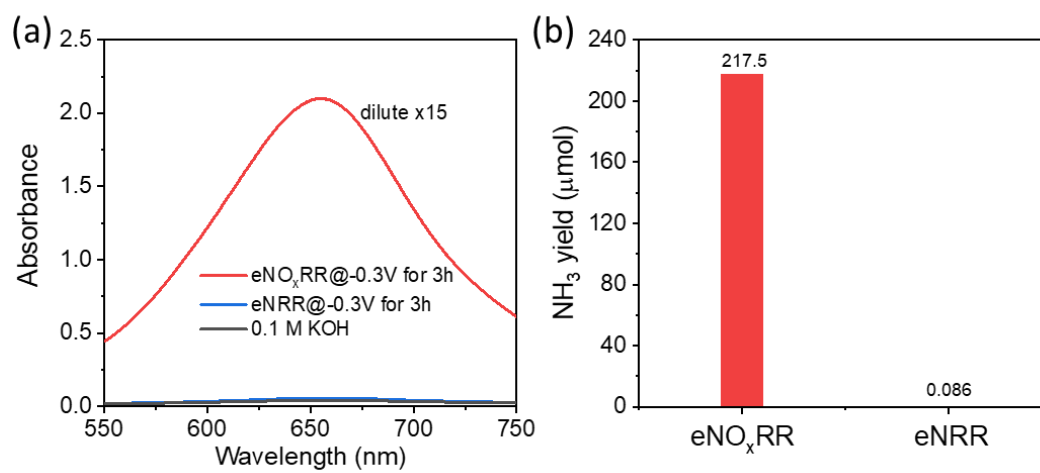


Figure S5. Comparison between the ammonia yield from the two-step N₂ fixation and eNRR process.

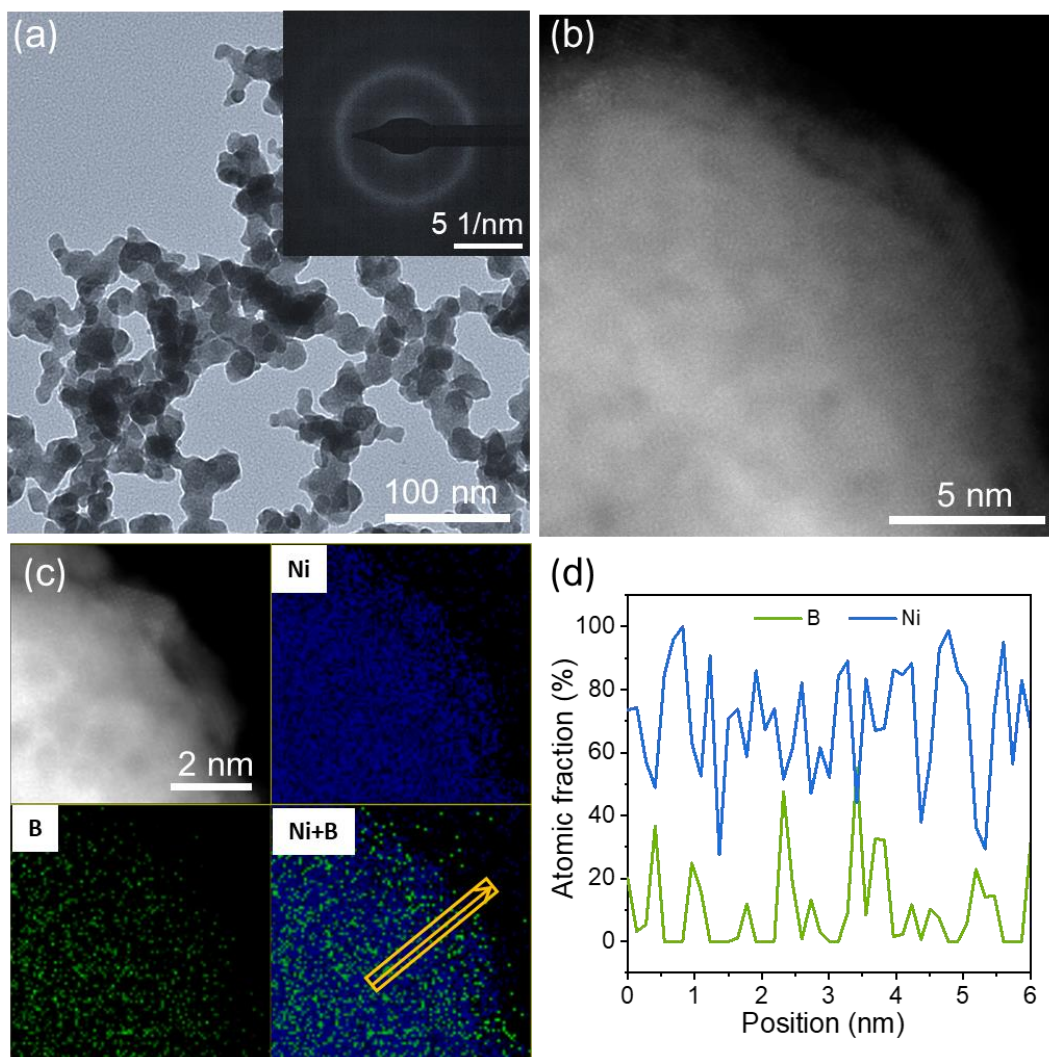


Figure S6. Microscopic characterization of $\text{Ni}_3\text{B}@ \text{NiB}_{0.72}$. (a) TEM image of $\text{Ni}_3\text{B}@ \text{NiB}_{0.72}$. Inset shows selected area electron diffraction pattern. (b) High-resolution TEM image showing amorphous structure. (c) EDX mapping showing distribution of B and Ni. (d) EDX linear-scan of selected area in (c).

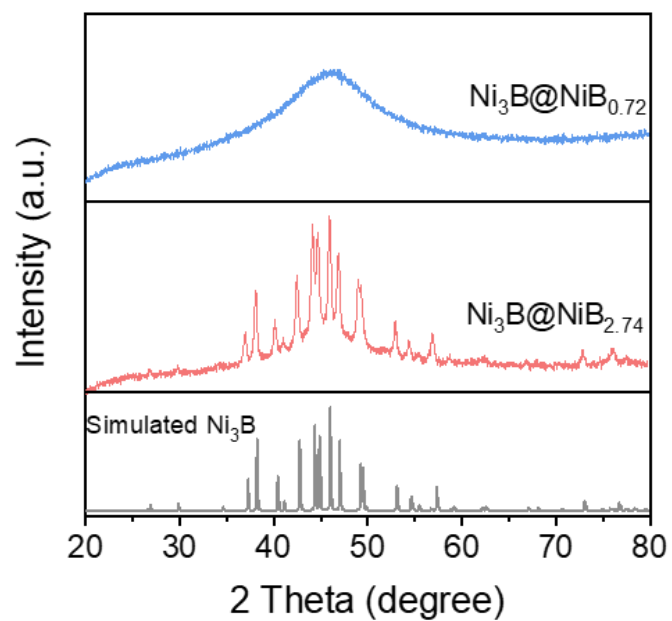


Figure S7. XRD patterns for $\text{Ni}_3\text{B@NiB}_{2.74}$ and $\text{Ni}_3\text{B@NiB}_{0.72}$.

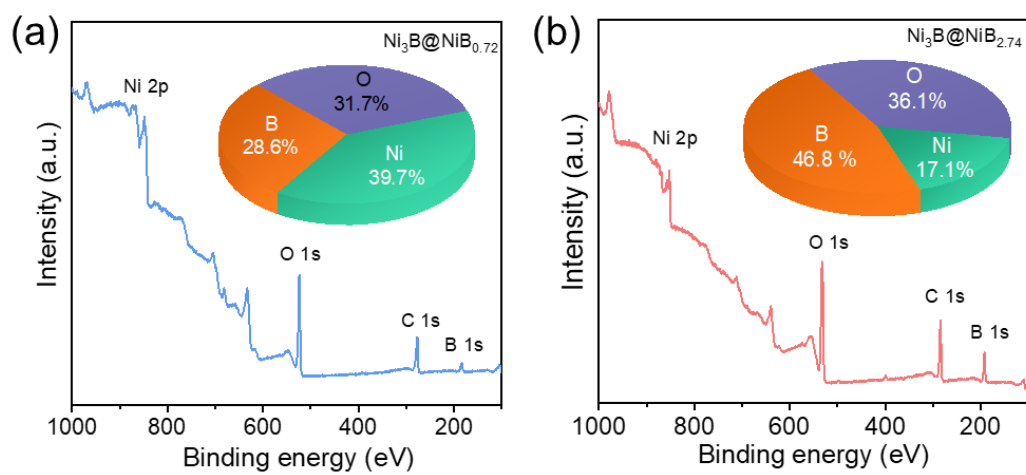


Figure S8. Surface atomic content of boron and nickel from XPS survey results.

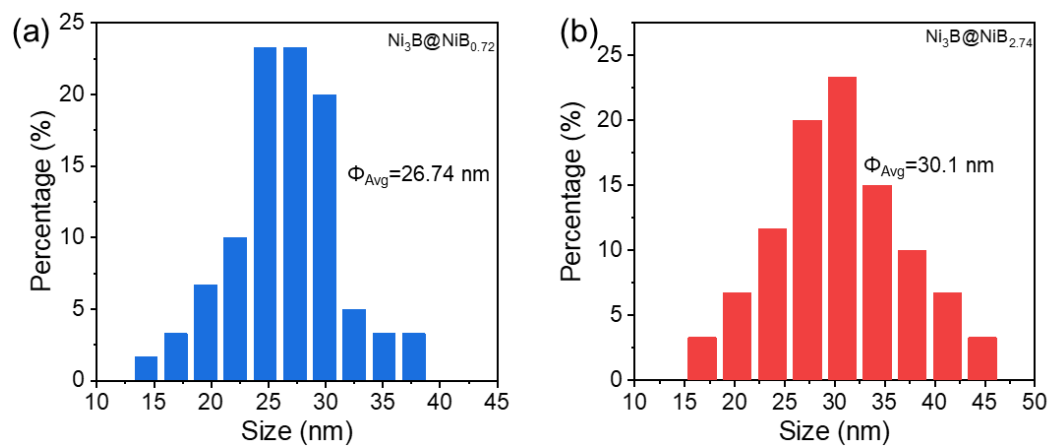


Figure S9. Particle size distribution for (a) $\text{Ni}_3\text{B}@\text{NiB}_{0.72}$ and (b) $\text{Ni}_3\text{B}@\text{NiB}_{2.74}$.

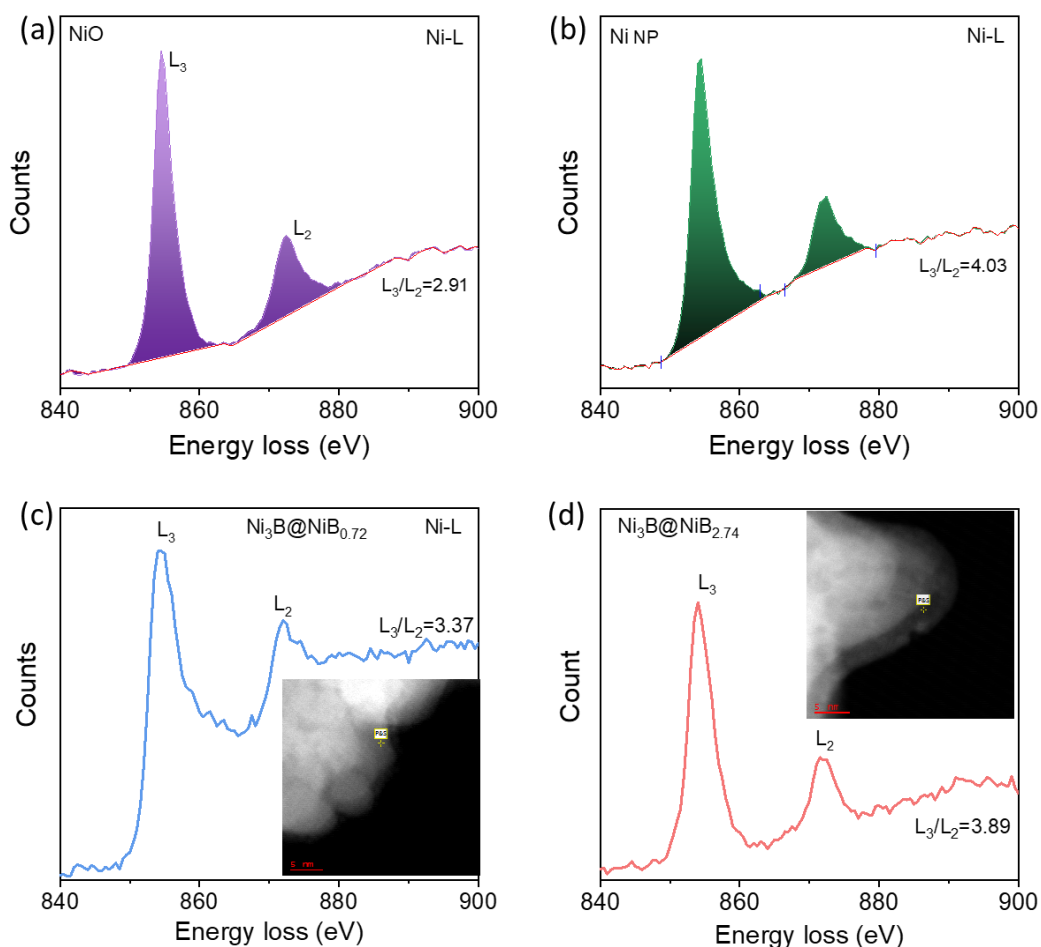


Figure S10. Ni-L EELS spectra for (a) NiO representing Ni^{2+} signal, (b) Ni NP representing Ni^0 signal, (c) surface region of $\text{Ni}_3\text{B@NiB}_{0.72}$, and (d) surface region of $\text{Ni}_3\text{B@NiB}_{2.74}$.

Note: EELS spectra were employed to determine the valence state of nickel sites on surface of the materials. It is known that the L_3/L_2 area ratio is significantly sensitive to the oxidation state of metals.^[4] The L_3/L_2 area ratio increases as the oxidation states of transition metals decrease.^[5, 6] Figure S10a and b show Ni-L edge EELS spectra adopted from the bulk area of the as-prepared NiO and Ni NP, representing the Ni^{2+} and Ni^0 signal, respectively. L_3/L_2 ratio values of 2.91 and 4.03 were obtained for Ni^{2+} and Ni^0 signals, respectively. Figure S10c and d show the Ni-L edge profiles adopted from the surface region of two samples. The L_3/L_2 area ratio on the surface of $\text{Ni}_3\text{B@NiB}_{0.72}$ and $\text{Ni}_3\text{B@NiB}_{2.74}$ were calculated to be 3.37 and 3.89, respectively, further suggesting the lower valence state of nickel on surface of $\text{Ni}_3\text{B@NiB}_{2.74}$ as compared with $\text{Ni}_3\text{B@NiB}_{0.72}$.

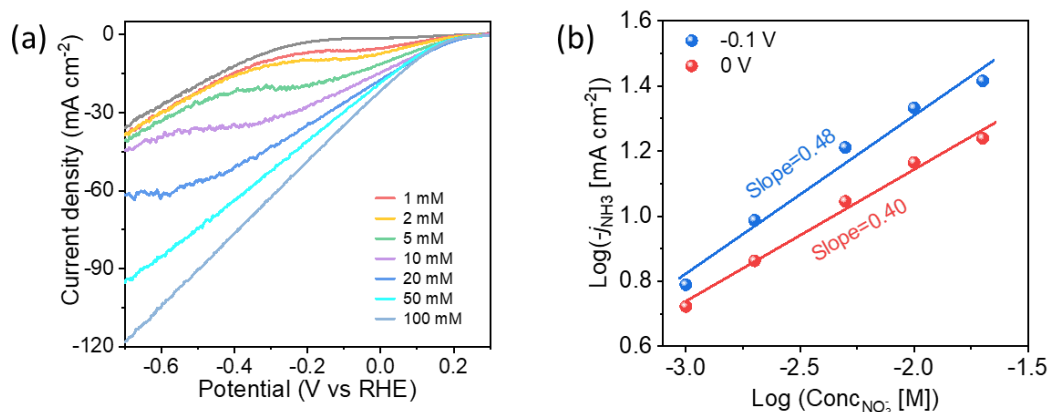


Figure S11. (a) LSV curves for $\text{Ni}_3\text{B@NiB}_{2.74}$ in 0.10 M KOH with varying nitrate concentration. (b) Reaction order with respect to NO_3^- concentration at 0 and -0.1 V vs RHE adopted from (a).

Note: The reaction order determination experiments were conducted by LSV under supplement addition of varying concentration of NO_3^- using $\text{Ni}_3\text{B@NiB}_{2.74}$ as catalyst. Current densities at 0 V and -0.1 V vs RHE were adopted because at these potentials the mass transfer of NO_3^- is not limited. The reaction order was obtained by plotting logarithm of NH_3 partial current density as y -axis and logarithm of nitrate concentrations as x -axis. According to the Rate Law, the slope represents the value of the reaction order. As is shown in Figure S11b, the low value reaction orders indicate a near zeroth order dependency for cathodic current with respect to nitrate concentration, suggesting favourable kinetics for eNO_3RR to NH_3 on $\text{Ni}_3\text{B@NiB}_{2.74}$.^[7, 8]

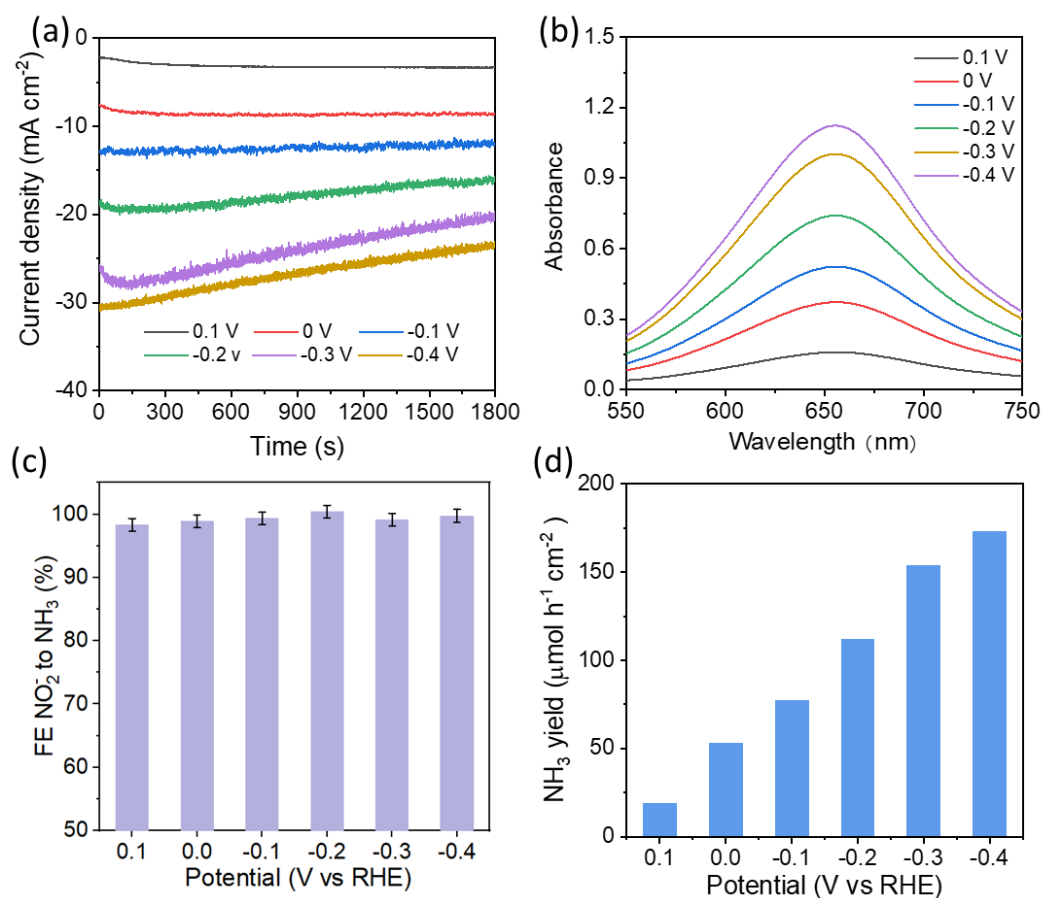


Figure S12. Nitrite reduction performance on $\text{Ni}_3\text{B@NiB}_{2.74}$ measured in 0.10 M KOH with 10 mM KNO_2 . (a) I-t curves for nitrite reduction on $\text{Ni}_3\text{B@NiB}_{2.74}$. (b) UV-vis spectra stained with indophenol indicator for $\text{Ni}_3\text{B@NiB}_{2.74}$ at varying potential (all sample solutions were diluted 10 x times before indophenol blue test). (c) Faradaic efficiency (FE). (d) Ammonia production rate for nitrite reduction to ammonia at varying potentials.

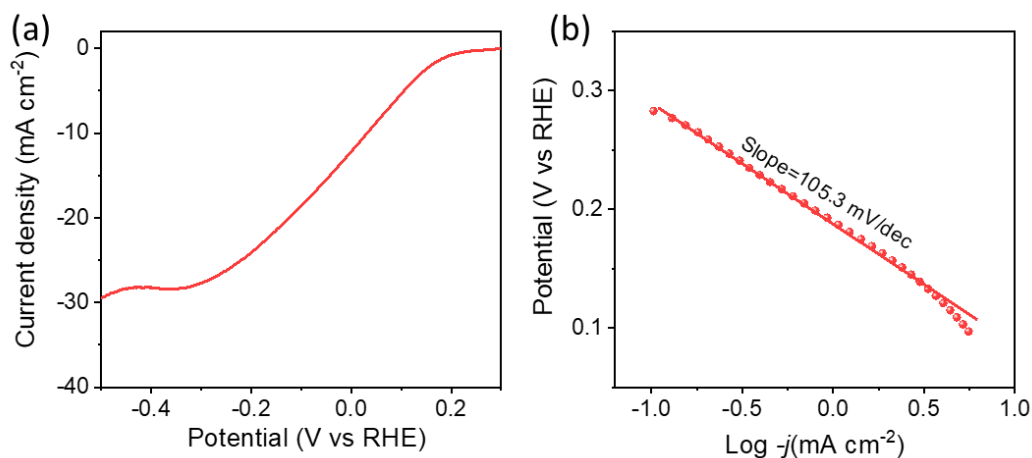


Figure S13. (a) LSV curve for nitrate reduction on $\text{Ni}_3\text{B@NiB}_{2.74}$ on rotating disk electrode (RDE) at a scan rate of 10 mV s^{-1} and rotating speed of 1600 rpm in 0.10 M KOH with 10 mM KNO_3 . (b) Corresponding Tafel slope collected in the kinetic control region in (a).

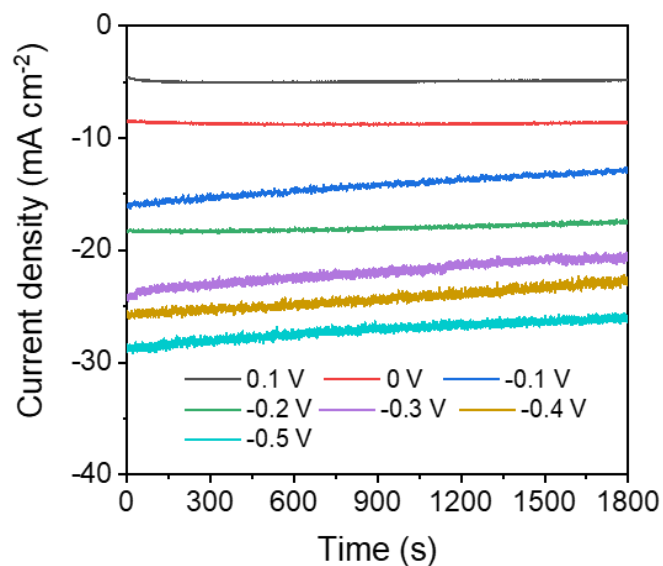


Figure S14. I-t curves for e NO_3RR on $\text{Ni}_3\text{B@NiB}_{2.74}$ in 0.10 M KOH with 10 mM NO_3^- .

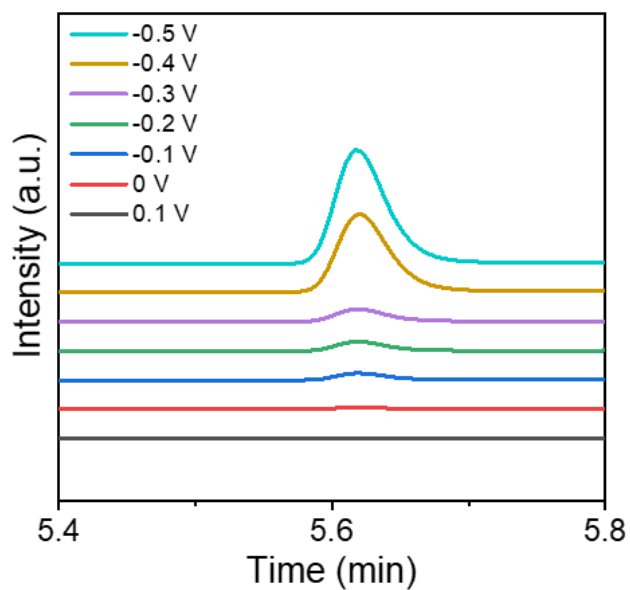


Figure S15. GC results for H₂ production at varying potential during eNO₃RR on Ni₃B@NiB_{2.74} in 0.10 M KOH with 10 mM NO₃⁻.

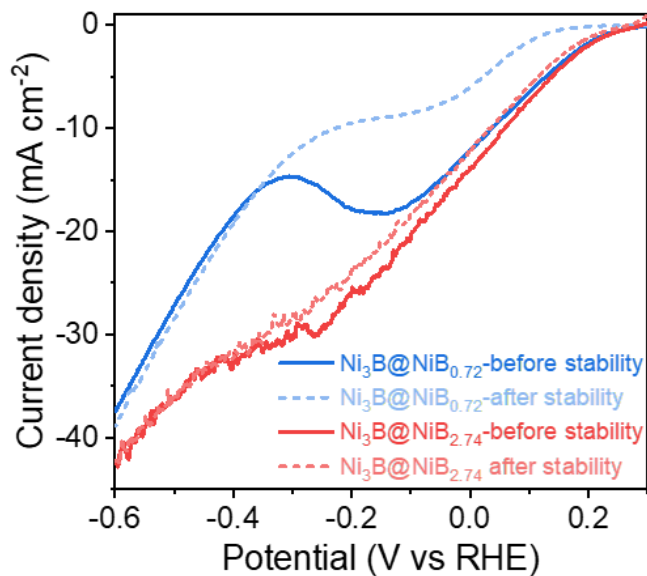


Figure S16. LSV curves before and after stability test for Ni₃B@NiB_{2.74} and Ni₃B@NiB_{0.72}.

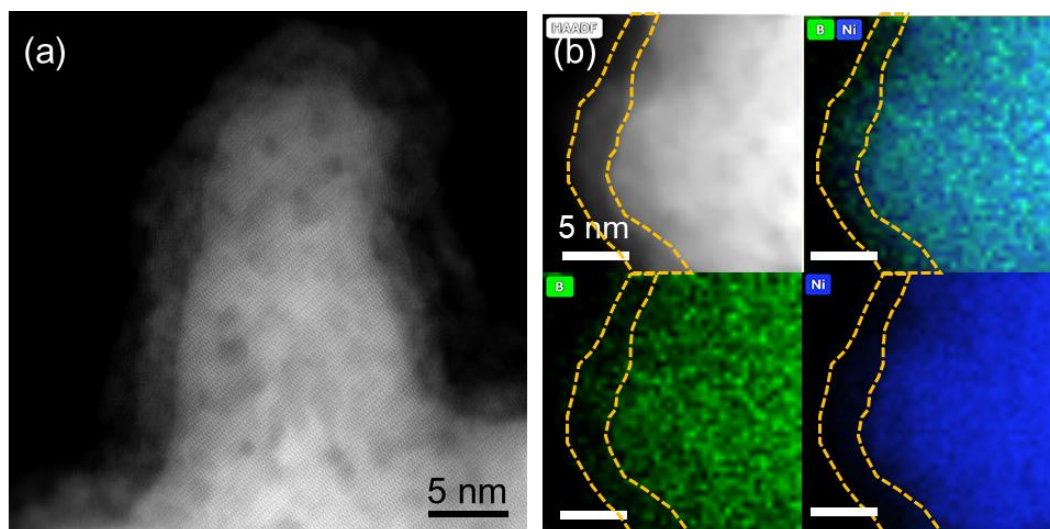


Figure S17. (a) TEM image and (b) elemental mapping images of $\text{Ni}_3\text{B}@\text{NiB}_{2.74}$ after stability test.

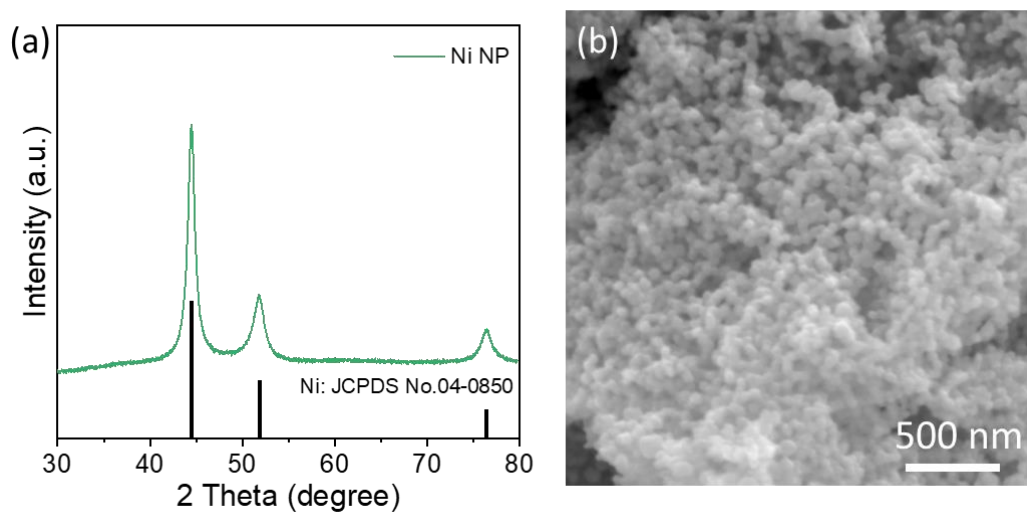


Figure S18. (a) XRD pattern and (b) SEM image for Ni NP.

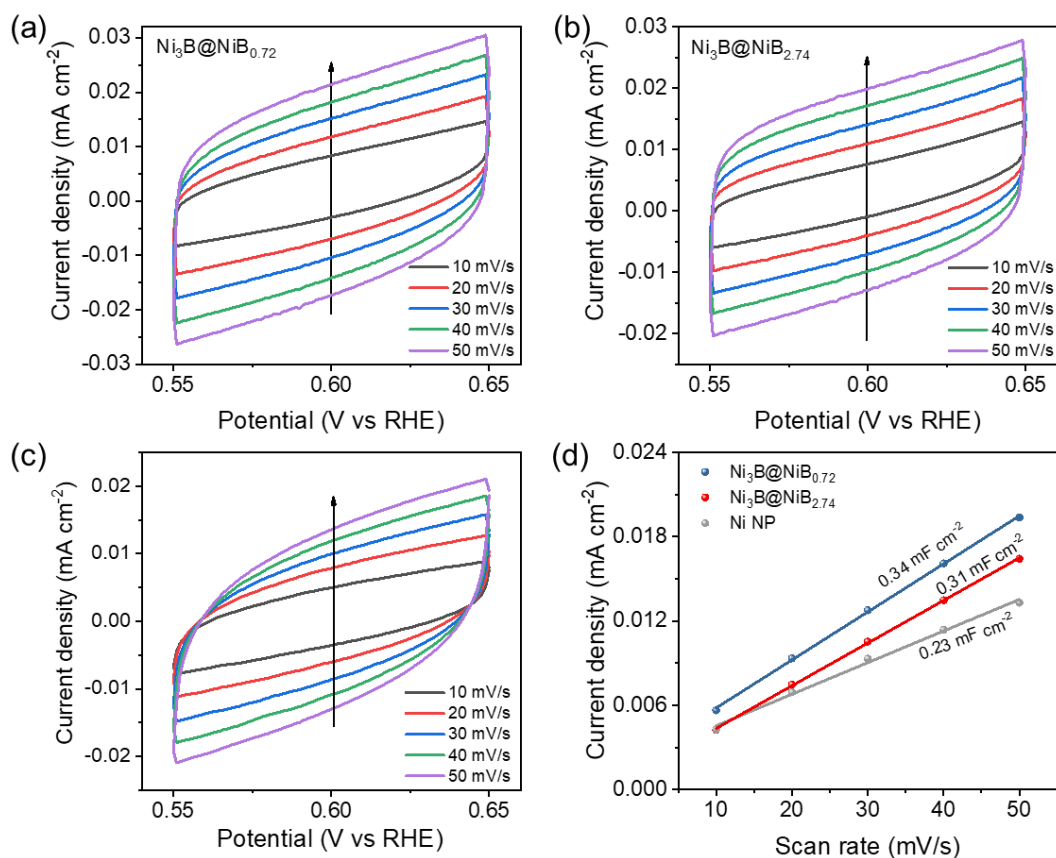


Figure S19. Determination of electrochemically active surface area. (a-c) CV curves for $\text{Ni}_3\text{B@NiB}_{0.72}$, $\text{Ni}_3\text{B@NiB}_{2.74}$ and Ni NP obtained in the capacitance region at varying scan rate. (d) Capacitance current density at 0.6 V vs. RHE as a function of scan rate. Note that the slope represents the double-layer capacitance (C_{dl}), which is positively related to electrochemically active surface area.

Note: The C_{dl} for $\text{Ni}_3\text{B@NiB}_{2.74}$ is calculated to be 0.31 mF cm⁻², slightly less than that for $\text{Ni}_3\text{B@NiB}_{0.72}$ (0.34 mF cm⁻²). This can be ascribed to the slight increase in particle size following annealing. Despite a lower ECSA, $\text{Ni}_3\text{B@NiB}_{2.74}$ exhibits significantly better eNO₃RR performance than that of $\text{Ni}_3\text{B@NiB}_{0.72}$, indicating that the higher electrochemical activity of the $\text{Ni}_3\text{B@NiB}_{2.74}$ originates from the surface boron-rich feature, rather than the difference in ECSA.

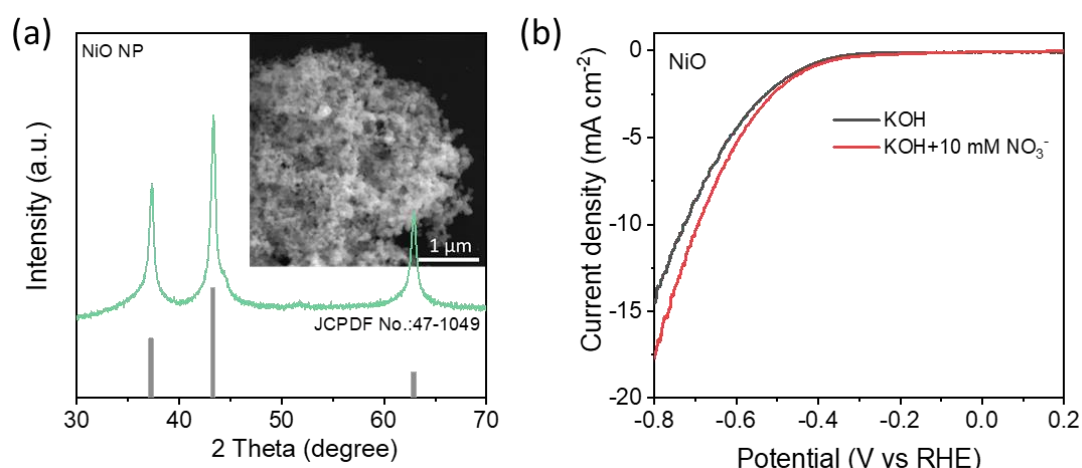


Figure S20. (a) XRD pattern for NiO nanoparticles sample. Inset shows corresponding SEM image. (b) LSV curves for NiO nanoparticles in 0.10 M KOH with and without 10 mM NO_3^- .

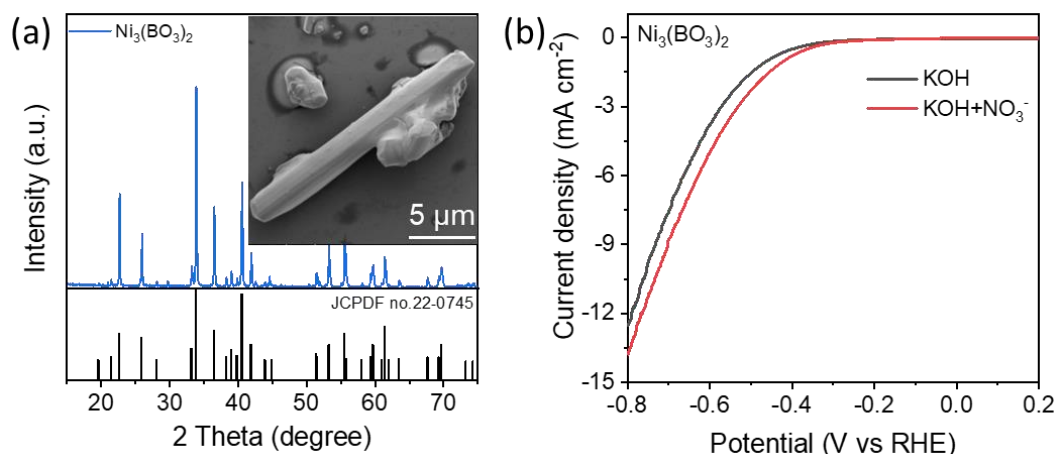


Figure S21. LSV curves for $\text{Ni}_3(\text{BO}_3)_2$ in 0.10 M KOH with and without 10 mM NO_3^- .

Note: A series of control experiments to examine the influence of oxygen on eNO_3RR were carried out because oxygen is unavoidable when handling the materials. When annealing $\text{Ni}_3\text{B@NiB}_{0.72}$ in air, the obtained NiO shows significantly degraded eNO_3RR performance (Figure S20). Because oxygen can exist in the form of nickel borate, we further synthesized a nanorod-like $\text{Ni}_3(\text{BO}_3)_2$. LSV measurement shows that $\text{Ni}_3(\text{BO}_3)_2$ exhibits very weak eNO_3RR activity (Figure S21). It is therefore concluded that surface oxygen and Ni^{2+} sites contributes little to eNO_xRR activity.

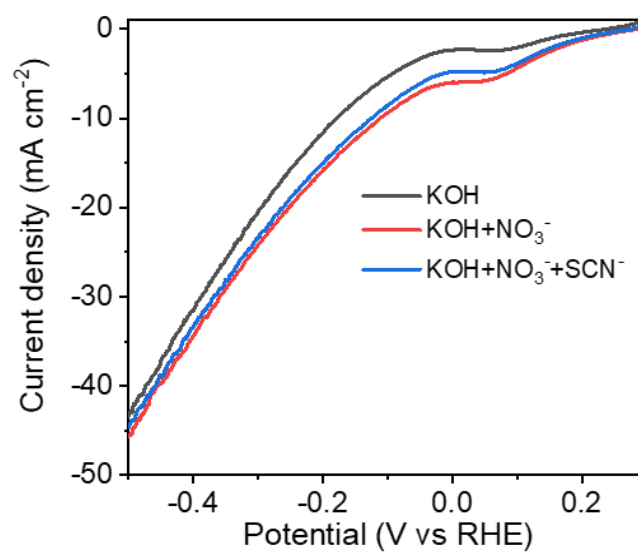


Figure S22. Result of KSCN poisoning experiment of Ni NP.

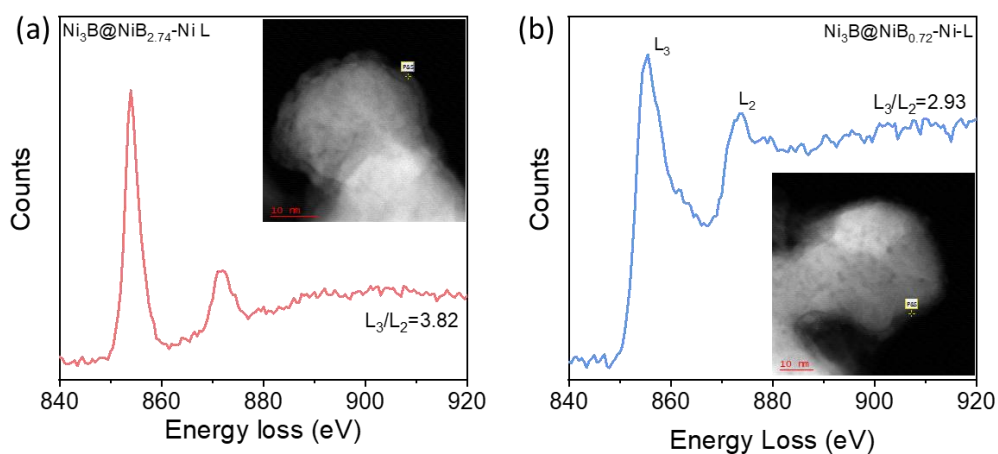


Figure S23. Ni-L EELS spectra for the surface region of (a) $\text{Ni}_3\text{B@NiB}_{2.74}$ and (b) $\text{Ni}_3\text{B@NiB}_{0.72}$ after long-term stability test.

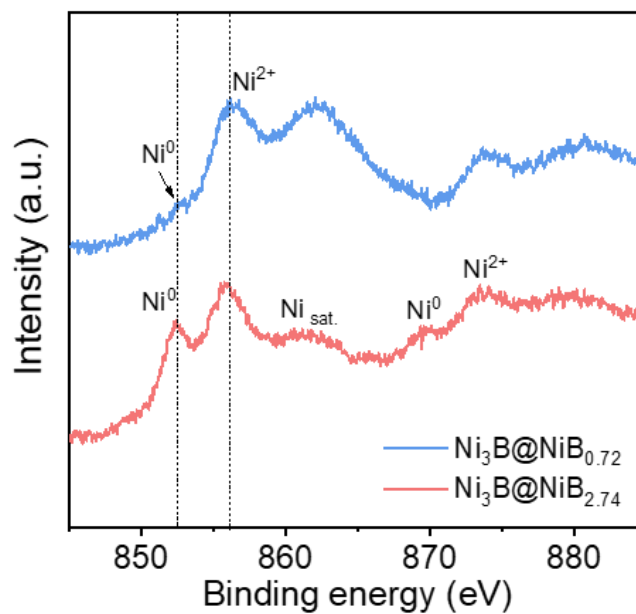


Figure S24. XPS spectra for $\text{Ni}_3\text{B@NiB}_{2.74}$ and $\text{Ni}_3\text{B@NiB}_{0.72}$ after long-term stability test.

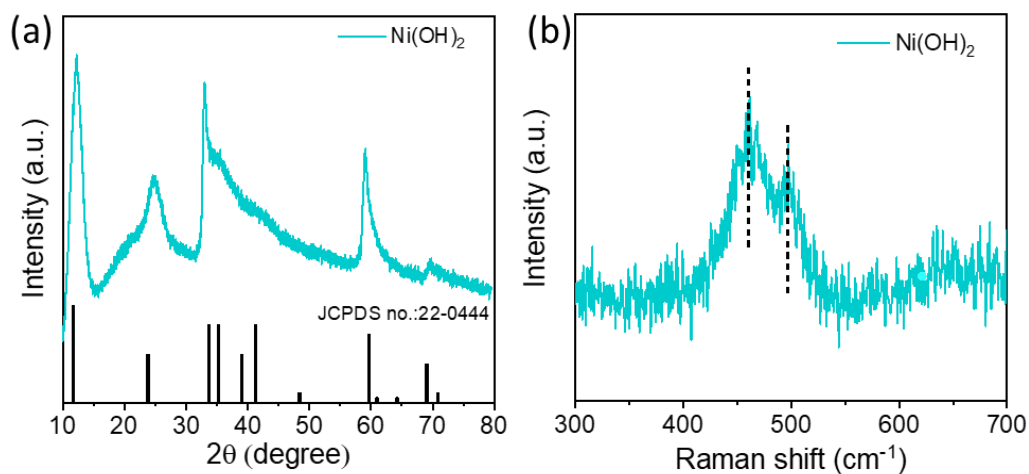


Figure S25. (a) XRD pattern and (b) Raman spectrum for as-synthesized $\text{Ni}(\text{OH})_2$.

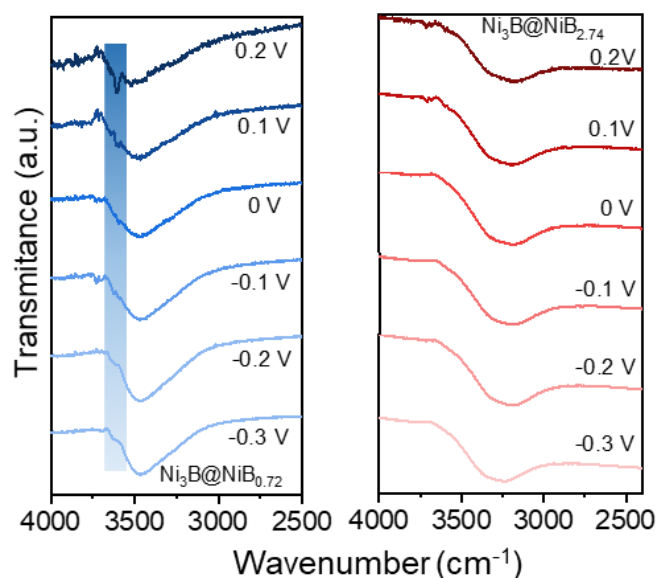


Figure S26. *In situ* ATR-SEIRAS for $\text{Ni}_3\text{B@NiB}_{0.72}$ (left) and $\text{Ni}_3\text{B@NiB}_{2.74}$ (right). Spectrum measured at open-circuit potential (OCP) was adopted as background spectrum.

Note: The sharp peak at a wavenumber $\sim 3611 \text{ cm}^{-1}$ on $\text{Ni}_3\text{B@NiB}_{0.72}$ can be attributed to the O–H vibration of hydrogen-bonded hydroxyl group in $\text{Ni}(\text{OH})_2$.^[9] The absence of this peak for $\text{Ni}_3\text{B@NiB}_{2.74}$ further demonstrates the alleviated formation of $\text{Ni}(\text{OH})_2$ thin-layer.

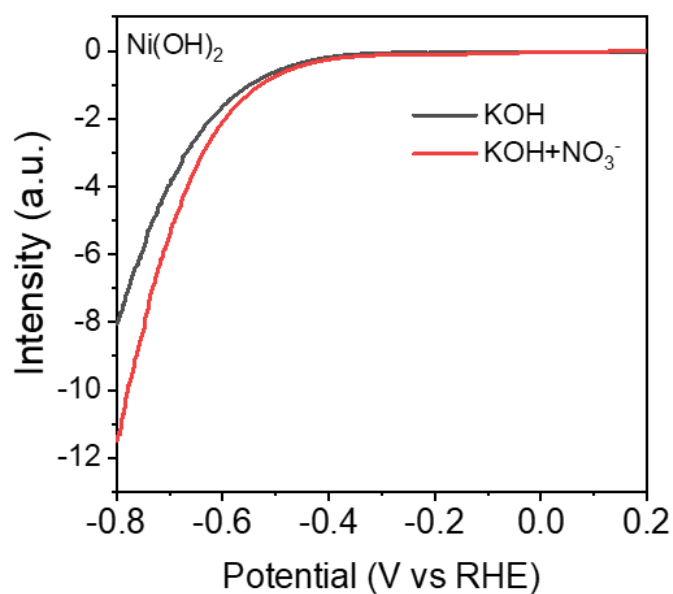


Figure S27. LSV curves for $\text{Ni}(\text{OH})_2$ in 0.10 M KOH with and without 10 mM NO_3^- .

Table S1. Comparison of batch experiment performance of Ni₃B@NiB_{2.74} with reported catalysts under ambient conditions.

Catalyst	Electrolyte	Potential or current density	Performance	Reference
Ni ₃ B@NiB _{2.74}	0.10 M KOH with ~ 4.5 mM NO _x ⁻	-0.3 V <i>vs</i> RHE	96.5% NO _x ⁻ consumption, 96.7% NH ₄ ⁺ yield in 3 h	This work
0.5% Zr-Ni	200 ppm NaNO ₃	/	100% NO ₃ ⁻ consumption, 89.5% NH ₄ ⁺ yield in 12 h	[10]
Ni	0.5 g L ⁻¹ Na ₂ SO ₄ with 50 mg mL ⁻¹ NO ₃ ⁻	/	36% NO ₃ ⁻ consumption, 25% NH ₄ ⁺ yield in 4 h	[11]
Ni NP	0.01 M NaOH with 10 mM NO ₃ ⁻	-1.1 V cell voltage	18% NO ₃ ⁻ consumption, 100% NH ₄ ⁺ yield in 24 h	[12]
Cu ₇₀ Ni ₃₀	0.01 M NaOH with 10 mM NO ₃ ⁻	-1.1 V cell voltage	71.5% NO ₃ ⁻ consumption, 75% NH ₄ ⁺ yield in 24 h	[12]
Ni	1 M NaOH with 20 mM NO ₃ ⁻	-1.2 V <i>vs</i> Hg/HgO	15.5% NO ₃ ⁻ consumption, 58% NH ₄ ⁺ yield in 24 h	[13]
Cu ₈₀ Ni ₂₀	1 M NaOH with 20 mM NO ₃ ⁻	-1.2 V <i>vs</i> Hg/HgO	50% NO ₃ ⁻ consumption, 88% NH ₄ ⁺ yield in 4 h	[13]
Cu ₈₀ Ni ₂₀	1 M NaOH with 20 mM NO ₂ ⁻	-1.2 V <i>vs</i> Hg/HgO	80% NO ₂ ⁻ consumption, 96% NH ₄ ⁺ yield in 4 h	[13]
Cu NS	0.1 M Na ₂ SO ₄ with 140 ppm NO ₃ ⁻	-20 mA cm ⁻²	99.7% NO ₃ ⁻ consumption, 93.3% NH ₄ ⁺ yield in 6 h	[14]
Cu NP	0.1 M K ₂ SO ₄ with 0.05 M NO ₃ ⁻	-1.5 V <i>vs</i> Ag/AgCl	90% NO ₃ ⁻ consumption, 77.3% NH ₄ ⁺ yield in 12 h	[15]
Cu ₆₀ Zn ₄₀	0.1 M K ₂ SO ₄ with 0.05 M NO ₃ ⁻	-1.5 V <i>vs</i> Ag/AgCl	99.1% NO ₃ ⁻ consumption, 75.2% NH ₄ ⁺ yield in 12 h	[15]
Cu/Cu ₂ O NWAs	0.5 M Na ₂ SO ₄ with 200 ppm NO ₃ ⁻	-0.85 V <i>vs</i> RHE	95.8% NO ₃ ⁻ consumption, 81.2% NH ₄ ⁺ yield in 2 h	[16]
TiO _{2-x} /CP	0.5 M Na ₂ SO ₄ with 50 ppm NO ₃ ⁻	-1.6 V <i>vs</i> SCE	95% NO ₃ ⁻ consumption, 87% NH ₄ ⁺ yield in 2 h	[17]

Table S2. Comparison of eNO₃RR activity of Ni₃B@NiB_{2.74} with previously reported catalysts under ambient conditions.

Catalyst	Electrolyte	Highest FE @ potential	NH ₃ yield rate (μmol cm ⁻² h ⁻¹)	Reference
Ni ₃ B@NiB _{2.74}	0.10 M KOH with 10 mM NO ₃ ⁻	98.7% @ -0.4 V vs RHE	107.1	This work
Ni ₃ B@NiB _{2.74}	0.10 M KOH with 100 mM NO ₃ ⁻	100% @ -0.2 V vs RHE	198.3	This work
Ni ₃ B@NiB _{2.74}	0.10 M KOH with 10 mM NO ₂ ⁻	100% @ -0.2 V vs RHE	172.9	This work
Ni NP	1 M NaOH with 20 mM NO ₃ ⁻	46.3% @ -1.2 V vs Hg/HgO	/	[13]
Cu/PTCDA	0.1 M PBS with 500 ppm NO ₃ ⁻	77% @ -0.4 V vs RHE	51.5	[18]
Cu/Cu ₂ O NWAs	0.5 M Na ₂ SO ₄ with 200 ppm NO ₃ ⁻	97% @ -0.85 V vs RHE	244	[16]
oxo-MoS _x	1 M PBS with 0.1 M NO ₃ ⁻	96% @ 0 V vs RHE	/	[8]
Cu nanosheet	0.1 M KOH with 10 mM NO ₃ ⁻	99.7% @ -0.15 V vs RHE	4.6	[19]
Cu ₅₀ Ni ₅₀	1 M KOH with 10 mM NO ₃ ⁻	93% @ -0.15 V vs RHE	/	[20]
TiO _{2-x} /CP	0.5 M Na ₂ SO ₄ with 50 ppm NO ₃ ⁻	85% @ -1.6 V vs SCE	50	[17]
Ru-ST-0.6	1 M KOH with 1 M NO ₃ ⁻	Near 100% @ -0.2 V vs RHE	1170	[21]

References

- [1] X. Yu, J. Zhao, L.-R. Zheng, Y. Tong, M. Zhang, G. Xu, C. Li, J. Ma, G. Shi, *ACS Energy Lett.* **2018**, *3*, 237-244.
- [2] X. Liu, W. Zhu, X. Cui, T. Liu, Q. Zhang, *Powder Technol.* **2012**, *222*, 160-166.
- [3] H. Miyake, S. Ye, M. Osawa, *Electrochem. Commun.* **2002**, *4*, 973-977.
- [4] R. D. Leapman, L. A. Grunes, P. L. Fejes, *Phys. Rev. B* **1982**, *26*, 614-635.
- [5] T. Riedl, T. Gemming, K. Wetzig, *Ultramicroscopy* **2006**, *106*, 284-291.
- [6] Y. Koyama, T. Mizoguchi, H. Ikeno, I. Tanaka, *J. Phys. Chem. B* **2005**, *109*, 10749-10755.
- [7] A. C. A. de Vooy, R. A. van Santen, J. A. R. van Veen, *J. Mol. Catal. A: Chem.* **2000**, *154*, 203-215.
- [8] Y. Li, Y. K. Go, H. Ooka, D. He, F. Jin, S. H. Kim, R. Nakamura, *Angew. Chem. Int. Ed.* **2020**, *59*, 9744-9750.
- [9] P. E. Lokhande, U. S. Chavan, *Mater. Sci. Energy Technol.* **2019**, *2*, 52-56.
- [10] I. Mikami, Y. Yoshinaga, T. Okuhara, *Appl. Catal. B* **2004**, *49*, 173-179.
- [11] W. Li, C. Xiao, Y. Zhao, Q. Zhao, R. Fan, J. Xue, *Catal. Lett.* **2016**, *146*, 2585-2595.
- [12] D. Reyter, D. Bélanger, L. Roué, *J. Hazard. Mater.* **2011**, *192*, 507-513.
- [13] L. Mattarozzi, S. Cattarin, N. Comisso, P. Guerriero, M. Musiani, L. Vázquez-Gómez, E. Verlato, *Electrochim. Acta* **2013**, *89*, 488-496.
- [14] T. Wu, X. Kong, S. Tong, Y. Chen, J. Liu, Y. Tang, X. Yang, Y. Chen, P. Wan, *Appl. Surf. Sci.* **2019**, *489*, 321-329.
- [15] C. Polatides, G. Kyriacou, *J. Appl. Electrochem.* **2005**, *35*, 421-427.
- [16] Y. Wang, W. Zhou, R. Jia, Y. Yu, B. Zhang, *Angew. Chem. Int. Ed.* **2020**, *59*, 5350-5354.
- [17] R. Jia, Y. Wang, C. Wang, Y. Ling, Y. Yu, B. Zhang, *ACS Catal.* **2020**, *10*, 3533-3540.
- [18] G.-F. Chen, Y. Yuan, H. Jiang, S.-Y. Ren, L.-X. Ding, L. Ma, T. Wu, J. Lu, H. Wang, *Nat. Energy* **2020**, *5*, 605-613.
- [19] X. Fu, X. Zhao, X. Hu, K. He, Y. Yu, T. Li, Q. Tu, X. Qian, Q. Yue, M. R. Wasielewski, Y. Kang, *Applied Mater. Today* **2020**, *19*, 100620.
- [20] Y. Wang, A. Xu, Z. Wang, L. Huang, J. Li, F. Li, J. Wicks, M. Luo, D.-H. Nam, C.-S. Tan, Y. Ding, J. Wu, Y. Lum, C.-T. Dinh, D. Sinton, G. Zheng, E. H. Sargent, *J. Am. Chem. Soc.* **2020**, *142*, 5702-5708.
- [21] J. Li, G. Zhan, J. Yang, F. Quan, C. Mao, Y. Liu, B. Wang, F. Lei, L. Li, A. W. M. Chan, L. Xu, Y. Shi, Y. Du, W. Hao, P. K. Wong, J. Wang, S.-X. Dou, L. Zhang, J. C. Yu, *J. Am. Chem. Soc.* **2020**, *142*, 7036-7046.

Chapter 6: Tailoring Selectivity of Electrochemical Hydrogen Peroxide Generation by Tunable Pyrrolic-Nitrogen-Carbon

6.1 Introduction and Significance

Electrochemical two-electron oxygen reduction to hydrogen peroxide (H_2O_2) is a promising route for on-site H_2O_2 generation as an alternative to the energy-intensive anthraquinone process. Compared with the scarce noble metals, carbon-based materials, especially nitrogen-doped carbon, are particularly promising due to their abundance, low cost and more importantly, the tunable surface and structure properties. However, the exact correlation between the N doping configuration and the ORR pathway remains controversial.

In this chapter, a scalable g- C_3N_4 -templated strategy was rationally designed and a nitrogen-rich porous few-layered graphene (N-FLG) was synthesized with tunable nitrogen doping and electrocatalytic activity towards H_2O_2 generation. Detailed mechanisms were revealed by *ex situ* x-ray adsorption near edge structure (XANES) characterization. Furthermore, a practical device combining H_2O_2 generation with biomass conversion was successfully fabricated. The Highlights of this work include:

1. *Novel material structure with high $2e^-$ ORR performance.* A novel porous few-layered graphene with selectively tuned pyrrolic-N doping was synthesized and a high H_2O_2 selectivity of over 95% in alkaline condition was achieved.
2. *Probing intermediates for mechanism study.* XANES spectra revealed the critical role of pyrrolic-N on electrochemical H_2O_2 production. Variable adsorption profiles of OOH^* and O^* intermediates during the ORR process and the closely dependent negative shifts of the pyrrolic-N peak were observed.
3. *Significant potential for real application.* A practical device coupling H_2O_2 generation with furfural oxidation was designed and assembled. A high yield rate of $9.66 \text{ mol h}^{-1} \text{ g}_{\text{cat}}^{-1}$ for H_2O_2

and $2.076 \text{ mol m}^{-2} \text{ h}^{-1}$ for 2-furoic acid were achieved at cathode and anode respectively under a small cell voltage of 1.8 V.

6.2 Tailoring Selectivity of Electrochemical Hydrogen Peroxide Generation by Tunable Pyrrolic-Nitrogen-Carbon

This chapter is included as it appears as a journal paper published by **Laiquan Li**, Cheng Tang, Yao Zheng, Bingquan Xia, Xianlong Zhou, Haolan Xu, Shi-Zhang Qiao.* Tailoring Selectivity of Electrochemical Hydrogen Peroxide Generation by Tunable Pyrrolic-Nitrogen-Carbon, *Advanced Energy Materials* 2020, 10, 2000789.

Statement of Authorship

Title of Paper	Tailoring Selectivity of Electrochemical Hydrogen Peroxide Generation by Tunable Pyrrolic-Nitrogen-Carbon
Publication Status	<input checked="" type="checkbox"/> Published <input type="checkbox"/> Accepted for Publication <input type="checkbox"/> Submitted for Publication <input type="checkbox"/> Unpublished and Unsubmitted work written in manuscript style
Publication Details	Laiquan Li, Cheng Tang, Yao Zheng, Bingquan Xia, Xianlong Zhou, Haolan Xu, Shizhang Qiao. Tailoring Selectivity of Electrochemical Hydrogen Peroxide Generation by Tunable Pyrrolic-Nitrogen-Carbon. Adv. Energy Mater. 2020,10, 2000789.

Principal Author

Name of Principal Author (Candidate)	Laiquan Li		
Contribution to the Paper	Research plan, materials synthesis, most of the physical characterization, electrochemical measurement, data analysis, and manuscript draft.		
Overall percentage (%)	85		
Certification:	This paper reports on original research I conducted during the period of my Higher Degree by Research candidature and is not subject to any obligations or contractual agreements with a third party that would constrain its inclusion in this thesis. I am the primary author of this paper.		
Signature		Date	29/07/2021

Co-Author Contributions

By signing the Statement of Authorship, each author certifies that:

- i. the candidate's stated contribution to the publication is accurate (as detailed above);
- ii. permission is granted for the candidate to include the publication in the thesis; and
- iii. the sum of all co-author contributions is equal to 100% less the candidate's stated contribution.

Name of Co-Author	Cheng Tang		
Contribution to the Paper	Discussion of research plan, Manuscript revision		
Signature		Date	29/07/2021

Name of Co-Author	Yao Zheng		
Contribution to the Paper	Helped to evaluate and edit the manuscript.		
Signature		Date	29/07/2021

Name of Co-Author	Bingquan Xia		
Contribution to the Paper	Helped with HPLC measurement		
Signature		Date	29/07/2021

Name of Co-Author	Xianlong Zhou		
Contribution to the Paper	Helped to use the flow cell		
Signature		Date	29/07/2021

Name of Co-Author	Haolan Xu		
Contribution to the Paper	Helped with the XPS measurement		
Signature		Date	29/07/2021

Name of Co-Author	Shi-Zhang Qiao		
Contribution to the Paper	Supervised development of work, helped in manuscript evaluation and acted as corresponding author		
Signature		Date	29/07/2021

Tailoring Selectivity of Electrochemical Hydrogen Peroxide Generation by Tunable Pyrrolic-Nitrogen-Carbon

Laiquan Li, Cheng Tang, Yao Zheng, Bingquan Xia, Xianlong Zhou, Haolan Xu, and Shi-Zhang Qiao*

The electrochemical reduction of O_2 via a two-electron reaction pathway to H_2O_2 provides a possibility for replacing the current anthraquinone process, enabling sustainable and decentralized H_2O_2 production. Here, a nitrogen-rich few-layered graphene (N-FLG) with a tunable nitrogen configuration is developed for electrochemical H_2O_2 generation. A positive correlation between the content of pyrrolic-N and the H_2O_2 selectivity is experimentally observed. The critical role of pyrrolic-N is elucidated by the variable intermediate adsorption profiles as well as the dependent negative shifts of the pyrrolic-N peak on X-ray adsorption near edge structure spectra. By virtue of the optimized N doping configuration and the unique porous structure, the as-fabricated N-FLG electrocatalyst exhibits high selectivity toward electrochemical H_2O_2 synthesis as well as superior long-term stability. To achieve high-value products on both the anode and cathode with optimized energy efficiency, a practical device coupling electrochemical H_2O_2 generation and furfural oxidation is assembled, simultaneously enabling a high yield rate of H_2O_2 at the cathode ($9.66 \text{ mol h}^{-1} \text{ g}_{\text{cat}}^{-1}$) and 2-furoic acid at the anode ($2.076 \text{ mol m}^{-2} \text{ h}^{-1}$) under a small cell voltage of 1.8 V.

developed as an attractive and alternative approach for on-site and on-demand H_2O_2 production, in that oxygen undergoes a two-electron pathway reduction.^[7–11] Moreover, the electrochemical H_2O_2 generation can be coupled with many other reactions, for example biomass conversion reactions, enabling the production of high-value products on both anode and cathode of the practical device within small energy input.

For H_2O_2 synthesis from two-electron oxygen reduction reaction (ORR), it requires an active and low-cost electrocatalyst which can selectively reduce O_2 to H_2O_2 instead of H_2O . It has been reported that ORR on some noble metals and their alloys such as Pt,^[12] Au,^[13] Pd,^[14] Pd-Hg,^[15] and Au-Pd^[16] follows a two-electron pathway with small overpotential as well as high H_2O_2 selectivity. However, the large-scale applications of noble metals are far more constrained by their scarcity. Carbon-based materials are therefore particularly promising due to their abundance, low cost, and high electrochemical stability under reaction conditions.^[8] More importantly, the tunable surface and structure properties make it possible to modify the electrochemical performance of the carbon-based electrocatalysts.^[17–19] Among various modification methods, nitrogen doping is of particular interest to induce efficient active sites with favourable electrochemical properties.^[20,21] However, the majority of these previous works have shown that N-doped carbon based electrocatalysts are prone to accelerate the four-electron ORR pathway under alkaline conditions.^[22,23] There is still limited understanding in identifying and tailoring the active nitrogen configuration for two-electron ORR pathway.

The two-electron pathway involves only one intermediate, namely OOH^* , while further reduction of OOH^* results in other two intermediates (O^* and OH^*), leading to a four-electron pathway.^[24,25] Probing the adsorbed intermediates on the surface of electrocatalysts during the electrochemical process could provide meaningful information in terms of the active sites and reaction pathways.^[26] Generally, mixed two-electron and four-electron pathways usually occur due to the lack of optimal electronic structure for either of them.^[27] To suppress the four-electron pathway, the key knob relies on preventing the bond-breaking reaction of $OOH^* + e^- \rightarrow O^* + OH^-$, and thus effectively preserving the OOH^* intermediate.^[24,28]

The two-electron pathway involves only one intermediate, namely OOH^* , while further reduction of OOH^* results in other two intermediates (O^* and OH^*), leading to a four-electron pathway.^[24,25] Probing the adsorbed intermediates on the surface of electrocatalysts during the electrochemical process could provide meaningful information in terms of the active sites and reaction pathways.^[26] Generally, mixed two-electron and four-electron pathways usually occur due to the lack of optimal electronic structure for either of them.^[27] To suppress the four-electron pathway, the key knob relies on preventing the bond-breaking reaction of $OOH^* + e^- \rightarrow O^* + OH^-$, and thus effectively preserving the OOH^* intermediate.^[24,28]

1. Introduction

Hydrogen peroxide (H_2O_2) is one of the most important industrial chemicals as a potential energy carrier and an environmentally friendly oxidant for various sanitization applications and environmental remediation.^[1–4] Nowadays, the large-scale manufacturing of H_2O_2 is dominated by the multi-step anthraquinone process, which is energy-intensive, waste-producing and difficult for on-site H_2O_2 production.^[4–6] Development of low-cost and decentralized H_2O_2 production is thus highly desired to reduce the cost for H_2O_2 synthesis, storage, and transportation. Recently, the oxygen electrochemistry strategy is

L. Li, Dr. C. Tang, Dr. Y. Zheng, B. Xia, X. Zhou, Prof. S.-Z. Qiao
School of Chemical Engineering and Advanced Materials
The University of Adelaide
Adelaide, SA 5005, Australia
E-mail: s.qiao@adelaide.edu.au

Prof. H. Xu
Future Industries Institute
University of South Australia
Adelaide, SA 5095, Australia

 The ORCID identification number(s) for the author(s) of this article can be found under <https://doi.org/10.1002/aenm.202000789>.

DOI: 10.1002/aenm.202000789

For example, Au surfaces with relatively weak oxygen binding energy could efficaciously prevent the breakage of the O–OH* bond, resulting in a highly selective two-electron pathway for H₂O₂ production.^[29] Hence, it is highly desirable to develop a catalyst platform with fine tunability in electronic structure for regulating the intermediate binding energy and ORR pathway, as well as improving the catalytic activities.

Herein, we elaborately designed a scalable g-C₃N₄-templated strategy to synthesize N-rich few-layered graphene (N-FLG) with tunable nitrogen doping and dependent activities toward H₂O₂ electro-synthesis. Using melamine and glycine as nitrogen sources for different nitrogen configurations, the nitrogen doping state on as-fabricated N-FLG could be effectively tuned by varying the mass ratio of the precursors. We experimentally observed a positive correlation between the content of the pyrrolic-N and the H₂O₂ selectivity. The critical role of the pyrrolic-N on two-electron ORR pathway was further elucidated by X-ray adsorption near edge structure (XANES) spectroscopy. Profiting from the optimized N configuration and the porous structure, the as-fabricated N-FLG-8 (mass ratio of melamine:glycine is 8) electrocatalyst exhibited excellent two-electron ORR performance in alkaline medium with high selectivity over 95% toward electrochemical H₂O₂ synthesis as well as superior long-term stability. When coupled with biomass conversion reaction (furfural oxidation), a practical device was assembled with the generation of high-value products (H₂O₂ on cathode and 2-furoic acid on anode) at high yield rates under a small cell voltage.

2. Results and Discussion

2.1. Material Synthesis and Characterization

As illustrated in Figure 1a, we synthesized the N-FLG-X by grinding a mixture of melamine and glycine with a mass ratio of X:1, followed by a two-step polymerization and carbonization

under Ar atmosphere. During the pyrolysis process, the melamine would transfer to melam, melem and finally to g-C₃N₄, resulting in nitrogen configurations in forms of pyridinic- and graphitic-N.^[30] Meanwhile, the dehydration process of glycine would occur on the in situ formed g-C₃N₄, resulting in a significant amount of N–H bond,^[31] which is expected to contribute to the formation of pyrrolic-N. Therefore, the nitrogen configuration on the final product would be adjusted by varying the mass ratio of melamine and glycine. It is noteworthy to mention that the in situ formed g-C₃N₄, which exhibits layered and lamellar structure (Figure S1, Supporting Information), could serve as a template for the final products. When the melamine was absent or in relatively low mass ratios, the glycine was prone to agglomerate into bulk lumps with low specific surface areas (Figure S2a–c, Supporting Information). When a higher mass ratio of melamine was applied, a well-defined porous graphene-like material with plenty of wrinkles could be obtained (Figure S2d, Supporting Information). For a fair comparison with similar nanostructure, here we adopted mass ratios of 8:1, 12:1, and 16:1, and the as-fabricated materials were denoted as N-FLG-8, N-FLG-12, and N-FLG-16, respectively. Figure 1b–d present the scanning electron microscope (SEM) image and bright-field transmission electron microscope (TEM) images of N-FLG-8 as a typical sample. With the help of the g-C₃N₄ template, the precursors transform into ultrathin graphene layers with a crumpled and wrinkle-rich morphology (Figure 1b,c). The graphene layers are abundant of in-plane holes with size less than 10 nm, and exhibit thickness of about six layers (Figure 1d). It is notable that the interplanar spacing is ≈0.44 nm, which is much larger than the theoretical thickness of monolayer graphene (0.335 nm).^[32] This can be further verified by the X-ray diffraction (XRD) pattern. As shown in Figure S3 in the Supporting Information, all the N-FLG samples exhibit a broad peak located at ≈25.6°, which is lower than the (002) peak (26.6°) of the standard graphite (JCPDS No. 26-1079). The enlarged interlayer distance can be attributed to the N-rich feature of the graphene layers,^[33,34] which is expected to facilitate

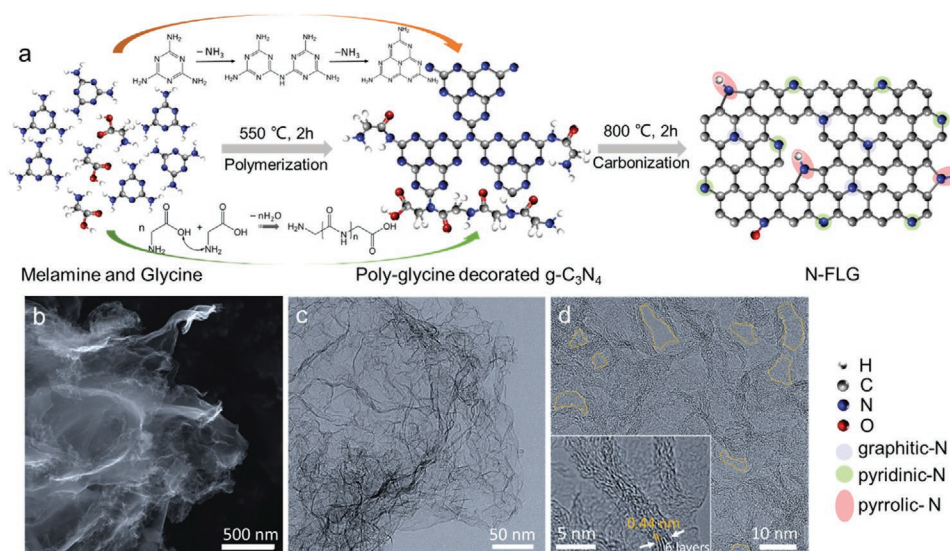


Figure 1. Synthesis of N-FLG and structure characterization. a) Schematic illustration of the synthesis of N-FLG. b) SEM image of N-FLG-8. c) Low-resolution and d) high-resolution bright-field TEM images of N-FLG-8.

the mass transfer during the fast electrochemical reactions. The energy dispersive spectroscopy (EDS) element mapping of N-FLG-8 (Figure S4, Supporting Information) suggests the homogeneous incorporation of N in the graphene nanosheets. N-FLG-12 and N-FLG-16 are also demonstrated to possess the similar 2D wrinkle-rich nanostructure (Figures S5 and S6, Supporting Information). The structural porosity was further investigated by nitrogen adsorption-desorption experiments (Figures S7–S9, Supporting Information). A high specific surface area of $358.8 \text{ m}^2 \text{ g}^{-1}$ is achieved for N-FLG-8, which is comparable to those of N-FLG-12 ($372.5 \text{ m}^2 \text{ g}^{-1}$) and N-FLG-16 ($397.0 \text{ m}^2 \text{ g}^{-1}$). Besides, the pore width of all the obtained graphene materials is mainly distributed within 2–10 nm, which is consistent with the TEM observations and further confirms their porous feature. The Raman spectra reveal similar intensity ratio of D and G bands (I_D/I_G) for N-FLG-8, N-FLG-12, and N-FLG-16, indicating their comparable defective contents (Figure S10, Supporting Information). Moreover, the similar double layer capacitances of the three samples reveal their analogous surface roughness with little differences in electrochemically active surface area (Figure S11, Supporting Information).

The chemical properties of the N-FLG samples were then investigated in detail by X-ray photoelectron spectroscopy (XPS) and XANES spectroscopy. As shown in Figure S12 and Table S1

in the Supporting Information, the XPS survey spectra reveal a high content of nitrogen in all samples (19.2 at% for N-FLG-8, 18.1 at% for N-FLG-12, and 16.5 at% for N-FLG-16), demonstrating their N-rich feature. The high nitrogen doping content is expected to effectively alter the electronic structure and facilitate the O_2 adsorption.^[35] As displayed in Figure 2a, the N 1s XPS spectra can be deconvoluted into four peaks, which are assigned to pyridinic-N (398.4 eV), pyrrolic-N (399.6 eV), graphitic-N (401.1 eV), and oxidized-N (402.7 eV).^[27,36,37] It is obvious that the percentage of pyrrolic-N significantly decreases from 24.9% for N-FLG-8 to 8.1% for N-FLG-16, while those of pyridinic-N and graphitic-N increase from 30.6% to 40.1% and 34.8% to 43.0%, respectively (Table S2, Supporting Information). Besides, from N-FLG-8 to N-FLG-16, the gradually decreased content of C–N bond and the increased content of C=N bond displayed in the high resolution C 1s XPS spectra also reveal the same trend for the nitrogen configuration variation (Figure S13 and Table S3, Supporting Information). It is further verified by the normalized N 1s K edge XANES spectra. As revealed in Figure 2b, a distinct decrease of pyrrolic-N from N-FLG-8 to N-FLG-16 is obviously observed, which is consistent with the XPS results. More specifically, from N-FLG-8 to N-FLG-16, the atomic content of pyrrolic-N significantly decreases from 4.8 to 1.3 at%, while those of pyridinic-N and

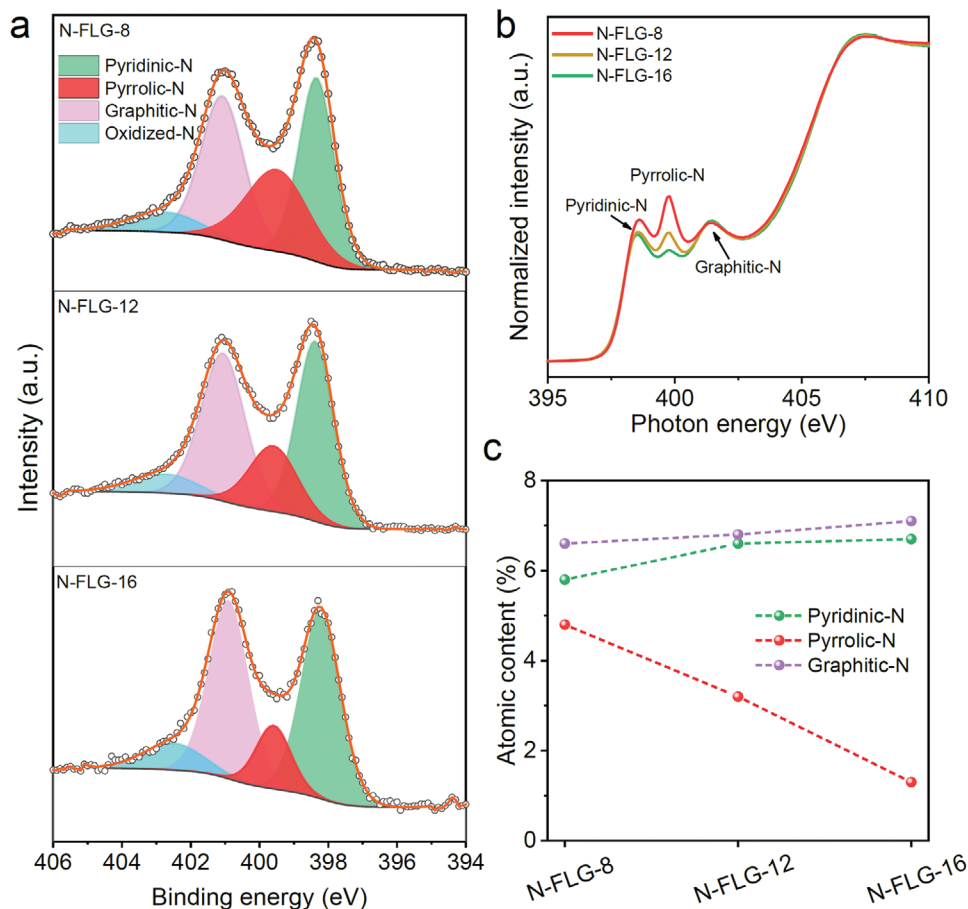


Figure 2. Composition investigation of N-FLG. a) High-resolution N 1s XPS spectra with peaks deconvoluted into pyridinic-N, pyrrolic-N, graphitic-N, and oxidized-N species. b) XANES spectra of N-FLG-8, N-FLG-12 and N-FLG-16. c) The atomic contents of pyridinic-N, graphitic-N, and pyrrolic-N for N-FLG-8, N-FLG-12, and N-FLG-16 derived from the XPS results.

graphitic-N slightly increase from 5.8 to 6.6 at%, and from 6.6 to 7.1 at%, respectively (Figure 2c; Table S2, Supporting Information). Therefore, by virtue of the in situ formed g-C₃N₄ as a template, we obtained hierarchical few-layered nitrogen-rich graphene materials with abundant in-plane pores, which are believed to enhance the mass transfer during the electrochemical reaction.^[19,21] In addition, due to the different polymerization processes, the nitrogen configuration was selectively tuned by varying the mass ratio of the nitrogen precursors. Compared with the conventional tuning method by controlling the annealing temperature,^[38] our method provides a more controllable and effective approach for selectively modifying the nitrogen configuration on carbon materials with similar nanostructures. It is expected to serve as a decent material platform for studying the structure-activity relation of N-doped carbon electrocatalyst at atomic level.

2.2. Electrocatalytic ORR Performances

The ORR performances were evaluated in 0.10 M KOH using rotation ring disk electrode (RRDE), with the collection efficiency being pre-calibrated by the redox reaction of [Fe(CN₆)₄]⁻/[Fe(CN₆)₃]⁻.^[39] Figure 3a shows the linear sweep voltammetry (LSV) curves collected at 1600 rpm in O₂-saturated electrolyte, together with the H₂O₂ detection current collected by the Pt ring electrode at a constant potential of 1.2 V versus reversible hydrogen electrode (RHE). The background current that arises from double layer capacitance was subtracted by recording the sweep profile at the same scan rate in N₂-saturated electrolyte. In the order from N-FLG-16, N-FLG-12, to N-FLG-8, increased ring currents, decreased disk currents, and negatively shifted onset potentials are obtained, suggesting a gradually tuned reaction pathway with a higher fraction of two-electron ORR. The calculated H₂O₂ selectivity and electron transfer number (*n*) are plotted in Figure 3b as a function of applied potential. N-FLG-8 delivers the highest H₂O₂ selectivity of over 95% and the lowest electron transfer number below 2.1 in a wide potential range from 0.30 to 0.70 V versus RHE. Such a high selectivity and activity toward electrochemical H₂O₂ generation is superior to most of the previously reported results (Figure S14 and Table S4, Supporting Information). H₂O₂ selectivity of ≈80% and ≈65% are observed on N-FLG-12 and N-FLG-16, respectively, suggesting that the nitrogen configuration could effectively tune the O₂-to-H₂O₂ selectivity. Accordingly, from N-FLG-8 to N-FLG-16, the electron transfer number is tuned from 2.01 to 2.81. Besides the good performance in alkaline solution, N-FLG-8 also exhibits decent H₂O₂ generation performance with a high selectivity of ≈80% in a neutral solution (Figure S15, Supporting Information). The electrochemical stability of N-FLG-8 was then evaluated using both RRDE test and bulk electrolysis. As shown in Figure 3c, the H₂O₂ selectivity could be maintained over 95% during 8 h continuous electrolysis at a fixed disk potential of 0.40 V versus RHE. Nearly identical LSV curves were obtained before and after the stability test (Figure 3d), with 98.5% of the H₂O₂ selectivity and 98.2% of the disk current being maintained (Figure 3e). When coated onto a gas diffusion layer (GDL) electrode and tested in a H-type cell, N-FLG-8 can deliver a steady-state current density as high as

−20 mA cm⁻² over 50 h (Figure S16, Supporting Information), demonstrating its excellent electrochemical stability and promising potential for practical applications.

2.3. The Activity Origin of H₂O₂ Generation

In spite of the similar nanostructure and specific surface area, obvious differences of ORR activity and selectivity are achieved on different N-FLG samples, which should be ascribed to the tuned nitrogen configurations. Although oxygen doping has also been reported to facilitate the two-electron ORR process,^[40,41] we claim that the nitrogen doping instead of oxygen doping plays the determining role in our case because of the much lower atomic contents (Table S1, Supporting Information) and similar configuration of oxygen dopants among all the three samples (Figure S17, Supporting Information). It is notable that nitrogen-doped carbon materials have been widely reported as superior four-electron ORR electrocatalysts,^[22,23] while they can also serve as highly selective two-electron ORR electrocatalysts.^[20,42,43] The exact correlation between the N doping configuration and the ORR pathway remains controversial, which limits the rational material design and performance optimization. Herein, we performed XANES spectroscopic characterization to probe the reaction intermediates and identify the real active sites for electrochemical H₂O₂ generation on N-FLG. Figure 4a–c presents the evolution of the carbon K edge XANES spectra of N-FLG-8, N-FLG-12 and N-FLG-16 before and after ORR process. On the basis of previous reports,^[44–48] the peak located at ≈287.5 eV is related to π*_{C–O–C, C–N} in the pristine sample before reaction, and the intensity increment after reaction can be assigned to the adsorption of intermediate species (O*) on carbon atoms.^[45] Besides, the peak located at ≈289.3 eV is attributed to the adsorption of OOH* intermediates.^[45,46] Generally, the OOH* intermediate evolves in both two-electron and four-electron pathways, while the O* intermediate only emerges in four-electron pathways. As shown in Figure 4a–c, N-FLG-8 exhibits the strongest intensity of C–OOH* peak and the lowest increment of C–O* peak after ORR, demonstrating its excellent selectivity toward two-electron ORR. Conversely, the significant increment of C–O* peak and the hardly any expansion of C–OOH* peak after ORR indicate a higher fraction of four-electron pathway process on N-FLG-16. This phenomenon can also be verified by the oxygen K edge XANES spectra, in which a distinct C–O* peak for N-FLG-16 while only a little increment for N-FLG-8 compared with the pristine spectra are observed after ORR (Figure S18, Supporting Information).^[48] Nitrogen K edge XANES spectra were further recorded to unravel the critical role of specific nitrogen configurations. As depicted in Figure 4d, we observed negative shifts of the pyrrolic-N peak after ORR, while the peak positions of the pyridinic-N and graphitic-N remained nearly unchanged for all the three samples. The negative shift can be ascribed to the distortion of heterocycles caused by the adsorption of intermediates on the carbon atoms near the pyrrolic-N.^[45] Remarkably, the negative shifts in nitrogen K edge spectra descend in the order: N-FLG-8 (0.20 eV) > N-FLG-12 (0.16 eV) > N-FLG-16 (0.14 eV), in well consistence with the intensities of the C–OOH* peaks in carbon K edges. Thus, it is rational

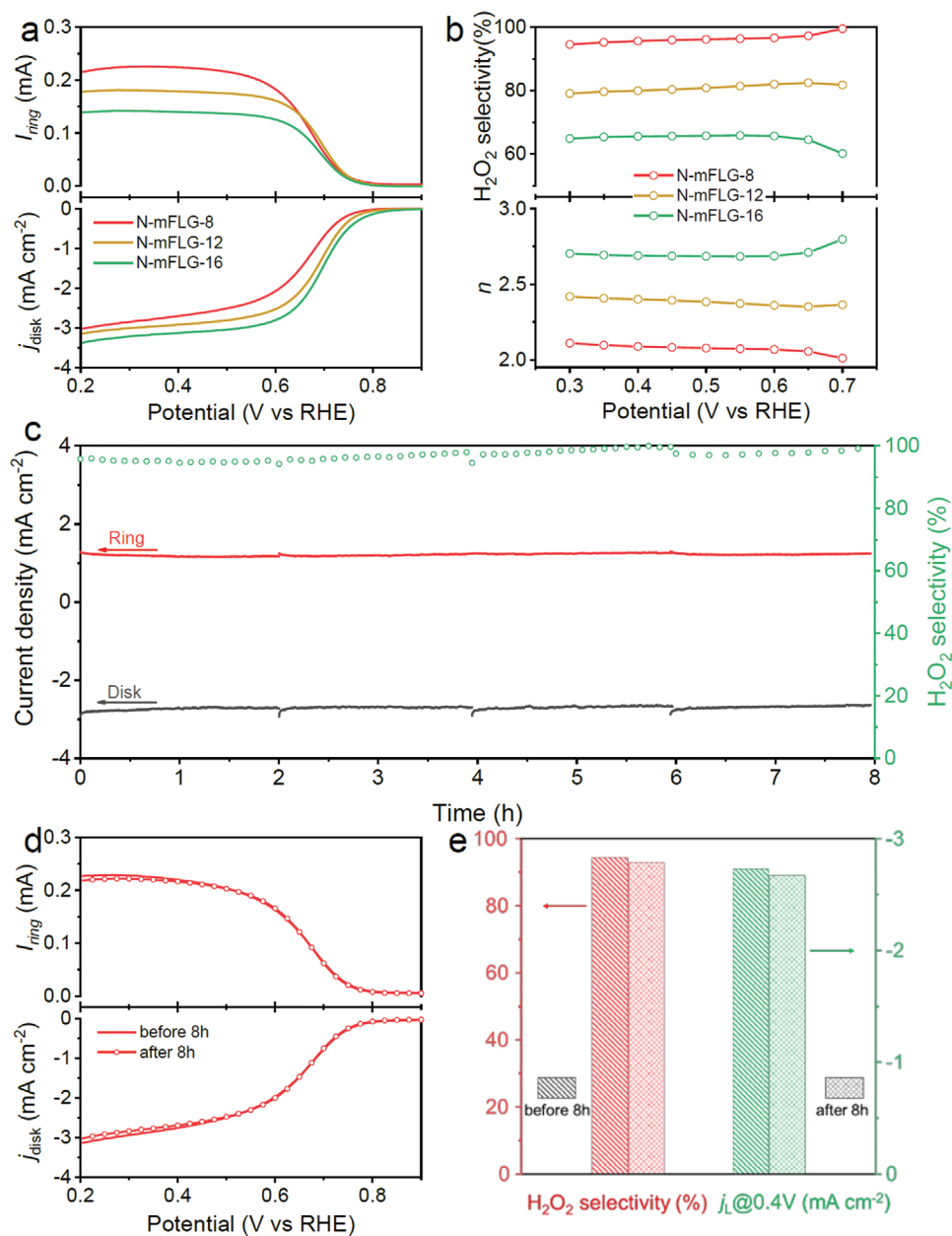


Figure 3. ORR performance of N-FLG in 0.10 M KOH. a) LSV curves of N-FLG-8, N-FLG-12, and N-FLG-16 recorded at 1600 rpm and at a rate of 5.0 mV s^{-1} , showing the ORR current density on the disk (j_{disk}) and the detected H_2O_2 currents on the ring electrode (I_{ring}). b) The calculated H_2O_2 selectivity and electron transfer number (n) during the potential sweep. c) Stability measurement of N-FLG-8 at a fixed disk potential of 0.40 V versus RHE. The Pt ring was refreshed every 2 h by rapid scan at potential range from 0 to 0.8 V versus RHE to remove the accumulated PtO_x , and the electrolyte was replaced to eliminate the influence of the accumulated H_2O_2 on the ring current during the continuous operation. d) LSV curves of N-FLG-8 and e) the H_2O_2 selectivity and diffusion-limiting disk current density (j_L) at 0.4 V versus RHE before and after 8 hour's stability test.

to conclude that the adsorption of OOH^* intermediates on the carbon atoms near the pyrrolic-N induces the distortion of heterocycles and results in the negative shifts of the pyrrolic-N peak. Furthermore, when correlating the atomic content of specific nitrogen configurations with H_2O_2 selectivity, a positive relationship between the pyrrolic-N content and the H_2O_2 selectivity is obtained (Figure 4e), whereas no such positive correlation can be found for either pyridinic-N or graphitic-N (Figure S19, Supporting Information).

It suggests that the much larger number of pyrrolic-N dopants in N-FLG-8 may alter the electronic structure toward optimized adsorption of OOH^* intermediate and thus lead to the superior selectivity of two-electron pathway. To further understand the promoting effect of pyrrolic-N on selective H_2O_2 generation, we then measured LSV in a H_2O_2 -containing (50 mmol L^{-1}) electrolyte. As shown in Figure S20 in the Supporting Information, the H_2O_2 reduction current decreases obviously on N-FLG-8 compared to N-FLG-12 and N-FLG-16,

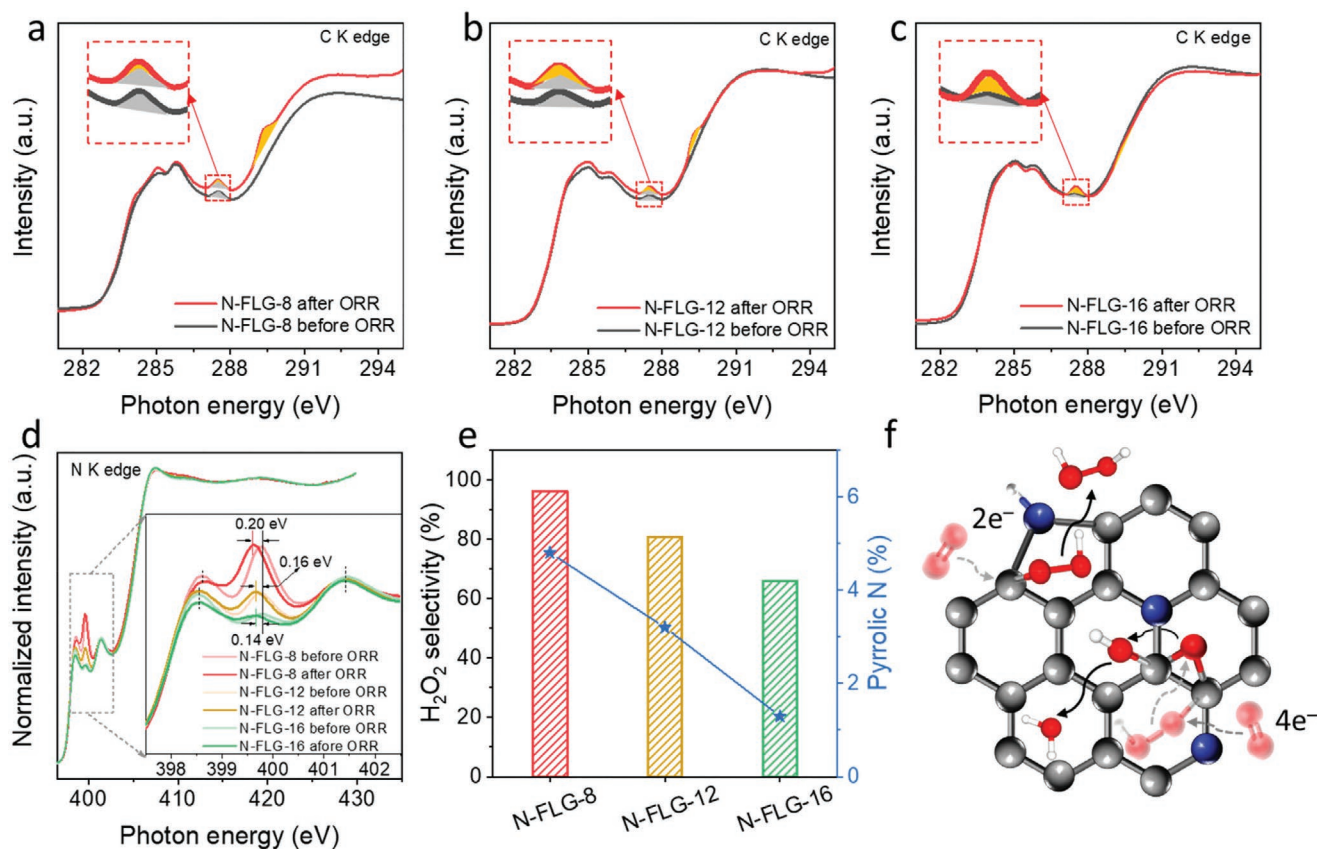


Figure 4. Elucidation of the activity origin for H₂O₂ generation. a–c) Carbon K edge and d) nitrogen K edge XANES spectra of N-FLG-8, N-FLG-12, and N-FLG-16 before and after ORR tests. In the insets of (a–c), the grey shadow presents the pristine peak before reaction and the orange shadow presents the peak increment after reaction. e) Relationship between H₂O₂ selectivity and atomic content of pyrrolic-N. f) Schematic diagram of two-electron and four-electron ORR pathways on N-FLG with different nitrogen configurations.

indicating an effectively hindered reduction of H₂O₂ to H₂O due to the presence of more pyrrolic-N dopants. It has been reported that nitrogen atoms with a higher electronegativity could activate π -conjugated system and impart positive charge on the adjacent carbon atoms, thus facilitating the adsorption of OOH* intermediates.^[49] However, the delocalized lone pair electrons from the pyridinic-N could aggressively induce charge transfer from the π orbital to the antibonding orbitals in O₂, resulting in significantly weakened O–O bond and further dissociation of OOH* intermediate into O* and OH*.^[20,50,51] The graphitic-N is reported to be positively charged and the carbon atoms surrounding graphitic-N may act as Lewis acids,^[52] which are not favorable for the adsorption of intermediates. Therefore, we propose that the OOH* intermediates could be substantially preserved with the presence of a high amount of pyrrolic-N, leading to a two-electron ORR pathway on the adjacent carbon atoms. Four-electron pathway is supposed to preferentially occur on the carbon atoms adjacent to the pyridinic-N rather than pyrrolic-N dopants (Figure 4f).

2.4. Practical Device Demonstration

To investigate the potential of the catalyst for practical application, we combined the electrochemical H₂O₂ generation with

biomass conversion for the purpose of producing valuable products on both cathode and anode. Furfural (FU), which is generally mass-produced by the dehydration of agricultural by-products,^[53,54] was here chosen as a substrate for electrochemical oxidation. The product of furfural oxidation, 2-furoic acid (FA), is widely used for preservative in industry, acting as bactericide and fungicide.^[53,54] The combination of H₂O₂ generation and FU oxidation was realized in a conventional flow cell with a two-electrode configuration (Figure 5a; Figure S21, Supporting Information). A GDL electrode (1.8 × 1.8 cm²) casted with N-FLG-8 electrocatalyst was used as the cathode electrode and a nickel foam was used as the anode electrode. The accumulated H₂O₂ yield on the cathode was quantified by Ce⁴⁺/Ce³⁺ colorimetric method (the standard curve is shown in Figure S22 in the Supporting Information), while the FA produced on the anode was determined by high performance liquid chromatography (HPLC). Figure 5b shows the polarization curves of the assembled flow cell with and without the presence of FU. Significantly increased current density and decreased cell voltage can be realized when replacing conventional oxygen evolution reaction (OER) by FU oxidation on the anode. Only a small cell voltage of 1.28 V, in contrast to 1.98 V in the absence of FU, is required to drive a high current density of 50 mA cm⁻², indicating the remarkable thermodynamic advantage of FU oxidation relative to water oxidation. Under the optimized mass

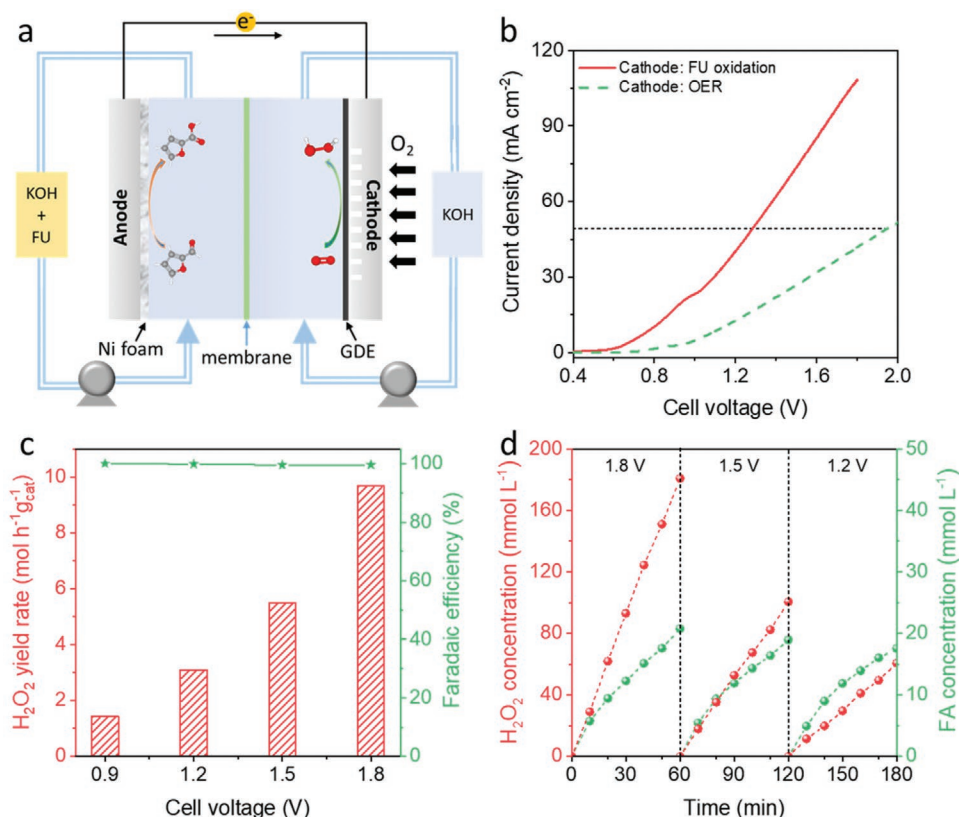


Figure 5. Application of N-FLG-8 in a practical flow cell device. a) Scheme of the flow cell coupling electrochemical furfural oxidation and H₂O₂ generation. b) LSV curves of the flow cell with or without furfural addition in the anode side. c) The H₂O₂ yield rates and faradaic efficiencies at different cell voltages. d) Stability test of the flow cell simultaneously generating 2-furoic acid and H₂O₂.

transfer in flow cell setup, the cell current can reach as high as 350 mA ($\approx 110 \text{ mA cm}^{-2}$) at the cell voltage of 1.8 V (Figure 5b).

Bulk electrolysis was then performed at different cell voltages of 0.9, 1.2, 1.5, and 1.8 V. As shown in Figure 5c, H₂O₂ yield rate of $9.66 \text{ mol h}^{-1} \text{ g}_{\text{cat}}^{-1}$ ($2.31 \text{ mmol h}^{-1} \text{ cm}^{-2}$) can be achieved at the cell voltage of 1.8 V, which outperforms most of the reported bulk H₂O₂ production in flow cell system (Table S5, Supporting Information). It is noteworthy to mention that high faradaic efficiencies of near 100% are realized at all the applied cell voltages, further demonstrating the exclusive selectivity for two-electron ORR pathway on N-FLG-8. This novel electrochemical device can be steadily operated for a long term with a stable current and product yield rate (Figure 5d; Figure S23, Supporting Information). Simultaneously, the continuous consumption of FU and production of FA on the anode were also confirmed by the HPLC results (Figure S24, Supporting Information). A high FU conversion rate of $\approx 70\%$ in 60 min with an average FA yield rate of $2.076 \text{ mol m}^{-2} \text{ h}^{-1}$ was achieved at the cell voltage of 1.8 V (Figure 5d).

3. Conclusion

In summary, porous N-rich few-layered graphene with controllable morphology, nanostructure and composition have been fabricated by a facile g-C₃N₄-templated method. By changing the mass ratio of the precursor materials, the content of

pyrrolic-N was selectively tuned. We revealed that the H₂O₂ selectivity could be effectively facilitated with the presence of the high amount of pyrrolic-N. The critical role of the pyrrolic-N was elucidated by the variable adsorption profiles of OOH* and O* intermediates on C K edge XANES spectra as well as the dependent negative shifts of the pyrrolic-N peak on N K edge XANES spectra. N-FLG-8 with the highest pyrrolic-N content and abundant in-plane pores was demonstrated to have superior activity toward electrochemical H₂O₂ synthesis, enabling high selectivity over 95% and excellent long-term stability. By virtue of the high activity of N-FLG-8, a practical device coupling electrochemical H₂O₂ generation with furfural oxidation was assembled, enabling simultaneous production of value-added products of H₂O₂ on cathode with a high yield rate of $9.66 \text{ mol h}^{-1} \text{ g}_{\text{cat}}^{-1}$ ($2.31 \text{ mmol h}^{-1} \text{ cm}^{-2}$) and FA on anode with a yield rate of $2.076 \text{ mol m}^{-2} \text{ h}^{-1}$ under a small cell voltage of 1.8 V. The selective nitrogen configuration tuning method and the identification of the favourable effect of pyrrolic-N to two-electron ORR pathway in this work provide new ideas for the design of advanced carbon-based electrocatalysts for various electrochemical and catalytic applications.

4. Experimental Section

Synthesis of N-FLG: In a typical procedure, melamine and glycine with various mass ratios (for example 8:1 for N-FLG-8) were first thoroughly ground in an agate mortar. The mixed powders were put into a porcelain

boat and then transferred to a tube furnace. The mixture was first heated to 550 °C in Ar atmosphere at a ramp rate of 2 °C min⁻¹. After keeping at 550 °C for 2 h, the annealing temperature was then elevated to 800 °C with a ramp rate of 3 °C min⁻¹ and kept at 800 °C for another 2 h. After cooling down naturally to room temperature, the resultant black product was grounded into powder using an agate mortar and directly used for the preparation of catalyst ink.

Imaging and Spectroscopic Characterization: Field-emission scanning electron microscope (SEM) images were collected on a FEI QUANTA 450 electron microscope. The TEM images, HAADF-STEM images and EDS mapping were collected on a FEI Titan Themis 80-200 operating at 200 kV. XRD patterns were obtained using a Rigaku MiniFlex 600 X-Ray Diffractometer with Co K α radiation. XPS data were collected under ultrahigh vacuum (<10⁻⁸ Torr) using a monochromatic Al K α X-ray source. Raman data were collected on a HORIBA LabRAM HR Evolution spectroscopy using the excitation wavelength of 532 nm. The absorbance data of spectrophotometer were collected on SHIMADZU UV-2600 ultraviolet-visible (UV-vis) spectrophotometer. Furfural and its oxidation product (2-furoic acid) were quantitatively determined by HPLC (Waters Alliance e2695 Separations Module).

Electrochemical Measurements: Electrochemical data were collected with a CHI 760e electrochemical workstation (CHI Instruments, Inc.). Three-electrode system was used in the electrochemical measurement in which an Ag/AgCl electrode was used as the reference electrode, a graphite rod as a counter electrode, and a RRDE (disk area: 0.247 cm²) with a Pt ring (ring area: 0.1866 cm²) as the working electrode. All potentials measured against Ag/AgCl electrode were converted to the RHE. To prepare the catalyst ink, 5.0 mg of the obtained catalyst powders and 0.5 mg of carbon black were dispersed in 960 μ L of the mixture of isopropanol and water (v/v = 1:1) and 40 μ L of 5 wt% Nafion solution. After ultrasonic treatment for 3 h, 5.0 μ L of the catalyst ink was drop-casted on to the disk electrode for the RRDE measurement.

The oxygen reduction activity was measured by cyclic voltammetry (CV) and LSV techniques in O₂ saturated electrolyte at a scan rate of 5.0 mV s⁻¹. Prior to the measurement, the Pt ring was first electrochemically cleaned by sweeping the potential between 0 and 0.8 V until steady CV curve was obtained. The electrolyte was first purged with N₂ and a LSV curve was recorded in N₂-saturated 0.10 M KOH at the rotating speed of 1600 rpm. Then, the electrolyte was purged with O₂ at least 30 min, and the LSV curve of ORR was collected in O₂-saturated 0.10 M KOH at the rotating speed of 1600 rpm. The capacitance or faradaic currents were then eliminated by subtracting the current measured in N₂-saturated electrolyte from that in O₂-saturated electrolyte. The ring currents were recorded by fixing the ring potential at 1.2 V versus RHE to detect the H₂O₂ produced on disk electrode. The collection efficiency (N) was determined to be 37.1% by the redox reaction of [Fe(CN)₆]⁴⁻/[Fe(CN)₆]³⁻. Selectivity of the catalysts toward H₂O₂ production was calculated based on the following equation

$$\text{H}_2\text{O}_2\% = \frac{200 \times I_{\text{ring}}/N}{|I_{\text{disk}}| + I_{\text{ring}}/N} \quad (1)$$

The electron transfer number at the disk electrode during ORR process was calculated as follows

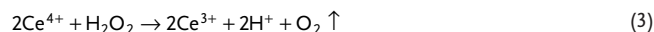
$$n = \frac{4|I_{\text{disk}}|}{|I_{\text{disk}}| + I_{\text{ring}}/N} \quad (2)$$

X-Ray Absorption Near-Edge Structure (XANES) Measurement: The K-edge X-ray absorption spectra of C, N, and O were measured on the soft X-ray spectroscopy beamline at the Australian Synchrotron. For the XANES measurements, the catalyst powder was supported on a porous copper foam under \approx 10 Ton pressure. The copper foams with catalyst powder were first injected to an ultrahigh vacuum chamber to collect the pristine spectra. For the XANES spectra after ORR process, the electrodes were then reacted at a fixed potential of 0.6 V versus RHE in an O₂ saturated 0.10 M KOH for 60 min. After the ORR process, the copper foam with catalysts was quickly dried by blowing Ar and subjected to the ultrahigh vacuum chamber for the data collection.

Measurement of Electrochemically Active Surface Area: The electrochemically active surface area was measured by double layer capacitance method. CV scans were conducted at the potential window from -0.05 to 0.05 V versus Ag/AgCl reference electrode with scan rates of 5, 10, 15, 20, and 25 mV s⁻¹. By plotting the $(j_a - j_c)/2$ at 0 V against the scan rate (j_a is the anodic current density and j_c is the cathodic current density), the slope value was calculated to be the double layer capacitance (C_{dl}).

Practical Device Assembly and Measurement: As shown in Figure S21 in the Supporting Information, a conventional flow cell was constructed to simulate a practical device, which couples electrochemical H₂O₂ generation with furfural oxidation. 40 mL of 1.0 M KOH solution with 30 mmol L⁻¹ of furfural continuously flowed through the anode chamber which was separated from the cathode chamber by a Nafion 117 membrane (Fuel Cell store). A nickel foam (4 cm²) was used as the anode electrode for furfural oxidation. The catalyst was dispersed onto a GDL electrode (1.8 \times 1.8 cm²) by a spray gun, resulting in a loading mass of 0.24 mg cm⁻². The cathode chamber was circulated with 40 mL of 1.0 M KOH under a flow rate of \approx 4 mL min⁻¹. High purity O₂ was continuously purged through the opposite side of the catalyst with a flow rate of \approx 5 mL min⁻¹. LSV was performed at a scan rate of 10.0 mV s⁻¹ with a cell voltage range from 0 to 2.0 V. The electrolysis was then carried out by employing different cell voltages for various durations to evaluate the actual production of H₂O₂. All the LSV measurements and bulk electrolysis for the flow cell were carried out without IR compensation.

Product Quantification: A Ce⁴⁺ titration method was used to quantitatively analyze the produced H₂O₂ based on the following equation



where the Ce⁴⁺ solution displayed yellow while the Ce³⁺ solution was colorless. The yield of H₂O₂ was then quantified by measuring the mole amount of the consumed Ce⁴⁺, which was determined by UV-vis spectrophotometry. A typical calibration curve was plotted by linear fitting the absorbance values at wavelength length of 320 nm for various known concentration of 0.01, 0.02, 0.05, 0.1, 0.2, 0.3, 0.4, and 0.5 mmol L⁻¹ of Ce⁴⁺ (Figure S22, Supporting Information). The standard solution of Ce⁴⁺ with the concentration of 0.5 mmol L⁻¹ was prepared by dissolving 16.65 mg of Ce(SO₄)₂ in 100 mL of 0.5 mol L⁻¹ H₂SO₄. To quantify the produced H₂O₂, sample solution was mixed with 0.5 mmol L⁻¹ Ce⁴⁺ solution by a volume ratio of 1:400 or 1:800. After standing for 2 h, the mixture solution was then measured by UV-vis spectrophotometry. The yield of H₂O₂ was finally determined based on the reduced Ce⁴⁺ concentration. For the anode product, the concentration of the produced 2-furoic acid was determined by HPLC equipped with an UV-vis detector. A mixture of ammonium acetate (70%) and methanol (30%) was used as the mobile phase with a flow rate of 0.6 mL min⁻¹. The wavelength of the detector was set to 245 nm.

The faradaic efficiency (FE) for H₂O₂ generation in flow cell was calculated as follows

$$\text{FE} (\%) = \frac{\text{mole of generated H}_2\text{O}_2 \times 2 \times 96,485}{\text{total consumed charge} (C)} \times 100\% \quad (4)$$

The FU conversion rate was calculated as follows

$$\text{Conversion rate}_{\text{FU}} (\%) = \frac{\text{mole of consumed FU}}{\text{mole of initial FU}} \times 100\% \quad (5)$$

The FA yield rate were calculated as follows

$$\text{Yield rate}_{\text{FA}} = \frac{C \times V}{A \times t} \quad (6)$$

where C, is the concentration of the produced FA, V, is the volume of the electrolyte in anode chamber, A, is the area of the anode electrode, and t, is the electrolysis duration.

Supporting Information

Supporting Information is available from the Wiley Online Library or from the author.

Acknowledgements

This work was financially supported by the Australian Research Council through Discovery Projects (DP160104866, DP170104464, and FL170100154). X-ray adsorption near edge structure measurements were undertaken on the soft X-ray beamline at Australian Synchrotron. SEM and TEM measurements were undertaken at Adelaide Microscopy, the Centre for Advanced Microscopy and Microanalysis.

Conflict of Interest

The authors declare no conflict of interest.

Keywords

electrochemical H₂O₂ generation, furfural oxidation, nitrogen doped graphene, oxygen reduction reaction

Received: March 1, 2020

Revised: March 16, 2020

Published online: April 17, 2020

- [1] S. Siahrostami, A. Verdaguer-Casadevall, M. Karamad, D. Deiana, P. Malacrida, B. Wickman, M. Escudero-Escribano, E. A. Paoli, R. Frydendal, T. W. Hansen, I. Chorkendorff, I. E. L. Stephens, J. Rossmeisl, *Nat. Mater.* **2013**, *12*, 1137.
- [2] Z. W. Seh, J. Kibsgaard, C. F. Dickens, I. Chorkendorff, J. K. Nørskov, T. F. Jaramillo, *Science* **2017**, *355*, eaad4998.
- [3] S. C. Perry, D. Pangotra, L. Vieira, L.-I. Csepei, V. Sieber, L. Wang, C. Ponce de León, F. C. Walsh, *Nat. Rev. Chem.* **2019**, *3*, 442.
- [4] J. M. Campos-Martin, G. Blanco-Brieva, J. L. Fierro, *Angew. Chem., Int. Ed.* **2006**, *45*, 6962.
- [5] S. Yang, A. Verdaguer-Casadevall, L. Arnarson, L. Silvioli, V. Čolić, R. Frydendal, J. Rossmeisl, I. Chorkendorff, I. E. L. Stephens, *ACS Catal.* **2018**, *8*, 4064.
- [6] S. Ranganathan, V. Sieber, *Catalysts* **2018**, *8*, 379.
- [7] A. Kulkarni, S. Siahrostami, A. Patel, J. K. Nørskov, *Chem. Rev.* **2018**, *118*, 2302.
- [8] M. Melchionna, P. Fornasiero, M. Prato, *Adv. Mater.* **2019**, *31*, 1802920.
- [9] Y. Jiang, P. Ni, C. Chen, Y. Lu, P. Yang, B. Kong, A. Fisher, X. Wang, *Adv. Energy Mater.* **2018**, *8*, 1801909.
- [10] C. Xia, Y. Xia, P. Zhu, L. Fan, H. Wang, *Science* **2019**, *366*, 226.
- [11] Z. Chen, S. Chen, S. Siahrostami, P. Chakthranont, C. Hahn, D. Nordlund, S. Dimosthenis, J. K. Nørskov, Z. Bao, T. F. Jaramillo, *React. Chem. Eng.* **2017**, *2*, 239.
- [12] C. H. Choi, M. Kim, H. C. Kwon, S. J. Cho, S. Yun, H.-T. Kim, K. J. J. Mayrhofer, H. Kim, M. Choi, *Nat. Commun.* **2016**, *7*, 10922.
- [13] D. Kim, H. Nam, Y.-H. Cho, B. C. Yeo, S.-H. Cho, J.-P. Ahn, K.-Y. Lee, S. Y. Lee, S. S. Han, *ACS Catal.* **2019**, *9*, 8702.
- [14] Y. L. Wang, S. Gurses, N. Felvey, A. Boubnov, S. S. Mao, C. X. Kronawitter, *ACS Catal.* **2019**, *9*, 8453.
- [15] A. Verdaguer-Casadevall, D. Deiana, M. Karamad, S. Siahrostami, P. Malacrida, T. W. Hansen, J. Rossmeisl, I. Chorkendorff, I. E. L. Stephens, *Nano Lett.* **2014**, *14*, 1603.
- [16] J. S. Jirkovský, I. Panas, E. Ahlberg, M. Halasa, S. Romani, D. J. Schiffrin, *J. Am. Chem. Soc.* **2011**, *133*, 19432.
- [17] Y. J. Sa, J. H. Kim, S. H. Joo, *Angew. Chem., Int. Ed.* **2019**, *58*, 1100.
- [18] Y. Liu, X. Quan, X. Fan, H. Wang, S. Chen, *Angew. Chem.* **2015**, *127*, 6941.
- [19] S. Chen, Z. Chen, S. Siahrostami, T. R. Kim, D. Nordlund, D. Sokaras, S. Nowak, J. W. F. To, D. Higgins, R. Sinclair, J. K. Nørskov, T. F. Jaramillo, Z. Bao, *ACS Sustainable Chem. Eng.* **2018**, *6*, 311.
- [20] D. Iglesias, A. Giuliani, M. Melchionna, S. Marchesan, A. Criado, L. Nasi, M. Bevilacqua, C. Tavagnacco, F. Vizza, M. Prato, P. Fornasiero, *Chem* **2018**, *4*, 106.
- [21] T.-P. Fellingner, F. Hasché, P. Strasser, M. Antonietti, *J. Am. Chem. Soc.* **2012**, *134*, 4072.
- [22] L. Dai, Y. Xue, L. Qu, H.-J. Choi, J.-B. Baek, *Chem. Rev.* **2015**, *115*, 4823.
- [23] Y. Zheng, Y. Jiao, L. Ge, M. Jaroniec, S. Z. Qiao, *Angew. Chem., Int. Ed.* **2013**, *52*, 3110.
- [24] H. A. Hansen, V. Viswanathan, J. K. Nørskov, *J. Phys. Chem. C* **2014**, *118*, 6706.
- [25] Y. Jiao, Y. Zheng, M. Jaroniec, S. Z. Qiao, *Chem. Soc. Rev.* **2015**, *44*, 2060.
- [26] L. Li, H. Yang, J. Miao, L. Zhang, H.-Y. Wang, Z. Zeng, W. Huang, X. Dong, B. Liu, *ACS Energy Lett.* **2017**, *2*, 294.
- [27] Y. Jiao, Y. Zheng, M. Jaroniec, S. Z. Qiao, *J. Am. Chem. Soc.* **2014**, *136*, 4394.
- [28] G.-L. Chai, Z. Hou, T. Ikeda, K. Terakura, *J. Phys. Chem. C* **2017**, *121*, 14524.
- [29] S. Siahrostami, A. Verdaguer-Casadevall, M. Karamad, I. Chorkendorff, I. Stephens, J. Rossmeisl, *ECS Trans.* **2013**, *58*, 53.
- [30] E. Wirnhier, M. B. Mesch, J. Senker, W. Schnick, *Chem. - Eur. J.* **2013**, *19*, 2041.
- [31] P.-C. Hsu, H.-T. Chang, *Chem. Commun.* **2012**, *48*, 3984.
- [32] P. L. de Andres, R. Ramírez, J. A. Vergés, *Phys. Rev. B* **2008**, *77*, 045403.
- [33] J. Liu, Y. Zhang, L. Zhang, F. Xie, A. Vasileff, S.-Z. Qiao, *Adv. Mater.* **2019**, *31*, 1901261.
- [34] W. Ding, Z. Wei, S. Chen, X. Qi, T. Yang, J. Hu, D. Wang, L.-J. Wan, S. F. Alvi, L. Li, *Angew. Chem., Int. Ed.* **2013**, *52*, 11755.
- [35] Y. Okamoto, *Appl. Surf. Sci.* **2009**, *256*, 335.
- [36] T. Xing, Y. Zheng, L. H. Li, B. C. C. Cowie, D. Gunzelmann, S. Z. Qiao, S. Huang, Y. Chen, *ACS Nano* **2014**, *8*, 6856.
- [37] C. Tang, H.-F. Wang, X. Chen, B.-Q. Li, T.-Z. Hou, B. Zhang, Q. Zhang, M.-M. Titirici, F. Wei, *Adv. Mater.* **2016**, *28*, 6845.
- [38] W. Zhang, S. Y. Bu, Q. H. Yuan, Q. Xu, M. Hu, *J. Mater. Chem. A* **2019**, *7*, 647.
- [39] R. Zhou, Y. Zheng, M. Jaroniec, S.-Z. Qiao, *ACS Catal.* **2016**, *6*, 4720.
- [40] H. W. Kim, M. B. Ross, N. Kornienko, L. Zhang, J. Guo, P. Yang, B. D. McCloskey, *Nat. Catal.* **2018**, *1*, 282.
- [41] Z. Lu, G. Chen, S. Siahrostami, Z. Chen, K. Liu, J. Xie, L. Liao, T. Wu, D. Lin, Y. Liu, T. F. Jaramillo, J. K. Nørskov, Y. Cui, *Nat. Catal.* **2018**, *1*, 156.
- [42] Y. Sun, I. Sinev, W. Ju, A. Bergmann, S. Dresp, S. Kühl, C. Spöri, H. Schmies, H. Wang, D. Bernsmeier, B. Paul, R. Schmack, R. Kraehnert, B. Roldan Cuenya, P. Strasser, *ACS Catal.* **2018**, *8*, 2844.
- [43] Y. Sun, S. Li, Z. P. Jovanov, D. Bernsmeier, H. Wang, B. Paul, X. Wang, S. Kühl, P. Strasser, *ChemSusChem* **2018**, *11*, 3388.
- [44] H. K. Jeong, H. J. Noh, J. Y. Kim, M. H. Jin, C. Y. Park, Y. H. Lee, *Europhys. Lett.* **2008**, *82*, 67004.
- [45] H. B. Yang, J. W. Miao, S. F. Hung, J. Z. Chen, H. B. Tao, X. Z. Wang, L. P. Zhang, R. Chen, J. J. Gao, H. M. Chen, L. M. Dai, B. Liu, *Sci. Adv.* **2016**, *2*, e1501122.
- [46] Y. Ye, A. Kawase, M.-K. Song, B. Feng, Y.-S. Liu, M. A. Marcus, J. Feng, E. J. Cairns, J. Guo, J. Zhu, *Nanomaterials* **2016**, *6*, 14.
- [47] Y. Jiao, Y. Zheng, K. Davey, S.-Z. Qiao, *Nat. Energy* **2016**, *1*, 16130.

- [48] D. Pacilé, J. C. Meyer, A. Fraile Rodríguez, M. Papagno, C. Gómez-Navarro, R. S. Sundaram, M. Burghard, K. Kern, C. Carbone, U. Kaiser, *Carbon* **2011**, *49*, 966.
- [49] S. K. Singh, K. Takeyasu, J. Nakamura, *Adv. Mater.* **2019**, *31*, 1804297.
- [50] C. V. Rao, C. R. Cabrera, Y. Ishikawa, *J. Phys. Chem. Lett.* **2010**, *1*, 2622.
- [51] D. Guo, R. Shibuya, C. Akiba, S. Saji, T. Kondo, J. Nakamura, *Science* **2016**, *351*, 361.
- [52] T. Kondo, S. Casolo, T. Suzuki, T. Shikano, M. Sakurai, Y. Harada, M. Saito, M. Oshima, M. I. Trioni, G. F. Tantardini, J. Nakamura, *Phys. Rev. B* **2012**, *86*, 035436.
- [53] A. M. Román, J. C. Hasse, J. W. Medlin, A. Holewinski, *ACS Catal.* **2019**, *9*, 10305.
- [54] X. Zhang, M. Han, G. Liu, G. Wang, Y. Zhang, H. Zhang, H. Zhao, *Appl. Catal., B* **2019**, *244*, 899.

ADVANCED ENERGY MATERIALS

Supporting Information

for *Adv. Energy Mater.*, DOI: 10.1002/aenm.202000789

**Tailoring Selectivity of Electrochemical Hydrogen Peroxide
Generation by Tunable Pyrrolic-Nitrogen-Carbon**

*Laiquan Li, Cheng Tang, Yao Zheng, Bingquan Xia, Xianlong
Zhou, Haolan Xu, and Shi-Zhang Qiao**

Copyright WILEY-VCH Verlag GmbH & Co. KGaA, 69469 Weinheim, Germany,

2020.

Supporting Information

Tailoring selectivity of electrochemical hydrogen peroxide generation by tunable pyrrolic-nitrogen-carbon

*Laiquan Li, Cheng Tang, Yao Zheng, Bingquan Xia, Xianlong Zhou, Haolan Xu, Shi-Zhang Qiao**

L. Li, Dr. C. Tang, Dr. Y. Zheng, B. Xia, X. Zhou, Prof. S. Z. Qiao
School of Chemical Engineering and Advanced Materials
The University of Adelaide
SA 5005, Australia
E-mail: s.qiao@adelaide.edu.au

Prof. H. Xu
Future Industries Institute
University of South Australia
SA 5095, Australia

1. Supplementary Figures

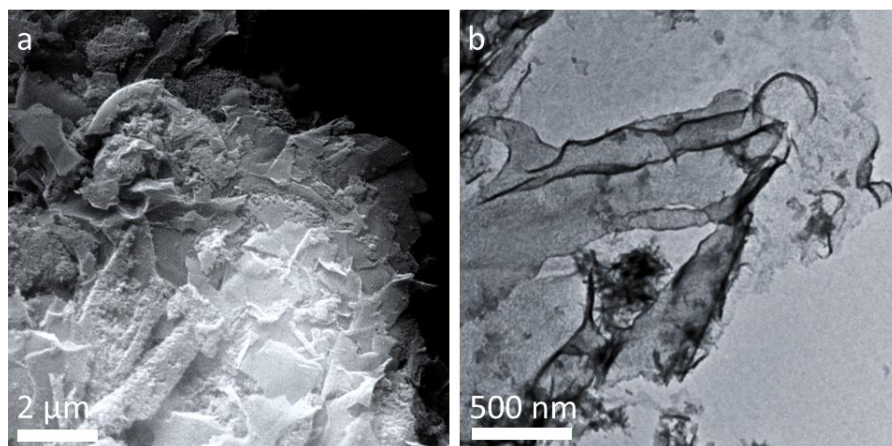


Figure S1. a) SEM image and b) TEM image of g-C₃N₄ precursor.

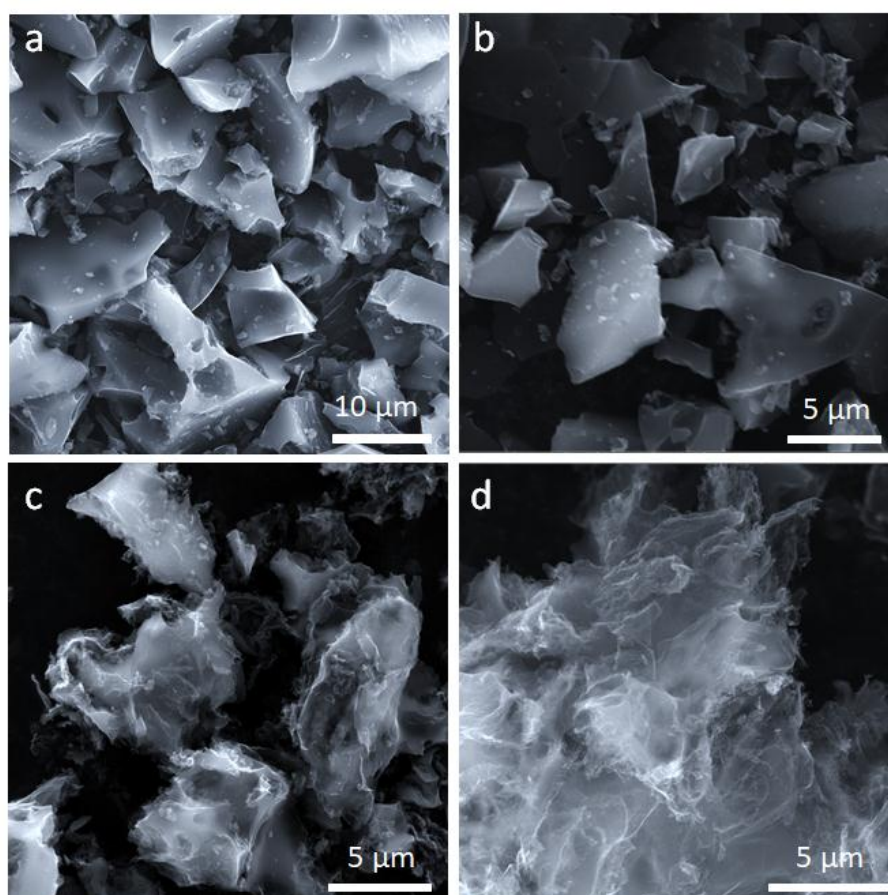


Figure S2. SEM images of the products obtained from different mass ratios of melamine: glycine. a) Absence of melamine. b) 1:1. c) 4:1. d) 8:1.

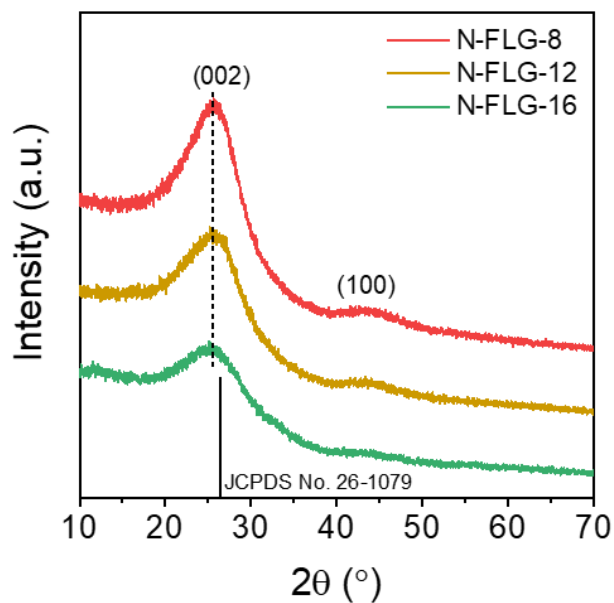


Figure S3. XRD patterns of N-FLG-8, N-FLG-12, and N-FLG-16.

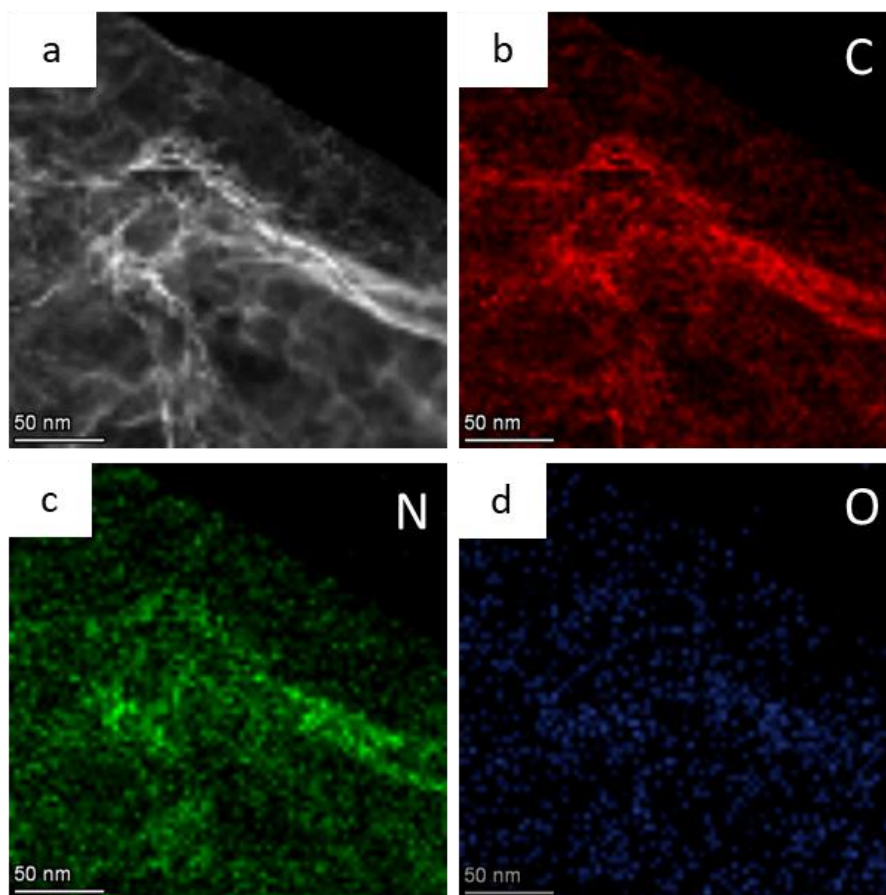


Figure S4. a) HAADF-STEM image of N-FLG-8 and its EDS element mapping images of b) carbon, c) nitrogen, and d) oxygen.

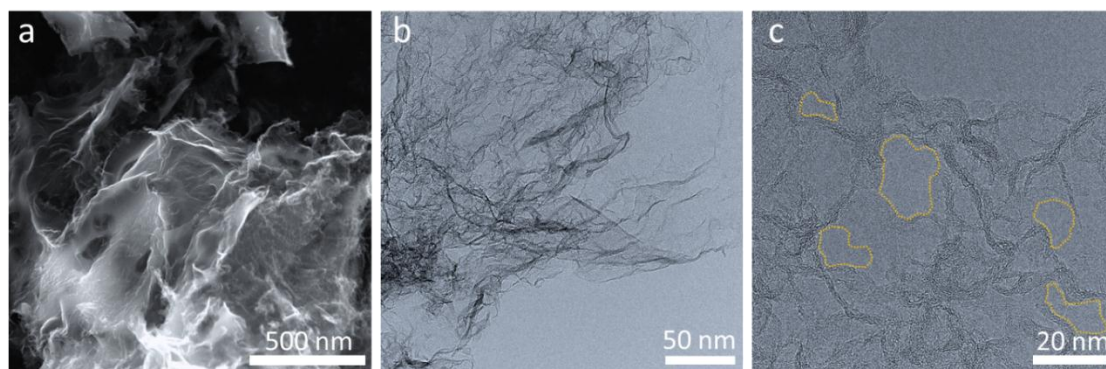


Figure S5. a) SEM, b) TEM, and c) high-resolution TEM images of N-FLG-12.

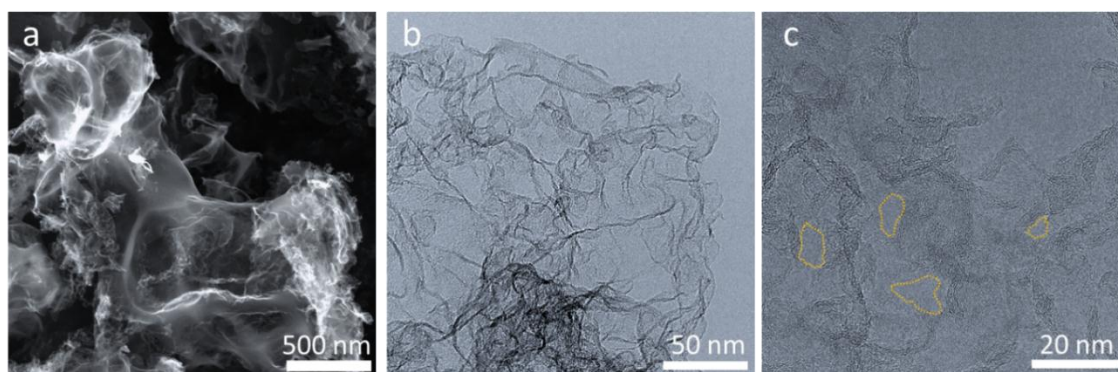


Figure S6. a) SEM, b) TEM, and c) high-resolution TEM images of N-FLG-16.

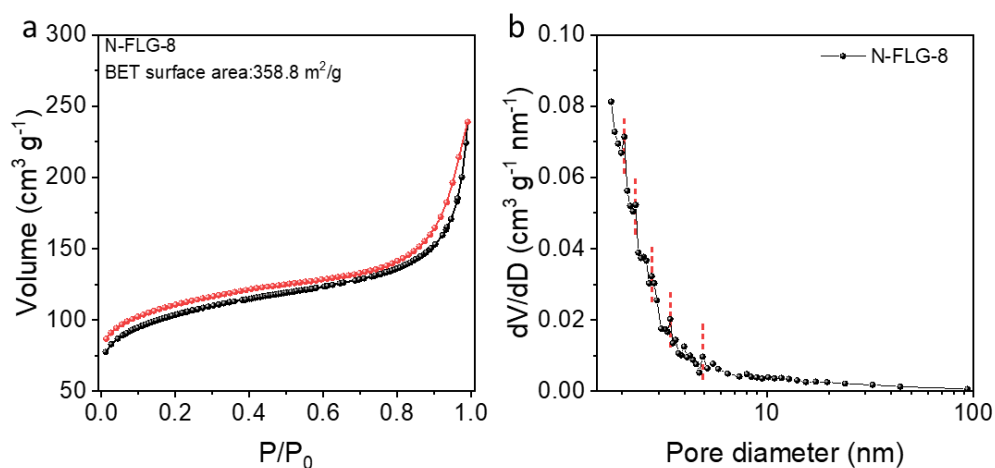


Figure S7. a) Nitrogen adsorption-desorption isotherm, and b) its corresponding pore distribution pattern of N-FLG-8.

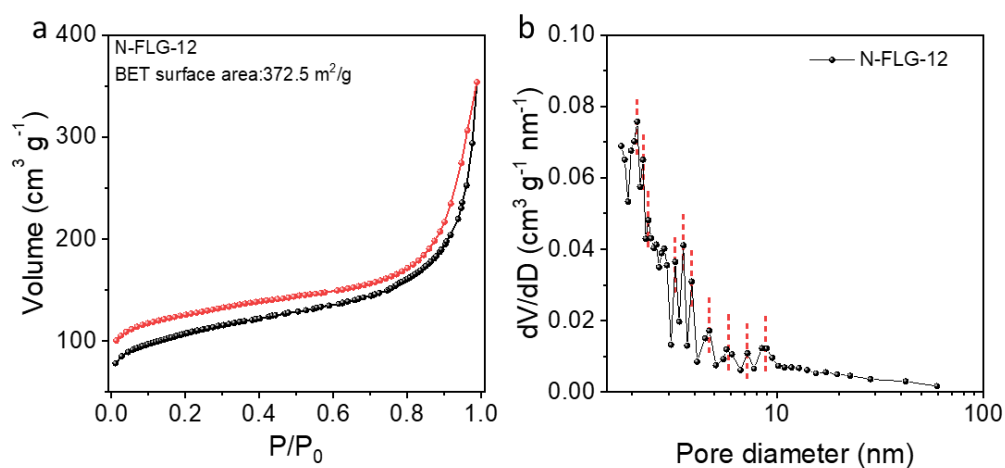


Figure S8. a) Nitrogen adsorption-desorption isotherm, and b) its corresponding pore distribution pattern of N-FLG-12.

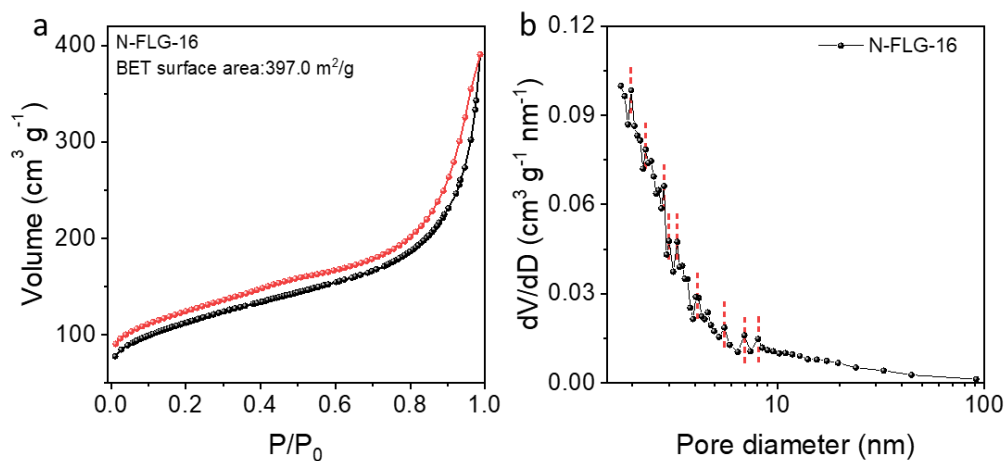


Figure S9. a) Nitrogen adsorption-desorption isotherm, and b) its corresponding pore distribution pattern of N-FLG-16.

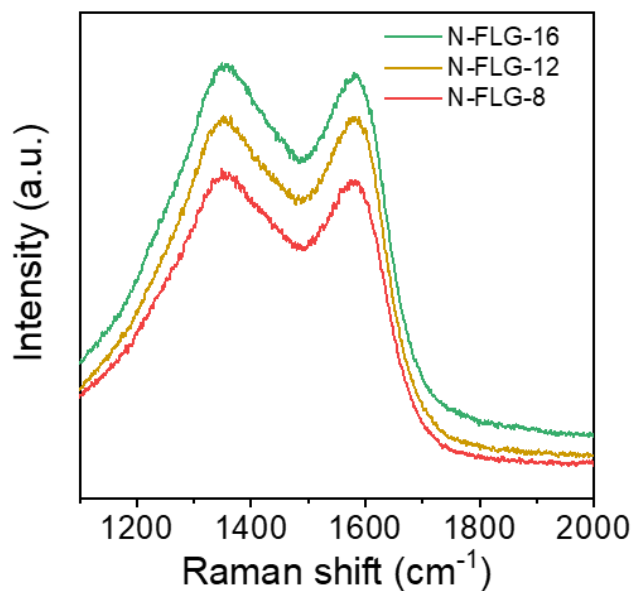


Figure S10. Raman spectra of N-FLG-8, N-FLG-12, and N-FLG-16 with I_D/I_G values of 1.01, 1.00, and 1.02, respectively.

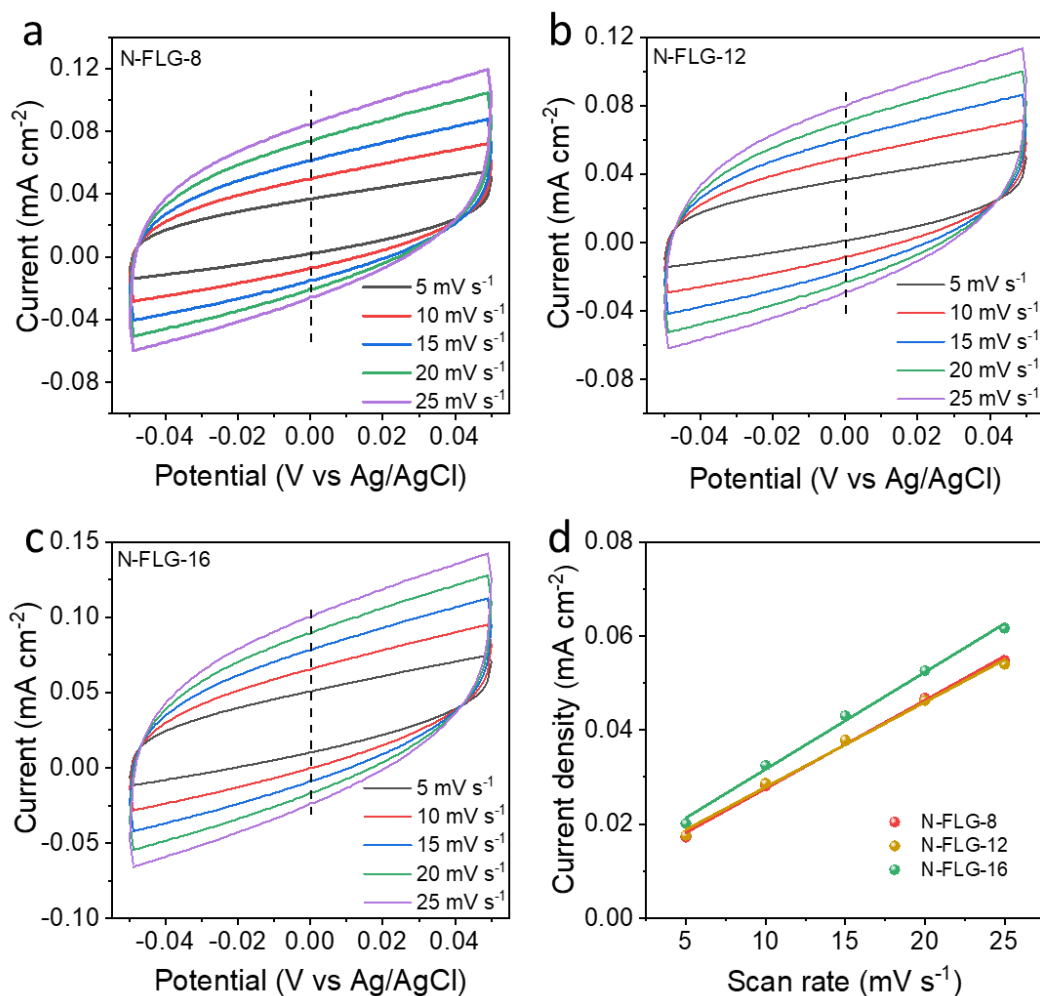


Figure S11. Determination of electrochemically active surface area. (a-c) CV curves of N-FLG-8, N-FLG-12 and N-FLG-16 obtained in the capacitance region at different scan rates. (d) The capacitance current densities ($(J_a - J_c)/2$) measured at 0 V vs. Ag/AgCl as a function of scan rate. Note that the slope value represents the double layer capacitance (C_{dl}), which is positively related with the electrochemically active surface area. The C_{dl} for N-FLG-8, N-FLG-12 and N-FLG-16 are calculated to be 1.88, 1.81 and 2.06 mF cm^{-2} , respectively.

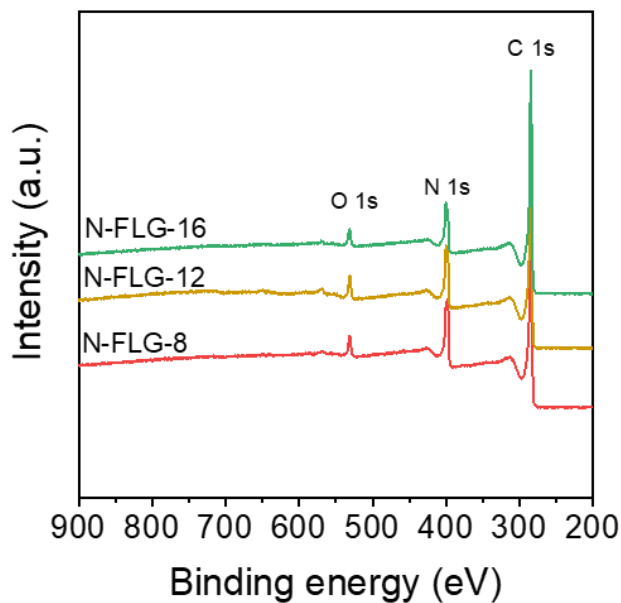


Figure S12. XPS survey spectra of N-FLG-8, N-FLG-12, and N-FLG-16.

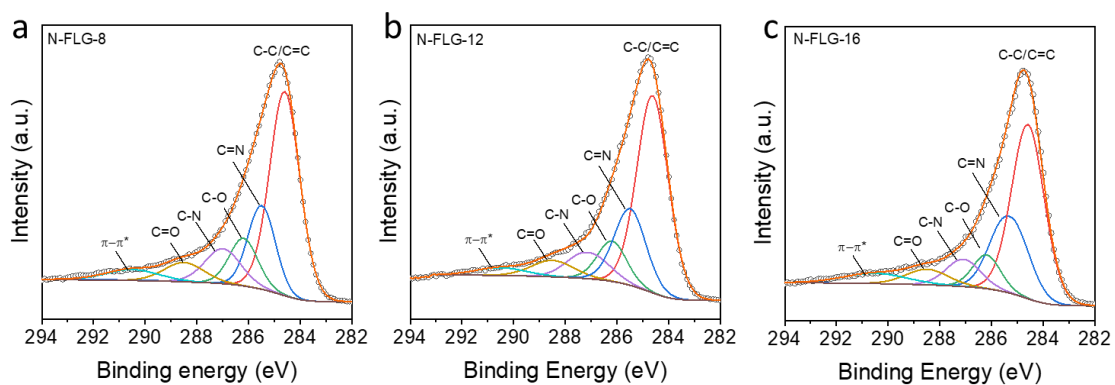


Figure S13. High-resolution C 1s XPS spectra of a) N-FLG-8, b) N-FLG-12, and c) N-FLG-16.

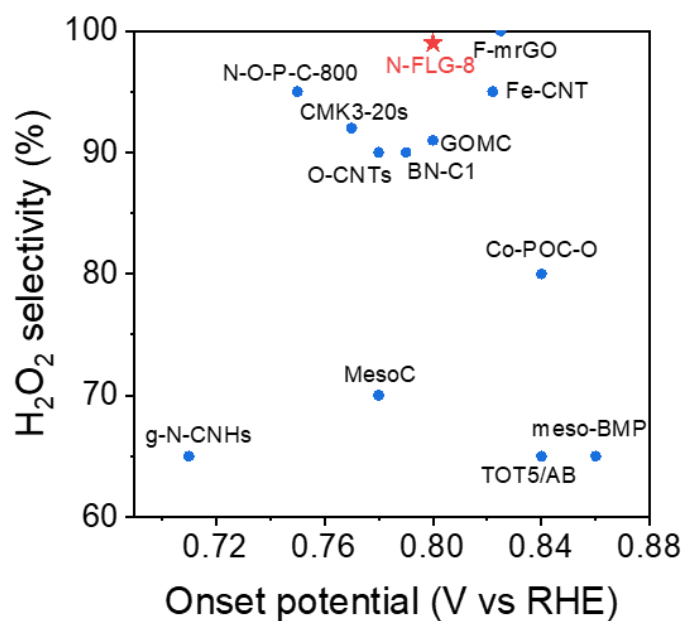


Figure S14. Comparison of the H₂O₂ selectivity on N-FLG-8 and other reported electrocatalysts in alkaline condition.

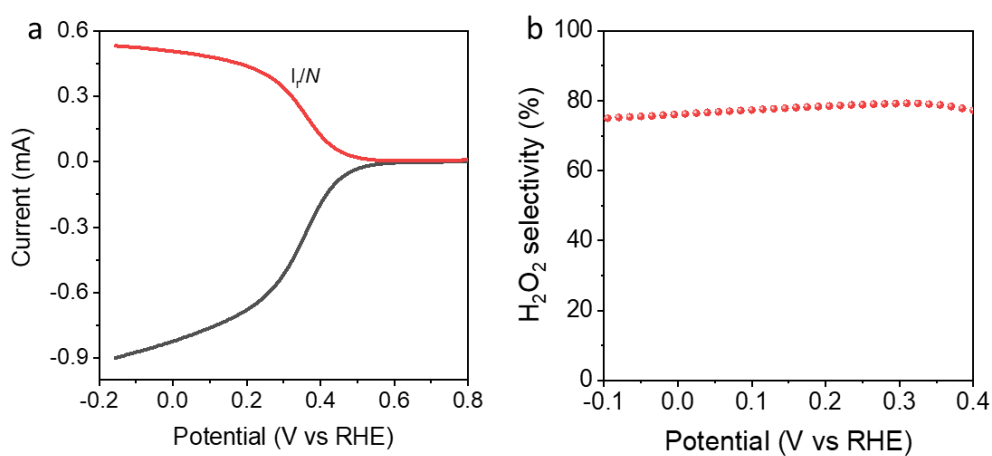


Figure S15. a) LSV curve of N-FLG-8 in 0.10 M Na₂SO₄, and b) its corresponding H₂O₂ selectivity.

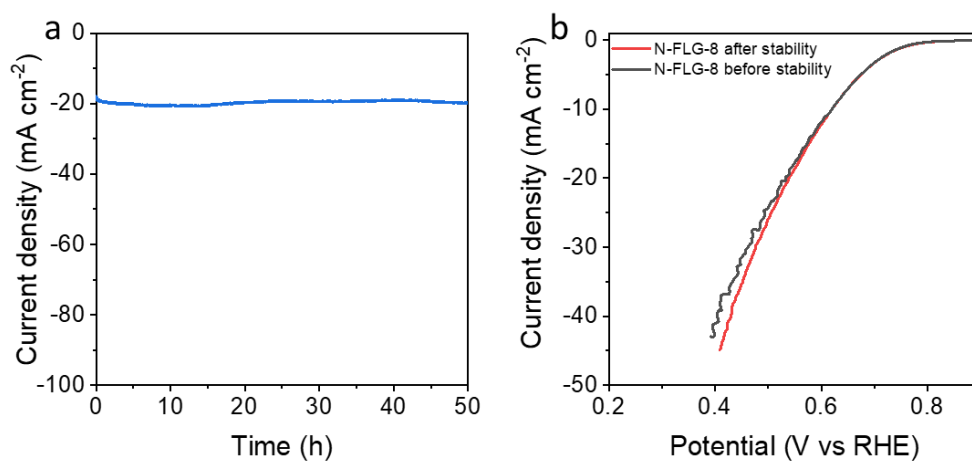


Figure S16. a) Stability test of N-FLG-8 on a GDL electrode. b) LSV curves before and after stability test.

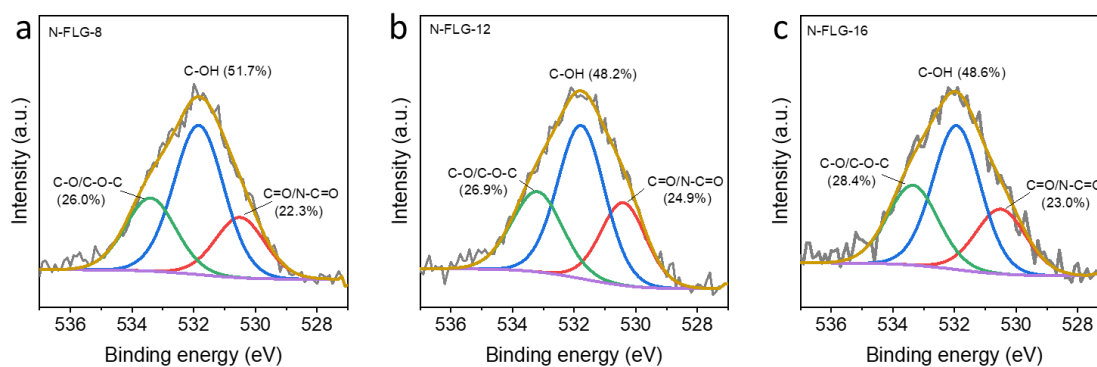


Figure S17. High-resolution O 1s XPS spectra of a) N-FLG-8, b) N-FLG-12, and c) N-FLG-16.

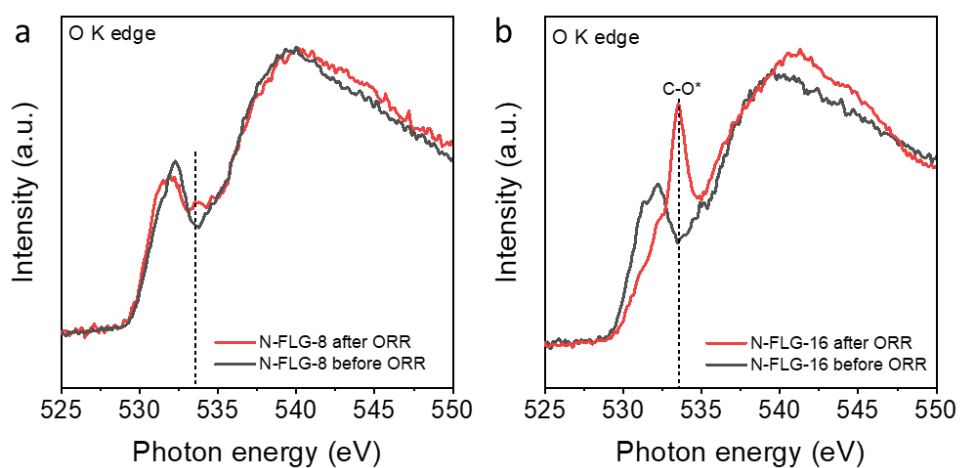


Figure S18. Oxygen K edge XANES spectra of a) N-FLG-8 and b) N-FLG-16 before and after ORR process.

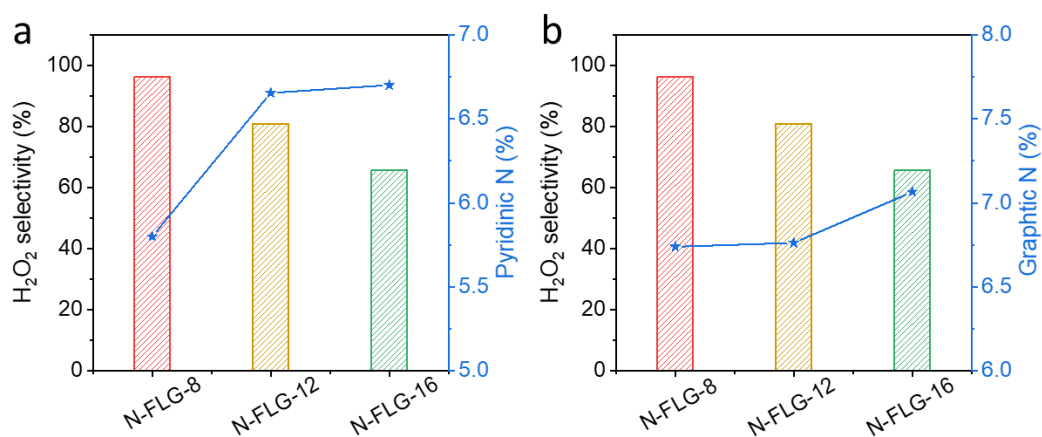


Figure S19. Relationship between H₂O₂ selectivity and atomic content of a) pyridinic N and (b) graphitic N.

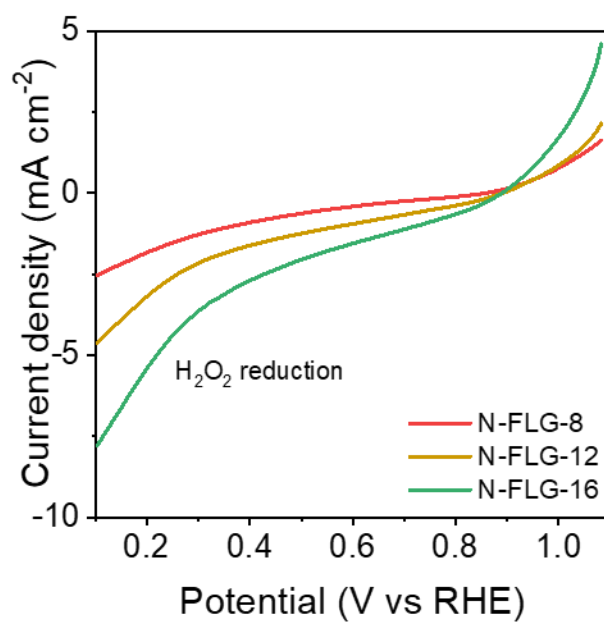


Figure S20. LSV curves of N-FLG-8, N-FLG-12, and N-FLG-16 in 0.10 M KOH containing 50 mM H₂O₂.

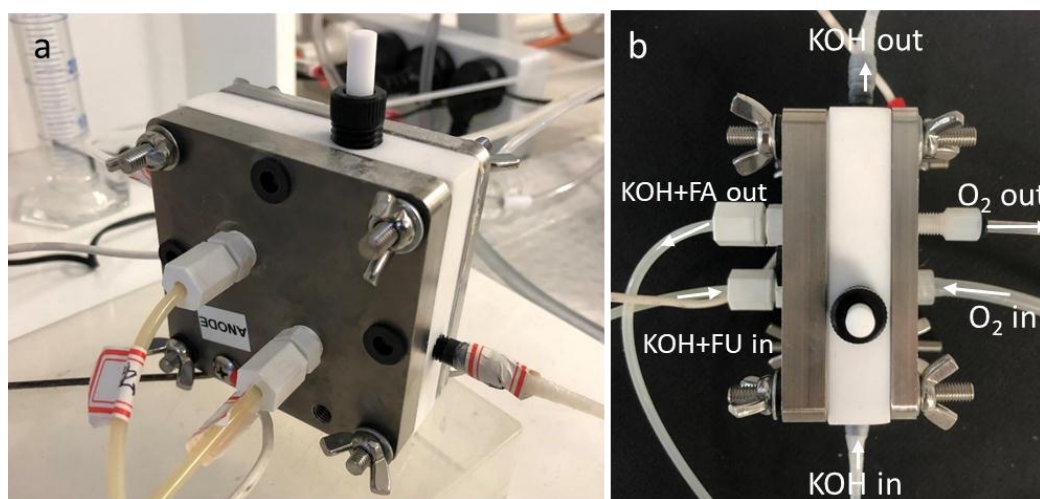


Figure S21. Digital photos of the assembled device.

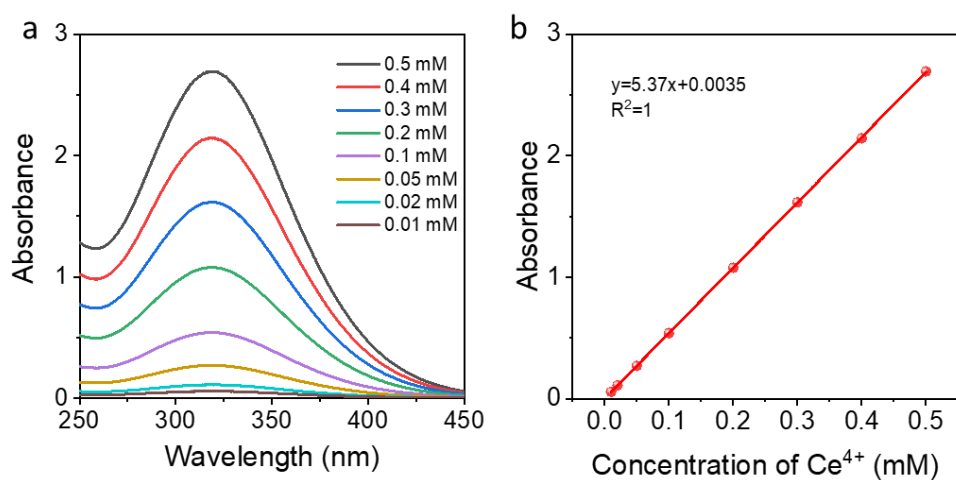


Figure S22. a) UV-vis spectra of Ce^{4+} solution with various concentrations and b) its corresponding standard curve.

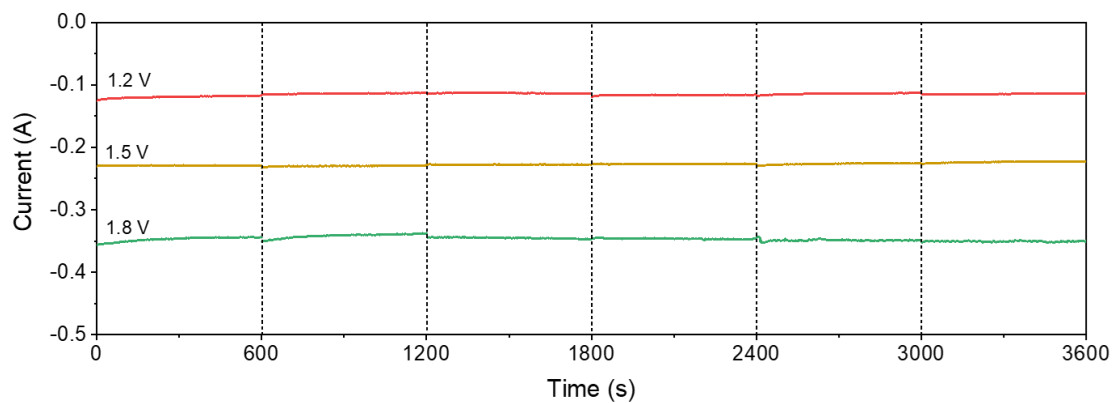


Figure S23. Current-time curves of N-FLG-8 in the flow cell configuration at cell voltages of 1.2, 1.5, and 1.8 V.

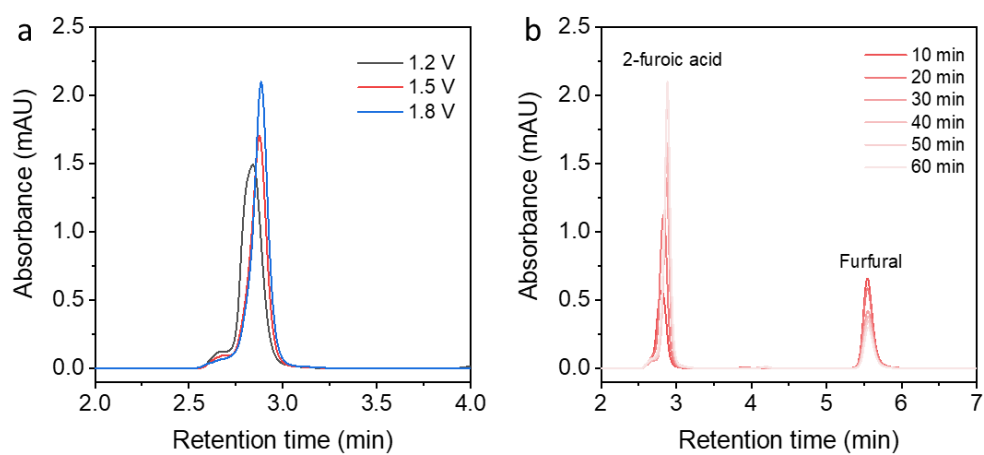


Figure S24. a) HPLC spectra of the anode electrolyte after electrolysis at cell voltages of 1.2, 1.5, and 1.8 V for 60 min. b) HPLC spectra of the anode electrolyte after electrolysis at cell voltage of 1.8 V for 10-60 min.

2. Supplementary Tables

Table S1. Atomic content of C, N and O for N-FLG-X according to XPS survey spectra.

Sample	C (at.%)	N (at.%)	O (at.%)
N-FLG-8	78.4	19.2	2.4
N-FLG-12	79.1	18.1	2.8
N-FLG-16	80.5	16.5	3.0

Table S2. Nitrogen content and percentage of different configurations for N-FLG.

Sample	Total N (at.%)	Pyridinic-N (%)	Pyrrolic-N (%)	Graphitic-N (%)	Pyridinic-N (at.%)	Pyrrolic-N (at.%)	Graphitic-N (at.%)
N-FLG-8	19.2	30.6	24.9	34.8	5.8	4.8	6.6
N-FLG-12	18.1	36.7	17.6	37.3	6.6	3.2	6.8
N-FLG-16	16.5	40.1	8.1	43.0	6.6	1.3	7.1

Table S3. Percentage of different bonds on C 1s spectra for N-FLG.

Sample	C–C/C=C (%)	C=N (%)	C–O (%)	C–N (%)	C–OOH (%)
N-FLG-8	49.3	19.1	10.2	10.3	6.2
N-FLG-12	50.9	20.2	9.8	8.9	5.8
N-FLG-16	48.8	24.5	8.0	7.9	5.6

Table S4. Summary and comparison of the H₂O₂ production performance of recently reported electrocatalysts.

Sample	Onset potential (V vs. RHE)	pH value	H ₂ O ₂ selectivity	Reference
N-FLG-8	0.8	13	>95%	This work
N-FLG-8	0.57	7	79%	This work
GOMC	0.77	13	92%	[S1]
O-CNTs	0.78	13	90%	[S2]
O-CNTs	0.52	7	85%	[S2]
g-N-CNHs	0.71	13	65%	[S3]
g-N-CNHs	0.53	7.4	80%	[S3]
F-mrGO	0.825	13	100%	[S4]
N-O-P-C-800	0.75	13	95%	[S5]
CMK3-20s	0.8	13	91%	[S6]
CMK3-20s	0.46	7	70%	[S6]
meso-BMP	0.86	13	~65%	[S7]
ToT5/AB	0.84	13	65%	[S8]
MesoC	0.78	13	70%	[S9]
Fe-CNT	0.82	13	95%	[S10]
Fe-CNT	0.52	7	90%	[S10]
Co-POC-O	0.84	13	80%	[S11]

Table S5. Summary and comparison of the bulk H₂O₂ production in flow cell system.

Catalysts	Anode reaction	Cell voltage (V)	Current density (mA cm ⁻²)	R_M (mol h ⁻¹ g ⁻¹ cat)	R_A (mmol h ⁻¹ cm ⁻²)	Faradaic efficiency (%)	Reference
N-FLG-8	FU oxidation	1.8	108.1	9.66	2.31	99.6	This work
N-FLG-8	FU oxidation	1.5	70.4	5.50	1.33	99.5	This work
N-FLG-8	FU oxidation	1.2	36.1	3.11	0.850	99.8	This work
N-FLG-8	FU oxidation	0.9	15.4	1.44	0.343	100	This work
CB-10%	OER	2.13	/	3.56	3.30	84	[S12]
CB-10%	HOR	0.61	/	3.66	3.40	90	[S12]
N-O-P-C-800	OER	1.3	/	0.54	/	93.1	[S5]
N-O-P-C-800	OER	2.5	/	0.8	/	94	[S5]
CMK3-20s	OER	1.8	/	1.28	/	91	[S6]
CMK3-20s	OER	2.4	/	1.8	/	95	[S6]
AC+VGCF	OER	/	59.4	/	0.228	26.5	[S13]
IGDE	OER	/	52	/	0.465	98.7	[S14]
AC(3.8 M HNO ₃)+VGCF	OER	/	40	/	0.6	31	[S15]
Co-C	HOR	0.1	30	0.06	0.2	30	[S16]
CoTPP/KB	HOR	/	95	/	0.95	55	[S17]
MnCl-OEP/AC	HOR	/	56.1	/	0.356	34.1	[S18]
CoN ₂ C _x	HOR	/	80	/	0.47	32	[S19]
VGCF+XC72	HOR	/	100	/	2	94	[S20]

Note: R_M is the H_2O_2 production rate normalized to the catalyst mass; R_A is the H_2O_2 production rate normalized to the electrode geometric area; OER is oxygen evolution reaction; HOR is hydrogen oxidation reaction.

3. Supplementary Reference

- [S1] Y. J. Sa, J. H. Kim, S. H. Joo, *Angew. Chem. Int. Ed.* **2019**, *58*, 1100.
- [S2] Z. Lu, G. Chen, S. Siahrostami, Z. Chen, K. Liu, J. Xie, L. Liao, T. Wu, D. Lin, Y. Liu, T. F. Jaramillo, J. K. Nørskov, Y. Cui, *Nat. Catal.* **2018**, *1*, 156.
- [S3] D. Iglesias, A. Giuliani, M. Melchionna, S. Marchesan, A. Criado, L. Nasi, M. Bevilacqua, C. Tavagnacco, F. Vizza, M. Prato, P. Fornasiero, *Chem* **2018**, *4*, 106.
- [S4] H. W. Kim, M. B. Ross, N. Kornienko, L. Zhang, J. Guo, P. Yang, B. D. McCloskey, *Nat. Catal.* **2018**, *1*, 282.
- [S5] H.-X. Zhang, S.-C. Yang, Y.-L. Wang, J.-C. Xi, J.-C. Huang, J.-F. Li, P. Chen, R. Jia, *Electrochim. Acta* **2019**, *308*, 74.
- [S6] Y.-L. Wang, S.-S. Li, X.-H. Yang, G.-Y. Xu, Z.-C. Zhu, P. Chen, S.-Q. Li, *J. Mater. Chem. A* **2019**, *7*, 21329.
- [S7] F. Hasché, M. Oezaslan, P. Strasser, T.-P. Fellingner, *J. Energy Chem.* **2016**, *25*, 251.
- [S8] T. Murata, K. Kotsuki, H. Murayama, R. Tsuji, Y. Morita, *Commun. Chem.* **2019**, *2*, 46.
- [S9] S. Chen, Z. Chen, S. Siahrostami, T. R. Kim, D. Nordlund, D. Sokaras, S. Nowak, J. W. F. To, D. Higgins, R. Sinclair, J. K. Nørskov, T. F. Jaramillo, Z. Bao, *ACS Sustainable Chem. Eng.* **2018**, *6*, 311.
- [S10] K. Jiang, S. Back, A. J. Akey, C. Xia, Y. Hu, W. Liang, D. Schaak, E. Stavitski, J. K. Nørskov, S. Siahrostami, H. Wang, *Nat. Commun.* **2019**, *10*, 3997.
- [S11] B.-Q. Li, C.-X. Zhao, J.-N. Liu, Q. Zhang, *Adv. Mater.* **2019**, *31*, 1808173.
- [S12] C. Xia, Y. Xia, P. Zhu, L. Fan, H. Wang, *Science* **2019**, *366*, 226.
- [S13] I. Yamanaka, T. Murayama, *Angew. Chem. Int. Ed.* **2008**, *47*, 1900.
- [S14] H. Luo, C. Li, C. Wu, X. Dong, *RSC Adv.* **2015**, *5*, 65227.
- [S15] T. Murayama, I. Yamanaka, *J. Phys. Chem. C* **2011**, *115*, 5792.

- [S16] W. Li, A. Bonakdarpour, E. Gyenge, D. P. Wilkinson, *ChemSusChem* **2013**, *6*, 2137.
- [S17] T. Iwasaki, Y. Masuda, H. Ogihara, I. Yamanaka, *Electrocatalysis* **2017**, *9*, 236.
- [S18] I. Yamanaka, T. Onizawa, H. Suzuki, N. Hanaizumi, N. Nishimura, S. Takenaka, *J. Phys. Chem. C* **2012**, *116*, 4572.
- [S19] I. Yamanaka, S. Tazawa, T. Murayama, T. Iwasaki, S. Takenaka, *ChemSusChem* **2010**, *3*, 59.
- [S20] I. Yamanaka, *Catal. Surv. Asia* **2008**, *12*, 78.

Chapter 7: Conclusion and Perspective

7.1 Conclusions

This Thesis focuses on the design, synthesis, and application of novel nanostructured materials for electrocatalytic production of portable fuels and value-added chemicals and the mechanistic understanding of these electrocatalysis processes. On basis of the works in this Thesis, following conclusions can be drawn:

1. Two-dimensional mosaic Bi nanosheets could be a superior NRR electrocatalyst after smart surface and electronic structure engineering. The high performance of Bi NS towards NRR could be attributed to the sufficient exposure of edge sites coupled with effective *p*-orbital electron delocalization. The semiconducting feature, which limits surface electron accessibility, effectively enhances the Faradaic efficiency. Both the structure engineering and electronic structure modulation should be considered when investigating the performance of a specific family of materials for electrocatalytic NRR.
2. Trace amount of nitrate and nitrite contamination in some commercial lithium salts were systematically identified, quantified and eliminated towards more reliable electrocatalytic NRR study. Even though those impurities exist in ppm or lower level, they could cause significant false positive results with deceptive reproducibility and accumulative effect, which may misguide researchers. The possible nitrate and nitrite contamination in the electrolyte can be efficaciously prejudged by simple spectrophotometric methods and can be effectively removed. Understanding the negative results is just as important as identifying positive results, especially at the current stage of NRR research.
3. A smart two-step N₂-to-NH₃ fixation through serial integration of plasma-driven N₂ oxidation with electrocatalytic nitrogen oxyanions reduction to ammonia was demonstrated, enabling facile N₂ activation and efficient and selective NH₃ production in each step. A novel

surface B-rich core-shell nickel boride nanoparticle electrocatalyst was developed and delivered a significant ammonia yield with high Faradaic efficiency. It is revealed that Ni sites are responsible for water dissociation to provide protons for NO_x^- hydrogenation. The enriched electron-deficient B sites on the surface could not only enhance adsorption of NO_x^- , but also suppress surface oxidation of Ni^0 sites and prevent overactive hydrogen evolution. The synergistic contribution from Ni and B sites lead to excellent activity, selectivity, and durability for eNO_xRR to NH_3 .

4. Porous N-rich few-layered graphene with controllable morphology, nanostructure and composition have been fabricated by a facile $\text{g-C}_3\text{N}_4$ -templated method. By changing the mass ratio of the precursor materials, the content of pyrrolic-N can be selectively tuned. H_2O_2 selectivity could be effectively facilitated with the presence of the high amount of pyrrolic-N. The selective nitrogen configuration tuning method and the identification of the favorable effect of pyrrolic-N to two-electron ORR pathway provide new ideas for the design of advanced carbon-based electrocatalysts for various electrochemical and catalytic applications.

In summary, these systematic works in this Thesis shed lights on the development of efficient electrocatalysts towards the production of portable fuels and value-added chemicals by rational materials design, advanced characterizations, and elaborate mechanism investigation.

7.2 Perspectives

Despite considerable progresses have been achieved in the research area of electrocatalytic nitrogen fixation and oxygen reduction, additional work needs to be done to expand the library of electrocatalytic refinery for sustainable production of fuels and value-added chemicals.

1. Expanding the library of nanostructured materials is still the key bone as the reaction performance depends heavily on the surface physicochemical properties of electrocatalysts. In this regard, exploring new material systems or smart modification methods based on existing

materials may provide opportunities to harvest new electrocatalysts with more favourable catalytic activity. Meanwhile, other factors that influence the activity and selectivity should also be considered, such as the electrolyte or solvent effect, the heterogenous interface, the applied bias potentials, the mass transfer of reactant, the reactor configurations.

2. To explore promising electrocatalysts, the atomic and molecular level understanding of the catalytic process is prerequisite and necessary. In situ/operando microscopic and spectroscopic techniques such as in situ X-ray microscopy, electron microscopy, SEIRS, SERS, etc, provide great chance monitoring the evolution of electrocatalyst surface, probing the key reaction intermediates, and identifying the real active sites. In addition, the recently developed operando computational modelling also provides critical insights on reaction thermodynamics and kinetics. Combining the above in situ characterizations with operando theoretical simulations, catalytic mechanisms under working conditions can be effectively and exclusively refined and identified, thus boosting the optimization of electrocatalysts.

3. Besides the nitrogen- and oxygen-based resources like N_2 and O_2 , carbon-based feedstock such as CO_2 can also be involved for production of various chemicals. For example, electrocatalytic coupling of CO_2 with N_2 provides an intriguing approach for direct urea production under ambient conditions. In the future, a wide range of integrated electrocatalytic processes can be further explored based on the bond cleavage and formation processes between C, H, O, N coupling to produce more complex and valuable fuels or chemicals such as $C_xH_yO_z$ (alcohols, aldehydes, carboxylic acids), $C_xN_yH_z$ (amines, nitriles), and $C_xN_yH_zO$ (amides).

To sum up, combining rational catalyst design and advanced characterizations, more advances in electrocatalysis are worthfully anticipated. Production of sustainable fuels and valuable chemicals from abundant feedstocks (eg. N_2 , O_2 , H_2O , CO_2 , biomass) through renewable energy driven electrocatalysis approach will substantially facilitate the development of neutral carbon footprints and sustainable society.

Appendix: Publications during PhD Candidature

- [1] **Laiquan Li**, Cheng Tang, Bingquan Xia, Huanyu Jin, Yao Zheng, Shi-Zhang Qiao.* Two-Dimensional Mosaic Bismuth Nanosheets for Highly Selective Ambient Electrocatalytic Nitrogen Reduction. *ACS Catalysis* 2019, 9, 2902-2908.
- [2] **Laiquan Li**, Cheng Tang, Dazhi Yao, Yao Zheng, Shi-Zhang Qiao.* Electrochemical Nitrogen Reduction: Identification and Elimination of Contamination in Electrolyte. *ACS Energy Letters* 2019, 4, 2111-2116.
- [3] **Laiquan Li**, Cheng Tang, Yao Zheng, Bingquan Xia, Xianlong Zhou, Haolan Xu, Shi-Zhang Qiao.* Tailoring Selectivity of Electrochemical Hydrogen Peroxide Generation by Tunable Pyrrolic-Nitrogen-Carbon, *Advanced Energy Materials* 2020, 10, 2000789.
- [4] **Laiquan Li**, Cheng Tang, Xiaoyang Cui, Yao Zheng, Xuesi Wang, Haolan Xu, Shuai Zhang, Tao Shao, Kenneth Davey, Shizhang Qiao.* Efficient Nitrogen Fixation to Ammonia through Integration of Plasma Oxidation with Electrocatalytic Reduction. *Angewandte Chemie* 2021, 60, 14131-14137.
- [5] **Laiquan Li**, Cheng Tang,* Huanyu Jin, Shi-Zhang Qiao.* Main Group Elements Boost Electrochemical Nitrogen Reduction. *Chem* 2021, minor revision before acceptance.
- [6] Huanyu Jin,[†] **Laiquan Li**,[†] Xin Liu,[†] Cheng Tang,[†] Wenjie Xu, Shuangming Chen, Li Song, Yao Zheng, Shi-Zhang Qiao.* Nitrogen Vacancies on 2D Layered W₂N₃: A Stable and Efficient Active Site for Nitrogen Reduction Reaction. *Advanced Materials* 2019, 31, 1902709. ([†] Equal contribution)
- [7] Dazhi Yao,[†] Cheng Tang,[†] **Laiquan Li**,[†] Bingquan Xia, Anthony Vasileff, Huanyu Jin, Yanzhao Zhang, Shi-Zhang Qiao.* In Situ Fragmented Bismuth Nanoparticles for Electrocatalytic Nitrogen Reduction, *Advanced Energy Materials* 2020, 10, 2001289. ([†] Equal contribution)
- [8] Cheng Tang,[†] Ling Chen,[†] Haijing Li,[†] **Laiquan Li**,[†] Yan Jiao, Yao Zheng, Haolan Xu,

Kenneth Davey, Shi-Zhang Qiao.* Tailoring Acidic Oxygen Reduction-selectivity on Single-Atom Catalysts via Modification of First and Second Coordination Spheres, *Journal of the American Chemical Society* 2021, *143*, 7819-7827. († Equal contribution)

[9] Huanyu Jin, Xin Liu, Shuangming Chen, Anthony Vasileff, **Laiquan Li**, Yan Jiao, Li Song, Yao Zheng, Shi-Zhang Qiao.* Heteroatom-doped Transition Metal Electrocatalysts for Hydrogen Evolution reaction. *ACS Energy Letters* 2019, *4*, 805-810.

[10] Huanyu Jin, Xuesi Wang, Cheng Tang, Anthony Vasileff, **Laiquan Li**, Ashley Slattery, Shi-Zhang Qiao.* Stable and Highly Efficient Hydrogen Evolution from Seawater Enabled by an Unsaturated Nickel Surface Nitride. *Advanced Materials* 2021, *33*, 2007508.